STRATIFIED WAVY OIL-WATER FLOWS

Chemical Engineering
University College London

Ph. D. Thesis

Alberto Hernández Barral

2014

Statement

I, Alberto Hernández Barral, declare and confirm that the work presented in this Thesis is my very own.

Whenever information provided has been consciously taken from other sources, as to show previous work, present other author's results or make comparisons or a point for discussion, etc., it has been so indicated in the text.

Alberto Hernández Barral
September, 2014

ABSTRACT

The structure of the oil-water interface of stratified flows in a 38 mm ID pipe is investigated in this Thesis with double-wire conductance probes. The fluids used – tap water and Exxsol™ D140 oil (ρ_o = 830 kgm^{-3}; μ_o = 0.0055 $kgm^{-1}s^{-1}$) – are pumped into the facility and brought together in a "Y" inlet section, designed to minimize the mixing between phases (r = 0.6 – 2.4; U_{mix} = 0.5 – 2.5 ms^{-1}). The piping is made of acrylic and the flow was observed with the aid of high-speed imaging. The waves seen on the oil-water interface further downstream the inlet consists of small 3D fluctuations, rather than 2D structures. Conductance probes are used to investigate the oil-water interface in cases where clear wavy structures cannot be followed or analyzed. The signal of interface height in time is found to be stationary and follow a Gaussian distribution when the signal is collected at 256 Hz during 4 min. Based on these properties, a thorough methodology for analysis is presented, which allows estimating time-average parameters of the flow and the power spectrum of the interface. This analysis reveals that, in fully-developed flow conditions, oil and water phases show very little slip and tend to flow both at roughly the mixture velocity regardless of the flow conditions. The power spectrum detects a unique frequency of 19 Hz, but reveals that mechanic vibrations propagating through the facility are a major contribution to the structure of the interface.

The 19 Hz frequency corresponds to clearly identifiable waves that develop at the inlet section only if the oil-to-water input ratio is different from 1. The power spectrum at the inlet tends to be dominated by this frequency. This finding is verified with the information of high-speed images. Wave characteristics and their evolution along the inlet are determined from high-speed images collected with a Phantom Miro 4 camera at 1,000 – 1,200 fps. The theoretical analysis of the stability of inlet waves suggests that their origin is a Kelvin-Helmholtz instability and characterizes the waves as dynamic in nature. The two types of oil-water interfaces seen (i.e. that at the inlet with 2D waves and that downstream the pipe with small 3D contributions) are discussed in this Thesis at length and abundant details are given.

TABLE OF CONTENTS

LIST OF FIGURES AND TABLES

CHAPTER 2: LITERATURE REVIEW

CHAPTER 3: EXPERIMENTAL FACILITY AND INSTRUMENTATION

CHAPTER 4 EXPERIMENTAL OBSERVATIONS

CHAPTER 5: DEVELOPMENT OF SIGNAL ANALYSIS METHODOLOGY

CHAPTER 6: TIME-AVERAGE FLUW PARAMETERS AND THE POWER SPECTRUM OF THE INTERFACE

APPENDIX 5: TWO-FLUID MODEL

APPENDIX 6: CONFERENCE PAPERS

LIST OF SYMBOLS

Most of the symbols employed in this Thesis to address mathematical operations, flow parameters or physical properties are widely used with the same or similar meaning in the literature. Only the letter **L** is used to refer to "litres", instead of **l**, as in $Lmin^{-1}$, in order to avoid confusion with the number 1.

All symbols used are explained in the text. However, a list of most used symbols is presented below for convenience.

A	Cross-sectional area
A_o, A_w	Area occupied by oil, water
b_0, b_1	Coefficients of linear regression
C_v	Wave velocity
D	Pipe diameter
f	Frequency
f_j	Correction fraction
f_s	Sampling frequency
$f_{\nabla\alpha}$	Stabilizing fore
FFT	Fast Fourier Transform
h_i	Interface height
$\bar{h}$	Total average interface height of all intervals
$\bar{h}_i$	Average interface height of an interval
$\overline{\overline{H}}$	Time-averaged interface height
i, j	Subscripts
KH	Kelvin-Helmholtz
m, m', M, M'	Number of intervals
m	Number of degrees of freedom
n, n', N, N'	Number of data points
Q_i	Normalized parameter
Q_o	Oil flow rate

Q_w	Water flow rate
r	Volume flow-rate input ratio
$r_{t,h}$	Input ratio of highest mixture velocity at which transition occurs
R	Mass flow-rate input ratio
R_{yy}	Auto-correlation function of data
Re	Reynolds number
Re_{so}, Re_{sw}	Superficial Reynolds number of oil, water
Re_o, Re_w	Actual Reynolds number of oil, water
s, s'	Standard deviations
S_o, S_w	Wetted perimeter of oil, water
S_i	Length of the interface
t, T	Time
t	t-distribution
u	Velocity
U_{mix}	Mixture velocity
u_{so}, u_{sw}	Superficial velocity of oil, water
u_o, u_w	Actual velocity of oil, water
W_u	Weighted mean velocity
y	Probe signal and data
y_n	n-Data point of probe signal
Y_n	De-trended n-data point of probe signal
y_c	Data point after correction factor
$\bar{y}_w$	Interface height at 100 % water during the calibration
$\tilde{y}_n$	Linear regression n-data point

Greek symbols

α	Level of significance
α_w	Water fraction
λ_w	Water cut
λ_o	Oil cut
μ_{hi}	Mean of average-interface-height distribution
μ_o, μ_w	Viscosity of oil, water
ν_o, ν_w	Kinematic viscosity of oil, water

π	Pi
ρ_o, ρ_w	Density of oil, water
ρ_r	Relative density of oil respect to that of water
σ^2_{hi}	Variance of average-interface-height distribution
Σ	Summation
χ^2	Chi-square distribution
Δt	Sampling time
ω_{hi}	Absolute uncertainty of interface height

PREFACE

-- Nihil sapientiae odiosius acumine nimio --

This is me standing before a reproduction of the water tank devised by Osborne Reynolds to conduct his famous dye experiments many years ago. The photograph was taken on a sunny Sunday afternoon (School of Mechanical, Aerospace and Civil Engineering (MACE), University of Manchester, Manchester, 17/08/2014).

This Thesis was successfully defended at University College London on 22nd July 2014.

ACKNOWLEDGEMENTS

It is certainly not an easy task to complete a PhD. The process is heavy with obscurities: some are derived from the research itself while others, the daunting ones, are born from all the uncertainties of the process, quite often depending on our own personal circumstances. The waters are never still. The PhD tends to be an experience rather than an occupation, and is entangled in our lives of the period, like the fibres of cellulose are woven in lignin. Some people –I have noticed–, the youngest especially, change and become more mature during the period. Those who are married or engaged reserve the best part of the work –the dedicatory and warmest words– to their families, fiancées or children. I have witnessed the extent to which the PhD emotions can permeate personal life. Hardly any feeling or decision concerning the PhD is isolated from the rest and this is what really makes it an ordeal for some of us. This is especially true at an age and in a time where youngsters are devoid of references and cannot really find what they want. In my particular case, the PhD penetrated my skin and crawled through my veins all the time. It was never an easy or superficial thing.

At the time I write this, more than one month has elapsed since I defended this Thesis. There is, finally, light in the horizon. Looking back, despite all difficulties, there are a few very positive accomplishments, a good number of great human experiences and some new opportunities to be pursued, all of which makes the decision to do a PhD a worthy one. I feel truly grateful to Professor Panagiota Angeli, my supervisor, first for giving me the opportunity to come to London, relate to the Chemical Engineering Department at University College London and grant me access to the combined scholarship with the Chevron Technology Company.

Most importantly, Angeli cared as much as I did about my PhD. This is something that I feel lucky about because, truth to be said, it is not the case of everyone. I thank her for all the weekly meetings, her dedication and close guidance. We managed to complete the final writing of this Thesis and publications during the last year 2014, with me already away in Manchester for work, which is something that could have not been possible or at least much more difficult without her determination and help.

The materials of this Thesis have been subjected to an important process of revision and corrections. This does not mean that the contents cannot be further improved or that are necessarily free from error, but gives indication of the level of thoughtfulness attempted. The text presented is the fruit of multiple discussions, journal peer reviews, conferences presentations and the Viva defence itself. In this sense, I feel satisfied with the seriousness of the work and I would be quite happy if the results and methodology are useful to others. Angeli is the first to be thanked for the output. Additionally, I would like to express my sincere gratitude to Dr. Lee Rhyne, of the flow assurance team of Chevron Technology Company, for all the meetings and time he has shared with us, his suggestions, support and kindness. Thanks go also to Dr. Karolina Ioannou (Chevron) and to Dr. Buddhika Hewakandamby (University of Nottingham) and Dr. George Manos (UCL) for their careful comments and corrections to the final version of the Thesis.

The work presented here is experimental. Perhaps triggered by the modern urgency to publish results, the classic problems of the epistemology are sometimes largely ignored and the role of instrumentation quite often misinterpreted. There are examples in this Thesis of the benefits that close attention to experimental measurements can bring to the research (see, for example, the section of trend removal in 5.2.1). I would like to thank Dr. Simon Barrass for all his wonderful help in the lab with instrumentation (he is a sharp man) and to Mike Gorecki for his practical suggestions. Thanks go to Graeme Smith, Erick Hermann and Elaine Briggs for all their kind help with the rig, orders and related projects. My appreciation goes to John Langdon for his help in the rig and, in a special manner, for his preparation of the inlet drawings that can be found in Chapter 3.

The high-speed equipment and the PIV system belonged to EPSRC. The scheme is wonderfully useful to all research community and I thank Adrian Walker and Paul Adkin (EPSRC) for their attention and for putting up with bad habits of students. Personal thanks go to Martin Hyde and Pratik Patel (TSI) for all the time they spent with us, and also to Gareth Morris (TSI). The work of Martyn Vale and Dave Ellis (IT Department) came at times when mostly needed.

My gratitude goes to all staff of the Chemical Engineering Department. Particularly, I am in debt to Pat Markey for attending the so many requests that I had for her. Thanks to Agatha Blaszczyk and Mae Oroszlany for helping with that bothersome part of orders and invoices and thanks indeed to Nelly – Nélida Martínez Rivera, her real, beautiful name– for print-outs and bindings.

The completion of the PhD is designed to be an individual accomplishment and there is no lack of opportunities to prove your stamina or to manage stress, strain or feelings of isolation. Difficulties are always an opportunity to improve, to achieve and, in the end, to seek satisfaction. But, lo and behold, true help received from people in the struggle –generous and genuine– is always the most memorable part and the soil from which gratitude blossoms in tender stems of green leaves. I am not talking about *quid pro quo* forms of relationships or the pragmatic help that one searches to avoid pain or to dodge fear. It is rather the help that does not duck the fight and let you go on your own. In this sense, starting from the end, I thank my dear friend Luigi Gargiulo for his invaluable favours during the final review and printing of the Thesis and his home made B&B for any of my excursions to London. Many thanks go to my fellow friend and countryman, Dr. Miguel Ardid, who submitted the Thesis on my behalf in a historical, glorious day. It is proper to say that he showed me some of the most lovable places that I know in London to eat, drink or just be. My invaluable friend Dr. Valentina Dore deserves an entire volume of appreciations that started my very first day at UCL. She helped me with almost everything and there is nothing else I could say to make her justice.

In the chapter of collaborations, I have a long list of acknowledgments to make. I thank my friend Lawrence Edomwonyi-Otu, for all his comments and discussions and, especially, for his trust. Thanks also to him, Maxime Chinaud and Kyeong Park for all their time and help in the lab during the spring and summer of 2013. Thanks to Dimitris Tsaoulidis, for his assistance with speed cameras and the tensiometer. I have warm memories of the students with whom I spent some time in the lab. I particularly thank Aaron Ebenezer for all his work and help with measurements on high-speed images. With Sam Bailey and Huma Akhtar we first cleaned the installation in the pre-historic age. The beginnings of imaging collection and the analysis of probe data took place with Cloe Dulcide and my friend David Kenny Onyekpe, to whom I also owe the possibility of working with MatLab® from

home. The mighty discovery of waves at the inlet with no split plate came in the era of Amanda Vo, Aaron Ebenezer and Chetan Kalsi. They took a couple of the photographs with inlet waves shown in Chapter 4. I would like to include in the list the brothers Saji and Rayan Khoury, students of Civil Engineering at Imperial College, whom I helped with their Fluid Mechanics and Statistics courses. It gave me ideas to my research and was a memorable experience but, most important, those tutorials gave me the sense of accomplishment that I so badly needed to carry on.

Finally, my sincere thanks to all friends with whom I crossed paths for a short or a long time and to those who had warm words for me when it was cold or just a smile in the dark. I can only name a few: Valentina Dore, María Atance, Hilary Rosen, Ana Gutiérrez, Miguel Ardid, Luigi Gargiulo, Marco Timillero, Eleftheria Polykarpou, Shane Morrin, Rema Abdulaziz, Chara Psyrraki, Alexander Nimmo, Sergio de Andrés, Sara Evangelisti, Sara Budinis, Marco Rotondi, Olga Parkes, Clara Tagliaferri, Limunga Meoto, Di Zhang, Qi Li, María Fernández, Toby Neville, Mozhdeh Noorkami, Krisztian Ronaszegi, Cenk Celik, Rafik, Confort and Christina, the Brazilians, the Sisters... And many others. Best wishes to all.

Super special thanks go to my sister María Hernández Barral and her “significant other” Guillermo López Barriuso, for their Love.

And to my parents, the luckiest Gift of all.

To my parents,

Soledad and Juan Manuel

CHAPTER 1
INTRODUCTION

1.1 INDUSTRIAL BACKGROUND

1.1.1 Technical overview of crude oil production

The common misconception on crude oil forming wide lagoons many miles deep into the crust of Earth seems to persist today. According to this view, more or less clean oil would be available once the liquid is pumped from the pool underneath. This picture, however, is far from reality.

Petroleum, in its primitive form, is the metabolic residue of anaerobic bacteria that feed on dead organic material reaching the bottom of the sea. These by-product compounds accumulated continuously at the bottom in association with other sediments (i.e. sand, mud, precipitates, calcareous skeletons) to form with time and pressure a sedimentary rock –the "source" rock. However, the final crude –a complex mixture of many hydrocarbon molecules, sulphur compounds and traces of other elements– is found in different underground reservoirs occupying the pores and cavities of porous strata, surrounded by impervious rock. Petroleum reached the reservoir after a long process of migration and accumulation, driven by gravity, surface tension and pressure differences. The simplest shape of the reservoir that favours this accumulation is the dome-shape structure or "anticline", a convex shape more or less hemispherical.

Oil reservoirs are large fields of certain porous rocks (i.e. limestone or sandstone) with inter-grain spaces, pores and fractures filled with liquid. Therefore, crude oil is not found clean, but containing solids, mud or sand. There is also natural gas and salty water in association with the crude in the reservoir. Free gas tends to occupy the cavities of the upper rock of the reservoir, while the salty water is in the lower part. Oil sits in between. The reservoir is under pressure and the oil contains dissolved gas. In these circumstances, the production rate and composition of the stream obtained at different wells across the reservoir field (i.e. oil, gas and water) may vary. Additionally, during

the oil exploitation of a reservoir during a period of ten, fifteen or twenty years, oil rates and composition of the stream usually change.

The reservoir has potential energy that can be used to force the oil out once the well has been drilled and cemented. Generally, the layer of water at the bottom, the free gas at the top and the gas dissolved in the oil, as well as the permeability of the crude oil through the reservoir rock, are "primary" mechanisms of oil production. They are known as water drive, gas cap drive, solution gas drive and gravity drainage mechanisms. It was obvious from the early days, however, that the amount of oil produced via primary mechanisms was far from the estimated total capacity of the reservoir. New, artificial or "secondary" recovery mechanisms were then introduced, the simplest method consisting of displacing the liquid of the reservoir rock with other fluids, i.e. water or gas. Water flooding is widely used: water more or less free of solids is introduced in the well under pressure, suitably mixed with solvents or chemical agents to improve the permeability of the liquids through the rock. Although secondary mechanisms of recovery can be thought of as measures implemented towards the end of the reservoir life, water flooding or gas drive tend to be used also at early stages to maintain the pressure of the reservoir.

As a conclusion of this quite brief overview of oil production (Lowson, 1970), it can be highlighted that the stream leaving the reservoir is a complex mixture of crude oil, salty water and gas that carries solids, sands or impurities. A primary separation of the phases is undergone in the platform forcing the mixture to pass through a battery of separators in series. It might be convenient to add a controlled amount of water to the separated crude, nevertheless, in order to improve the technical and economical efficiency of its transfer to the refinery. The general problem of oil-water mixing that poses complications during separation steps and the transport of crude at different stages constitutes the background of this investigation.

1.1.2 The problem of oil-water mixtures

It is well-known that a mixture of oil and water left to rest will eventually separate completely. In the reality of an oil production platform, however, the conditions and details of the operations can pose additional problems to the separation. In offshore structures, for example, the platform experiences some motion due to the sea waves and, as a consequence, oil and water are sloshed back and forth in the separator, promoting the formation of droplets and jeopardizing the separation.

The flow of gas on top of a layer of liquid already separated may also cause entrainment and carry droplets through the outlet stream (Rhyne, 2014). There is a number of ancillary elements in the separators, such as perforated baffle plates to avoid sloshing, or vane packs that collect the liquid-laden gas and subject it to several, sudden changes of direction, to help separate the liquid. Oil companies have access to a large number of correlations to predict entrainment in gas-liquid and, to a lesser extent, in liquid-liquid mixtures. In addition, Computational Fluid Dynamics (CFD) techniques are usually employed to estimate the time frame of certain phenomena. For example, CFD codes can calculate the instant at which a droplet of liquid carried by the gas will hit the vane. However, more important is to predict the behaviour of the droplet after that instant, whether it would break into smaller drops or form a layer of liquid that drain back into the separator (Rhyne, 2014). In order to answer this type of questions, basic research and experimental observations in the laboratory are still needed.

There is also a significant interest in further investigating the behaviour of oil-water mixtures during oil transportation. In early years, it was noted that the energy consumption during the transportation of heavy oil across long distances could be reduced if water was added (Russell et al., 1959, Charles et al., 1961). The flow pattern displayed by the mixture affects the pressure drop along the pipe and other transport properties as the mass and heat transfer coefficients. The understanding of the physics behind the oil-water flows and, particularly, the drop formation, may also help better predict flow pattern transition in those applications.

This investigation has been sponsored and supported by Chevron Energy Technology Company and University College London, and is most generally intended as an experimental work to better understand how the interface in oil-water stratified flows evolves when transition to dispersed patterns is approached. The insights and information that could be gathered may help design better separators and further improve computational models for transport and separation in the field.

1.1.3 Lack of data in oil-water flows

As indicated, there is a large volume of experimental work in the gas-liquid literature in the form of correlations to predict flow pattern transitions or validate models for onset of drop entrainment. Knowledge has been gathered from experience

in many industries and applications with gas-liquid flows. Sometimes experiments were designed based on the assumptions of a given model. For example, with the aim of investigating the cooling capacity of a thin film of liquid (i.e. in a nuclear reactor), Ishii and Grolmes (1975) studied the entrainment of liquid (and further atomization) into a fast gas-phase, flowing on top, as a consequence of shear. This problem can be seen as somehow related to that of gas flowing on top of liquid in a platform separator or a pipe. The important assumption made by the authors was that liquid drops developed in the gas mainly from roll waves at the interface of the liquid film. They were able to write the criteria for drop formation in terms of non-dimensional groups, for laminar, transition and turbulent regimes. Constants and coefficients of the dimensionless numbers were found based on a roll-wave model with certain assumptions. For example: 1) the drag force of the gas acting on the crest of the wave is greater than the force due to the gas-liquid surface tension; 2) the motion of the crest with respect to the liquid film can be described by a shear model with the surface tension of the liquid and the amplitude of the wave crest as parameters.

This kind of work is very limited in liquid-liquid, oil-water flows, though, and a thorough description of mechanisms of drop formation has not been presented or discussed yet. There might be reasons to expect mechanisms of entrainment in oil-water flows to be different from gas-liquid, since the density, viscosity and velocity of the phases are within the same range of magnitude in the former case. Significant could be as well the fact that gases are compressible, while liquids are not. Woodmansee and Hanratty (1969), for example, suggested that the primary destabilization force in gas-liquid annular flow is the pressure variation due to the compression of the gas on the wave crest. A number of models incorporate the effect of pressure differences on the leeward and windward sides of the waves (e.g. Trallero, 1995). If compressibility of the fluids plays any role in gas-liquid drop formation, it would not be the case for oil-water flows, although pressure changes within the phases can be expected if there are interfacial waves, as predicted by the Bernoulli equation.

The example of drops detaching from roll-like waves has served as the starting point to investigate the phenomenon of drop entrainment in oil-water flows. Two-fluid and stability models consider clear 2D wave structures on the interface of a stratified flow. Al-Wahaibi (2006) pointed out that these models do not provide

information about the drop formation mechanism and, following the work in gas-liquid, he presented a force-balance model to predict the entrainment. He assumed that a drag force exists due to the difference of oil and water phase velocities and that entrainment would only occur whenever the drag force exceeds the stabilizing effect of the surface tension. Additionally, Al-Wahaibi considered the likely capacity of the drag to deform the leading edge of the wave and predicted that the wave would end up flat at this edge, when break-up and drop formation take place. The author performed further experiments with stratified flows towards the validation of the model (Al-Wahaibi, 2006; Al-Wahaibi and Angeli, 2011), but the results were not conclusive.

1.2 OBJECTIVES

The initial, specific aim of this Thesis was to extend these investigations as to understand better the formation of drops from interfacial oil-water waves and provide reliable data into the liquid-liquid literature. However, it was soon evident that clear wavy structures, like those on which models and assumptions were based, did not develop along the pipe. On the contrary, the overall shape of the oil-water interface was found to consist of small, 3D fluctuations regardless of the input parameters of the flow. Clear 2D waves could be generated in the inlet section when the oil-to-water input ratio was different from 1, but those structures were seen to vanish in the pipe downstream the inlet junction. These phenomena are presented and described in detailed in this work.

These findings established the following objectives of the Thesis:

- Provide observations on patterns and interfacial waves of stratified oil-water flows in a horizontal pipe and descriptions of drops at the boundary with dual-continuous flow.
- Describe and analyze the interface of stratified oil-water flows along the pipe.
- Describe and find wave characteristics at the inlet section against the flow parameters.

1.3 THESIS STRUCTURE

The Thesis is structured in 8 chapters (this introduction; literature review; description of the experimental rig and instrumentation; four chapters of results and discussion; and the final conclusions and suggestions for the future) and 6 appendices.

Stratified oil-water mixtures have been investigated experimentally in pilot-scale rigs with different objectives along the years. Different flow patterns seen in pipes and pattern transitions have been reported, and flow parameters such as pressure drop, water fraction or actual phase velocities have been estimated in relation to specific flow patterns. Chapter 2 presents a summary of the previous work and the results obtained, first generally on oil-water mixtures and then, particularly, on stratified flows. The use of conductance probes in the literature of experimental oil-water flows is reviewed next in the chapter. In this work, conductance probes are used to investigate the nature and properties of the oil-water interface in stratified flow. Even though probes have been used to study non-stratified flows and non-stationary signals, the use of probes to stratified flow is quite unique in oil-water applications. Further, the application of visual techniques such as high-speed imaging to two-phase flows is summarized. Visual techniques seem convenient to explore the wave characteristics in cases where the interface presents clearly visible and identifiable wavy structures. However, as discussed in the chapter, visual analysis of fluctuating interfaces, where small contributions (i.e. 3D) determine the overall interface shape, is difficult. In such cases, the statistical analysis of the conductance probe signal is a better approach. Finally, the literature review of Chapter 2 introduces the theoretical model of stability analysis of waves, against which the observed stability of inlet waves will be compared in the last chapter.

Chapter 3 gives a detailed description of the experimental set-up of this work and the instrumentation. The important parts dealing with the practical operation and maintenance of the rig and the calibration of the conductance probes are briefly introduced in the chapter, but a comprehensive description of both is included in Appendices 1 and 2, respectively.

The following four chapters present the results of this Thesis. Results have been divided into four distinct parts that are, nevertheless, fully connected to each other: experimental observations; development of procedure for data analysis; time-average parameters of the flow and power spectra of the interface; and stability of

inlet waves. Bearing in mind the general objective of exploring the physics of stratified oil-water flows and their evolution towards drop formation, significant time has been devoted to observe carefully oil-water flows in the laboratory, sometimes with the aid of a high-speed camera. The analysis proposed and all other quantitative results have been prompted by the laboratory observations. A full description and discussion of the flow patterns, drops and drop formation, comparison with literature, the problem of the inlet geometry and a brief account of pressure drop measured in stratified flow is given in Chapter 4. Preliminary results on the structure of the flow acquired via Particle Image Velocimetry are also included. This technique is introduced in the Appendix 1, as it could constitute an extension of this work for the future.

The comprehensive investigations done with the double-wire conductance probes in oil-water stratified flows are covered in Chapter 5. First analysis of the data showed that the probe signal displays three most relevant properties: randomness, stationarity and normality. These features, verified along this work, reveal the nature of the stratified oil-water interface, and have led to the establishment of a solid methodology for data analysis. A comprehensive methodology to collect, treat, analyze and interpret the data is presented and discussed. The procedure is based on well-established statistical tools that can be generally applied to other fluids or pipe diameters in stratified flows. The statistical methods used and their application to the analysis of the oil-water interface probe signal can be seen in detail in Appendix 3. Both the procedure and its application to stratified oil-water flows constitute an original contribution to the field.

The results of the conductance probe data analysis are discussed in Chapter 6 and presented in two groups: time-average parameters of the flow (i.e. water fraction, actual phase velocities and Re numbers) and spectral density analysis. Both types of results complement and support each other and have led to important conclusions. A detailed description of the general procedure and its application to the experimental oil-water data is included in Appendix 4. The results are compared and discussed in the chapter against the predictions of the standard two-fluid model. The relevant aspects of the model are covered in Appendix 5.

The observation of waves at the inlet section only in cases when the input ratio is different from 1 (wave disappear shortly afterwards, and the interface becomes fluctuating) initiated a different work direction. The fourth and final chapter of results, Chapter 7, carries an investigation of the wave characteristics of inlet waves. Observations and measurements were used to discuss the nature of the waves and possible causes that may create or dampen them shortly after the inlet junction. Along with suggestions for future work, conclusions are presented in Chapter 8. Finally, Appendix 6 collects conference papers presented with related oil-water work.

CHAPTER 2
LITERATURE REVIEW

2.1 EXPERIMENTAL OIL-WATER STUDIES

2.1.1 Flow patterns and flow pattern maps

When oil and water flow simultaneously in a pipe, different flow patterns can develop depending on the flow parameters (mixture velocity and input flow rate ratio), the properties of the fluids (density, viscosity and surface tension) and the pipe size, inclination and inlet geometry.

A number of investigative efforts have been done along the years in order to describe oil-water flow patterns, represent in graphs their boundaries and predict transitions from one to another by application of appropriate models. Observation and description of flow patterns can be somehow subjective. Within the first 20 years of investigations, up to 14 different patterns were reported (Russell et al., 1959; Malinowsky, 1975; and Oglesby, 1979). The introduction of advanced techniques and instrumentation in the 1990s allowed a more detailed description of certain flow regimes (i.e. dispersed) by several authors (Trallero, 1995; Nadler and Mewes, 1997; Angeli and Hewitt, 1998). In order to illustrate the most common appearance of oil-water mixtures in horizontal pipes, the six patterns presented by Trallero (1995) plus three more found in flows involving heavy crude oils (Xu, 2007) are presented in Figure 2.1. Several authors have investigated flow patterns with crude oils or model oils of high viscosity (Mu, 2001; Yao and Gong, 2004; Yao, 2006). The annular and various stratified flows shown in Figures 2.1g – 2.1i, with the water phase free of drops and segregated were also reported by Wang et al. (2011) in actual crude oil, especially at higher flow rates. The authors only found water-in-oil emulsions in the crude oil, while experiments with a model oil of the same viscosity (0.6 Pa·s) produced also oil-in-water emulsions. Natural surfactant agents in the crude such as asphaltenes were accounted for the difference.

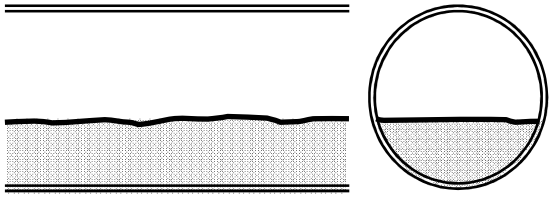

a. Stratified flow (ST)

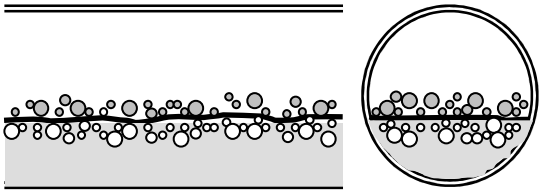

b. Stratified with mixing at the interface flow (DC & MI)

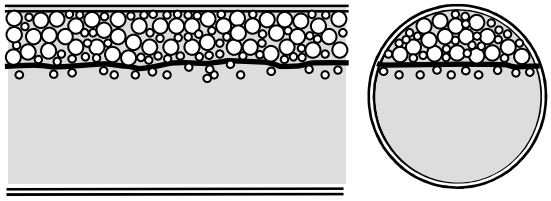

c. Dispersion of oil in water and water (Do/w & w)

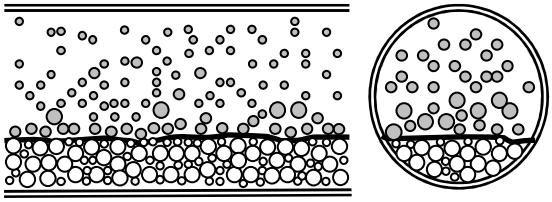

d. Dispersion of water in oil and oil in water (Dw/o & Do/w)

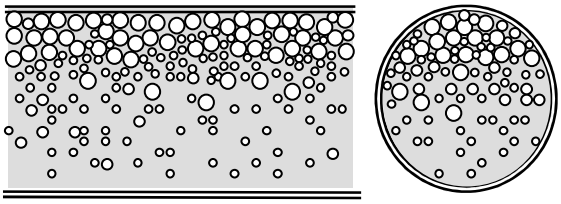

e. Oil in water emulsion (o/w)

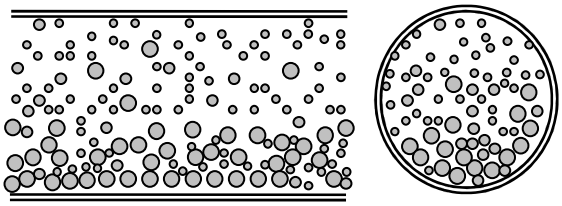

f. Water in oil emulsion (w/o)

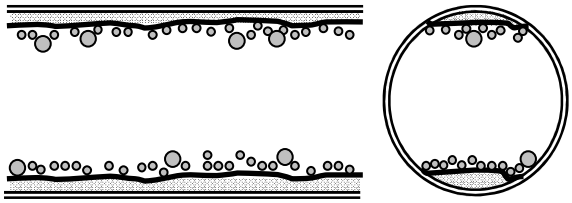

g. Annular flow (AN)

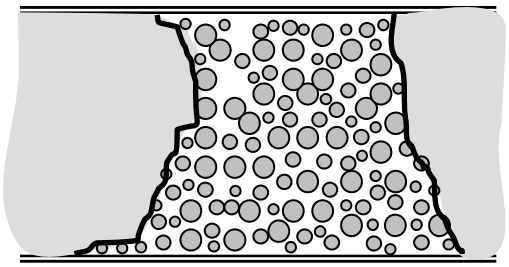

h. Slug flow (S)

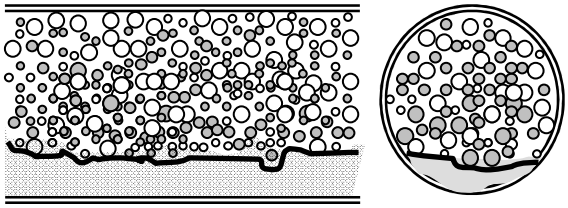

i. Comprehensive stratified flow (CST)

Figure 2.1 Classification of oil-water horizontal flow patterns

The most basic separated oil-water regime is the stratified flow (Figure 2.1a). Both phases flow as a continuous medium without entrainment of drops and showing a clear interface of separation between them. Under certain conditions, entrainment would occur. The so-called stratified flow with mixing at the interface (Figure 2.1b) is a form of stratified flow with both phases carrying drops regularly distributed around both sides of the interface. The phases, however, retain their continuity. Part of the oil or water phases can break into dispersion, although the interface of separation can still be observed (Figures 2.1c and 2.1d). Trallero (1995) named the dispersed patterns with no visible interface *emulsions* (Figures 2.1e and 2.1f). Emulsions are characterized by one continuous phase occupying the entire section of the pipe as continuous, while the other is distributed in drops, fully dispersed. Usually, if the dispersed phase is oil, drops tend to occupy the top part of the pipe, while the opposite is true for water drops.

Experimental discrimination among dispersions and the pattern in Figure 2b is usually difficult and subjective. As example, the stratified with mixing at the interface regime of Trallero (1995) and Nädler and Mewes (1997) had been previously called semi-segregated or semi-mixed by Oglesby (1979) and Vedapuri and Jepson (1997) and was later referred to as stratified wavy with entrainment or drops (Soleimani, 1999; Valle and Kvandal, 1995; and Angeli and Hewitt, 2000). Additionally, despite the fact that instrumentation to investigate drop size and phase distribution has been largely used with multiple purposes, a common criterion to differentiate between stratified patterns with drops does not exist. Lovick and Angeli (2004) introduced the common term “dual continuous” flow to describe all patterns in Figures 2.1b – 2.1d and the general case of two continuous phases with drops separated by an interface.

The flow patterns observed in a specific oil-water system are reported in 2D plots called *flow pattern maps*, where the flow pattern is shown in terms of the flow conditions (i.e. usually superficial velocities of the phases or other parameters resulting from the combination of those). Taitel and Dukler (1976) dedicated their classic paper on prediction of pattern transitions in horizontal or slightly-inclined gas-liquid flows to Ovid Baker, who is credited to have provided the first graphical representation of flow patterns (1954). In the oil-water literature, investigators usually represent the experimental patterns by plotting the superficial velocity of oil in the x

axes and that of water in the y axes. Figures 2.2 – 2.4 show, as example, three flow pattern maps found by different authors.

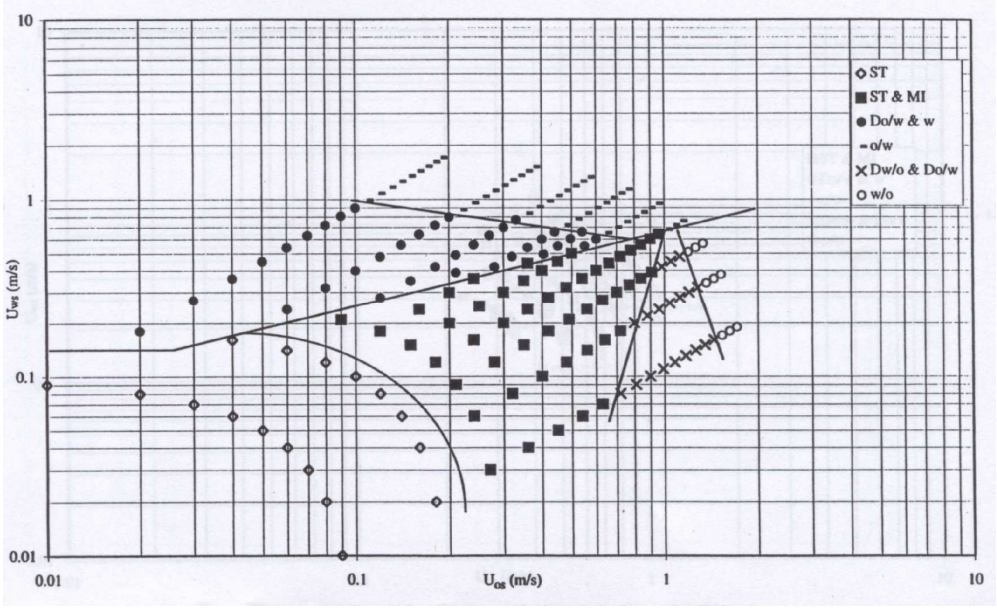

Figure 2.2 Experimental flow pattern map, Guzhov et al. (1973)
D = 39.4 mm, $\mu_o / \mu_w = 21.8$, $\rho_o / \rho_w = 0.898$, $\sigma = 0.045$ Nm
(from Trallero, 1995)

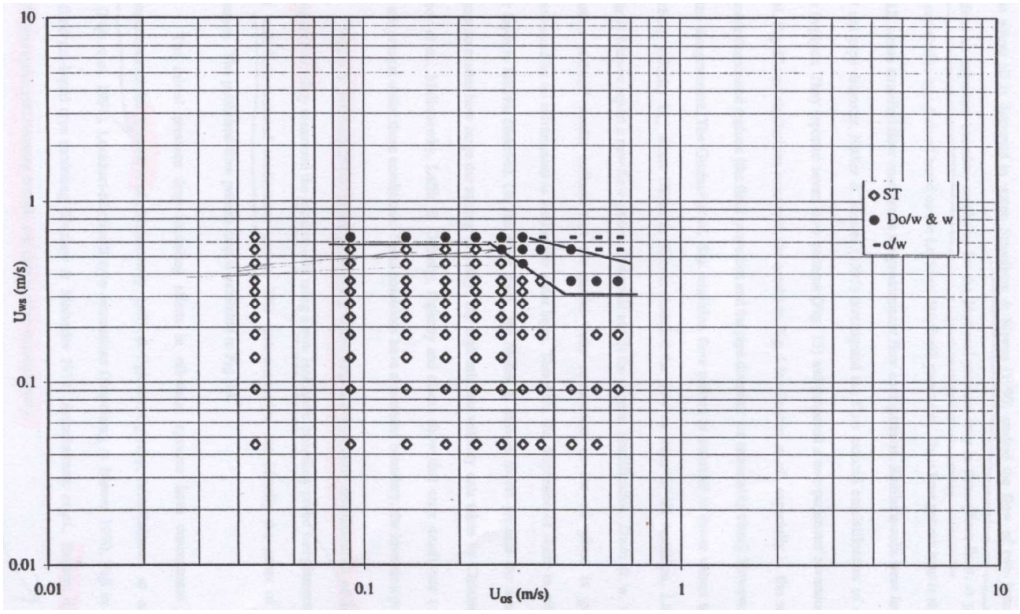

Figure 2.3 Experimental flow pattern map, Cox (1985)
D = 50.8 mm, $\mu_o / \mu_w = 1.54$, $\rho_o / \rho_w = 0.76$
(from Trallero, 1995)

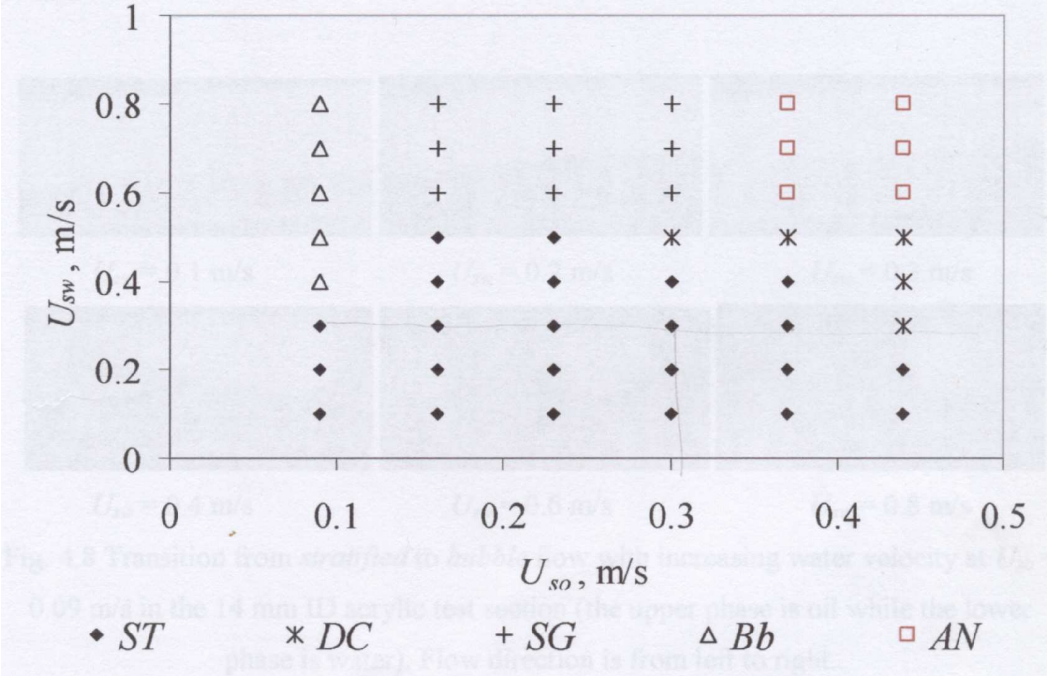

Figure 2.4 Experimental flow pattern map, Al-Wahaibi (2006)

D = 14 mm, $\mu_o / \mu_w = 5.5$, $\rho_o / \rho_w = 0.83$, $\sigma = 0.039$ Nm

A different flow pattern map has been used by several authors to show results found in oil-water mixtures. For example, Valle (2000) carried out experiments to find the effect of the fluid properties on flow patterns and other parameters of the mixture using four different crude oil systems plus one model Exxsol™ D60 oil, water and N_2 at different conditions of pressure and temperature. Results were reported in plots of the mixture velocity and the water cut, λ_w (i.e. the volumetric input fraction of water in the pipe). Figure 2.5 shows, as an example, the flow pattern map of Exxsol™ D60 oil and water, found using conductance probes. Valle also reported other flow properties of the mixtures (such as pressure drop or the slip ratio, i.e. the oil-to-water ratio of actual velocities) against the water cut.

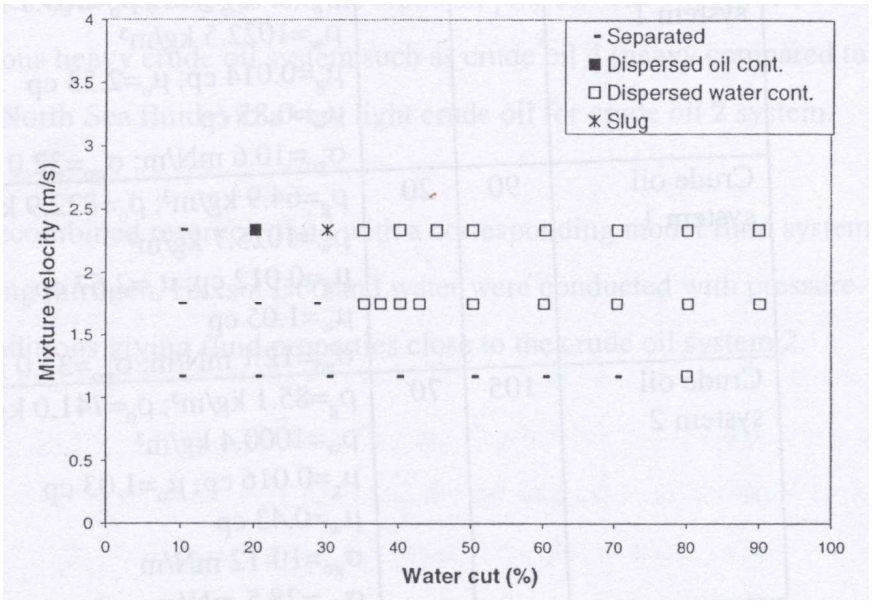

Figure 2.5 Experimental flow pattern map, Valle (2000)

D = 77.9 mm, $\mu_o / \mu_w = 2.0$, $\rho_o / \rho_w = 0.756$, $\sigma = 0.030 – 0.035$ Nm

Additionally, Figure 2.6 presents Lovick and Angeli (2004) results in a flow pattern map of the mixture velocity against the oil cut, λ_o (i.e. the volumetric input fraction of oil in the pipe).

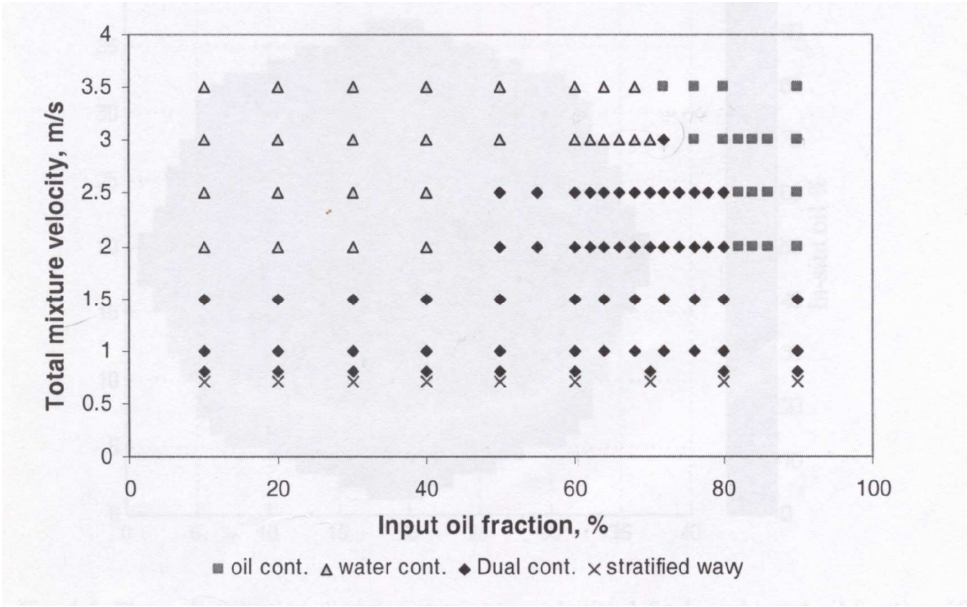

Figure 2.6 Experimental flow pattern map, Lovick and Angeli (2004)

D = 38.1 mm, $\mu_o / \mu_w = 5.5$, $\rho_o / \rho_w = 0.83$

The common note of these flow patterns is the predominance of stratified flow at relatively low mixture velocities (i.e. below 1 ms^{-1}) for almost all the range of input oil ratios or water cuts. This result will be challenged by the observations of this investigation where stratified flow is not observed at low mixture velocities if the oil-to-water input ratio (i.e. ratio of oil-to-water superficial velocities) is sufficiently different from 1.

2.1.2 Summary of experimental work

Table 2.1 gives a summary of relevant experimental oil-water studies in horizontal pipes performed by different authors in decades of investigation.

Mainly aimed at finding mechanisms to reduce the energy consumption during oil transportation, pressure drop has been routinely reported in the course of experimentation. The pioneering works of Russell et al. (1959) and Charles et al. (1961) showed that pressure drop and energy consumption during oil transport could be reduced by a significant factor (i.e. from 1.7 for 6.29 cp oil to 10 for 65 cp oil; and up to 500 for 1,000 cp oil) if the mixture was forced to flow in annular flow, with a thin layer of water in the outside enclosing the core of oil at the centre. Further, Guzhov et al. (1973) found that the two-phase oil-water flow increases with the addition of water in oil-water emulsions, compared to that of single-phase oil. Additionally, they observed a peak at the transition from dispersed flows to stratified with mixing flow. Nädler and Mewes (1997) also reported pressure gradient peaks at the boundaries of dual continuous flow and fully-dispersed flow. Other peaks in pressure drop were found in association with the phenomenon of phase inversion between oil and water dispersions by Angeli and Hewitt (1998).

Table 2.1 Summary of experimental studies of oil-water flows in horizontal pipes

AUTHOR	PIPE **Material**; **Size**(mm);	OIL ρ_o(kgm^{-3}); μ_o(Pa·s)	INTERF. TENSION σ(mN·m)	FLOW U_{mix}(ms^{-1}); r	METHOD	DATA STUDIED
Russell et al. (1959)	**; 20.3; 10.7 m (tube length); "Y" config. 48 ˚	834; 0.018	**	0.053 – 2.08; **	**	Pressure drop; Hold-up; Flow patterns
Charles et al. (1961)	**; 26.4; 8 m (tube length)	998; 0.0063, 0.017, 0.065	**	0.035 – 1.98; **	**	Pressure drop; Phase fraction; Flow patterns
Cengel et al. (1962)	**; 22.2(OD); 3.2 m (tube length)	834; 0.018	**	0.90 – 9; **	**	Pressure drop
Sleicher (1962)	**; 38.1; 11.9 m (tube length)	700 – 1585; 0.0005 – 0.032	8.1 – 45	0.56 – 2.4; Very high	**	Drop size; Fluid properties; Pipe length; Turbulence
Charles and Lilleleht (1966)	**; 15.9; 4.9 m (tube length)	825; 0.0055	**	**	**	Pressure drop
Ward and Knudsen (1967)	**; 21.1; 2.9 m (tube length)	789, 875, 890; 0.001, 0.016, 0.214	28, 49, 52	0.7 – 7.6; Very small – **	**	Oil-water distributions; Velocity profile; Drop size distributions
Collins and Knudsen (1970)	**; 19.0; 11.0 m (tube length)	785 – 875; 0.001 – 0.018	13 – 40	4.33 – 6.7; Very small – **	**	Drop size distribution; Fluid Properties; Flow rates
Guzhov et al. (1973)	Steel; 39.4;	896; 0.022	44.8	0.3 – 1.6; 0.43 – 9	Visual observation	Flow patterns; Pressure drop
Malinowsky (1975)	Steel; 38.4; "T" config.	850; 0.005	22.3	0.6 – 2; 1.2	Visual observation	Flow patterns (dispersions); Pressure drop
Wicks and Fraser (1975)	**; 25.4;	Kerosene and water	**	**	**	Flow patterns

Table 2.1 Summary of experimental studies of oil-water flows in horizontal pipes (Cont.)

AUTHOR	PIPE **Material**; **Size**(mm);	OIL ρ_o(kgm^{-3}); μ_o(Pa·s)	INTERF. TENSION σ(mN·m)	FLOW U_{mix}(ms^{-1}); R	METHOD	DATA STUDIED
Kubie and Gardner (1977)	**; 17.2; 4 m (tube length)	828 – 884; 0.0007 – 0.0048	4.7 – 14.5	0.85 – 3.40; Very high	**	Pressure Drop
Karabelas (1978)	**; 50.4; 32.3 m (tube length)	798, 890; 0.0018, 0.015	32 – 35	1.23 – 3.12; **	**	Drop size; Drop distribution
Cox (1985)	Acrylic; 50.1; "T" config.	754; 0.0014	**	0.7 – 1; 0.43 – 3.2	Visual observations	Flow patterns
Scott (1985)	Acrylic; 50.1; "T" config.	754; 0.0014	36	0.25 – > 3; 0.05 – 19	Visual observations	Flow patterns
Arirachakaran et al. (1989)	**; 26.6, 41.0; 6.1 m, 12.8 m (tube length)	868, 898; 0.005 – 2.1	29 – 32	0.47 – 6.8; **	**	Pressure drop; Mixture velocity
Stapelberg et al. (1991)	**; 38.1; 29.7 m (tube length)	850; 0.03	**	0.08 – 0.10; **	**	Pressure drop; Oil-water stratified flow
Pal (1993)	**; 8.9 – 25.5; 4.9 m (tube length)	780; 0.0025	**	0 – 20; Very high – very low	**	Pressure drop; Unstable and stabilized dispersions
Stapelberg and Mewes (1994)	**; 23.8, 59, 120, 328; "T" config.	850; 0.030	50	0.10 – 1.85; **	**	Flow patterns; Pressure drop
Kurban et al. (1995)	Glass - Acrylic; 2.4; **	803; 0.0016	**	**	Photography; Conductance probes	Flow patterns; Drop size distribution
Trallero (1995)	Acrylic; 50.1; 15.5 m (tube length)	884; 0.029	36	0 – 3.4; 0.05 – 19	**	Flow patterns; Pressure drop; Hold-up
Valle and Kvandal (1995)	Glass; 37.5; "Y" config.	794; 0.0024	37.3	0.85 – 1.7; 0.3 – 2.1	Conductivity probes; Sample probes	Flow patterns; Pressure drop

Table 2.1 Summary of experimental studies of oil-water flows in horizontal pipes (Cont.)

AUTHOR	PIPE **Material**; **Size**(mm);	OIL ρ_o(kgm^{-3}); μ_o(Pa·s)	INTERF. TENSION σ(mN·m)	FLOW U_{mix}(ms^{-1}); r	METHOD	DATA STUDIED
Nädler and Mews (1995)	Perspex; 59; Cone-shaped layer	850; 0.022 – 0.035	**	0.3 – 1.6; 0.25 – 19	Conductivity probe	Flow patterns; Pressure drop
Trallero et al. (1996)	Acrylic resin; 5.1;	852; 0.029	**	**	Visual observation	Flow patterns
Angeli (1996)	Stainless steel; 24.3	801; 0.0016	17	0.3 – 1.3; 0.47 – 3.4	Visual observation; Impedance probes	Flow patterns
Nädler and Mews (1997)	Perspex; 59	841; 0.022 – 0.035	**	0.3 – 1.6; 0.25 – 19	Conductivity probes	Flow patterns
Vedapuri and Jepson (1997)	Plexiglass; 101.2	**; 0.002	**	0.4 – 1.4; 0.25 – 4	Iso-kinetic probe	Flow patterns
Valle and Utvik (1998)	**; 77.9; 100 m (tube length)	791; 0.001	28.5	0 – 4.7; **	**	Flow patterns; Pressure drop; Hold-up
Soleimani et al. (2000)	**; 24; 9.7 m (tube length)	801; 0.0016	17	0 – 7.2; **	**	Flow patterns; Pressure drop
Angeli and Hewitt (2000)	Acrylic; 24	801; 0.0016	17	0.3 – 1.6; 0.49 – 1	Visual observation; Impedance probes	Flow patterns
Elseth (2001)	Stainless steel; 56.3	790; 0.0016	43	0.7 – 2.5; 0.18 – 1.5	Visual observation; Gamma densitometer	Flow patterns
Simmons and Azzopardi (2001)	PVC; 63; **	684; 0.0011	**	**	Optical techniques; Particle size analyzer	Flow patterns; Drop size
Mu (2001)	Steel: 25.4; **	930; 0.31	**	**	High-speed photography	Flow patterns
Lovick and Angeli (2004)	Stainless steel; 38; **	828; 0.0055	39.4	0.8; Very small – very high	Visual observation; Impedance probes	Flow patterns
Yao and Gong (2004)	Steel; 25.4 mm; **	0.973; 572	**	**	High-speed photography	**

Table 2.1 Summary of experimental studies of oil-water flows in horizontal pipes (Cont.)

AUTHOR	PIPE **Material**; **Size**(mm);	OIL ρ_o(kgm^{-3}); μ_o(Pa·s)	INTERF. TENSION σ(mN·m)	FLOW U_{mix}(ms^{-1}); r	METHOD	DATA STUDIED
Ioannou et al. (2005)	Steel, Acrylic; 60 mm, 38 mm	796; 0.0017	31.2	3.5 – 7; Very small – very high	Impedance probes;	Pressure drop; Phase inversion
Raj et al. (2005)	Acrylic; 25.4; **	787; 0.0012	45	0.6 – 2.2; 0.43 – 1	Visual observations	Flow patterns
Rodriguez and Oliemans (2006)	Steel; 82.8 mm; 15 m (pipe length)	830; 0.0075; Brine water	**	0.04 – 5.55	Video recording; Gamma densitometry	Flow pattern; Water fraction; Pipe inclination
Yao (2006)	Steel; 25.4 mm; **	0.973; 572			High-speed photography	**
Al-Wahaibi (2006)	Acrylic; 14 mm, 38 mm; "T", "Y" config.	828; 0.0055	39.2	0.2 – 1.5; Very small – very high	High-speed photography; Conductance probes	Flow patterns; Onset Entrainment
Hu (2007)	Stainless steel; 38 mm; Vertical pipe	828; 0.005;	36.6	**	Impedance probes; Hot-film anemometer	Drop size Distribution; Turbulence structure
Ngan et al. (2011)	Acrylic; 38 mm; "Y" config. Dispersion	828; 0.0055	41 – 48	**	Conductance probes; ER Tomography	Pressure drop; Drop size Distribution; Effect of water viscosity
Al-Wahaibi and Angeli (2011)	Acrylic; 38 mm;	828; 0.0055	39.2	0.2 – 1.5; Very small – very high	Conductance probes	Wave characteristics
Wang et al. (2011)	Stainless steel; 25.4 mm 50 m (pipe length)	**; 0.628	10.3	**	Visual observations;	Pressure drop; Flow patterns; Transitions

Trallero (1995), Valle and Kvandal (1995) and Nädler and Mewes (1997) found that the pressure gradient of oil-water was reduced compared to that of single-phase oil during dual continuous flows. Lovick and Angeli (2004) investigated the pressure drop of dual continuous (DC) flows in different conditions and at mixture velocities up to 3.5 ms^{-1}. In all cases the pressure drop of single-phase oil was greater than that of single-phase water and decreases smoothly with the addition of water down to a minimum at input oil fraction close to 80 %. His results show, however, fluctuations between 60 and 80 % input oil fraction for all cases. Pal (1993), Soleimani (1999) and Lovick and Angeli (2004) found evidence of drag reduction effect on the pressure gradient of oil-water flows and Lovick suggested that the trends observed in DC flow could be explained by the difference in the magnitude of drag reduction.

Angeli and Hewitt (1998) and Lovick and Angeli (2004) studied the effect of the initial conditions on the pressure gradient by pre-wetting the experimental pipes with either oil or water prior to experiments. They all found that the initial wetting conditions have an effect on the pressure gradient in both acrylic and stainless-steel and that the difference was in the range of 3.6 % to 5.8 % for 2 ms^{-1} and 3 ms^{-1}, respectively (Lovick and Angeli, 2004). Additionally, as expected, the pressure drop is affected by the pipe material. Angeli and Hewitt (1998) compared results in stainless steel and acrylic pipes of about the same ID, 24 mm, using light oil (ρ = 800 kgm^{-3} and μ = 0.0016 Nm) and water for superficial velocities in the range from 0.11 to slightly above 2.5 ms^{-1} and found it to be larger in stainless steel in all cases.

The fluid properties used in the experimentations are responsible for significant differences in the flow patterns and parameters. Theoretically and experimentally it has been found that larger differences between the densities of the phases tend to enhance the stratification and expand the region at which separated flow is observed (Yih, 1980; Trallero, 1995). Similarly, in other type of applications, McClarey and Mansoori (1978) found experimentally that a larger difference in density makes more difficult the formation of dispersions. As opposed, oil-water systems of similar densities seem to be more prone to develop non-stratified patterns, such as annular or slug flows (Charles et al., 1961).

Regarding viscosity, Xu (2007) has indicated that a system of water and heavy oil can lead to certain flow patterns not observed in mixtures involving light oil. In the case of dispersions with water as the continuous phase, Arirachakaran et al. (1989) concluded that the effect of oil viscosity on the flow pattern is small. On the contrary, if the continuous phase is oil, transition to dispersed flows or emulsions tends to occur at lower mixture velocities for oils of high viscosity (167 cp) and, surprisingly, at higher mixture velocities for oils of medium viscosity (32 cp), in comparison to results with light oils (Oglesby, 1979). Different authors have provided experimental correlations to predict the phase inversion as a function of the viscosity of the phases (Yeh et al., 1964; Arirachakaran et al., 1989; Ngan et al., 2009).

The influence of viscosity on the transition between stratified and DC flows can be hinted from the flow pattern maps shown in Figures 2.2 – 2.4, although perhaps a specific experimentation is still needed to identify the influence of this parameter alone on the onset of entrainment. In this sense, it is not easy to quantify the effect of density, viscosity or surface tension alone without affecting any of the other parameters (Valle, 2000; Ngan et al., 2011). The effect of surface tension on oil-water dispersions was investigated by Ngan et al. (2011) by adding glycerol to the water phase. The authors managed to change the surface tension by 6 – 14 % without affecting the density and the viscosity by more than 1 %. Perhaps for this reason, the pressure drop was not seen to change significantly with respect to flows without glycerol. Ngan et al. found that the surface tension has no effect on the phase fraction at the onset of phase inversion, although it tends to delay the propagation of such inversion from the centre of the pipe to the wall if increased. Additionally, the size of water drops after the inversion seemed to be reduced for larger surface tension values. The size of oil drops before the inversion remained unaffected. A “defoaming agent” or other surface-tension reducing chemicals have been traditionally used in the field to break down emulsions in the platform separators in an attempt to minimize losses of oil production (Lowson, 1970). As opposed, it has been theoretically shown that increased oil-water interfacial tension can retard or delay the onset of entrainment in stratified flows by preventing the growth of interfacial waves (K-H instability; Valle, 2000; Al-Wahaibi, 2006).

Several authors have performed experiments with oil-water mixtures using different pipe diameters (Arirachakaran et al., 1989; Stapelberg and Mewes, 1991; Pal, 1993; Al-Wahaibi, 2006). Valle (2000) compared the work of Stapelberg and Mewes (1991) with that of Nädler and Mewes (1995) (who used the same working fluids in a pipe 38 mm ID as compared to 59 mm ID) and found that the stratified region decreased in the pipe of larger diameter. This conclusion is somehow unexpected, and Valle pointed out that the mixture velocities that Stapelberg studied were relatively low (i.e. up to 1 ms^{-1}). Comparisons between different pipe diameters are generally difficult because of the inherent problem to match both the input parameters and the actual Re numbers of the phases in the pipe. When comparing the flow patterns in two pipes of different diameters, important wall effects on the flow were reported by Barral et al. (2013) in a small 14-mm ID pipe, sufficient to generate a non-stationary and meandering stratified pattern, normally unstable, that could break in slug flow further downstream.

Two parameters are frequently used in the literature to report results on flow patterns and to model or predict transitions: the hold-up volume and the slip ratio. The hold-up volume or water hold-up is a term adopted from the gas-liquid literature that accounts for the *actual* fraction of water at some instant of time. In dispersed flows, local water hold-up is the volume fraction of water at a certain location within the pipe. In stratified flow, water would occupy the bottom of the pipe and the hold-up would just be the ratio of this fraction of area with respect to the pipe cross-sectional area (i.e. equivalent to the water fraction).

Experimentally, the water fraction has been commonly measured by means of quick-closing valves. In this way, the flow is suddenly brought to a full stop and the fluid inside a small pipe section is immediately enclosed by two quick-closing valves. The mixture is left to stratify and the volume of each phase is then measured. This technique was used, for example, by Lovick and Angeli (2004). Water fractions were also measured via impedance probes and results compared. 6 % differences were found. A different procedure involves the use of Electrical Resistive Tomography, especially useful in non-stratified flows or with non-transparent pipes, which allows capturing the volume fraction of each phase and their distribution across the section, without stopping the rig (Lovick and Angeli, 2004; Ngan, 2010). The phase fraction distributions were reported then by means of contour maps. Gamma densitometry is,

finally, another technique employed to measure in-situ water fraction (Rodriguez and Oliemans, 2006).

The ratio of actual average velocities of oil and water in the pipe when the flow is fully-developed is known as the slip. Generally, the experimental measurement of actual velocities is more difficult than that of volume fractions, particularly close to the pipe wall or the oil-water interface. Traditionally, hot-film anemometry has been used or even Pitot tubes. However, non-intrusive optical techniques, such as Laser Doppler Anemometry (LDA) and Particle Image Velocimetry (PIV), have been introduced to study oil-water flows recently. The great advantage of PIV against LDA is its ability to measure the instantaneous velocity in multiple points within a plane section of fluid, while LDA provides velocity measurements at one specific point in the flow field (Westerweel, 1993; Adrian, 2005). Matching refractive indexes, avoiding reflections (especially in oil-water flows with rough interfaces), oil haziness and the necessity of high-speed data collection are difficulties to be resolved in order to successfully apply PIV to the investigation of oil-water stratified flows.

The slip ratio depends on the physical properties of the fluids, flow patterns and geometries (Valle, 2000), and parameters such as the pressure drop of the mixture have been seen to depend on it. Hu and Angeli (2006) were able to measure slip in vertical flows. Lum et al. (2004) found slip very close to 1 in horizontal flows involving oil of low viscosity. Recently, Kumara et al. (2010) have applied PIV to measure the phase velocity of oil-water mixtures, velocity profiles and to provide information about the turbulent structures of the phases. Experiments were carried out in a 56-mm ID stainless steel pipe using low-viscosity Exxsol™ D60 oil (ρ_o = 790 kgm^{-3}, μ_o = 0.0016 $kgm^{-1}s^{-1}$) at room temperature and atmospheric pressure. The authors studied the effect of pipe inclination on the flow at two mixture velocities, 0.50 ms^{-1} and 1 ms^{-1} and found that this parameter has a significant effect on both the velocity profiles and Re stresses. Investigation using gamma densitometry has corroborated that oil and water tend to flow with no slip (i.e. similar actual velocities) in horizontal pipes. Slip only becomes different than 1 even at inclinations as low as ± 1 º. A similar investigation to measure velocity profiles and the turbulence structure of the phases using PIV is currently in preparation by Chinaud et al. (2014) using more viscous oil (μ = 0.0055 $kgm^{-1}s^{-1}$) and investigating the flow at different stages of

development; Birvalski et al. (2013) has also presented work in this direction of stratified air-water flows in a horizontal pipe.

There are, however, parameters that seem to affect the flow patterns and their evolution along the pipe that have been omitted in the literature, at least in practice. One of them is temperature. Most of the experimental investigations are at room temperature and under the assumption that the process is largely isothermal. Despite the fact that room conditions can significantly change from winter to summer, the importance of heat transfer between two phases at the same temperature can be certainly considered small, in theory. In practice, oil and water have different heat capacities and the heating effect of the pumps is different from each other, which can readily create differences of temperature of 5 – 10 ºC. This difference is sufficient to reduce the viscosity; for example, that of Exxsol™ D140 oil can decrease as much as 30 %, as reported by the manufacturer (from 5.6 cp at 25 ºC to 3.8 at 38 ºC). Furthermore, the solubility of water in the oil (in the range of ppms) is affected by temperature differences. This has been seen to make the oil hazy or cloudy under certain conditions and can limit the use of instrumentation. Heating treatment has been traditionally used in the field with the purpose of breaking down emulsions in the separator (Lowson, 1970). Perhaps more important is the effect that the design of the inlet section or the presence of ancillary piping parts, such as seals, flanges or other auxiliary elements can have on the flow. Different types of inlet have been introduced in the investigation of stratified or non-stratified patterns, but a thorough description is not usually available in the literature. External elements can promote the formation of drops or foams that are quite stable; particularly, it is well-known that drops are quite difficult to coalesce once they form in platform separators (Lowson, 1970). In summary, design details of the experimental rig can have a substantial effect on the observed flows which, if not properly mentioned, might pose difficulties in comparing published results and drawing reliable conclusions.

2.1.3 Oil-water stratified flows

Part of the experimental summary presented is concerned with stratified oil-water flows. This pattern is regarded as one of the basic flow configurations that can occur in industrial processes (Brauner and Moalem Maron, 1989), particularly in pipelines during oil transportation (De Castro et al., 2012). Stratified flow is usually

employed as a starting point to investigate the onset of entrainment and the formation of dispersions. Unlike the gas-liquid case, where different processes of drop formation has been established (e.g. Ishii and Grolmes, 1975), the mechanism of entrainment in oil-water flows is not thoroughly understood. A number of authors have recognized this fact in the last years and made new efforts towards a better understanding. Investigations have been projected mainly towards the study and prediction of drop formation via the stability analysis of suitable stratified flow models.

The first model on liquid-liquid flows (Brauner and Moalem Maron, 1989) was based on the assumption that the oil and water phases satisfy their individual continuity and momentum equations. The model predicts the equilibrium interface height and the pressure drops of the mixture via closure relations based on the definition of friction factors and shear stresses as defined for the single-phase flow. In the model, oil and water flow completely separated with a flat interface. However, oil-water flows had been generally reported to develop wavy interfaces, both with low and high viscosity oils (e.g. Trallero, 1995; Jayawardena et al., 2000; Bannwart et al., 2004). The authors presented a new model of stratified flow stability with interfacial waves (Brauner and Moalem Maron, 1992). It was found that the stratified regime in oil-water flows was stable between two lines plotted on a graph of oil and water superficial velocities representing the theoretical limits deduced from the stability analysis of the model. Although the authors attempted comparisons with experimental data, the information available was found insufficient to provide reliable conclusions.

Apart from interfacial waves, the consideration of a flat interface seems to be limited mainly to gas-liquid flows (Brauner et al., 1996). In oil-water mixtures, the effect of interfacial tension can produce curved interfaces, although the pipe size and fluid properties seem to have an effect as well (Ng et al., 2001). Brauner et al. proposed a new stratified model to account for the curvature of the interface (Brauner et al., 1998), which agreed well with some experimental data (Raj et al., 2005).

Furthermore, Ulmann and Brauner (2006) presented a new set of closure relations along with a modified two-fluid model (MTF), in order to consider entrainment and the effect of interfacial waves on the shear stresses. The MTF relations were tested against the experimental air-water data of Espedal (1998), obtained in a 60-mm ID pipe with rough wall and inclinations up to 3º, in stratified flow when both phases were turbulent. Figure 2.7 shows comparisons of the model

with experimental data on water hold-up and pressure drop. As can be seen, the comparisons were better for hold-up. However, Hadžiabdić and Oliemans (2007) pointed out that no oil-water data was used to validate the model. Despite the efforts done through the years, the amount of experimental oil-water data available seems insufficient to thoroughly validate theoretical models, as noted by several authors (e.g. Xu, 2007), which has led to direct comparisons with gas-liquid data.

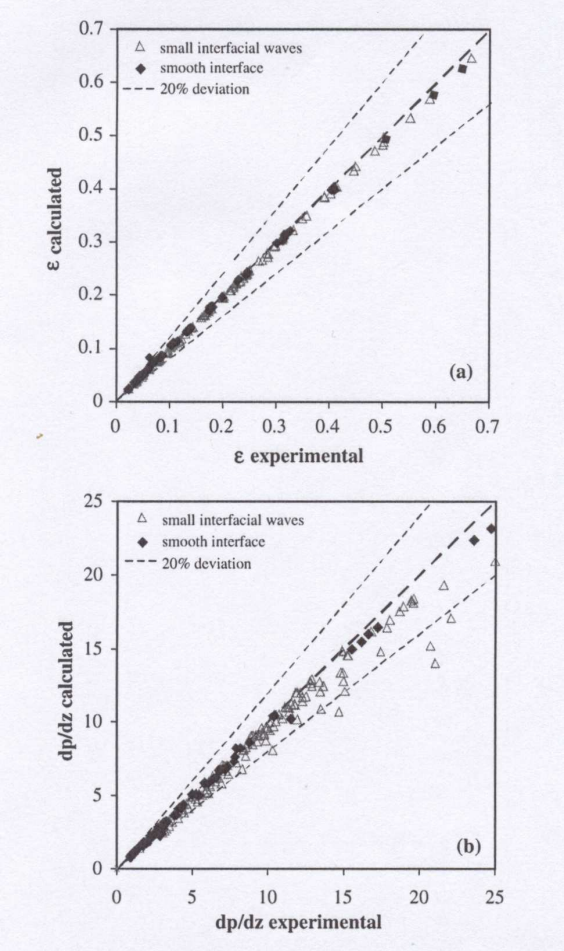

Figure 2.7 Effect of interfacial waves on the hold-up volume and the pressure drop using MTF closure relations, (Ulmann and Brauner, 2006)

The review of the literature shows how much dependant results are on the experimental conditions and how many parameters can affect the flow (fluid properties, pipe size and design, pumps, materials, inclination, instruments and operations). Due to the sizes of the experimental rig usually employed, most works published are limited to one pair of fluids and are often restricted to one facility. As a consequence, the oil-water literature is rather a scattered record of experimental data

from which correlations have not been established. In this sense, the experimental methodology developed in this Thesis to investigate stratified flows is believed to have general applicability to different fluids regardless of the pipe diameter and will, hopefully, be a useful contribution to the research community.

Al-Wahaibi (2006) pointed out that the stability models of stratified flows do not give indication of the mechanism of drop formation. There is very little work done on the physical forces that lead to entrainment and the issue remains unclear. Following developments in the gas-liquid literature, Al-Wahabi hypothesized that a drag force would exist due to differences between oil and water velocities and that entrainment would only occur whenever the drag force exceed the stabilizing effect of the surface tension. The drag would deform the leading edge of the wave. The net surface tension acting on a crest has only a "y" component if the wave is not deformed (Figure 2.8) but, as the drag acts on it, the "x" component of the force at the trailing edge would be larger than that at the front. As a consequence, the wave is expected to end up flat at the leading edge. At this point, break-up and drop formation would take place.

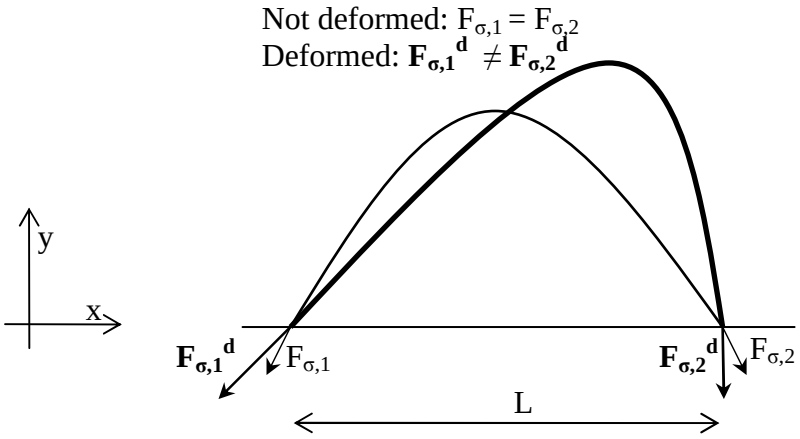

Figure 2.8 Superficial forces in a deformed and non-deformed wave (Al-Wahaibi, 2006)

The criterion for which drop entrainment would occur was found by the author to be:

$$C_d A_{wave} \rho_w \frac{(u_o - u_w)^2}{2} \geq \sigma S_i \frac{\lambda}{L}, \qquad (2.1)$$

where A_{wave} and λ are the wave amplitude and wavelength and u_o and u_w are the oil and water velocities, respectively; S_i , ρ_w, σ and C_d are the interface line perpendicular to the flow, the density of water, the oil-water interfacial tension and the drag coefficient, respectively.

Al-Wahaibi carried out experiments in order to find wave characteristics suitable for validating the model (Al-Wahaibi, 2006; Al-Wahaibi and Angeli, 2011), but results remained inconclusive. One of the difficulties is that no data correlations exist in the literature to compute C_d. The author used a correlation from gas-liquid. The verification of this mechanism is, nevertheless, subjected to the existence of interfacial waves like that in Figure 2.8. It will be demonstrated in this Thesis that the oil-water interface tend to present 3D fluctuations at fully-developed conditions rather than clearly identifiable 2D structures. This can also be one of the difficulties encountered by Al-Wahaibi, as he used a high-speed camera to calculate wave characteristics. The reasons for wave absence in the pipe (2D structures are only seen at the inlet, where the two phases join) are suggested in this work, and a thorough statistical methodology to investigate fluctuating oil-water interfaces via double wire, parallel conductance probes will be presented. This is an original approach to investigate oil-water stratified flows.

2.2 USE OF CONDUCTANCE PROBES AND HIGH-SPEED IMAGING IN OIL-WATER STUDIES

2.2.1 General uses of conductance probes

Conductance probes (particularly double wire probes), have been used extensively since the 1960s to measure liquid film thickness in gas-liquid flows (Jurman et al. 1989; Azzopardi 1997; Wang et al. 2004; Kadri et al. 2009). Webb (1970) and later Chu (1973) used them in annular flows to study liquid film wave characteristics and extract fundamental frequencies via power spectrum analysis of the signal collected. Andritsos (1992) employed a set of two double wire probes to study gas-liquid annular flows using liquids of different viscosities in pipes of diameters 95 mm and 25 mm ID. Using a sampling frequency of 250 Hz, the cross correlation of the signal of the two probes revealed the wave velocity while the power spectrum showed low frequency

contributions at 5, 8 or 15 Hz. Ring conductance probes have also been commonly used to study waves in annular flows (e.g. Azzopardi 1986). Recently, Alamu and Azzopardi (2011) applied the probes to investigate air-liquid flows in a splitter. The spectrum of the signal was calculated via the Fourier Transform of the auto-correlation function. The data from conductance probes have been widely used to calculate different parameters of gas-liquid flows, mostly in vertical and inclined pipes. Different types of probes have been applied, for example, to determine liquid hold-up (Tsochatzidis et al. 1992; Fossa 1998), void fraction (Alamu and Azzopardi 2011), interfacial velocity and interfacial area concentration (Wu and Ishii 1999; Kim et al. 2000). Probes have also been used to identify flow patterns and to estimate bubble chord lengths in non-stratified flows (Hernández et al. 2006).

In liquid-liquid applications, recent efforts have focused on the estimation of the water fraction in oil-water pipe flows under different flow patterns. Multiple needle-conductance probes of small dimension are commonly used for this purpose. Zhai et al. (2012), for example, suggested a methodology using mini-conductance probes located at different depths within the pipe. The technique was able to provide reliable results in separated flows, even when there was significant concentration of drops entrained in the phases. Xu et al. (2012) presented a technique to measure water hold-up in horizontal wells with low production using 24 needle probes mounted in 12 arms around the circumference of the pipe. The authors acknowledged the importance of treating the data prior to analysis. The signal collected from the probes was normalized to eliminate the effect of water salinity and a least-square procedure was implemented to harmonize the experimental signal using the data from the calibration of the probes.

More recently, several investigators have attempted the identification of flow patterns in oil-water flows by analysing conductance probe signals, for example Jin et al. (2003), Hernández et al (2006), Sun et al. (2011) and Du et al. (2012). Given the complexity of such flows, including many non-stratified patterns, the authors needed to use complex mathematical techniques in order to deal, in many cases, with non-stationary data. Jin et al. (2003) employed mini-conductance needle probes and an array of four ring stainless-steel electrodes flush on the inner pipe wall and suggested a procedure to predict the flow pattern of upward oil-water mixtures by estimating fractal, chaos and Kolmogorov entropies from the data. Irregular and sudden changes in the Kolmogorov entropy were found to be related to complex power spectra. In a similar set-

up, several authors have worked recently with different fluid mixtures. Du et al. (2012) investigated dispersed upward oil-water flows and noted that the fluctuations of the signal were non-stationary random. For this reason, they analysed the data in terms of Time Frequency Representation (TFR), with Adaptive Optimal Kernel (AOK) to improve the performance of the spectrum. A similar approach was used in upward gas-liquid flow by Sun et al. (2011). Wang et al. (2010) studied non-linear oil-water flows in inclined pipes using Recurrence Quantification Analysis (RQA). Jana et al. (2006) attempted the characterization of flow patterns using optical probes. They followed a double analysis of the time-series data collected. First, they reported probability density functions (pdf) of different parameters and, second, they performed a wavelet transform based on the theoretical work by Drahos et al. (2004). Chakrabarti et al (2006) used the signal from double-wire probes to detect phase inversion in oil-water dispersed flows, while Oliemans (1986), Bai (1995), Bannwart (1998) and Rodriguez and Bannwart (2006) studied wave characteristics in annular flows of heavy viscous oil-water mixtures.

2.2.2 Investigations of the oil-water interface

The shape and characteristics of the interface during the stratified flow of oil-water mixtures in horizontal or slightly inclined pipes have been the objects of many investigations. As already indicated, it is generally assumed in the literature that the flow might generate interfacial waves that could grow unstable from which drops would detach. The appearance of drops in stratified or annular flows defines the onset of entrainment and the transition towards other flow regimes. These phenomena have been discussed in e.g. Trallero (1995), Al-Wahaibi and Angeli (2007) and Al-Wahaibi et al. (2007).

Different wave types have been identified in gas-liquid flows (Andritsos and Hanratty, 1987); visualisation techniques are often used for their study, particularly when the waves appear as large, almost two dimensional and readily identifiable structures (Andritsos, 1992).

The types of interfacial waves seen in oil-water flows depend on the fluid properties. With high viscosity oils, two dimensional structures tend to form that can be studied with visual techniques (Bai, 1995). With the aim of improving lift–off for heavy oil recovery, Oliemans et al. (1987) investigated interfacial waves in annular flow. Rodriguez and Bannwart (2006) also studied annular flows in vertical pipes, and

measured wave characteristics using image analysis. Recently, other parameters of the flow (e.g. water fraction) were determined from image analysis in systems involving heavy oils (Riano et al., 2013).

Similarly, Al-Wahaibi and Angeli (2011) investigated the characteristics of oil-water flows from visual inspection and analysis of images using low-viscosity oil. Stratified flows with low viscosity oils, however, can exhibit fluctuating interfaces where visual analysis can be challenging because of the lack of easily identifiable wave structures. Such interface shapes make very difficult the quantitative analysis of wave characteristics via imaging, even when complex mathematical treatments are used. De Castro et al (2012) investigated stratified oil-water flows with viscous oil (0.3 Pas). They identified interfacial waves and classified them in three groups according to size using high-speed imaging. They further employed Fourier filters to treat the images and allow for graphical analysis. Although the authors were able to report wave lengths and amplitudes, this procedure required a large simplification, as only the so-called intermediate waves were filtered in for analysis.

2.3 STABILITY ANALYSIS OF INTERFACIAL WAVES

Even though the liquid-liquid interface with low viscosity oils may not present large, almost two-dimensional waves downstream the pipe under fully-developed conditions, such structures can develop under different circumstances (for example, at the inlet section when the oil-to-water input ratio is different from 1, as it will be shown in this work). From a theoretical point of view, wave structures can be subjected to stability analysis in order to determine their connection to drop entrainment.

The first way to investigate the stability of any physical system is to impose very small disturbances (ideally, *infinitesimal*) on an equilibrium position or state and decide whether the system eventually dampens the perturbations or rather becomes unstable and evolves towards another equilibrium state. In the wave theory, this has been done by subjecting the wave to small disturbances in comparison with its amplitude which allows neglecting quadratic and higher-order terms in the mathematical operations (i.e. linear stability analysis). The classic Kelvin-Helmholtz instability, which appears at the interface of two inviscid, stratified fluids of different density moving with relative velocity different from 0, is one example of linear stability theory (Acheson, 1990).

It can be shown that two superposed fluids, incompressible and non-viscous, flowing with different velocities lead to an irrotational flow (Yih, 1981). In these circumstances, there is a velocity potential for each phase that must satisfy the Laplace equation. The usual kinematic conditions of the linear theory should also be satisfied at the interface; furthermore, the phase pressures and surface tension allow establishing the dynamic boundary condition needed. Usually, the disturbance introduced is made periodic. These assumptions allow writing a system of equations that can be solved to satisfy the boundary conditions. The result gives the final condition for KH stability (Acheson, 1990; Drazin and Reid, 2004):

$$\left(u_w - u_o\right)^2 < 2\frac{\rho_o + \rho_w}{\rho_o \rho_w}\sqrt{g\sigma\left(\rho_w - \rho_o\right)}, \qquad (2.2)$$

where u_o and u_w are the actual phase velocities of oil and water, respectively; ρ_o and ρ_w, their densities; σ is the oil-water surface tension; and g is the gravity constant. The stratified flow would be then stable if the velocity difference between the phases is less than the term in the RHS, computed for the specific properties of the fluids considered.

The inviscid stability model was extended to oil-water flows involving viscous oils to account for shear stresses by Barnea and Taitel (1993). Trallero (1995) followed and expanded this work and provide numerous comparisons against experimental data. Occasionally, though, experimental results proved to be contrary to expectations. For example, it was argued that the inviscid model would be sufficient to predict the stability of stratified mixtures in the case of low-viscosity oils, while a complete viscous approach would be required if heavy oils were involved. However, the viscous model was found to predict better experimental data with low viscosity oil (Barnea and Taitel, 1993; Trallero, 1995). The theoretical analysis has also been extended to consider non-linear terms. Barnea and Taitel (1989) used the method of normal modes to solve the system of algebraic equations after linearization against mean values at the position of equilibrium.

The stability analysis of stratified oil-water flows does not provide any information on other flow pattern transitions. The models were further extended as to be used as discriminators of different flow pattern transitions. Brauner and Moalem

Maron (1992) and Trallero (1995) used the Hinze (1955) model of drop breakage and coalescence and followed a *structural* stability analysis of the equations in order to obtain solutions both in the stratified and non-stratified regimes. Trallero (1995) completed the work of Barnea and Taitel (1993) by considering the sheltering effect experienced by the trailing edge of the wave from the upper liquid. He further compared the final model with his own experimental data, obtained in 50-mm ID pipe with 30 cp oil viscosity. The agreement was remarkable in this case. However, the model failed to reproduce the experimental flow pattern maps of other authors (e.g. Nädler and Mewes, 1995, taken in similar conditions). In general, the model presented by Trallero under-predicted the area of dispersed flow when compared to experimentation (Guzhov et al., 1973; Oglesby, 1979; Nädler and Mewes, 1995; and Cox, 1995). Valle (2000) argued that the reason was probably because several parameters of the model were adjusted against specific data. Brauner and Moalem Maron (1992) developed a model mainly applicable to flows involving oil of high viscosity, which has not been thoroughly tested or compared to that of Trallero, probably due to shortage of experimental data. Overall, despite the increasing complexity of the analyses, the resultant models are difficult to validate or apply in practice and have not yet provided good conclusive agreement with the experimental data. For the purpose of the present work, however, the classic linear stability analysis seems appropriate to investigate interfacial waves at the inlet and to compare with the results obtained with the high-speed camera.

2.4 COROLLARY

The problem of oil-water mixing is relevant to a number of operations involving oil, from its initial separation in the oil platform to the numerous challenges concerning its transport to the refinery over long distances. Unlike the gas-liquid case, transition from stratified oil-water flow to dispersed patterns is not well investigated. There have been significant efforts to develop models than can predict the properties of the flow in the field (i.e. water fraction, pressure drop, etc.) but there is little amount of data suitable for validation of the models. Sometimes, comparisons between different experimental works are difficult. The mechanisms of drop formation are not entirely understood and, even though insights from the gas-liquid literature are normally used, oil and water have densities and viscosities of the same

order of magnitude and tend to flow at similar velocities in the pipes, which may necessitate different modelling approaches.

There is evidence in the gas-liquid literature that transition to dispersed patterns and drop formation is linked to the instability or deformation of interfacial waves. Investigation of waves in the oil-water via visual techniques has been proved difficult, since clear 2D structures, as those reported in gas-liquid, are normally not found in stratified flows of oil and water in horizontal pipes.

Double-wire conductance probes are a straightforward and inexpensive technique for investigations of two-phase flows that has widely been used in the past with different purposes. Given its ability to collect signal from the oil-water interface at high sampling frequency, the technique seems to be promising in the investigation of the interfacial phenomena when waves cannot be distinguished or studied with visual techniques. The probes could provide valuable experimental data of stratified flows with different fluids and pipe sizes and help improve models and better understand the phenomena that lead to the transition to dispersed patterns.

CHAPTER 3
EXPERIMENTAL FACILITY AND INSTRUMENTATION

3.1 EXPERIMENTAL FACILITY

The experiments with stratified oil-water flows have been performed in the large-scale, multi-phase flow facility located in the Chemical Engineering Department at University College London (UCL). The rig consists of an assembly of acrylic sections which allows visual inspection of the flows, plus equipment (oil-water separator, pumps, tanks and valves) and the instrumentation. The test fluids used are tap water (ρ_w = 1000 kgm^{-3}, μ_w = 0.001 $kgm^{-1}s^{-1}$) and Exxsol™ D140 oil (ρ_o = 830 kgm^{-3}, μ_o = 0.0055 $kgm^{-1}s^{-1}$). Figures 3.1a and 3.1b show two photographs of the rig.

Figure 3.2 shows a schematic diagram of the experimental facility used in this work. The test fluids, oil and water, are stored separately in two 800-L tanks made of fibreglass. Two identical Ingersoll-Dresser centrifugal pumps (with rated power 7.5 kW and head about 60 meters, the characteristic curve can be seen in Appendix 1) bring the fluids separately into the inlet of the test section. The individual circuits of oil and water have been represented by different types of lines in the diagram, continuous for the water and dashed for the oil. The bypass of the oil and water pumps can be regulated with the oil and water gate valves VRO and VRW, respectively. Two more gate valves, VFO and VFW, allow controlling the flow rate of each phase going into the inlet of the test section. Flow rates are measured via variable-area flow meters (ABB Instrumentation Ltd.) with 50 mm ID, in the range of 0 – 240 $Lmin^{-1}$ and with 1 % full-scale accuracy (i.e. for a measured 60 $Lmin^{-1}$ flow rate, the actual value would be 60.0 ± 0.6 $Lmin^{-1}$) The signal of the measurement can be collected at high sampling frequency (i.e. 256 Hz) and stored within in a computer via LabView™. The test pipe is made of acrylic material (i.e. Perspex) and comes in sections of 1 or 2 m in length. The ends of the sections are flat flanges with grooves to accommodate O-rings made of EPR.

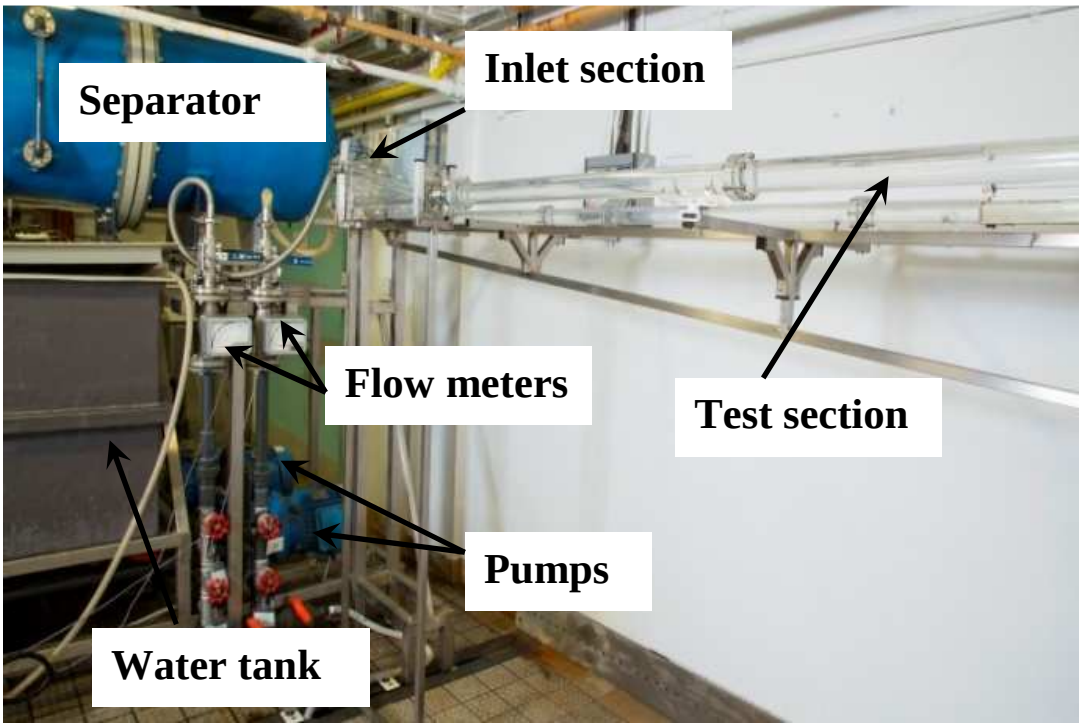

a. Tanks, separator and the inlet section

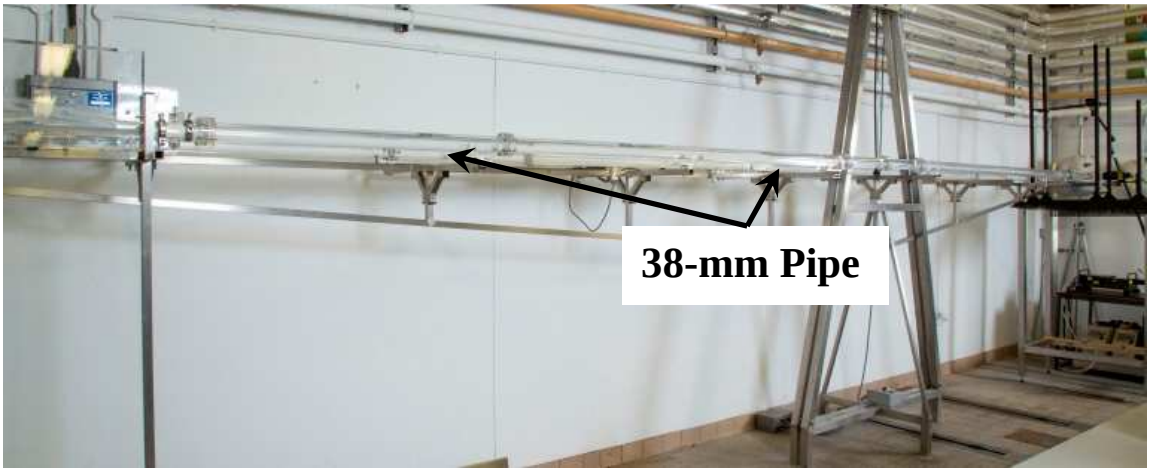

b. Acrylic test section

Figure 3.1 Photographs of the experimental facility

Downstream the inlet, the pipe sections stretch horizontally about 7 m. Two 90º elbows, connected by a short pipe section of about 0.9 m, return the mixture into a separator. Some of the pipe sections allow pressure drop measurements. Ports have size ¼" NPT (National Pipe Thread) and were fitted with stainless-steel 316 quick-connectors (FTI Fittings).

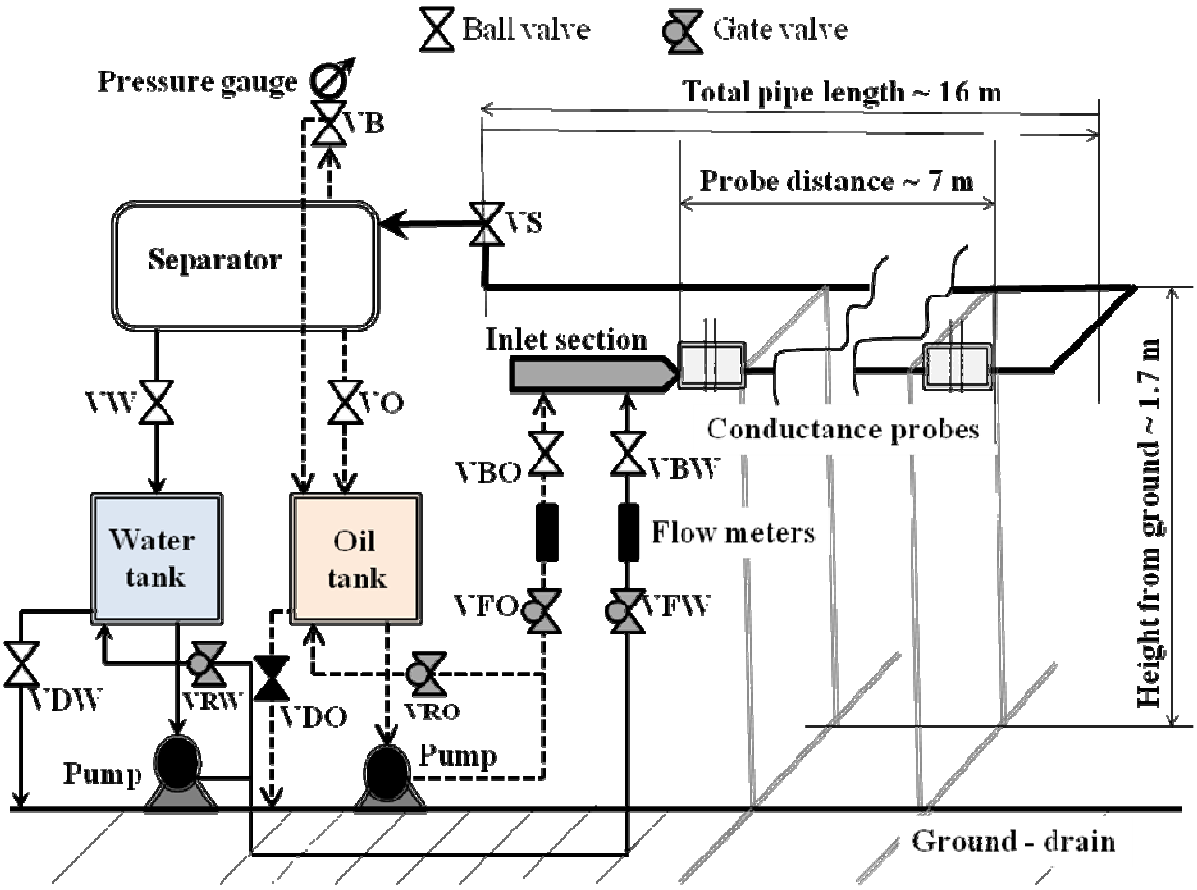

Figure 3.2 Sketch of the experimental facility

The separator is a vessel with 0.8 m^3 liquid capacity, about 2 m long and 0.7 m in diameter. The interior is built in polypropylene. Inside the vessel sits the coalescer, made of thin wires of two different materials (polypropylene and stainless steel), weaved in a mesh (KnitMesh™). The wires are selectively wetted by each of the fluids, which help the coalescence and separation of drops. The mesh also helps break the turbulence of the oil-water flow and accelerate the separation. Oil is returned to the tank from the top of the separator, while the water leaves the vessel through the bottom. For the experimental flow rates used the separation oil-water is complete. Oil and water returns can be controlled by the ball valves VO and VW, respectively.

During the experimentation, these valves were used to control the level of the liquids in their respective tanks and the location of the oil-water interface inside the separator. The Standard Operating Procedure for the operation of the facility is included in Appendix 1. In Figure 3.2, the ball valve VB was kept open at all times, to ensure that air trapped in the separator during shut downs could freely move at start up. For that, a bleeding line from the top vent of the separator was directed to the oil tank, along with a pressure gauge. The connection is ½" BSP (British Standard Parallel thread).

Table 3.1 shows the properties of the oil used in this investigation. Specifications of the product can be found in Appendix 1, as given by the supplier (Multisol Group). The surface tension of water and oil, σ_w and σ_o, respectively, measured using a Kruss Processor Tensiometer K-12 (method of contact angle) at 22 °C was σ_w = 0.072 and σ_o = 0.028 Nm^{-1}, respectively, although de-ionized (D.I.) water was used. The oil-water (D.I.) interfacial tension at that temperature is 0.0396 Nm^{-1}. These values agree well with those reported by other investigators (Al-Wahaibi, 2006).

Table 3.1 Oil Exxsol™ D140 properties

OIL EXXSOL D140							
	Temperature, °C						
PROPERTY	0	15	20	25	38	40	50
Viscosity, mPa s				5.66	3.76	2.73	
Density, kg/L	0.851	0.84	0.836	0.833	0.823	0.822	0.815
KinViscosity, mm2/s				6.8		4.6	3.6
Cp, kJ/kg K		1.91	1.93	1.95	2	2.01	2.05
				ASTMD1218		ASTD7042	

The temperature of the water was seen to vary from 7 – 10 °C in winter time to above 20 °C in the summer. The temperature of the oil in the tank during the experimentation was monitored by means of a digital thermometer (Velleman), with uncertainty ± 1°C and maintained within the limits 22 – 30 °C. It can be seen that the density does not change by more than 1 %; however, viscosity may be reduced from 5.66 cp to 3.76 cp (i.e. 30 %). Based on the predictions of the two-fluid model, however, this factor seems not to be sufficient to have an important effect on the flow, as the oil can be already classified as of low-viscosity. Improvements are, nevertheless, suggested at the end (Chapter 8).

3.2 INLET SECTION

In order to enhance stratification, an asymmetric inlet section, Y-shaped, was used to bring the oil and water together. Figures 3.3, 3.4 and 3.5 describe the inlet section in detail. The inlet consists of two ducts of the same diameter and material as the pipe (i.e. 38 mm ID and acrylic). The upper duct is inclined about 14° downwards and the lower one is horizontal. Oil enters the pipe through the top duct and water merges through the bottom one while both ducts come together at the inlet section. Due to the difference in fluid densities, this configuration minimizes mixing at the entrance. As can be seen in the figure, the size of the ducts in the inlet reduces after joining in one until the size becomes that of the pipe diameter at the exit of the inlet section. This geometry has an effect on the flow pattern and on the Kelvin-Helmholtz waves that develop at the inlet as it will be seen. Alternatively, a split plate can be located at the joint point in order to keep the phases separated down to the exit of the inlet (Figure 3.6). However, this configuration does not enhance stratification as it is usually assumed. The particular case of oil-water stratified flows with a split plate in the inlet section is discussed later and compared to that without split plate (Chapter 4). At this point, it can be said that the details of the inlet design have been found to have a large influence on the experimental results.

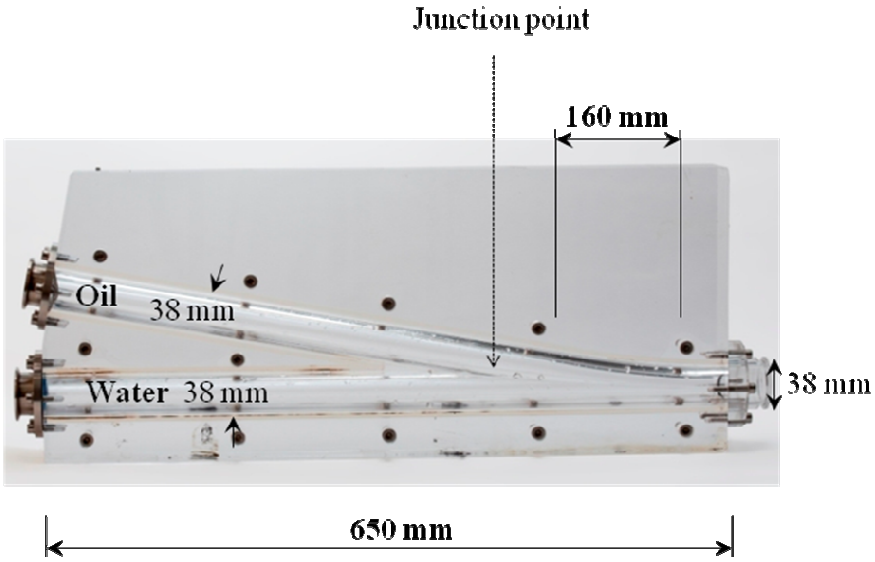

Figure 3.3 Basic view and dimensions of the inlet section

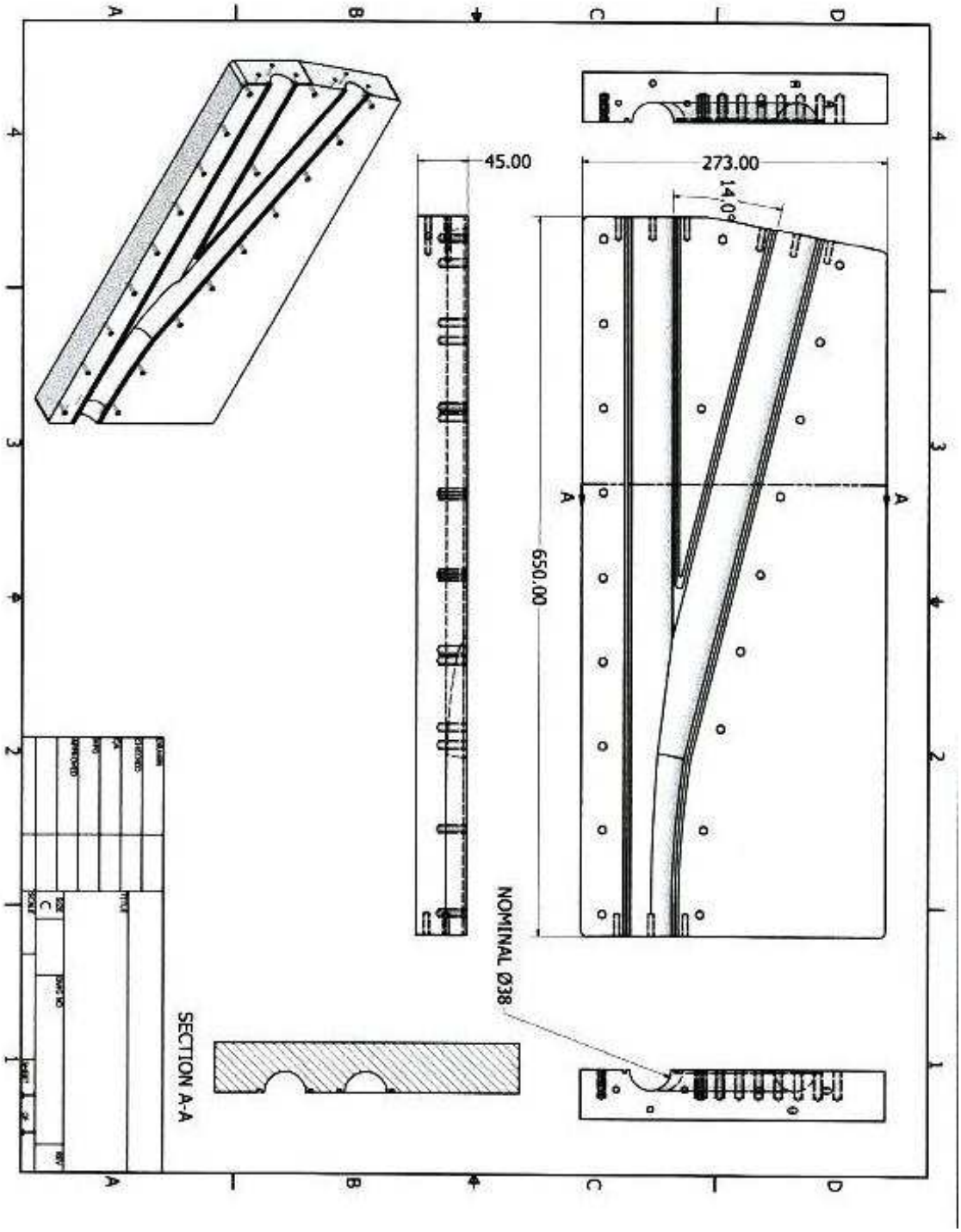

Figure 3.4 Mechanical drawing of the inlet section
(Courtesy of John Langdon, Ch. Eng. Workshop - UCL)

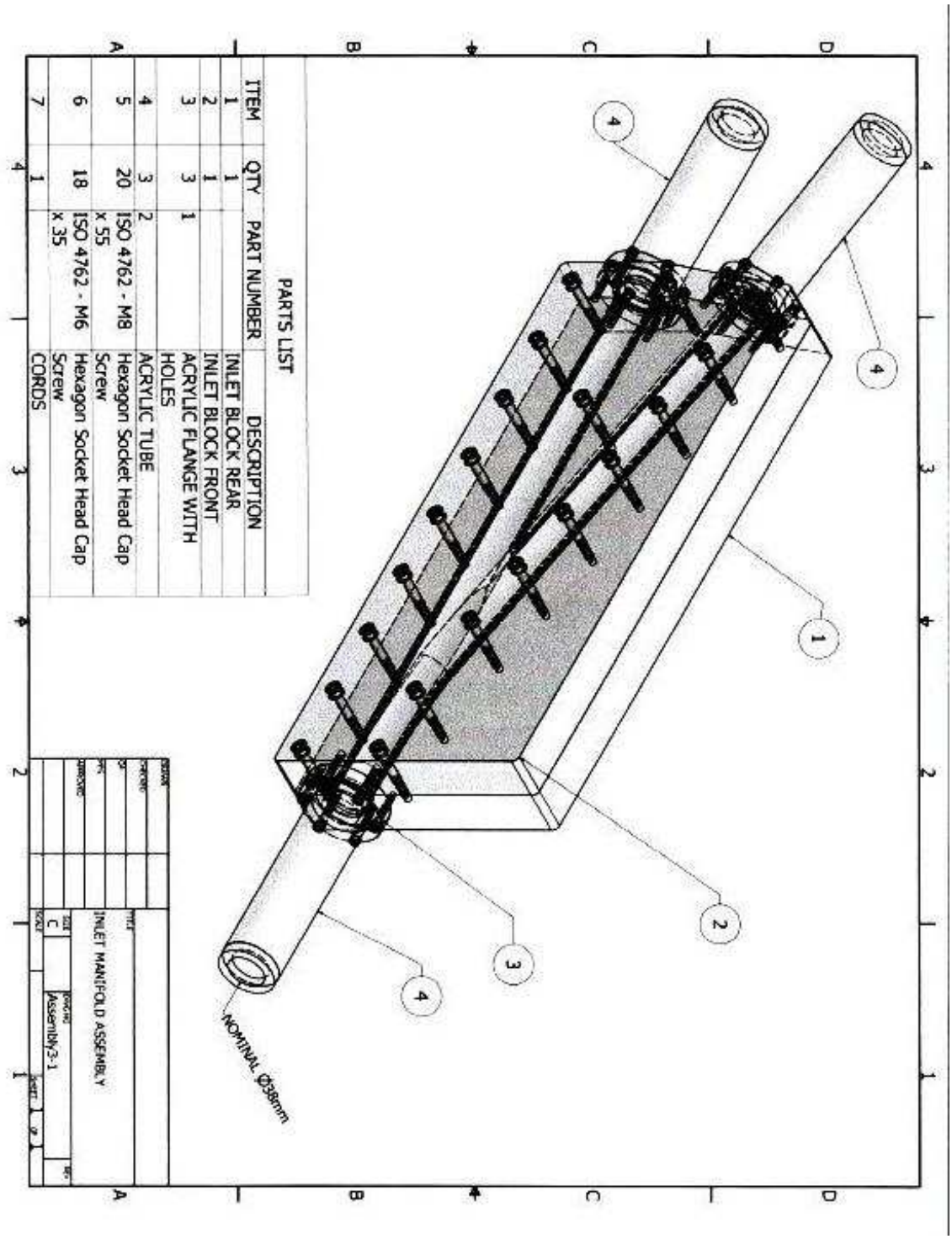

Figure 3.5 Inlet assembly

(Courtesy of John Langdon, Ch. Eng. Workshop - UCL)

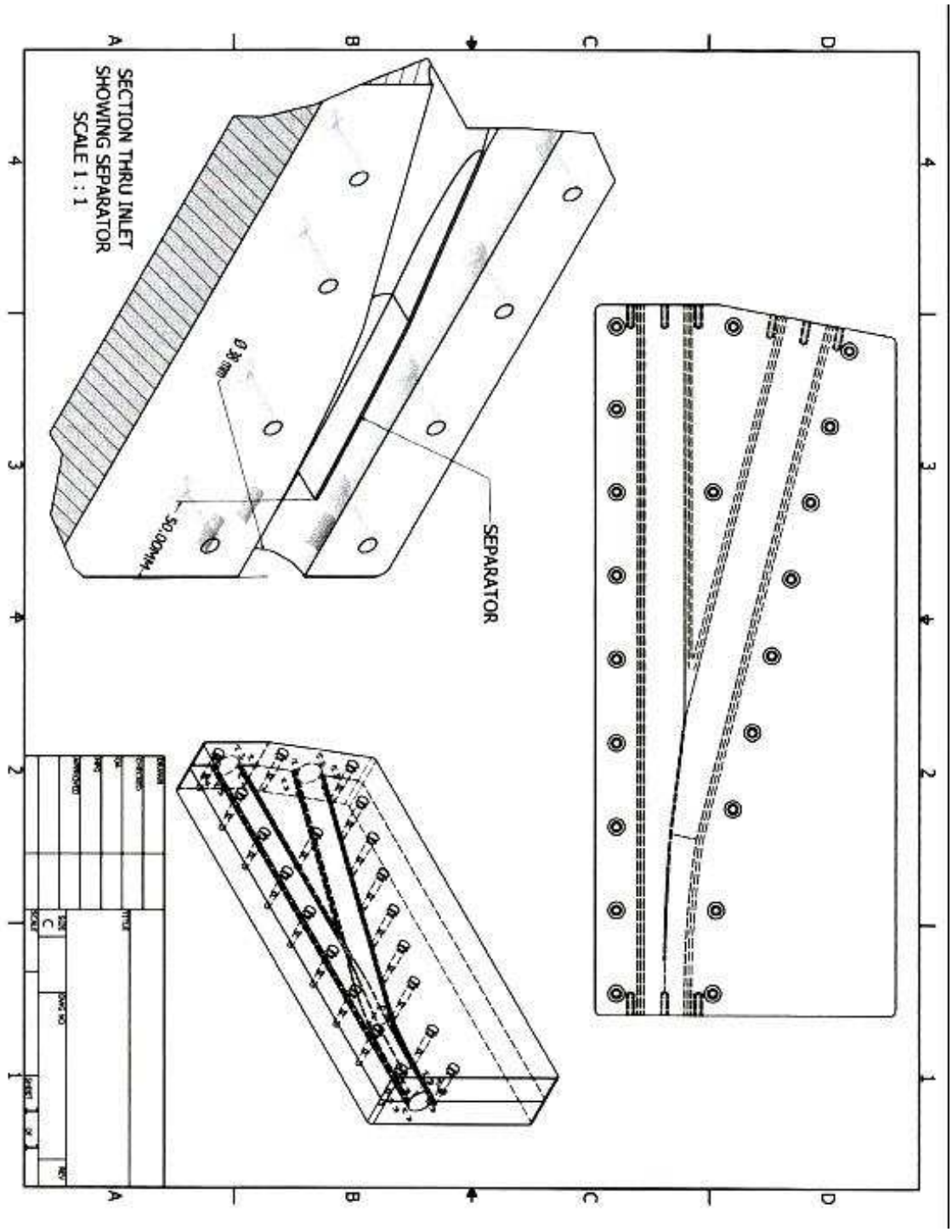

Figure 3.6 Mechanical drawing with split plate

(Courtesy of John Langdon, Ch. Eng. Workshop - UCL)

3.3 INSTRUMENTATION

Mainly, two types of instruments have been used in this investigation: a high-speed camera and double-wire conductance probes. Occasionally, a water manometer was set up *ad hoc* to measure pressure drop along the pipe.

Since the facility is made of transparent acrylic, oil-water flows could be visualized along the pipeline. Direct observation of the flow led to important insights and ideas about the nature of the oil-water interface, the formation of Kelvin-Helmholtz (KH) waves at the inlet or the identification of flow patterns (Chapter 4). Further investigation was done both at the inlet and 7 m downstream using a Phantom Miro 4 High-Speed Camera. Images were collected at high rates (i.e. 1,000 – 1,200 frames per second, fps) with exposure time 92 μs and adjustable focal distance (24 – 85 mm). The quality of the images was improved by using back-lighting and translucent paper in between the light spot and the pipe. The conclusions obtained in Chapter 7 on the evolution and stability of inlet waves are based on the analysis of high-speed images collected. The list of parts of the camera is given in Appendix 1.

The structure of the oil-water interface as well as the estimation of time-average parameters of the flow have been investigated via double-wire conductance probes. It is a well-known technique that allows collecting sample data at high frequency. In this work, two double-wire probes were used. The probes consist of two parallel stainless steel wires, 0.5 mm in diameter, located either 2 mm apart (probe 1) or 5 mm apart (probe 2), and stretched along the vertical pipe diameter (see Figures 3.7a and 3.7b). The probe section is identical in dimensions in both cases. The probes were located either immediately after the inlet section (Figure 3.8) or further downstream the pipe at about 7 m from the inlet (~180 D) where the flow is assumed to be fully-developed. In many experiments only one probe was used (either the 2 mm or the 5 mm), but signal was also collected sometimes simultaneously with both probes. In such cases, the 5 mm probe was placed close to the inlet and the 2mm one in the downstream location. No other instrumentation was placed before or between the probes, in order to minimize flow disturbances. It was confirmed that, when both probes were present, the first probe did not affect the signal of the second one. In the presentation of the results, the type, number and location of the probes are clearly given when needed.

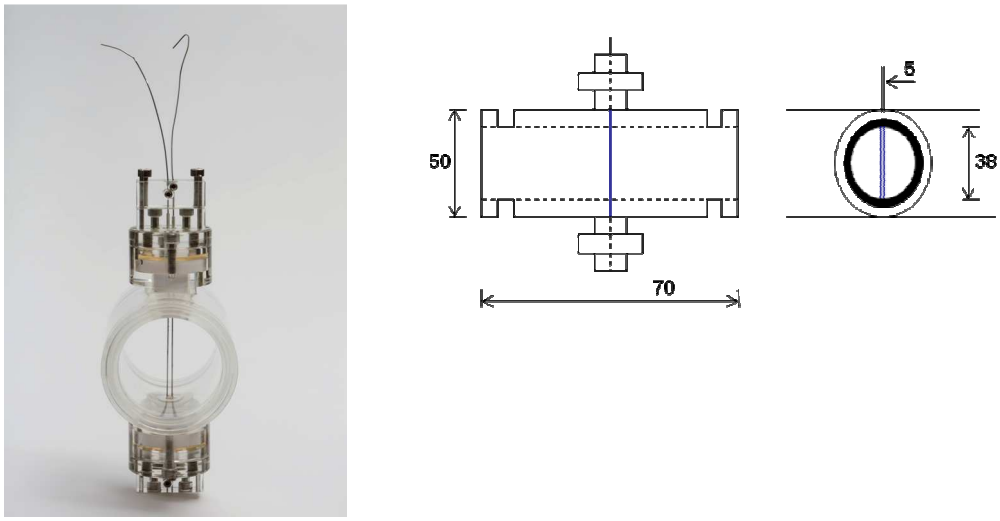

a. Photograph of 2-mm probe **b.** Drawing of 5-mm probe (measuremens in mm)

Figure 3.7 Double-wire conductance probe

The probes recorded the height of the interface over time and returned a signal of voltage. The overall set-up is designed to have negligible impedance (i.e. all resistance is due to conductance). The signal can be collected and stored on a computer using Lab View™ via an electronics box at high frequency (i.e. 256 Hz). The conductance of tap water is significantly larger than that of oil and the read-out of the probe signal was a very small number (order 10^{-4}) when there was only oil in the pipe. In this way, the signal collected with the probes in stratified oil-water flows can be calibrated to give the change of interface in time. Since the oil is in practice non-conductive compared to water, an off-line calibration was preferred in which air was used instead of oil (air is not conductive). This procedure was found to be significantly more precise and cleaner than the equivalent involving oil since a flat interface was readily obtained without any of the issues introduced by the oil. The uncertainty of the calibration preparations in the laboratory (i.e. measure of water volumes) was 1.8 %, while the data acquisition system introduced an average 0.7 % error. A good calibration line between the signal and the interface height was found, with uncertainty 1.3 %. The calibration process is described in detail in Appendix 2.

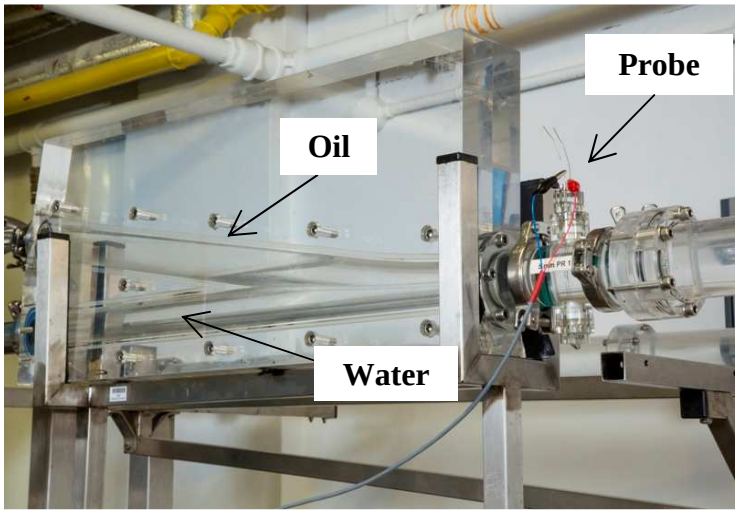

Figure 3.8 Inlet section and conductance probe installed at Position 1

A significant amount of work was done with Particle Image Velocimetry during this research. Since this technique could be a further extension of the Thesis in the future and the preliminary results do not constitute a fundamental part of the conclusions, details are not included in the text but in Appendix 1.

CHAPTER 4
EXPERIMENTAL OBSERVATIONS

4.1 INPUT PARAMETERS

The experimental facility described in the previous chapter was used extensively to observed and investigate the flow of stratified oil-water mixtures. Different flow patterns can be generated by choosing the flow rates of oil and water. Therefore, assuming that the flow is essentially isothermal, the dynamics and parameters of the mixture downstream the pipe in fully-developed conditions (equilibrium interface height and water fraction, actual phase velocities and Re numbers) as well as its development in the inlet section are determined only by the input parameters, namely the volumetric flow rates or superficial velocities of oil and water. The superficial velocity or linear velocity of a phase is its volumetric flow rate per unit of cross-sectional area of the entire pipe. Derived from superficial velocities, $u_{s,o}$ (oil) and $u_{s,w}$ (water), there are two useful input parameters commonly employed in the investigation of stratified flows, the mixture velocity, U_{mix}, and the oil-to-water input ratio of volumetric flow rates, r, defined as:

$$U_{mix} = u_{s,o} + u_{s,w} \tag{4.1}$$

$$r = \frac{u_{s,o}}{u_{s,w}} \tag{4.2}$$

The mixture velocity gives indication of the total flow rate per unit of cross-sectional area of pipe regardless of the composition, while the input ratio is a dimensionless parameter that states the composition of the flow and differentiates qualitatively flows dominated by oil ($r > 1$) or water ($r < 1$).

The flow rates of oil and water are linked to the mixture velocity and input ratio by solving simultaneously the system of Equations 4.1 and 4.2. These relations are shown below and allow generating flows of any input ratio and mixture velocity desired by selecting the appropriate pair of flow rates in the laboratory.

$$Q_o = U_{mix} \frac{r}{1+r} A \tag{4.3}$$

$$Q_w = U_{mix} \frac{1}{1+r} A \quad , \tag{4.4}$$

where Q_o and Q_w are flow rates and A is the cross-sectional area of the pipe.

4.2 FLOW PATTERNS

Oil-water flow patterns with input ratios between 0.25 and 4 and U_{mix} between 0.6 and 2.4 ms^{-1} were investigated with the aid of the high speed camera 7 m downstream the inlet section (at a distance of about 180 times the pipe diameter, 180 D). Flow rates could be selected by operating the valves and input ratios and mixture velocities calculated via Equations 4.3 and 4.4. Typically, a range between 20 $Lmin^{-1}$ and 60 $Lmin^{-1}$ was investigated in steps of 5 $Lmin^{-1}$.

Three main patterns were identified: 1) stratified flow, with both continuous phases flowing completely separate; 2) dual continuous flow, where both phases retain their continuity showing a clear interface of separation, but drops of variable size of one phase appear regularly in the other, distributed next to the interface; and 3) *intermediate* flow, characterized by a quite rough interface and the presence of sporadic, tiny drops of one phase into the other. Fig. 4.1 shows the boundaries of transition between the patterns as observed experimentally. The lines of constant flow rates of oil and water were calculated via Equations 4.3 and 4.4 and values are given in $Lmin^{-1}$. It can be seen that any flow desired for inspection or investigation afterwards could be readily generated in the laboratory using this map.

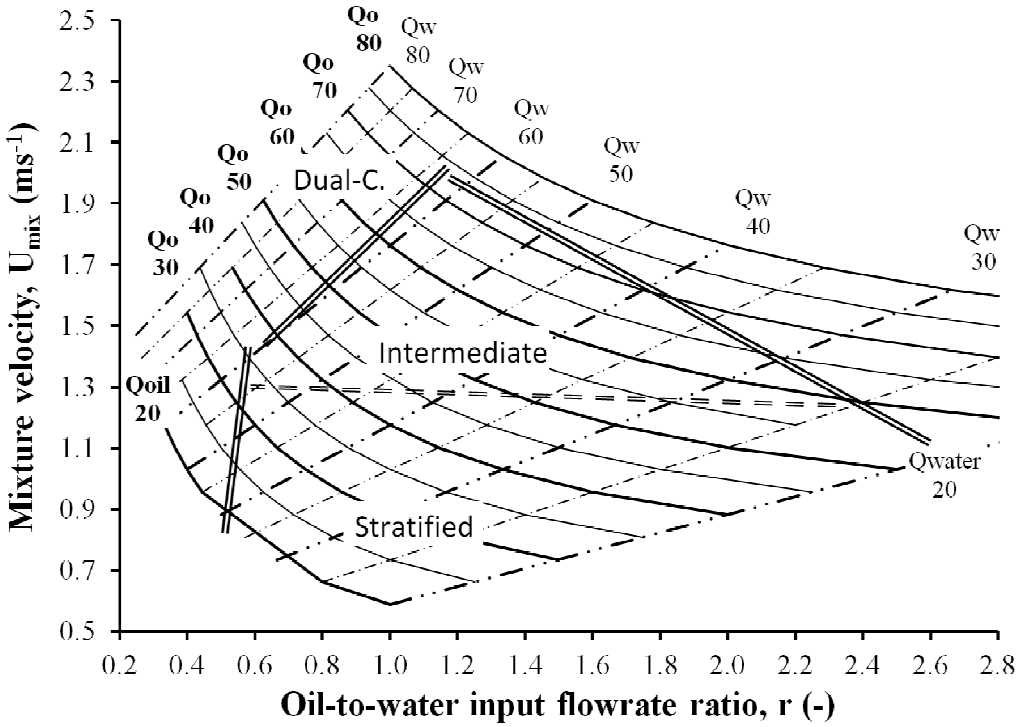

Figure 4.1 Experimental flow pattern map

The patterns are affected by both the mixture velocity and the oil-to-water input ratio. The roughness of the interface downstream the inlet is seen to increase only with increasing mixture velocity (Figures 4.2a – 4.2d), whereas transition to dual continuous pattern, with clear drops, is mainly related to the input ratio becoming sufficiently different from 1 (Figures 4.3a and 4.3b). At input ratios around 1, stratified flow prevails at mixture velocities up to 1.2 ms^{-1}. As the mixture velocity increases further, the flow pattern becomes intermediate (Figures 4.2c and 4.2d). The width of the intermediate region decreases with the mixture velocity and reduces faster along the boundary at input ratios $r > 1$. At even higher mixture velocities, dual continuous flow establishes.

At low input ratios ($r < 0.60$) a direct transition from stratified to dual continuous flow occurs. This transition is seen even at low mixture velocities, where is sharp, almost independent of the mixture velocity. On the contrary, transition along the entire range of input ratios $r > 1$ is dependent both on mixture velocity and input ratio.

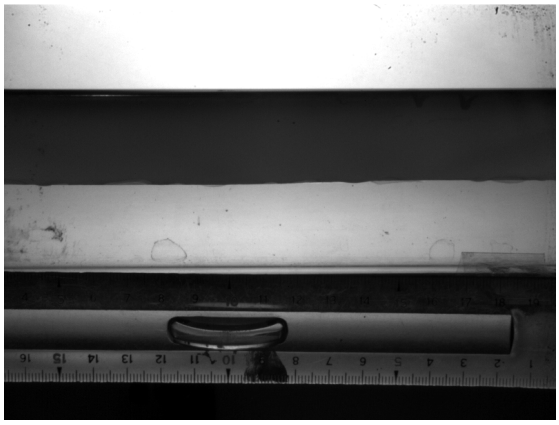

a. U_{mix} = 0.6 ms^{-1}

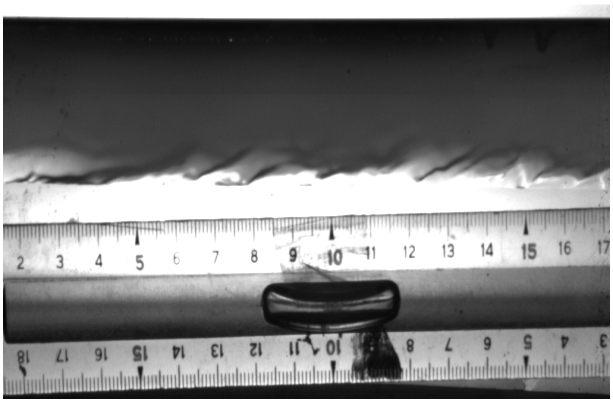

b. U_{mix} = 0.85 ms^{-1}

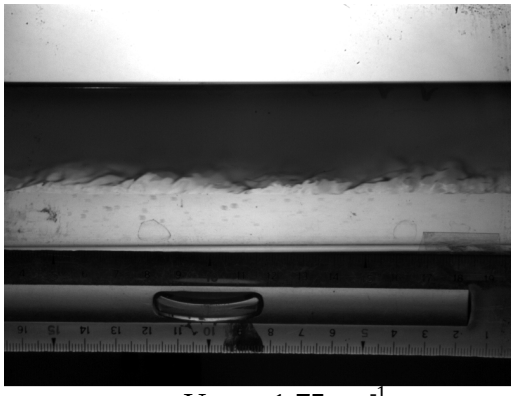

c. U_{mix} = 1.75 ms^{-1}

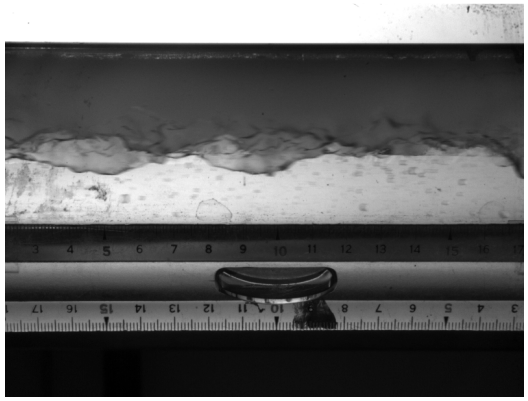

d. U_{mix} = 2.05 ms^{-1}

Figures 4.2 Roughness of the interface with increasing mixture velocity (r = 1)

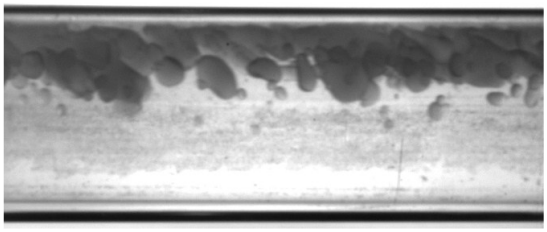

a. r < 1
(r = 0.3; U_{mix} = 1.35 ms^{-1})

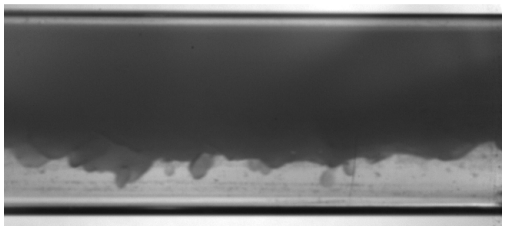

b. r > 1
(r = 4; U_{mix} = 1.45 ms^{-1})

Figures 4.3 Dual continuous flow

The asymmetry of the boundaries of the stratified or the intermediate flow to dual continuous flow at r < 1 and r > 1 (Figure 4.1) implies that the formation of drops is delayed in the case of large input ratios (i.e. large oil fractions). At U_{mix} = 1.4 ms^{-1}, for example, with only 35 % oil fraction in the pipe (r = 0.55), the flow pattern is dual continuous: numerous drops of different sizes are seen and the interface is relatively smooth (Figure 4.4a). As opposed, at the same mixture velocity and similar water fraction (33 %, r = 2), the flow is in the intermediate regime: only small and sporadic drops are seen and the interface is rougher (Figure 4.4b). Additionally, there is a qualitative difference in the dual continuous regime between flows at low and large input ratios. For similar mixture velocities, drops are larger and of similar size in the case of small input ratios, while they are generally smaller with variable sizes at large input ratios (Figures 4.5a and 4.5b, respectively).

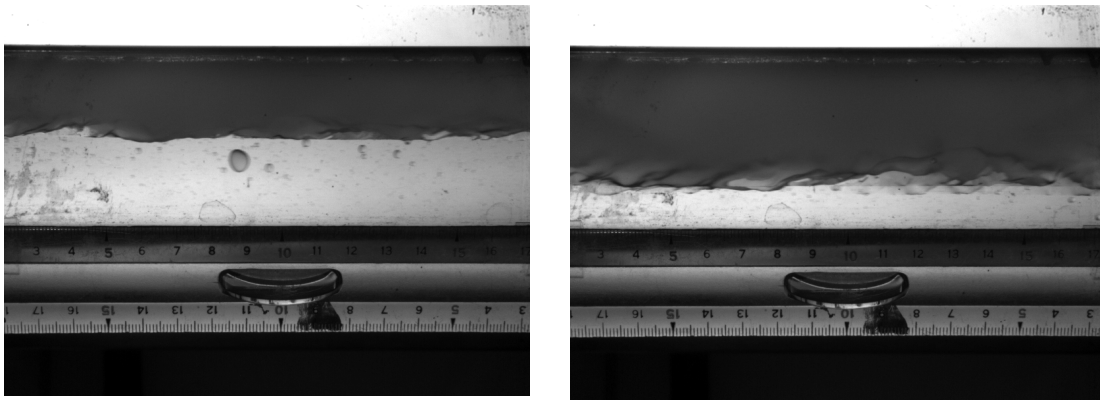

a. Dual-continuous flow ($r = 0.55$; $U_{mix} = 1.4\ ms^{-1}$)

b. Intermediate flow ($r = 2$; $U_{mix} = 1.4\ ms^{-1}$)

Figures 4.4 Asymmetry of transition boundaries at r < 1 and r > 1

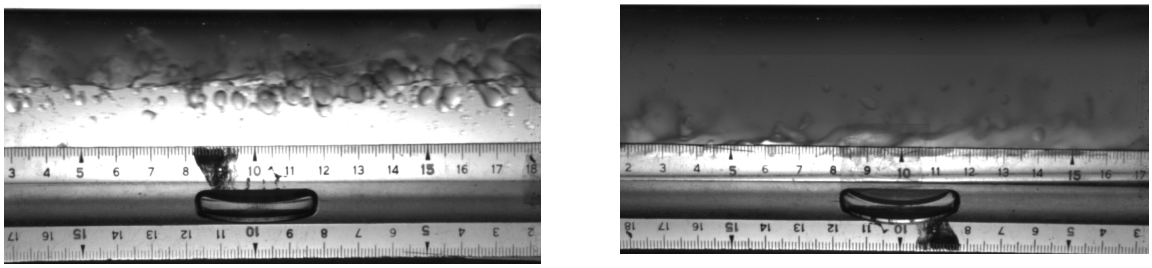

a. r = 0.25; $U_{mix} = 1.5\ ms^{-1}$

b. r = 4; $U_{mix} = 1.5\ ms^{-1}$

Figures 4.5 Drops in dual-continuous flow at r < 1 and r > 1

At input ratios r < 1 or r > 1, clear interfacial waves were seen to develop and grow at the inlet (Figures 4.6a and 4.6b). In dual continuous flow, drops are seen immediately after the inlet junction; drop formation can be related to such waves, possibly via the Kelvin-Helmholtz (K-H) instability mechanism, as investigated in Chapter 7.

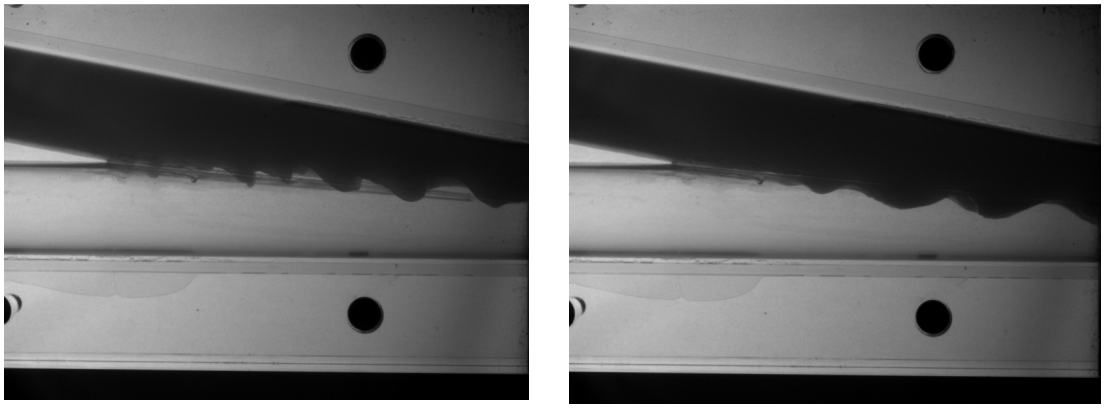

a. r < 1 (r = 0.60; U_{mix} = 1.2 ms^{-1})

b. r > 1 (r = 2.15; U_{mix} = 1 ms^{-1})

Figures 4.6 Interfacial waves at r ≠ 1 in the absence of split plate

However, in all cases with r close to 1 no interfacial waves are seen at the inlet. Figures 4.7a and 4.7b present two additional high-speed photographs at the inlet with and without waves, depending on the input ratio. Finally, Figures 4.8a and 4.8b show an example of how the waves that developed as 2D structures at the inlet eventually vanished further downstream the pipe for all cases considered. This important observation will be largely discussed in the following chapters.

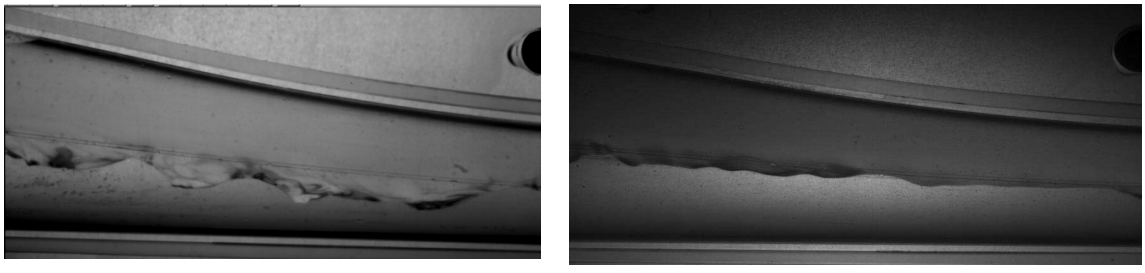

a. r = 2.5; U_{mix} = 1.1 ms^{-1}

b. r = 1; U_{mix} = 2 ms^{-1}

Figures 4.7 Oil-water interface at the inlet section

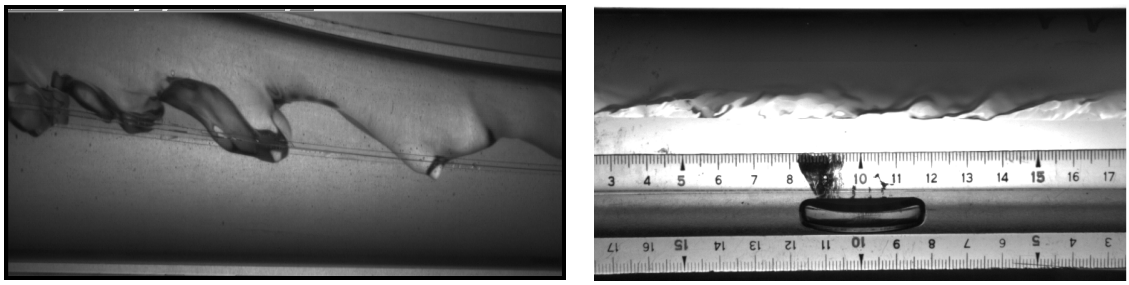

a. Inlet **b.** Downstream the pipe

Figures 4.8 Evolution of the oil-water interface (r = 0.5; U_{mix} = 1 ms^{-1})

The absence of inlet waves at input ratios close to 1 may explain the existence of the large intermediate region at those conditions that extends to high mixture velocities with very small and sporadic drops (Figure 4.1). The Re numbers of both the oil and water phases increase as the mixture velocity increases; the increased level of turbulence in the two phases explains the roughness of the interface in the intermediate region. The sporadic, small drops that might develop in the pipe could result from increased mixing close to the inlet. Quite occasionally, drops may detach from stretched patches of the fluids along the test section (Figures 4.9a and 4.9b). However, this latter scenario was seen very rarely, and it can be concluded that drop formation and, ultimately, the development of flow patterns take place almost completely at the inlet, or shortly afterwards.

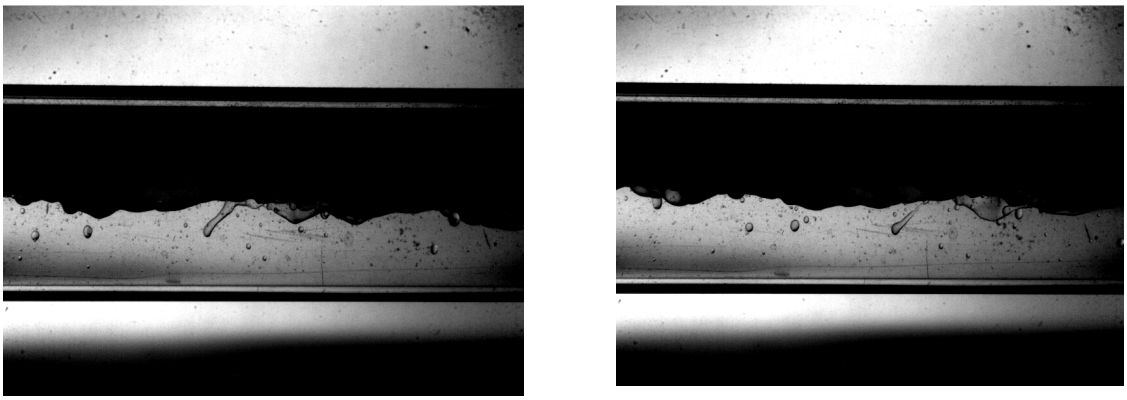

a. t = 0 s **b.** t = 30 ms

Figures 4.9 Rare drop formation in pipe (r = 1.1; U_{mix} = 1.75 ms^{-1})

In previous literature, stratified flow has been seen to prevail at all phase fractions when the mixture velocities are low (e.g. see patterns in Trallero 1995; Lovick and Angeli, 2004; Al-Wahaibi 2006). This is in contrast with the results of the current work where, even at the very low mixture velocities, stratified flow was not seen at low and high phase ratios (Figure 4.1). This was also reported in a recent study by Kumara et al. (2009). At horizontal flows they observed the dual continuous pattern (quoted as "stratified with mixing at the interface") at low mixture velocities and very small or large water fractions (0.1 and 0.9, or input ratios 9 and 0.11, respectively); in our study the boundaries of stratified flow at low mixture velocities occurred at much more moderate input ratios (see Figure 4.1). At higher mixture velocities in the map by Kumara et al. the transition from stratified to dual continuous flow was given as a straight line at constant mixture velocity while it varied with mixture velocity in our study and reached a maximum at r=1.2. In both studies drops in dual continuous flow would be present immediately above or below the interface, and no coherent waves were seen. Interestingly, Kumara et al. did not observe the intermediate pattern. The different fluid properties, pipe diameter and material (790 kgm^3 against 830 kgm^3 in density, 1.64 cp against 5 cp in viscosity; 56 mm against 38 mm in pipe diameter, and steel against acrylic) may account for these differences in the boundaries or, perhaps, some subjective element of judgement.

It was observed that the highest mixture velocity achieved in stratified pattern occurred at input ratio r = 1.2, but not 1, as expected. It can be readily noted that the value 1.2 corresponds to the water-to-oil density ratio of the fluids employed in the experimentation. Since the input ratio can be written as follows:

$$r = \frac{\rho_W}{\rho_O} R , \qquad (4.5)$$

where R is the mass flow-rate oil-to-water ratio and ρ_o and ρ_w are the densities of oil and water, respectively, Equation 4.5 implies that the dual continuous flow is mostly delayed when oil and water flow at equal mass flow rates, rather than volumetric flow rates. As a result, it could be hypothesized that a criterion of transition to dual continuous flow could be:

$$\frac{\rho_o}{\rho_w} \cdot r_{t,h} = 1 \quad , \tag{4.6}$$

where $r_{t,h}$ is the input ratio at transition (t) to dual continuous flow at the highest (h) mixture velocity. Equation 4.6 was found to describe the transition to dual continuous flow in horizontal pipes in several flow pattern maps available in literature (as shown in Trallero, 1995: Scott, 1985; Nädler and Mewes, 1995; and Valle and Kvandal, 1995). It should be mentioned here, however, that it is often difficult to apply Equation 4.6 to literature data because flow pattern classifications can be different, while boundary lines between patterns are usually drawn from a discrete set of experimental points and are approximate. Additionally, the design of the inlet may affect significantly the development and boundaries of the flow patterns.

4.3 INFLUENCE OF THE INLET GEOMETRY

In the investigation of stratified flows, a split plate is sometimes used within the inlet geometry in order to minimize the mixing of the fluids and, therefore, enhance stratification (Kumara et al., 2009; Ngan et al., 2011; Al-Wahaibi and Angeli, 2011). A plate was also available in this work. The inlet section is composed of two slabs of acrylic that are mounted and tightened together; the split plate can fit into thin grooves rimmed along the contour of the semi-cylindrical ducts of each slab. The split plate runs from the junction point down to 50 mm prior to the end of the inlet section (Figure 3.6). For convenience, Figure 4.10 shows schematically the location.

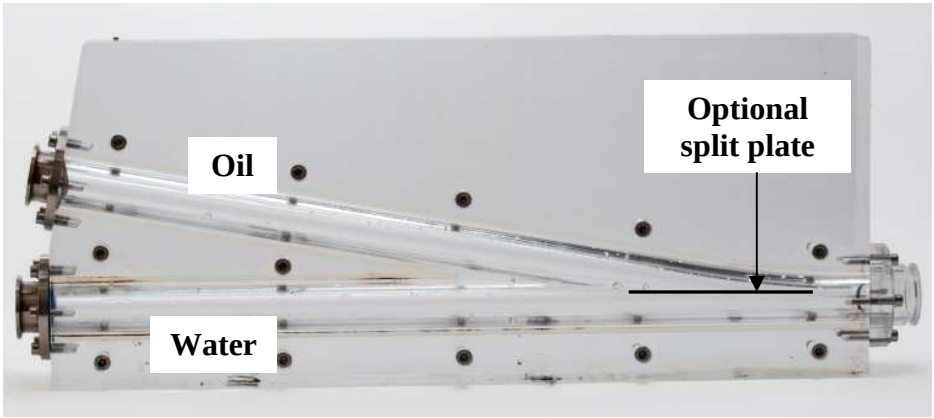

Figure 4.10 Inlet section with or without split plate

Contrary to expected, the split plate was found to have a detrimental effect on stratification. Figure 4.11 compares the flow pattern map downstream the pipe with and without split plate. It can be seen that the boundaries of flow pattern transitions are affected and the area of stratified flow is more limited. The intermediate flow was not observed when the split plate was in place and the stratification area was surrounded entirely by dual-continuous flow. However, one interesting resemblance is the asymmetry of the boundaries in both scenarios, with a sharper transition to dual-continuous flow at input ratios r < 1, roughly independent on the mixture velocity.

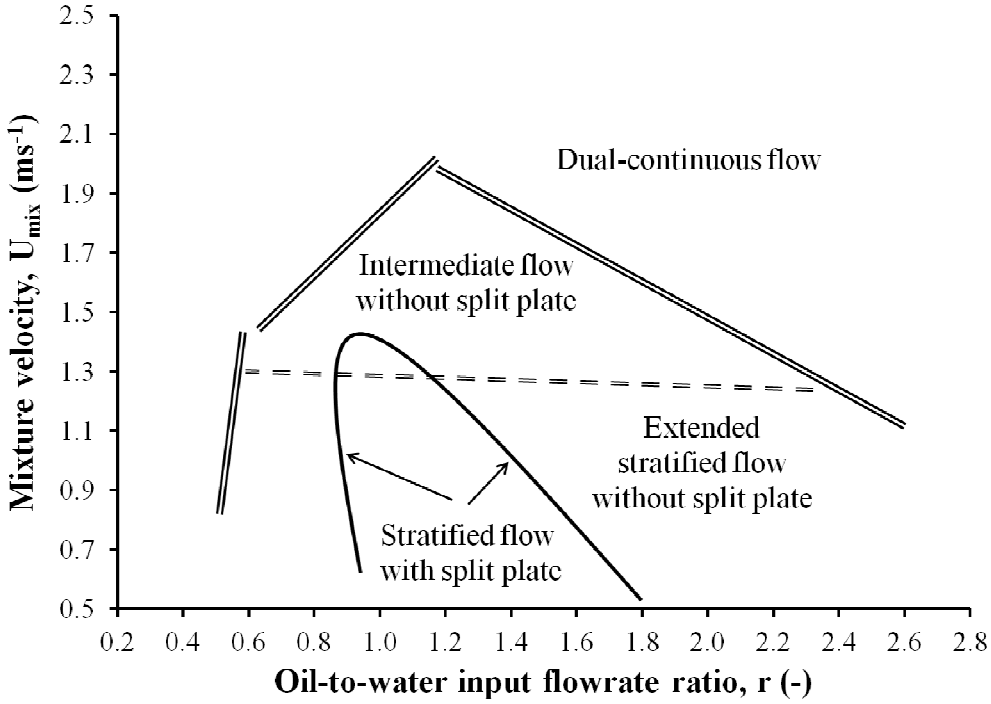

Figure 4.11 Comparison of flow patterns with and without split plate

Most significant, clear 2D waves were not seen to develop at the junction of both phases when experiments were run with the split plate in the inlet. Instead, at conditions sufficient to generate dual continuous flow, a stream of drops generated at the junction. Figure 4.12a shows the dual continuous flow near the inlet and compares it with the stratified flow seen at the same flow conditions in the absence of the split plate (Figure 4.12b).

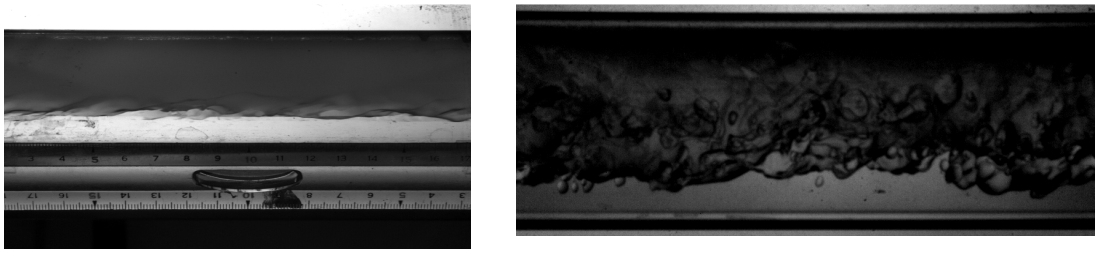

a. Without split plate **b.** With split plate

Figure 4.12 Oil-water mixture shortly after the inlet (r = 2; U_{mix} = 1.5 ms^{-1})

4.4 VELOCITY PROFILES

The oil and water phases in the stratified flows investigated are mostly in the turbulent regime. This is particularly true for the water phase, while low mixture velocity flows result in oil Re numbers in the transition region from laminar to turbulent flow (i.e. 2,000 – 6,000). As indicated in Chapter 2, Particle Image Velocimetry (PIV) is a powerful technique for the investigation of velocity profiles and turbulence properties. During the studies of this Thesis, PIV instrumentation was available and preliminary tests were conducted to investigate its specific application to stratified oil-water flows in pipes. A brief review of the technique and a summary of the work can be found in Appendix 1 and in one of the conference papers attached at the end.

The turbulence of single-phase water at low flow rates was verified via Particle Image Velocimetry by comparing the time-average velocity profile with the expected turbulent profile following the classic Prandtl one-seventh power law. It is well-known that, if the friction factor is written according to the Blausius equation, i.e. smooth pipes, the velocity profile in single-phase and turbulent flow can be approximated as (Coulson and Richardson, 2010):

$$\frac{u_y}{u_{y,max}} = \left(1 - \left|\frac{y}{R}\right|\right)^{\frac{1}{7}}, \qquad (4.7)$$

where y is the distance from the center of the pipe; R is the radius of the pipe; u_y is the phase velocity at a distance y from the center of the pipe; and $u_{y,max}$ is the maximum local phase velocity (y = 0). Figure 4.13 compares the turbulent profile expected from Equation 4.7 and the experimental data obtained via Particle Image Velocimetry. The data shown is an average of several instantaneous velocity profiles collected at a time distance of 0.14 s from each other (i.e. 7 Hz PIV pair-image collection). The case shown in the figure is that of water at the flow rate of 20 $Lmin^{-1}$; turbulent profile in the water phase was therefore verified at lowest flow rate. It can be seen that experimental results could not be obtained very close to the wall. This is due to practical difficulties in obtaininig good vector fields near rigid boundaries because of reflections and changes in the refractive index. These two problems and additional issues near the interface in two-phase flows are difficulties for the application of the technique to the investigation of oil-water stratified flows.

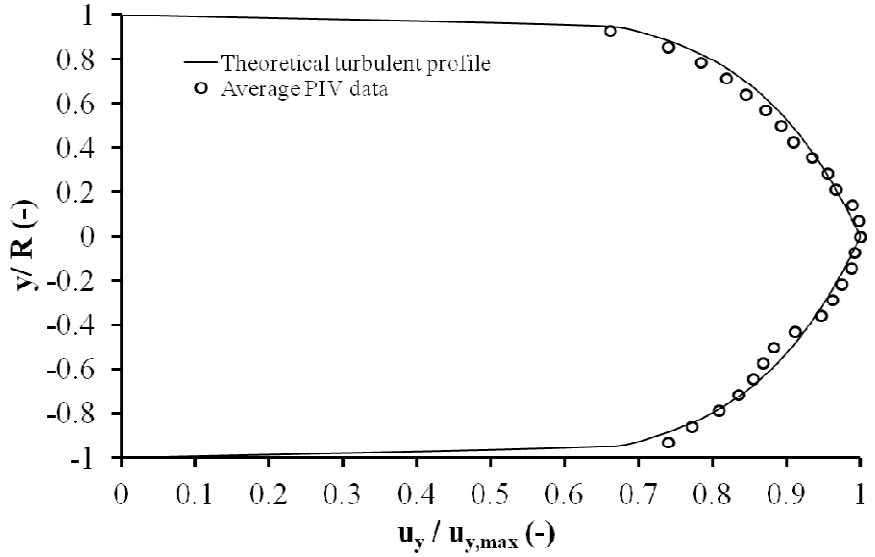

Figure 4.13 Turbulent profile in single-phase water via PIV
(Q_w = 20 $Lmin^{-1}$, Re_w = 11,200)

In two-phase flow, differences in fluid properties may necessitate the use of different seeding particles. Some authors have been able to report velocity profiles across the entire section of the pipe in oil-water stratified flows (e.g. Kumara et al., 2010). Preliminary checks in the laboratory suggest that standard glass, silver-coated particles

(ρ_s = 1.03 gcm^{-3}) are suitable only for the water phase. Instantaneous velocity profiles could be measured at different oil-water stratified flows. As example, Figure 4.14 shows the instantaneous water phase velocity averaged at different locations on the same image. The interface value is also a spatial average along the image of fluctuating interface. In general, the bottom of the pipe seems to give the usual steady decrease of velocity to the instantaneous profile, while measurements near the interface were found greatly variable from one instant to another. However, the average profiles of vorticity as measured with PIV seem only different from 0 near the interface and towards the bottom of the pipe. These preliminary results seem to imply that at locations sufficiently far from the wall and the bottom of the pipe, the flow of the water phase at fully-developed conditions is determined by turbulence (i.e. randomness), which justifies a line of future investigation of fluid phases based on turbulence analysis (Chapter 8).

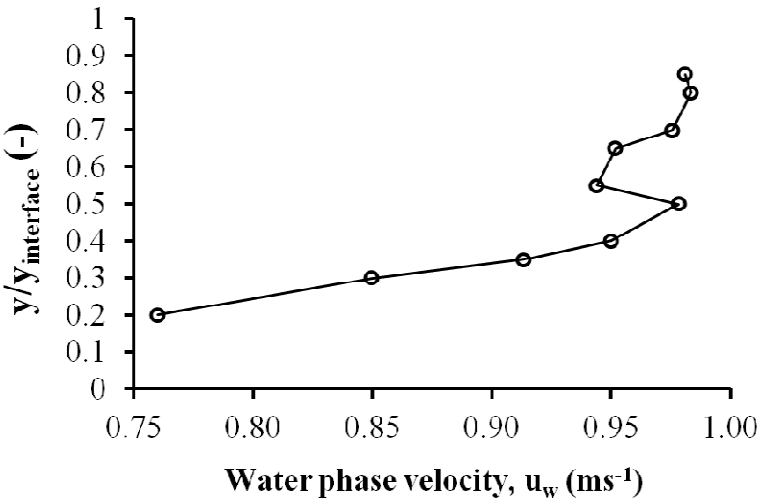

Figure 4.14 Instantaneous water phase velocity profile (r = 1; U_{mix} = 0.9 ms^{-1})

4.5 COROLLARY

These observations of experimental oil-water flows in the laboratory suggest that the development of interfacial waves is not necessarily linked to increasing mixture velocities and that there is no significant evolution of waves or drop formation downstream the pipe. On the contrary, the waves develop at the inlet if the input ratio is different from 1, and dampen and vanish shortly afterwards. These two results are important contributions of the present work and triggered an entirely new approximation to the investigation stratified oil-water flows. Based on the absence of clear wavy structures downstream of the pipe and its apparently fluctuating structure, a method to study such interfaces was fully developed on statistical grounds and is presented in the following chapter. The complete methodology and approach is an original contribution to the field of oil-water flows.

CHAPTER 5
DEVELOPMENT OF SIGNAL ANALYSIS METHODOLOGY

5.1 INTRODUCTION

The observations in the lab presented in the previous chapter showed two different types of oil-water interfaces that occur in oil-water flows under the conditions indicated. One type reveals clear waves at the interface, developing at the inlet, in the immediate trail of the junction point of the two fluids. The second type of interface occurs further downstream the pipe, where the flow can be considered fully-developed, and looks rather like a surface affected by 3D fluctuations, without readily identifiable waves. Transition from the first type of interface (wavy) to the second (fluctuating) takes place in a pipe distance no longer than 2 meters from the inlet regardless of the flow conditions. The inverse development has never been observed; in other words, the fluctuating interface seems to be a stable or fully-developed form of the oil-water flow in pipes, as investigated.

The study of these type of interfaces via high-speed imaging is quite difficult and impractical and, from an experimental point of view, probably inappropriate. No waves are distinctly seen to travel as coherent structures along the flow. Perturbations on the interface are, on the contrary, very small in all directions and occur in a short time frame. On the contrary, waves at the inlet, clearly identifiable, can be followed as they travel at a speed comparable to the mixture velocity in ms^{-1}. These verifications suggest that the fluctuating oil-water interface requires a different treatment. The visual aspect of the interface allows the assumption that every point of it can oscillate around an equilibrium value more or less freely, somewhat affected by randomness. For this reason high-frequency double-wire conductance probes can be used to collect the signal of the oil-water interface of stratified flows, as to produce a statistical record of sufficient length to contain all the features of the fluctuation. Since only the interface very near the wall of the pipe seems significantly affected by the wettability of the pipe material, almost all the points of the interface would be expected to oscillate in the same manner, and the effect of those near the wall on the entire signal record is expected to be quite small.

As introduced in Chapter 3, the conductance probe consists of two parallel stainless-steel wires, 0.5 mm in diameter, located a few millimetres apart (probes with wires 2-mm and 5-mm apart have been used in this work) and stretched along a pipe diameter at the central plane of the pipe. During the stratified oil-water flow, the probe signal provides a measurement of the interface height variations over time. The impedance of the overall set-up is designed to be negligible (i.e. it is assumed that all resistance is due to conductance). The signal was related to interface height through an off-line calibration procedure where air was used instead of oil, as they are both non-conductive (Appendix 2). The probe signal was found to give a linear response against the water interface height. No other instrumentation was placed before the probe, in order to minimize flow disturbances.

Different sampling frequencies and collection times were tested during the first stages of this investigation with conductance probes. In the end, it was found that 4-min data series collected at 256 Hz normally produced random, stationary and Gaussian records of interface height over time, if spurious trends introduced by the instrumentation were removed and the data was properly treated prior to analysis. Furthermore, this sampling frequency satisfies the Shannon theorem (1949) and, therefore, the records can be used to perform spectral density analysis of the interface. A typical record of the random variation of the interface with time as obtained with the probe at 256 Hz sampling frequency is given in Figure 5.1. The continuous line is a superimposed moving average with 12 points showed solely as guidance to the eye. It should be emphasized that Figure 5.1 shows the instantaneous height of the interface at a single location within the pipe (i.e. at the location of the conductance probe). All data-points are physical measurements and, as consequence, all must be considered for analysis.

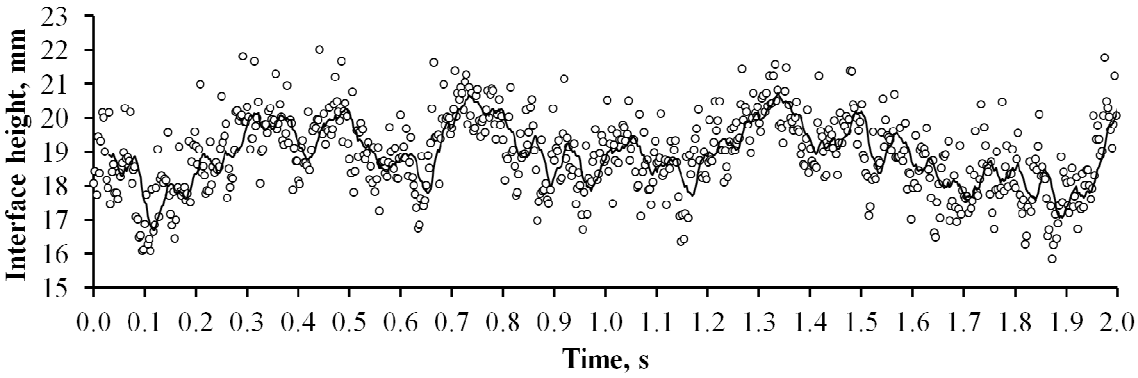

Figure 5.1 Typical raw signal from 2-mm conductance probe downstream the pipe ($r = 1$; $U_{mix} = 0.75$ ms^{-1})

As mentioned, it was found that the oil-water interface records have the characteristics of randomness, stationarity and normality. These three properties of the signal are investigated in this chapter. This result is remarkable and has not been generally recognized in the literature, at least not explicitly. Particularly, the features of normality and stationarity might establish a qualitative difference with respect to signal records obtained using different techniques from other flow patters (i.e. dispersed). Furthermore, the properties of stationarity and normality of the signal allow the complete and convenient data analysis procedure presented in the next sections and leads to the results and conclusions of the following chapters.

5.2 DATA PRE-TREATMENT

5.2.1 Trend Removal

It was found that the probe signal as recorded can contain spurious trends. The introduction of spurious trends in time-series data has long being recognized and explained (Bendat and Piersol, 2010). It is usually due to a velocity drift phenomenon in the electric equipment or the integration of random, low frequency-noise in the converting box, or both. It is an inherent problem of data acquisition.

Figure 5.1 does not show this phenomenon, but the trends become apparent when the cumulative signal average is plotted over time. An example is shown in Figure 5.2, where averages were calculated in intervals of 40 data-points. The line of the data as collected (i.e. raw data) shows in this case a clear trend downwards during the 4-min

collection time, but upwards trends were also found. There are well-known statistical methods available to identify trends in random records without the necessity to turn to time-consuming graphs, nevertheless somewhat subjective. One of them, the method of *reverse arrangements*, verifies that the record data is independent (i.e. shows no trends) and serves also as test of stationarity (Bendat and Piersol, 2010). It is important to say that the absence of a trend in a plot like Figure 5.2 is not a sufficient condition for stationarity. Occasionally raw data showing less obvious trends have been found non-stationary. For this reason, all signals used in this investigation have been properly treated prior to analysis and stationarity checked against the reverse arrangement method at the 90 % confidence level. A discussion of the method of reverse arrangements and its application to the oil-water interface data can be found in Appendix 3.

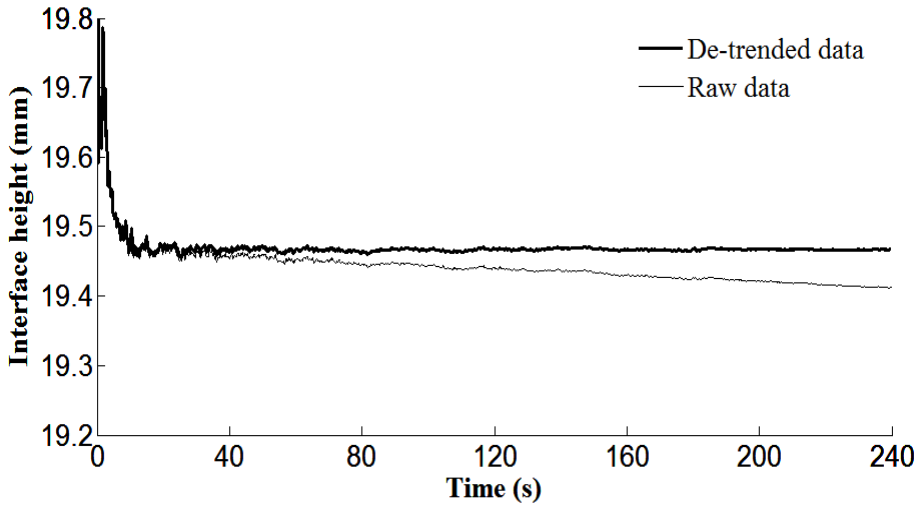

Figure 5.2 Cumulative average of interface height against time

($r = 0.86$; $U_{mix} = 0.84\ ms^{-1}$)

In this work, a best-fit straight line was calculated from the data of the signal applying the least-squares method, in order to ensure that trends were removed from experimental records. This approach was found satisfactory at the 90 % confidence level. In fact, a more complex fit to a polynomial of order 2 (see, for example, Bethea et al., 1995) was also tried, but generally did not make the data stationary.

The best-fit line can be written as:

$$\tilde{y}_n = b_0 + b_1(n\Delta t), \tag{5.1}$$

where $\tilde{y}_n$ is the corresponding interface height computed from the fitted line; Δt is the inverse of the sampling frequency (256 Hz); n varies from 1 to N, where N = 61,440 is the size of the sample (4 min x 60 s min^{-1} x 256 data-points s^{-1} = 61,440 data points); and the coefficients of the fitted line, b_0 and b_1, are calculated as (Bendat and Piersol, 2010):

$$b_0 = \frac{2(2N+1)\sum_{n=1}^{N} y_n - 6\sum_{n=1}^{N} n y_n}{N(N-1)} \tag{5.2}$$

$$b_1 = \frac{12\sum_{n=1}^{N} n y_n - 6(N+1)\sum_{n=1}^{N} y_n}{N(N-1)(N+1)\Delta t} \tag{5.3}$$

The values y_n are those of the raw signal. Each data point of the sample is further corrected by the corresponding value of the regression line per:

$$Y_n = y_n - \tilde{y}_n \tag{5.4}$$

The result of this procedure is a new time series record, Y_n, without any trend and of mean equal to 0. The values of the interface height can be obtained by simply adding the coefficient b_0 to all the data-points of the new record.

Figure 5.2 shows the correction of the trend once this procedure was applied to the raw data signal of the example. Trends in records were also identified during the calibration, where the interface was perfectly still, and the same treatment was applied to each calibration point.

5.2.2 Correction factors

The temperature and salinity of the tap water used in the experiments, as expected, varied with time. Such variations are difficult to study systematically. In this work, a procedure involving correction factors was adopted to neutralise the effect of the weather and daily or seasonal variations on the probe measurements. The use of correction factors was found successful to ensure that the results from two sets of data

collected for the same flow conditions at different moments in time are reproducible. A unique correction factor referred to a common standard value was calculated for each oil-water flow record collected. In order to find each correction factor, single phase water was run before and after the data collection and the average of both values, $\tilde{y}_{water}$, was compared to the calibration point at 100% water, y_c. The correction factor, f_j, was estimated as follows:

$$f_j = \frac{\tilde{y}_{water}}{y_c}, \tag{5.5}$$

where the subscript j refers to each oil-water combination.

Finally, all data-points of the 4-min oil-water record were multiplied by the factor f_j. The flow rate of water chosen seemed not to change the factor found, but a flow rate of 60 $Lmin^{-1}$ was used in all cases. Some more detail is given in Appendix 1. Correction factors calculated for the data of each oil-water flow (usually in the range 1.05 – 1.35) can be found in Appendix 4.

5.3 RANDOMNESS, NORMALITY AND STATIONARITY OF DATA

It was found that the samples collected from the probe at 256 Hz over 4 minutes, once de-trended, exhibited the features of a random and stationary process that followed a Gaussian distribution. These three features (randomness, stationarity and normality) are of fundamental importance to justify the methodology and procedures of analysis presented in this chapter. Additionally, it implies that the oil-water interface of stratified flows investigated at the fully-developed stage behave indeed as a random, fluctuating surface rather than as a wavy structure. This implication is in agreement with the experimental observations downstream the pipe. There are, nevertheless, periodic contributions of wave-like phenomena imposed on the interface signal, but such sinusoidal components are the exception in an otherwise random vibrational response (Bendat, 1962).

5.3.1 Randomness

The randomness of oil-water flow conductance probe data can be demonstrated in three different ways. First, the de-trended experimental records clearly point to the probability distribution function of a random (i.e. Gaussian) variable, and not to the well-known distribution of a sinusoidal or periodic signal (Bendat, 1962). Figures 5.3a – 5.3d show four examples of interface height distributions found in the laboratory. In the figures, the experimental data is organized in 100 histograms and compared to the theoretical Gaussian distribution with mean and variance equal to the average and square standard deviation of the 4-min sample of data, respectively.

Direct inspection of power spectrum of the signal is a second way to verify the randomness of the signal. Results of Spectral Density Analysis are shown at length in the next chapter. The spectra of oil-water interfaces reveal a wide range of frequency contributions even though, under certain circumstances, only a couple of groups of frequencies prevail and dominate over a large range of random contributions.

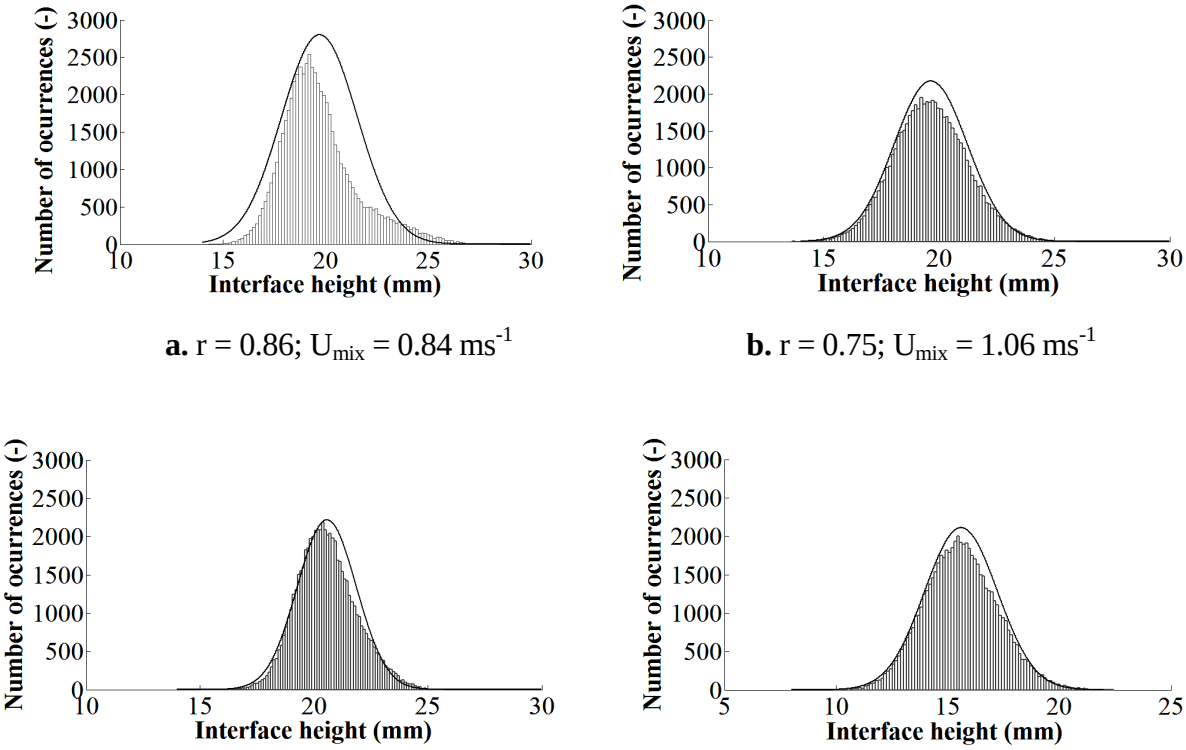

a. r = 0.86; U_{mix} = 0.84 ms^{-1}

b. r = 0.75; U_{mix} = 1.06 ms^{-1}

c. r = 1; U_{mix} = 0.63 ms^{-1}

d. r = 1.43; U_{mix} = 1.26 ms^{-1}

Figures 5.3 Random (Gaussian) probability distribution of the experimental data

Finally, the auto-correlation function of the signal gives a third indication of randomness. The auto-correlation function of the oil-water interface has been routinely calculated during the analyses, as an intermediate step leading to the spectrum of the signal. It typically approaches to 0 as the time delay becomes large (i.e. delays $\tau > 0.5$ s for oil-water data), which is opposed to the perpetual oscillations expected if the signal was periodic. A random signal means that frequencies and amplitudes of the oil-water interface are varying in time randomly and that its evolution can only be investigated via statistical methods (Bendat, 1962). No analytical description of the process can be conceived, although experimental data can always be *compared* to analytical models of vibration.

5.3.2 Normality

As it has been indicated, the oil-water interface data generally follows a Gaussian distribution once de-trended. This property of the signal is clearly demonstrated in Figures 5.3a – 5.3d. The first figure (Figure 5.3a) shows, however, deviations. Records that failed a formal test of normality were seen to have a similar shape, showing a long tail at the higher heights. Generally, even good fits and data verified to be Gaussian seem to have slight deviations at the top and top-right side of the distribution. This aspect can be seen in Figures 5.3b – 5.3d.

However, it is known that interpretation of experimental probability distributions is often difficult or misleading since the shape of the distribution is heavily affected by the number of histograms used. As a consequence, comparison of cumulative density functions is normally more useful. Figure 5.4a shows a comparison of the experimental cumulative density function with that expected from a Gaussian distribution. The agreement is very good for the case illustrated. Normality can be further inspected via q-q plots and Figure 5.4b shows the comparison for the same experimental record. It can be seen that deviation occur at the percentiles away from the mean and that it seems particularly large towards the right side. This observation is in agreement with those made on Figures 5.3a – 5.3d. The normality of all oil-water experimental data has been tested formally by applying a Chi-Square goodness-of-fit test with 12 class intervals and 3 degrees of freedom to the oil-water data (Appendix 3). The interface signal has been found to follow a Gaussian distribution at the 90 % confidence level.

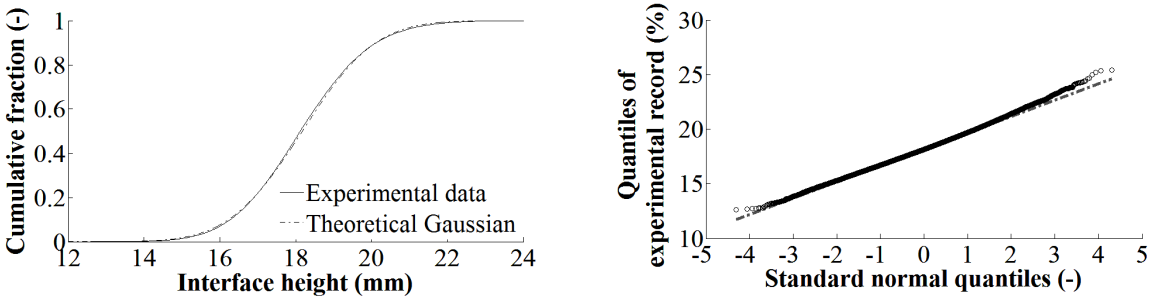

a. Cumulative density function **b.** Quantile-quantile (q-q) plot

Figures 5.4 Verification of normality of experimental data (r = 0.86; U_{mix} = 0.84 ms^{-1})

5.3.3 Stationarity

A random process is a collection of random variables. In the case of the oil-water flow, the data of interface height as a random process is expected to be formed by the contributions of random variables. The probability distribution of the process is the joint distribution of those of the individual random variables, whatever they are. Generally, a random process is said to be stationary if the joint distribution of all the variables is invariant in time (Balakrishnan, 1995). The observation that the interface height signal is Gaussian implies that the signal remains Gaussian at all times. The Normal probability distribution is characterized by two parameters, the mean and the variance and, therefore, the oil-water interface signal is stationary if the mean and the variance do not change in time.

Non-parametric tests have been proposed to readily verify the stationarity of experimental records without the need to assume a suitable probability distribution for the data. The test of Reverse Arrangements has been used in this investigation with this purpose (Appendix 3).

Whenever these verifications are made from finite experimental data taken as stationary, the *Ergodic Principle* is tacitly applied. The principle states that the mean and the variance of the infinite random process are essentially equal to those calculated from finite, experimental data. A formal sufficient condition for this principle exists and can be proved that it is satisfied by the signal of a random stationary and Gaussian process (Balakrishnan, 1995). The consequence is that proper statistical information on the oil-water interface can be obtained from experimental data of a single sample, provided that the record is long enough to be stationary. Ergodicity allows time-average parameters of the flow and power spectrum of the interface to be estimated from only one 4-min sample. Furthermore, the time-average estimate of the auto-correlation function of an ergodic record is known to be equal to the theoretical auto-correlation function of the process, feature that becomes important when estimating the power spectrum from application of Wiener-Khinchine Theorem.

Figures 5.5a and 5.5b show two examples of how the average and the variance of the experimental data have been seen to change as the size of the sample increases. It can be concluded that both the mean and variance do not appreciably change with respect to the entire record (i.e. 61,440 data-points) for samples having more than 30,000 values.

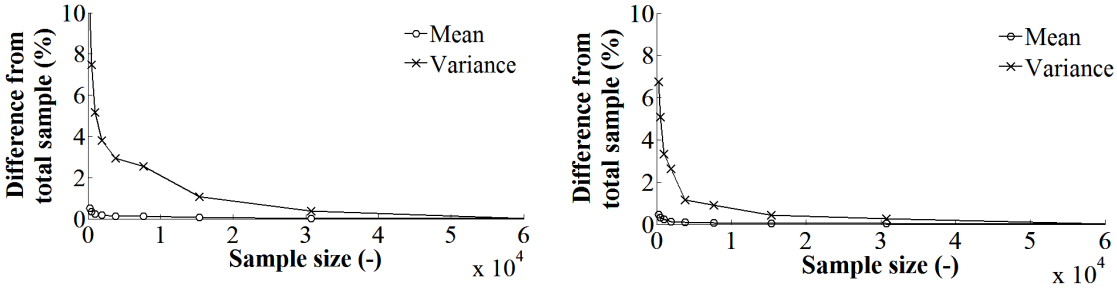

a. r = 0.86; U_{mix} = 0.84 ms^{-1} **b.** r = 1.63; U_{mix} = 0.84 ms^{-1}

Figures 5.5 Verification of stationarity against sample size

In strict terms, the application of the test of Reverse Arrangements along with this *ad hoc* verification of stationarity of the experimental 4-min record shows that the oil-water interface can be considered *weakly stationary*, which means that the mean and auto-correlation function or variance (i.e. first and second-order moments) are invariant in time. In the case of the data analyzed this verification is sufficient proof of complete stationarity. Weakly-stationary data following a Gaussian distribution is strongly-stationary since all high-order statistical parameters are written in terms of the mean and the auto-correlation function (Bendat and Piersol, 2010).

5.4 JUSTIFICATION OF THE SAMPLING FREQUENCY

As discussed, experimental data of oil-water interfacial height was collected by the conductance probes at 256 Hz during 4 minutes. The 256 Hz sampling frequency was found to be high enough to capture all random phenomena without the risk of missing any possible periodicities of the oil-water interface signal (i.e. no aliasing).

Additionally, the Shannon Theorem (1949) seems to be satisfied. According to the theorem, if there is no energy at frequencies larger than a maximum, f_{max}, then the signal representing the interface height as a function of time can be completely determined from a discrete set of values as long as the values are sampled at time intervals, Δt, no larger than:

$$\Delta t \leq \frac{1}{2f_{max}} \tag{5.6}$$

Equation 5.6 can be re-written:

$$f_s \geq 2f_{max} \tag{5.7}$$

The minimum sampling frequency required is, thus, equal to twice the maximum frequency contained in the signal. The upper limit of the spectrum, f_{max} (i.e. half the sampling frequency), is known as the Nyquist frequency. In the present study, the spectra of oil-water flows were found to have small contributions at frequencies larger than 60 Hz. Therefore, Equation 5.7 justifies further the selection of f_s = 256 Hz (i.e. data points separated by Δt = 3.90625 ms). Finally, Fast Fourier Transform (FFT) algorithms can be extensively applied to perform spectral density analysis of the interface signal. The frequency 256 Hz is suitable for the task, since it is a power of 2 (256 Hz = 2^8). Perhaps, it can be suggested to extend the period to 256 s in further experimentation (instead of 4 min = 240 s), as to have an overall record of 2^{16} data points.

5.5 ESTIMATION OF TIME-AVERAGE FLOW PARAMETERS

The de-trended data of oil-water interface height collected with the probes allows two types of data analysis: first, the calculation of time-average parameters of the phase flow such as water fraction, actual velocities and Re numbers; and, second, the estimation of power spectrum and identification of contributing frequencies.

Following the previous discussion, the 4-min record can be broken into 20 intervals of 12 seconds with the same properties of the record. In this way, the time-average or equilibrium interface height can be found with confidence intervals (see, for example, Bendat and Piersol, 2010). The calculation of confidence intervals is important because it gives an idea of how good the estimation of the interface height is from only one 4 min sample. For each interval, an average height, $\bar{h}_i$, is calculated and, from these 20 averages, a total average, $\bar{\bar{h}}$, and a standard deviation, s, are found. Therefore, a normalized parameter, Q_i, is computed for each interval as:

$$Q_i = \frac{\left|\bar{h}_i - \bar{\bar{h}}\right|}{s}\sqrt{M}, \tag{5.8}$$

where M is the number of intervals (i.e. 20).

The Q_i value of each interval is compared with the corresponding percentile of the t distribution at 90 % confidence level (Appendix 4). If Q_i is less than or equal to the t distribution percentile, the corresponding interval is accepted. Otherwise, it is rejected. A final average, $\overline{\overline{H}}$, is calculated from all accepted M' intervals, which is the final average interface height for this oil-water flow rate combination. In general, M' is different from M.

Since the probe signal from which the interface height is calculated is normal, it can be assumed that the time-average interface height is a variable normally distributed, of mean value μ_{hi} and unknown variance σ_{hi}^2. The confidence interval can be mathematically estimated as follows (Bendat and Piersol 2010):

$$\left(\overline{\overline{H}} - \frac{s' t_{m;\alpha/2}}{\sqrt{M'}}\right) \leq \mu_{h_i} < \left(\overline{\overline{H}} + \frac{s' t_{m;\alpha/2}}{\sqrt{M'}}\right), \tag{5.9}$$

where $\overline{\overline{H}}$ is the calculated interface height; M', the number of accepted intervals; s' is the standard deviation of the M' values and $t_{m;\alpha/2}$ is the percentage point of the t distribution for m degrees of freedom (m = M' – 1) with confidence level 1 – α. The absolute uncertainty of the time-averaged interface height calculated is given by:

$$\omega_{hi} = \pm \frac{s' t_{m;1-\alpha/2}}{\sqrt{M'}} \tag{5.10}$$

From the interface height, h_i, the time-averaged water fraction, α_w; oil and water actual phase velocities, u_o and u_w, respectively; and actual Re numbers, Re_o and Re_w, can be readily calculated using the mathematical relations in a pipe of diameter D (see for example, Brauner and Moalem Maron 1989). Table 5.1 summarizes this information. In the table, $u_{s,o}$ and $u_{s,w}$ are the superficial oil and water velocities respectively; ρ_o and ρ_w, the oil and water densities; μ_o and μ_w, the viscosities; and D_o and D_w, the effective diameters of oil and water phases. The latter parameters can be written in terms of the pipe cross-sectional area occupied by the phases and wetted perimeters which, in turn, are functions of the interface height:

$$D_o = \frac{4A_o}{S_o + S_i} \tag{5.11}$$

$$D_w = \frac{4A_w}{S_w + S_i} \tag{5.12}$$

An adjustable definition of the effective diameter have been used in gas-liquid and liquid-liquid applications depending on the phase velocities (Brauner and Moalem Maron, 1989), but the unique expression of Equations 5.11 and 5.12 is proposed in stratified oil-water flows, since phase velocities are of similar order in all cases and because the assumption of the bottom fluid (i.e. water) flowing as a free surface seems not justified. Codes of data treatment, correction factors and estimate time-average parameters as well as experimental results are presented in Appendix 4.

Table 5.1 Definitions of time-average parameters in pipes

Parameter	Equation	No.
α_w	$\frac{1}{\pi}\left[\pi - \arccos\left(2\frac{h_i}{D}-1\right) + \left(2\frac{h_i}{D}-1\right)\left(\left(1-\left(2\frac{h_i}{D}-1\right)^2\right)^{\frac{1}{2}}\right)\right]$	(5.13)
u_o	$u_o = \frac{u_{s,o}}{1-\alpha_w}$	(5.14)
u_w	$u_w = \frac{u_{s,w}}{\alpha_w}$	(5.15)
Re_o	$Re_o = \frac{\rho_o u_{s,o}}{(1-\alpha_w)\mu_o} D_o$	(5.16)
Re_w	$Re_w = \frac{\rho_w u_{s,w}}{\alpha_w \mu_w} D_w$	(5.17)

5.5.1 Uncertainty of the estimation

The computation of Equation 5.10 to estimate the width of the confidence interval revealed that new experimental measurements are expected to be within less than 0.1 % of the estimated interface height in most of the cases at the 90 % confidence level (Appendix 4). The confidence intervals are found independent of the flow parameters (i.e. mixture velocity). This result indicates how good the estimation is.

The overall uncertainty of the absolute value of the interface height is, however, a combination or propagation of the uncertainties of the calibration, regression and correction of the data, the uncertainty of the estimation and any other introduced by the acquisition system. Uncertainties are not fixed, but depend on the measured value. For the sake of simplicity, typical values of the flow parameters in oil-water stratified flow have been taken in the evaluation. The following uncertainties have been calculated for the overall estimation of the interface height, ε_{hi}: 1) the experimental uncertainty of laboratory preparations of the probe section before calibration, ε_m = 1.8 %; 2) the uncertainty of the acquisition system, ε_s = 0.8 % (this must be counted twice, since the signal was collected during the experimental campaigns as well as for calibration of the probe); 3) uncertainty introduced by the calibration curve, ε_c = 1.3 %; 4) uncertainty derived from the application of correction factors, ε_f = 2 %; and 5) the uncertainty introduced by the interface height estimation procedure, ε_a = 0.1 %. Assuming that all errors are independent from each other, the overall uncertainty of the interface height is found to be roughly 3 %:

$$\varepsilon_{hi} = \left(\varepsilon_m^2 + 2\varepsilon_s^2 + \varepsilon_c^2 + \varepsilon_f^2 + \varepsilon_a^2 \right)^{\frac{1}{2}} = \ldots \cong 3\% \qquad (5.18)$$

Any possible effect that the de-trending procedure might have on the uncertainty has been neglected, although a 1% uncertainty could be considered, since the procedure is essentially a fitting to a regression line. The overall error, however, is only slightly affected, and an estimate of 3 % can still be considered. The propagation of this uncertainty when determining time-average parameters can be calculated using Equations 5.13 – 5.16 and assuming that errors are independent. The uncertainty in the

experimental measurements of the flow rates is considered 1 % (Chapter 3) rates and further 0.9 % uncertainty estimated in the calculation of superficial velocities (see Appendix 4). The fluid properties are considered constants. To demonstrate the uncertainties involved a water fraction of $\alpha_w = 0.5$ is considered for further evaluations. This should be representative of a large number of stratified flow cases since large differences from this value result in non-stratified patterns. The calculation of the effective diameter from the interface height does not add any error at $\alpha_w = 0.5$ and, therefore, has been taken as 3 %. Estimations of uncertainty around the centre of the pipe and nominal velocities of 1 ms^{-1} for time-average parameters are: 1) 3.8 % for the water fraction, ε_α; 2) 5.5 % for the actual velocities of the phases, ε_{uo} and ε_{uw}; 3) 6 % for the actual Re numbers of the phases, ε_{Reo} and ε_{Rew}, for nominal actual velocity in each phase equal to 1 ms^{-1}. The details of the uncertainty analysis of the calibration can be found in Appendix 2, while those of the time-average parameters are in Appendix 4.

5.6 SPECTRAL DENSITY ANALYSIS

The power spectrum of the wavy interface signal has been estimated by the extensive use of the Fast Fourier Transform algorithm (FFT). From the spectrum, contributing frequencies to the interface and their relative importance can be obtained. It is worth mentioning here that the procedure for estimating the power spectrum is not a direct application of FFT to the probe data, but it is built from robust information on the statistical structure of the signal (i.e. stationarity and normality). The spectrum obtained from a simple FFT of the oil-water interface signal data is often noisy and unclear, and might include artefacts from the algorithm that cannot be evaluated and may lead to spurious results.

5.6.1 The Fast Fourier Transform algorithm (FFT)

The Fourier Transform of a given signal in time, x(t), can be obtained from the solution of an improper integral that brings the signal into the frequency domain, X(f). However, in most practical applications, the available data is a sample of discrete values collected over a finite interval of time, as it is the case of the current experimental data obtained with the conductivity probe (i.e. sampling at 256 Hz over 4 min). A discrete substitute to the Fourier Transform operation is therefore required. Furthermore, the substitute must uniquely represent the fluctuations of the interface regardless of the

sample size. This can be ensured by applying the Sampling Theorem (Shannon, 1949), as discussed in the previous sections.

The calculation of the discrete Fourier Transform may require significant computation memory and time, especially when treating large data records. In practice, commercial software offers the possibility of computing the discrete Fourier Transform via simple built-in algorithms, known as the Fast Fourier Transform (FFT) algorithms, generally in use for almost fifty years (Cooley and Tuckey, 1965). The FFT is a powerful tool suitable for the estimation of the power spectrum, but must be applied carefully depending on the particular data to be analyzed.

5.6.2 Procedure to estimate the power spectrum

According to the Wiener-Khinchine theorem the two-sided power spectrum of a time-series record in the frequency domain (i.e. includes positive and negative frequencies) equals the Fourier Transform of the auto-correlation function of the record, as long as the record is stationary and follows a Gaussian distribution. Mathematically, the theorem is expressed as follows:

$$S(f) = \int_{-\infty}^{+\infty} R_h(\tau) e^{-j2\pi\tau} d\tau, \qquad (5.19)$$

where, S(f) is the two-sided power spectrum in the frequency domain, τ represents time delay and $R_h(\tau)$ is the auto-correlation function for a given time delay. Since the record is stationary and ergodic, Equation 5.19 can be time-limited so that only the 4 min sampling time is considered, and the spectrum obtained will be the complete process spectrum:

$$S(f) = \int_{0}^{T} R_h(\tau) e^{-j2\pi\tau} d\tau, \qquad (5.20)$$

where T is the sampling time, equal to 4 min.

The auto-correlation function is an even function, which is an important property. If the integrand of Equation 5.19 is expanded using Euler's relationship, the imaginary part (the sin function, odd) will vanish, because the improper integral of the product of an even and an odd function is 0. As a consequence, the power spectrum turns out to be the Fourier cosine transform of the auto-correlation function. Because of that, the power spectrum is a positive, real and even function of the frequency. The last property (i.e. even function) explains why the power spectrum is the mirror image of itself with respect to the Nyquist frequency.

Equation 5.20 provides a way to estimate the power spectrum of the interface of oil-water flows as long as a time-averaged estimate of the auto-correlation function is calculated. This is defined as (Auñón and Chandrasekar, 1997):

$$R_h(\tau) = \lim_{T \to \infty} \frac{1}{2T} \int_0^T h(t)h(t+\tau)dt\,, \tag{5.21}$$

where h(t) is the instantaneous value of interface height collected at time t, between 0 and T. Generally, there are two main groups of alternative procedures to estimate the auto-correlation function in Equation 5.21, either via direct discretisation and computation of the equation, or via the FFT algorithm. Since central and non-central moments are equal for records of de-trended data, direct computation can be achieved with Equation 5.22:

$$R_{YY}(k) = \frac{1}{N-k} \sum_{n=1}^{N-k} Y_n Y_{n+k}\,, \tag{5.22}$$

where $R_{YY}(k)$ is the auto-correlation function for time delay k; Y_n is the experimental de-trended data; and N, the total number of data points (i.e. 61,440). Usually, however, computation of the auto-correlation function via FFT is a more convenient approach since it is significantly faster and avoids the necessity to select a suitable, discrete time delay, k. In this direction, there are two main groups of procedures to estimate Equation 5.21, the ensemble average and the periodogram methods. The ensemble average method is the finally selected procedure to compute the auto-correlation function, since the spectra given by the periodogram seems to be less detailed than those via

ensemble (Auñón and Chandrasekar, 1997). In the case of oil-water flows, this was seen to be the case, although both approaches led to the same spectrum. The ensemble average methodology is based on the resemblance of the time-averaged auto-correlation function (Equation 5.21) and the convolution of the time signal, h(t) * h(t), given as:

$$h(t) * h(t) = \int_{-\infty}^{+\infty} h(t)h(t+\tau)d\tau \tag{5.23}$$

The Convolution Theorem establishes that the convolution operation between two signals in the time domain, h(t), can be calculated from the product of each signal in the frequency domain, H(f) (i.e. product of their Fourier Transforms). As a consequence, the convolution of a time signal with itself is equal to the product of its Fourier Transform and its conjugate:

$$h(t) * h(t) = H(f)H^{*}(f) = \left|H(f)\right|^{2}, \tag{5.24}$$

where the symbol * represents the convolution operation and the symbol * (superscript) indicates the conjugate of a complex variable. Using the Convolution Theorem and the similarities between the time-average auto-correlation function (Equation 5.21) and the auto-convolution of the interface signal (Equation 5.23), it is possible to prove mathematically that the auto-correlation of a finite sample is estimated following these steps (Auñón and Chandrasekar, 1997): 1) computation of the FFT of the treated time-series data; 2) computation of the square of the absolute value of the FFT; 3) application of the inverse FFT (IFTT) on the result and division by the total number of data points in the signal. These operations lead to the complete auto-correlation function estimate of the oil-water interface data.

Following the above approach, the auto-correlation function of the oil-water experimental data obtained in this work can be estimated by only using the FFT algorithm extensively. However, the procedure is not free from pitfalls and introduces spurious effects that need to be accounted for. The first one is the so-called *circular convolution problem* (Auñón and Chandrasekar, 1997; Bendat and Piersol, 2010). The

FFT applied to the record treats the data as a periodic sequence of period T (i.e. 240 s). As a result, only the first period has the real data, while subsequent periods are just a repeat of the same data. For a given delay, τ, it is clear that there is a collection of times, t, where signal values x (t + τ) belong to the original record (i.e. t + τ < T), while at other times, t', signal values x' (t' + τ) fall out of the original record. As a consequence, the function computed via the FFT is not composed just of values $R_h(\tau)$. The procedure to avoid the circular problem consists of adding zeros at the end of the time record of the signal and prior to any computation (zero padding). In this investigation 69,632 zeros have been added for the record to have a total size of 2^{17}. The effect of doubling the size of the record is to avoid completely the problem. However, in this investigation, the auto-correlation function of the oil-water interface signal generally decays quite fast (see Figure 5.6a: normally after about 0.5 s) and, in this case, the circular problem is not very important. In fact, the zero-padding was found not to have any effect on the auto-correlation function of the oil-water interface signal.

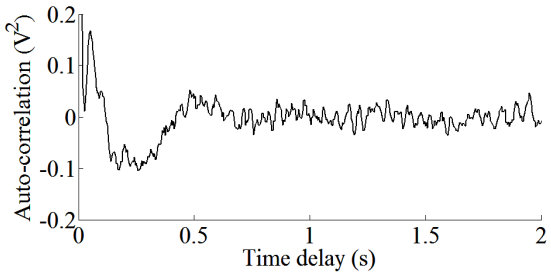

a. Without Hamming truncation

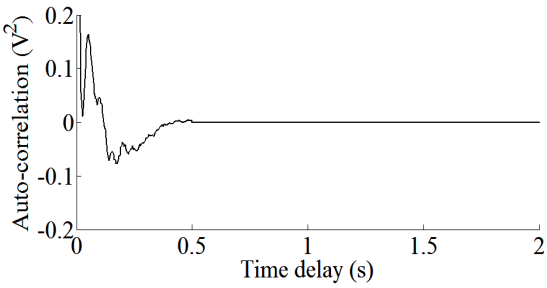

b. With Hamming truncation (τ = 0.5 s)

Figures 5.6. Estimate of the auto-correlation function (r = 0.81; U_{mix} = 1.33 ms^{-1})

The second effect is the excessive noise introduced in the power spectrum by the auto-correlation estimate (i.e. non-smooth, rugged profile). This effect makes difficult the analysis of the spectrum. Figure 5.6a shows the typical auto-correlation estimate of a stratified oil-water interface signal. The function decays rapidly and fluctuates around 0 after around 0.5 s. These fluctuations are seen to affect the final spectrum by making it significantly noisier without providing additional useful information. To avoid this, a truncation operation can be performed that uses a window function (Figure 5.6b), according to which all the values of the auto-

correlation estimate are set to 0 after 0.5 s and those before are modified by a cosine operation. The window function is applied to the estimate of the auto-correlation function prior to the final FFT. In this way, the spectrum is smooth as a result of the convolution of the auto-correlation and the window. A cosine squared window function type (Harris, 1978) has been applied:

$$w(n) = \cos^2\left[\frac{t}{T}\pi\right] = \psi + (1-\psi)\cos\left[\frac{t}{T}\pi\right] \qquad (5.25)$$

Equation 5.25 is usually known as the Hanning window, as it was introduced by Julius Hann, with weight coefficient $\psi = 0.5$. If the coefficient is slightly modified to 0.54, a different transformation is obtained, known as the Hamming window, after the American mathematician. In this investigation, the Hamming window was applied to the data of the auto-correlation function, following the suggestion of Auñón and Chandrasekar (1997). Supported by Figures 5.6a and 5.6b, all values of the auto-correlation at $t > 0.5$ s were made 0, while those at $t < 0.5$ were transformed via multiplication by the window function given in Equation 5.25 with $\psi = 0.54$. A comprehensive review of the use of windows in harmonic analysis can be found in Harris (1978). Figures 5.7a and 5.7b show the smoothing effect that this approach has on the final spectrum.

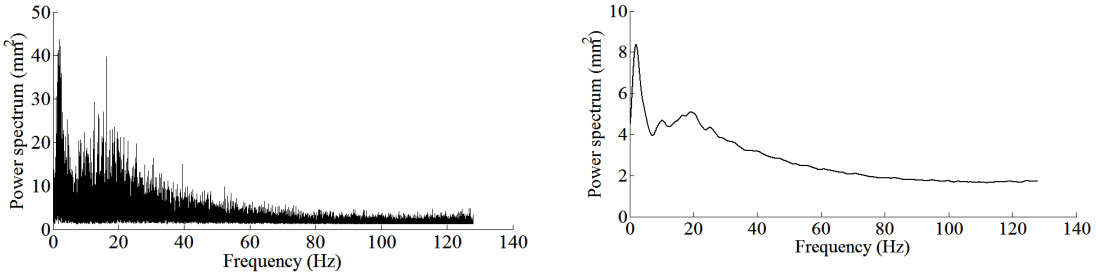

a. Without Hamming truncation **b.** With Hamming truncation ($\tau = 0.5$ s)

Figures 5.7. Power spectrum estimate via the Wiener – Khinchine theorem ($r = 0.81$; $U_{mix} = 1.33$ ms^{-1})

Combining all these considerations, the following steps were followed to estimate the power spectrum of the conductivity probe pre-treated signal (i.e. after trend removal and correction factors applied) and can be proposed as spectral density analysis of stratified wavy oil-water flows:

a) Extend the discrete time-series record with the proper number of zeros. The total number of data points must be a power of 2. In this investigation, zeros were added up to a total number of 2^{17} data points.

b) Compute the FFT of the resultant record.

c) Square the absolute value of the resulting FFT record.

d) Perform the inverse Fast Fourier Transform (IFFT). The auto-correlation function is the IFFT divided by the total number of data-points (i.e. 2^{17}). The result gives the complete auto-correlation function. Since the second-half of the data-points is the mirror image of the first one, in practice, only the first half is needed. In practice, the first 61,440 data points were taken (i.e. 240 s).

e) Apply a suitable window function to the auto-correlation function estimate within a proper time interval. In this investigation, a Hamming cosine window over a period of 0.5 s was found justifiable and satisfactory.

f) Apply FFT to the computed auto-correlation function after windowing treatment. The absolute value is the two-sided spectral density estimate of the oil-water interface signal. As only positive frequencies have meaning, the resulting vector is multiplied by 2 to find the one-sided power spectrum (Bendat and Piersol, 2010). Since the spectrum is a mirror image with respect to the Nyquist frequency, only the first half of the one-sided spectrum is taken.

5.6.3 Validation of the power spectrum estimate

It was desirable to find a suitable indication of the goodness of the power spectrum calculated via the procedure presented. With this purpose, the so-called *average power of the random process* offers a straightforward way to validate the spectrum estimate. Equation 5.19 can be inverted to:

$$R_h(\tau) = \int_{-\infty}^{+\infty} S(f) e^{j2\pi f} df \qquad (5.26)$$

In the special case of no time delay, $\tau = 0$, Equation 5.26 becomes:

$$R_h(0) = \int_{-\infty}^{+\infty} S(f)df = E\left[h(t)^2\right], \qquad (5.27)$$

which is the most general definition of the auto-correlation function for $\tau = 0$: the expectation of the time-series data squared (i.e. moment of order 2 of the data), E[ ]. It is common to refer to the quantities in Equation (5.27) as the average power of the random process (Auñón and Chandrasekar, 1997). Once an estimate of the spectrum has been found, Equation 5.27 must be satisfied, thus validating the procedure. In practice, the average power found in this investigation from the auto-correlation and from the expectation of the time-series data was exactly the same. When computed from the spectrum estimate (middle term in Equation 5.27), it was usually within 5 % of that value, although it was 10% different or slightly more in about 10 – 12 % of all cases.

Different oil-water flow rate combinations collected repeatedly at different days, sometimes weeks apart were further compared, and results were found reproducible. Table 5.2 compares results obtained for two almost identical, stratified oil-water flows at $r < 1$ ($U_{mix} = 0.77$ and $r = 0.7$) and at $r > 1$ ($U_{mix} = 0.85$ ms^{-1} and $r = 1.65$) and Figures 5.8a and 5.8b show their respective spectra. The 2-mm conductance probe was used to collect this data about 7 m downstream the pipe. The average interface height, h_i, was estimated as described in this chapter and the actual velocities of the two phases, u_o and u_w, calculated from Equations 5.14 and 5.15, respectively; The average power was estimated via Equation 5.27. The table and figures illustrate the level of reproducibility that can be achieved. A summary of results can be found in Appendix 5.

Table 5.2. Comparison of two similar oil-water flows on different days

Exp. No.	U_{mix}, ms^{-1}	r	h_i, mm	u_o, ms^{-1}	u_w, ms^{-1}	Average power, mm^2
29	0.78	0.69	20.58	0.83	0.86	1.68
43	0.76	0.68	21.48	0.86	0.80	1.71
24	0.84	1.63	14.73	0.91	0.92	1.91
35	0.84	1.67	14.62	0.92	0.91	2.08

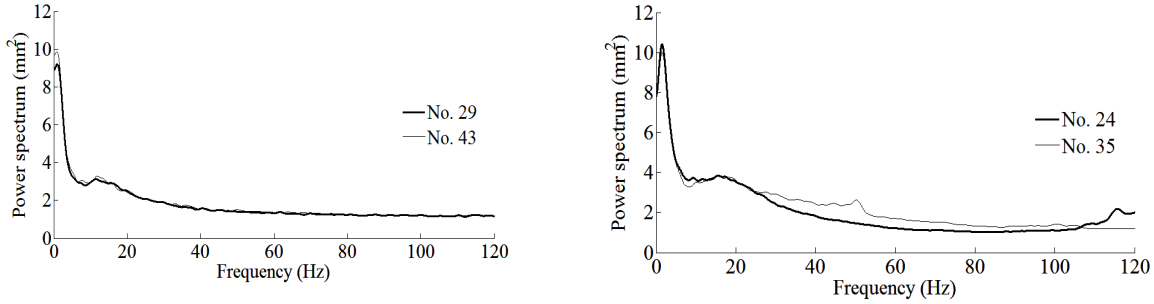

a. r = 0.7; U_{mix} = 0.77 ms^{-1} **b.** r = 1.65; U_{mix} = 0.84 ms^{-1}

Figures 5.8. Spectra of the same oil-water flow rates collected at different days

It has already been stated that differences in the water temperature and salinity can affect the probe data collected at different days or experimental campaigns. Correction factors based on single-phase data collected immediately at the moment of experimentation and compared to a fixed calibration point were introduced with the purpose of eliminating the effect. However, in the course of months of investigations, different calibrations were performed, usually after cleaning or maintenance operations and, in general, whenever was needed. Although the fixed calibration data-point was that of 100 % water, small differences were naturally expected from one calibration to another due to temperature and salinity variations. This slight effect was found, however, to affect notably the absolute value of the power spectrum. As an example, Figures 5.9a and 5.9b show the power spectra of two pairs of equal experimental conditions performed under different calibration campaigns. All the data was collected with the 2 mm probe downstream the pipe. In both cases the lines from different calibration bases are roughly parallel for most part of the spectrum and differences are up to 50 % (Figure 5.9b). Therefore, care was taken not to compare data obtained under different calibration bases. It must be emphasized that the results discussed in the following sections are based on data belonging to the same “calibration campaign”, and that cross-comparisons have been carefully avoided. This difficulty could be surpassed by introducing a straightforward improvement to the computation of correction factors, included in Appendix 4.

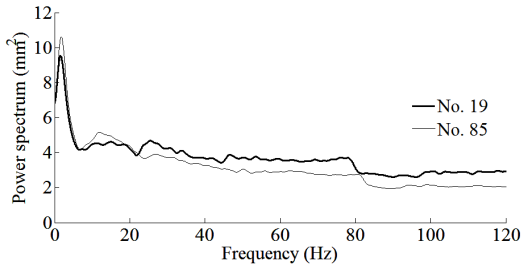

a. r = 1; U_{mix} = 0.9 ms^{-1}

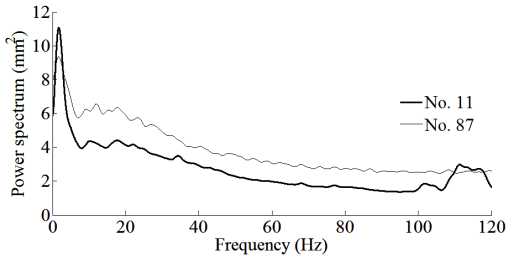

b. r = 1.6; U_{mix} = 1.20 ms^{-1}

Figures 5.9. Spectra of the same oil-water flow referred to different calibration bases

5.7 COROLLARY

As a summary, conductance probes seem a relatively straightforward and inexpensive technique to investigate oil-water stratified flows with fluctuating interfaces. This type of interface has been seen downstream the pipe in fully-developed stratified oil-water flows. The probes can provide time-series records of the oil-water interface. Provided that a suitable sampling frequency is found, that spurious trends introduced by the acquisition instruments in the data are removed and variations of water temperature and salinity accounted for, the probe record is stationary and Gaussian. Statistical tools to verify those features have been suggested and a general procedure has been established as to provide two types of information about the flow. First, time-averaged parameters, such as equilibrium interface heights and water fractions, actual phase velocities and phase Re numbers can be calculated. Second, the power spectrum of the interface, showing frequency contributions to the fluctuations and their relative importance can be estimated. Figure 5.10 presents a summary of the suggested methodology. The importance of this procedure for the research of stratified flows is that, if the oil-water interface is found typically fluctuating, stationary and Gaussian after treatment, it would be applicable to other fluid systems to generate results readily comparable to each other. The results obtained using tap water and Exxsol D140 oil in a 38-mm ID pipe are discussed in the following chapter.

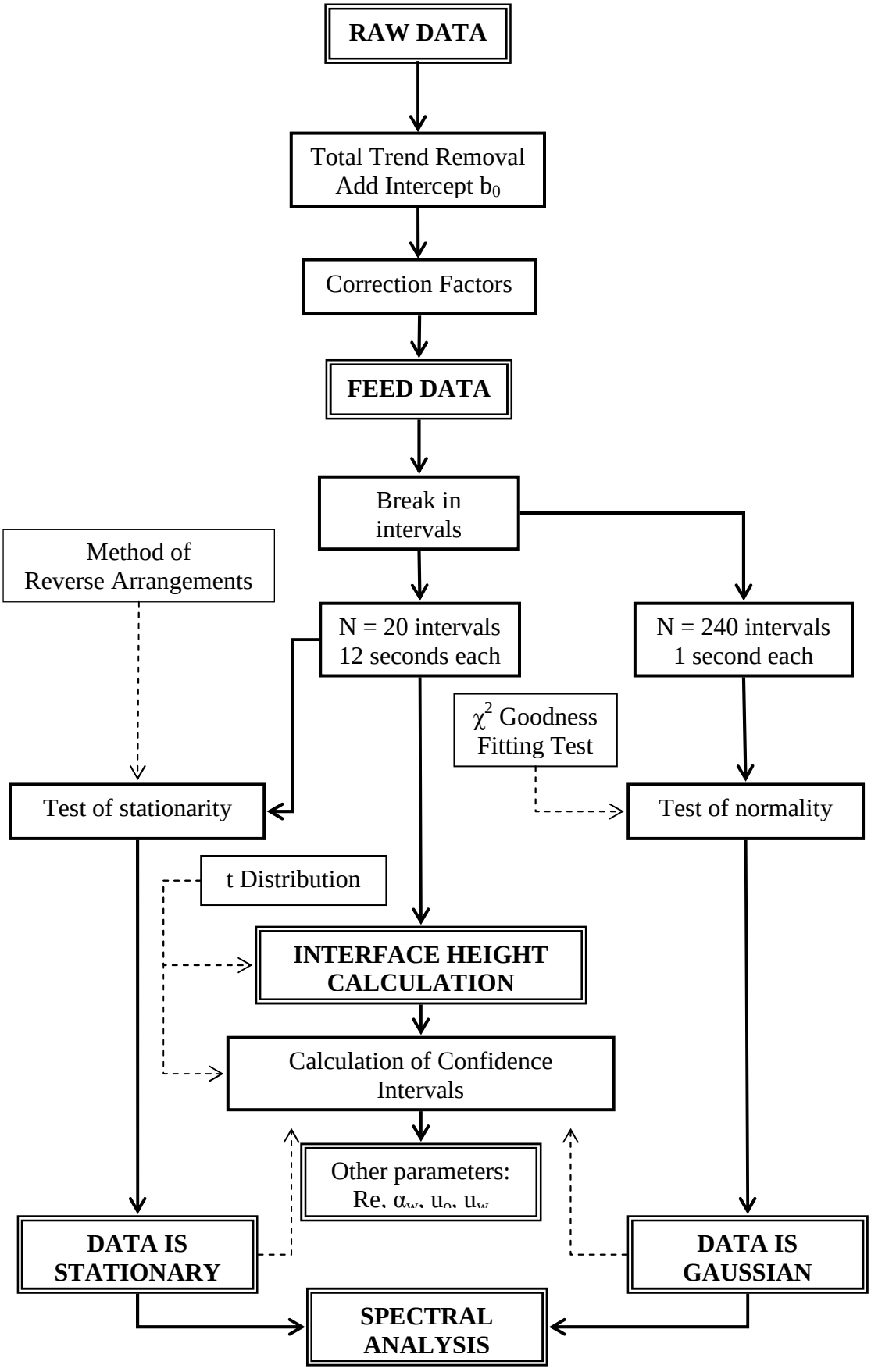

Figure 5.10 General procedure to analyze conductance probe data

CHAPTER 6

TIME-AVERAGE FLOW PARAMETERS AND POWER SPECTRUM OF THE INTERFACE

6.1 TIME-AVERAGE PARAMETERS

The methodology developed in the previous chapter allows calculating time-average parameters of the flow in fully-developed and steady-state conditions (i.e. downstream the pipe), particularly the equilibrium height of the interface (i.e. water fraction) and the actual velocity and Re numbers of the phases. In this section, comparisons are presented with the standard two-fluid model (see Appendix 5). Both results and comparisons lead to contributions of this work, such as the realization that horizontal and stratified oil-water flows tend to show very little slip between the phases, which can justify the absence of clear wavy structures downstream the pipe. The approximation to this results presents, nevertheless, more deviations at input ratios $r > 1$

6.1.1 Water fraction

The water fractions calculated from the time-average interface heights are shown in Figure 6.1a against the input ratio for a number of oil-water combinations within the stratified flow. A similar trend is also found when the interface height is plotted. The experimental data are in good agreement with the predictions of the two-fluid model (Brauner and Moalem Maron 1989). Deviations are found ± 2 % for input rations between $r = 0.75 – 2$, but increase outside that range, more at $r > 1$ (Figure 6.1b). The line predicted by the two-fluid model is independent of the pipe diameter at $D = 38$ mm and above (Appendix 5).

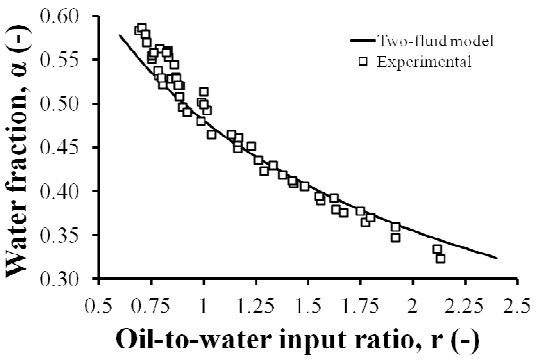

a. Experimental data and model

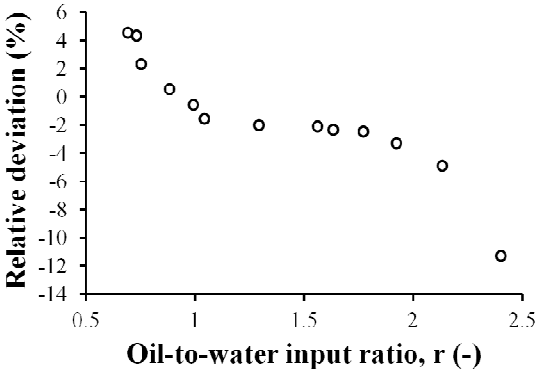

b. Deviation

Figures 6.1 Time-average water fraction against oil-to-water input ratio

As can be seen, the water fraction is a unique function of the oil-to-water input ratio and does not depend on the mixture velocity. This is in agreement with previous literature results with low viscosity oils. Lum et al. (2004) calculated average in situ water fraction using quick closing valves and phase distribution diagrams from an impedance probe. Kumara et al. (2009) used gamma densitometry.

Figures 6.2a and 6.2b show the relation between oil and water input and phase, estimated fractions in the pipe. The parallel lines show results from the 2-fluid model and are different for each fluid. The dots are experimental data. Notice that the oil input fraction added to the water input fraction of each experimental value gives 1, as expected. At $r > 1$ (more oil than water), experiments coincide with model. However, at $r < 1$, experimental results differ significantly from those of the model. This could be due to the increasing effect of the oil viscosity as the layer of oil becomes thinner in the pipe or any effects on the curvature of the interface. The actual Re_o numbers are in the transition regime at all conditions, but it is possible that this had a larger effect on the flow at $r < 1$. However, Re_o numbers can be low or high within the transition regime at $r < 1$. At $r = 0.75$, for example, the two-fluid model predicts $\alpha_w = 0.54$ (Figure 6.1a). The oil effective diameter for that water fraction is found 0.0212 m (Equation 5.11 and see Appendix 5 for definitions). At three different mixture velocities, 0.7 ms^{-1}, 0.9 ms^{-1} and 1.1 ms^{-1} the oil flow rate and superficial velocity can be calculated using Equation 4.3 and the actual oil velocity from Equation 5.14. The actual, estimated oil Re numbers in the pipe for these cases are found to be 3840, 4930 and 6050, respectively.

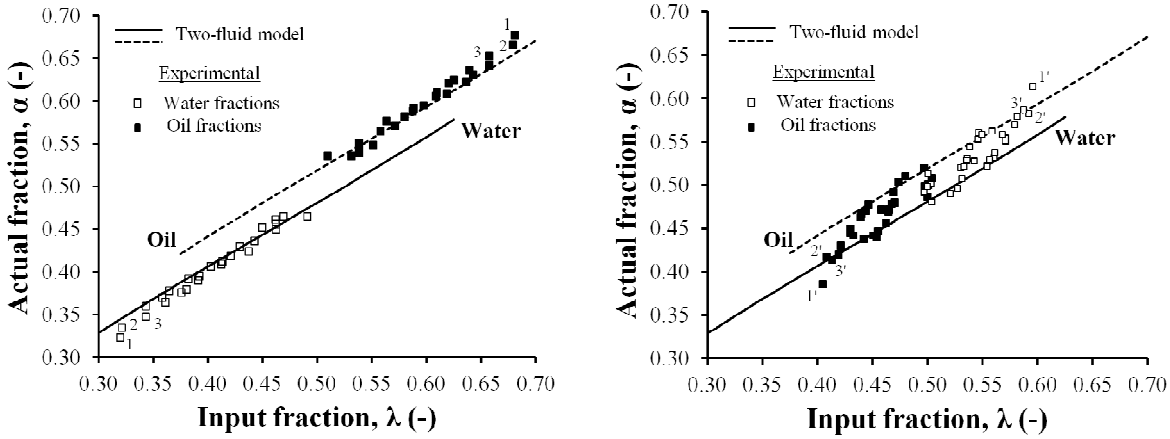

a. r > 1 **b.** r < 1

Figures 6.2 Input and actual oil-water fractions

6.1.2 Reynolds numbers and actual phase velocities

The experimental interface height and water fraction were used to estimate the Reynolds numbers of the oil (Re_o) and water (Re_w) phases in stratified flow. Both Reynolds numbers were found to increase with mixture velocity. Re_w takes values from 14000 to 36000 at mixture velocities 0.7 ms^{-1} to 1.3 ms^{-1}, while Re_o is in the range of 2000 – 6000 at mixture velocities 0.6 ms^{-1} to 1.4 ms^{-1}. Therefore, the water phase is always turbulent, while the oil phase is in the transition region from laminar to turbulent flow. The oil-to-water Re number ratio follows a linear trend when plotted against the input ratio r (Figure 6.3). This implies that for a given change in the oil-to-water input ratio, the Re numbers ratio is expected to change proportionally, regardless the variation of the Re number of the individual phases.

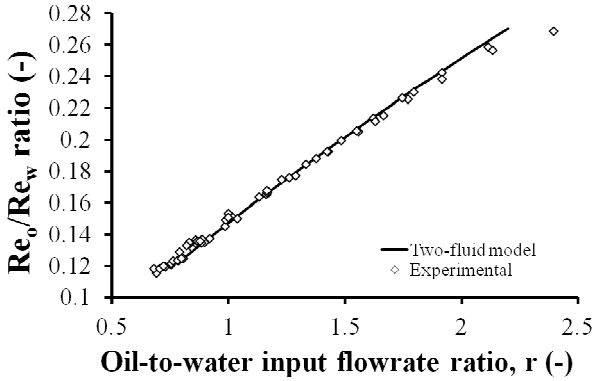

Figure 6.3 Phase oil-to-water Re ratio against the input ratio, r

In all cases, the actual Re numbers were found to be larger than their respective superficial values. This can be seen in Figures 6.4a and 6.4b, where a plot of the ratio of actual-to-superficial Re numbers is given as a function of the oil-to-water input ratio. The ratio of Re is always larger than 1. The relevance of these figures is that: 1) they first indicate the factor by which the turbulence of the phases increase with the respect to the superficial quantities in stratified flow (i.e. 1.2 – 1.4 for most of the range of input ratios); 2) the trend is quite clear and independent of the mixture velocity (i.e. the overall flow); and 3) that, given the relation between the input ratio and the water fraction (Figure 6.1a) and the claim that such relation could be independent of the pipe diameter, based on the two-fluid model prediction, the factors in Figures 6.4a and 6.4b would be only a function of the fluid properties.

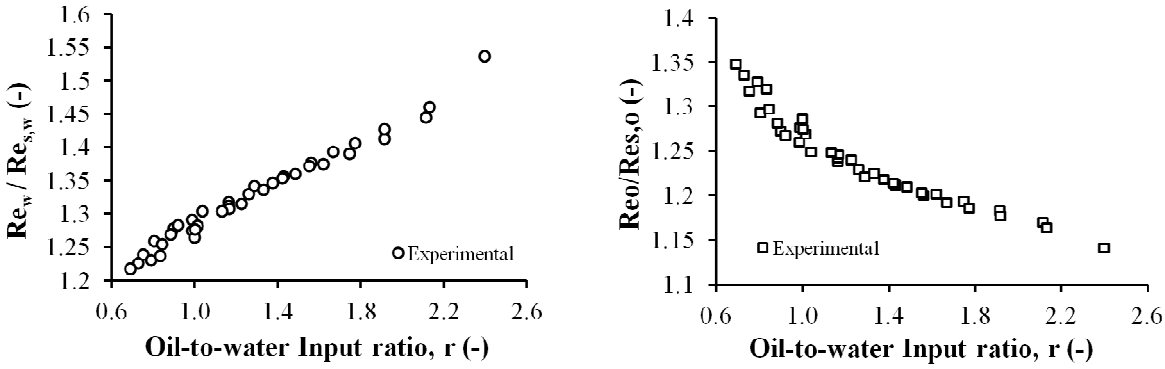

a. Water phase **b**. Oil phase

Figure 6.4 Ratio of actual-to-superficial Re numbers against the input ratio, r

The plot of the velocity ratio (ratio of actual oil-to-water average velocities) against the mixture velocity (Figure 6.5) suggests that, downstream the inlet and in fully-developed flow, there is no significant difference in the velocities of the two phases. Velocity ratios close to 1 were also found during horizontal flows with low viscosity oils by Lum et al. (2004) and Kumara et al. (2009). This result could explain the presence of fluctuations in the interface rather that the K-H waves seen at the inlet when the velocities of the phases are different (i.e. $r \neq 1$). It is interesting that large scale coherent wave structures were seen by Kumara et al. (2010) in $+5^{o}$ inclined flows, when the velocity ratios were different than 1. These results suggest that interfacial waves in oil-

water flows develop as a result of velocity difference between the phases, while an increase in mixture velocity only produces a rougher interface and seems to play a less important role on the development of waves. The waves observed at the inlet are dissipated downstream the pipe and the fluctuations seen at the interface are driven by the turbulence and the pressure fluctuations within each phase or any other contributions.

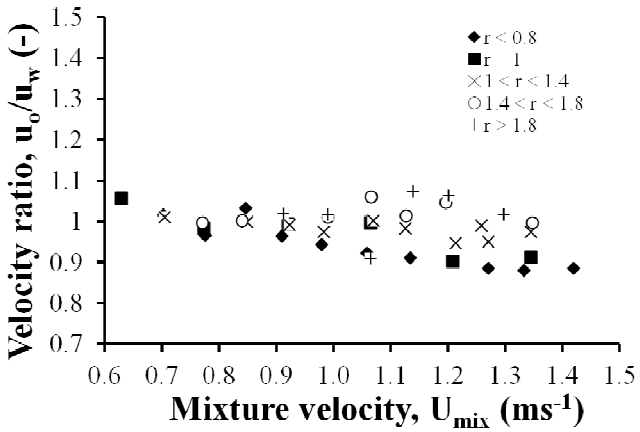

Figure 6.5 In-situ oil-to-water velocity ratio

There is a clear linear relationship between the mixture velocity and the addition of the actual velocities of the fully-developed flow (Figure 6.6). Such relation is also predicted by the two-fluid model. Experimentally, the slope of the line is about 2.2. Since both phases tend to flow with equal velocity (Figure 6.5), this last result indicates that each phase adjusts itself to flow at roughly the mixture velocity.

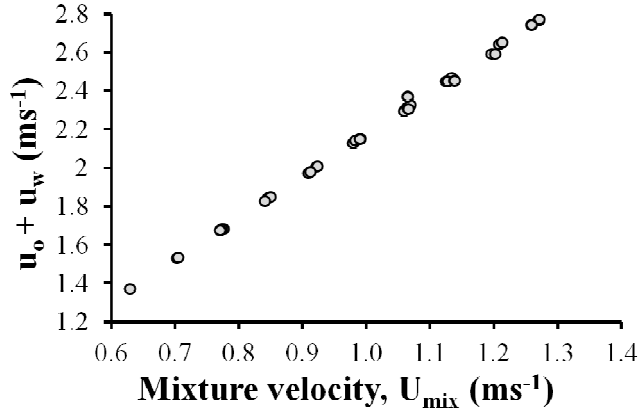

Figure 6.6 Relation between mixture velocity and the actual phase velocities

6.1.3 Effect of drops on conductance probe results

It is important to mention here that this procedure to determine overall parameters of the fully-developed flow from probe data has been found to be valid only for stratified flow when no drops (or only sporadic, tiny drops) are present. Drops are seen to distort significantly the time-series record and to introduce deviations in the average results from the trends found in stratified oil-water flows. The results and previous figures represent only conditions within the stratified flow when no drops that could affect the signal were present. Some measurements were nevertheless carried out at higher mixture velocities, within the intermediate regime. The corresponding slip ratios are shown in Figure 6.5 for input ratios between 0.8 and 1.4.

The effect of the drops on the interface height and the actual phase velocities can be seen in Figures 6.7a and 6.7b. Far from having physical meaning, the deviations found in the results are the consequence of drop disturbance on the signal. In this sense, conductance probes are considered in this Thesis a tool for investigating stratified flows, rather than a technique to discriminate flow regimes.

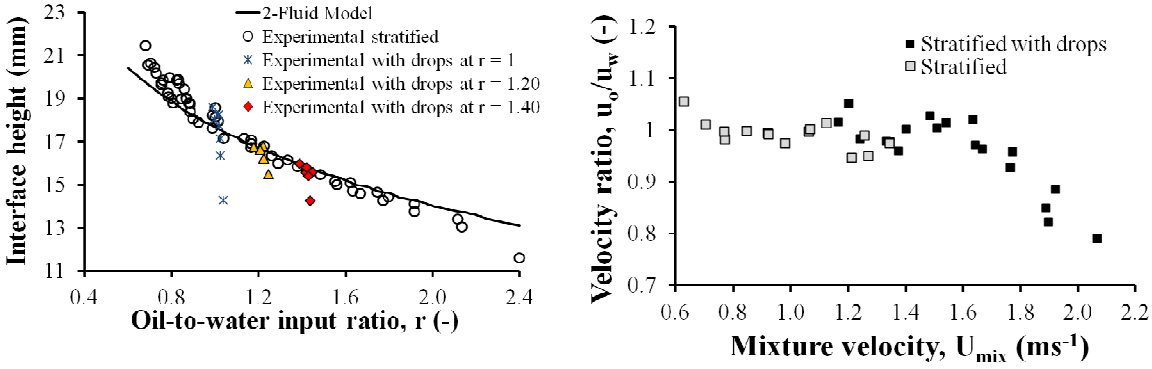

a. Interface height **b**. Actual velocities

Figures 6.7 Effect of drops on time-average results

6.2 SPECTRAL DENSITY ANALYSIS

The power spectra of experimental data were investigated following the procedure described in the previous chapter. Two double wire conductance probes were used for the investigations of the oil-water interface structure (Chapter 2), located either immediately after the inlet section (Position 1) or further downstream the pipe at about 7 m from the inlet (~180 *D*) where the flow is assumed to be fully developed (Position 2). In the presentation of the results, the type, number and location of the probes are clearly given

6.2.1 Interface roughness and average power of the random process

The findings indicate that there is a direct relation between the average power of the data (Equation 5.27) and the waviness of the interface seen with the high speed imaging. A noticeable jump in the absolute value of the power can be seen to differentiate the stratified and the intermediate regions (Figure 6.8). These results agree with the observation of an intermediate region as a separate pattern characterised by a very rough interface.

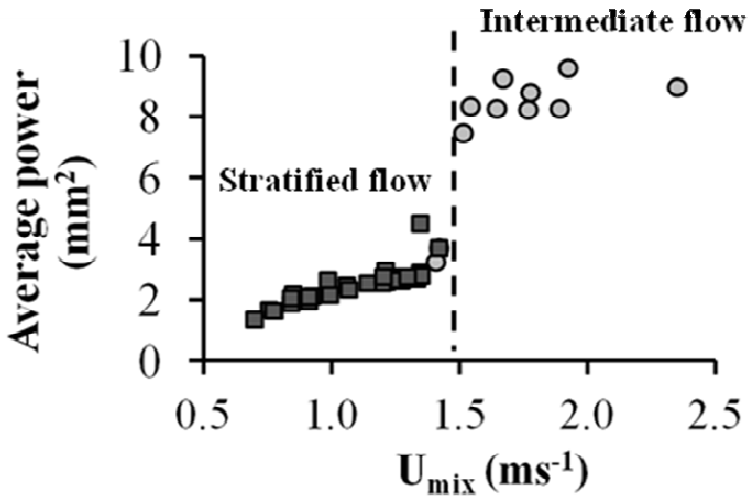

Figure 6.8 Average power of the spectrum against mixture velocity (2 mm probe, Position 2)

6.2.2 Influence of the mixture velocity on the spectrum

The influence of the mixture velocity has been investigated at different input ratios, r. Figures 6.9a – 6.9d compare pairs of the same input ratio, r = 0.8, 1.2, 1.5 and 2 at different mixture velocities (2 mm probe downstream the pipe).

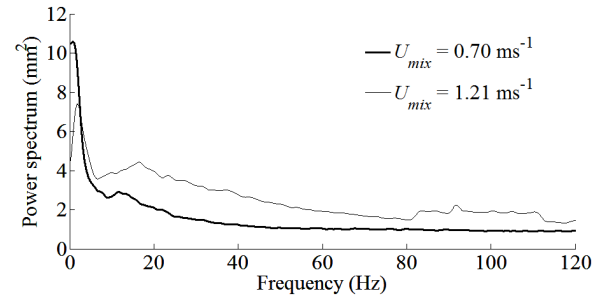

a. r = 0.8

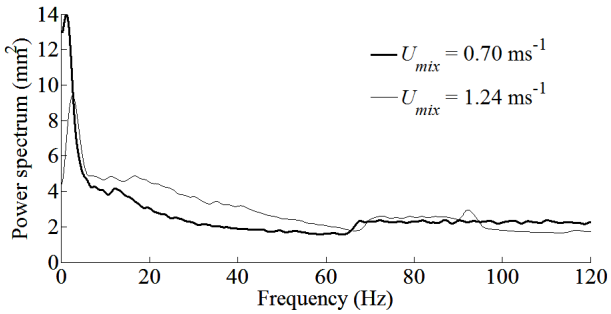

b. r = 1.2

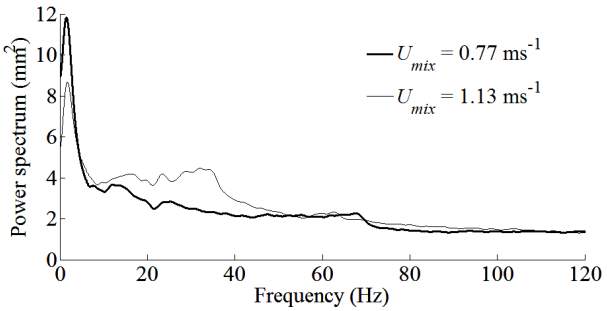

c. r = 1.5

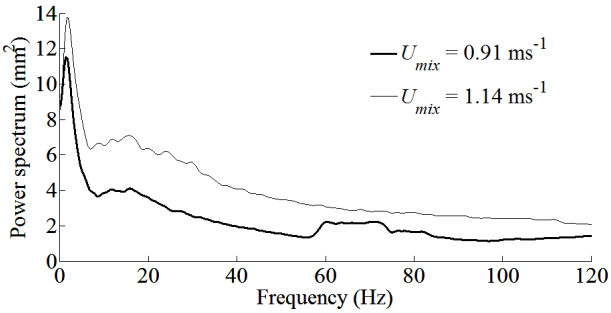

d. r = 2

Figures 6.9 Effect of mixture velocity on the power spectrum (2 mm probe, Position 2)

The graphs reveal that the power increases generally for most of the frequencies of the spectrum as the mixture velocity increases except from the peak at the 2 – 3 Hz, which tends to lose importance at higher mixture velocities. As a consequence, the average power tends to be higher with increasing mixture velocity. The redistribution of power with increasing velocity is not uniform, however, and the power in the range of frequencies 10 – 30 Hz increases more compared to the rest. On the contrary, spectra seem to be largely unaffected by mixture velocity very close to the inlet, where easily identifiable waves are clearly observed, as it will be shown (Figures 6.11a – 6.11d and Figures 6.12a – 6.12d).

6.2.3 Contributing frequencies

It has been verified that the pumps induce mechanical vibrations in the experimental facility. This contribution is a characteristic peak at about 2 – 3 Hz which tends to dominate over all other frequencies, especially at low mixture velocities. These results seem to suggest that, at low mixture velocities, the structure of the interface could almost entirely be described by external factors as, for example, induced mechanical vibrations, in the absence of any other disturbances. For signals collected in Position 2, there are two other ranges of frequencies with increased power compared to the rest of the spectrum. These are the frequencies between 10 – 30 Hz (that carry typically 40 % of the maximum 2 – 3 Hz peak value), and larger frequencies, typically important above 60 Hz (that carry about 25 % of the maximum peak value). The range of frequencies between 10 – 30 Hz corresponds to the frequencies of the large waves seen at the inlet, which were verified by high speed video recording. Even when no distinct waves are identified downstream the pipe, those frequencies remain in the fluid. The range of higher frequencies (> 60 Hz) is in agreement with the fluctuations seen at the oil-water interface downstream the test section, which increase with mixture velocity. These frequencies, though, could also be affected by the data acquisition system.

To facilitate the study of the changes in these frequencies with flow conditions both groups are substituted by *weighted averages*, calculated as follows:

$$f_r = \frac{\sum_{i=a}^{b} f_i p_i}{\sum_{i=a}^{b} p_i}, \qquad (6.1)$$

where f_r is the representative frequency of the group; f_i is each individual frequency within a range of interest (for example, 10 Hz – 30 Hz or 60 Hz – 100 Hz); and p_i is the power of frequency f_i in the spectrum. When all the frequencies in a group have approximately the same power, Equation 6.1 becomes the arithmetic mean.

For oil-water flow rate combinations within the stratified regime the weighted frequencies found are always the same, 19.4 ± 2.5 % Hz for the first group and 79.3 ± 2.5 % Hz for the second (Appendix 4). These average frequencies do not seem to depend on mixture velocity or input ratio. Although the average frequencies seem to be independent of the flow conditions downstream the pipe, their importance within the spectrum increases with the mixture velocity. To demonstrate this, the power of the nearest frequency of the spectrum is attributed to the average frequency. This approximation is acceptable since the resolution of the spectrum is high compared to the precision of the frequencies shown here (i.e. 4.16 10^{-3} Hz, - 1 / 240 s - against 19.4 Hz).

The increase in the weighted frequency with mixture velocity for both frequency groups is seen in Figures 6.10a and 6.10b, where the power of the frequency is given as a percentage of the power of the maximum peak of the spectrum at 2 – 3 Hz. The data-points were collected at different conditions, but a general trend with the mixture velocity can be seen. No trend has been found against the oil-to-water input ratio.

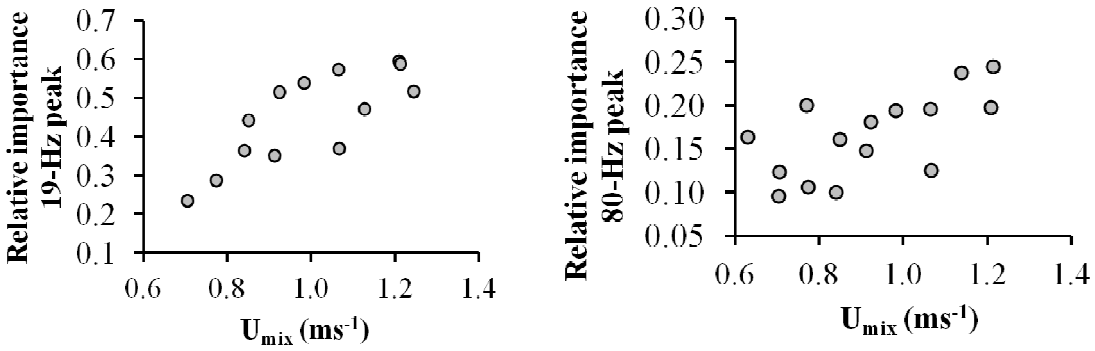

a. 19-Hz peak **b.** 80-Hz peak

Figures 6.10 Effect of mixture velocity on weighted frequencies (2 mm probe, Position 2)

6.2.4 Comparison of the spectra at inlet and downstream the pipe

Interestingly, the same representative frequencies have been obtained when analyzing the data collected close to the test section inlet. In particular, the weighted frequency of 19 Hz is always computed at the inlet regardless of the mixture velocity and for both input ratios $r < 1$ and $r > 1$. The spectra of several oil-water flows at the inlet (Position 1) are compared to those at 7 m downstream the inlet (Position 2) in Figures 6.11a – 6.11d and Figures 6.12 a – 6.12d for $r < 1$ and $r > 1$, respectively. Data was collected simultaneously in both locations, using the 5 mm probe at the inlet and the 2 mm one downstream. In order to compare the data collected from the two probes, the normalized power, found by dividing the power values with the maximum value, is used. The data indicate that contributing frequencies do not depend on the mixture velocity, although at Position 2 the relative importance of the contributing frequencies generally increases with the velocity at the expense of the pump contribution.

As can be seen in Figures 6.11, for $r < 1$ the 19 Hz peak is not clearly seen in the spectra taken at the inlet and the low frequency contributions occur over a wide range. Downstream the pipe, however, the 19 Hz peak is clearly separated from the one due to mechanical vibrations. In contrast, for $r > 1$ (Figures 6.12) the 19 Hz contribution in the spectra at the inlet is more prominent than for $r < 1$. This difference is attributed to the geometry of the inlet. At input ratios $r < 1$ (water flowrate higher than that of the oil) the interface height is close to the upper pipe wall. The waves that develop on the interface

are seen to collapse against the top wall shortly after the inlet junction as they enter the test section. This would reduce the wave amplitudes and may have an effect on the signal of the probe in Position 1, which is located a few centimetres away from the inlet junction. At 7 m downstream the inlet (Position 2) and for both input ratios the main peak is that of the pump while the peak at 19 Hz is still present but not as prominent. This finding agrees with the observation that almost two-dimensional waves develop at the inlet with large amplitudes at input ratios different from 1; these waves reduce in amplitude significantly and acquire a complex three-dimensional configuration further downstream the pipe. In both Figures 6.11 and 6.12 the normalized spectra lines at the inlet are always above those at 7 m downstream. This suggests that the importance of the contributing frequencies seen at the inlet diminishes downstream in favour of the low frequency due to mechanical vibrations. This is particularly obvious for the characteristic frequency at19 Hz.

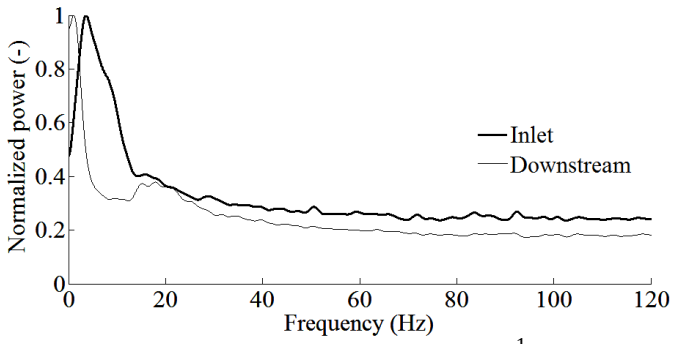

a. r = 0.57; U_{mix} = 0.81 ms^{-1}

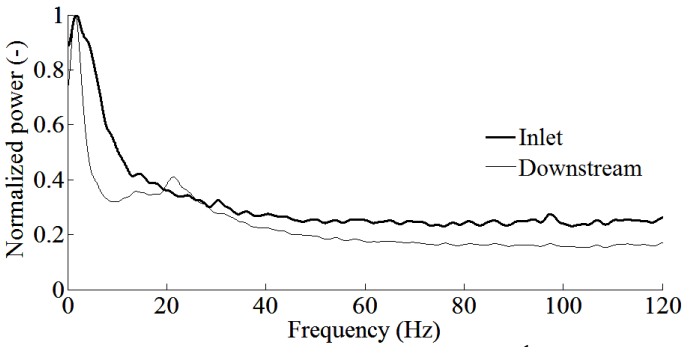

b. r = 0.63; U_{mix} = 0.96 ms^{-1}

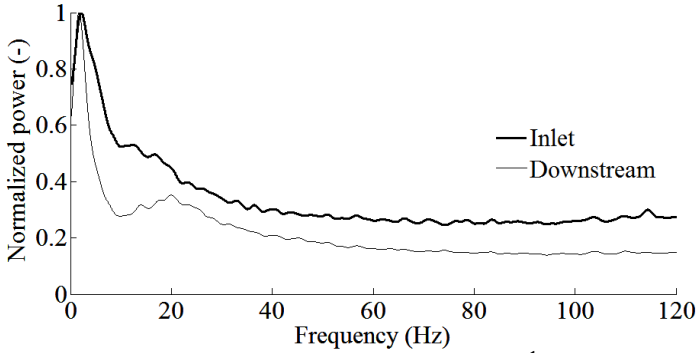

c. r = 0.67; U_{mix} = 1.10 ms^{-1}

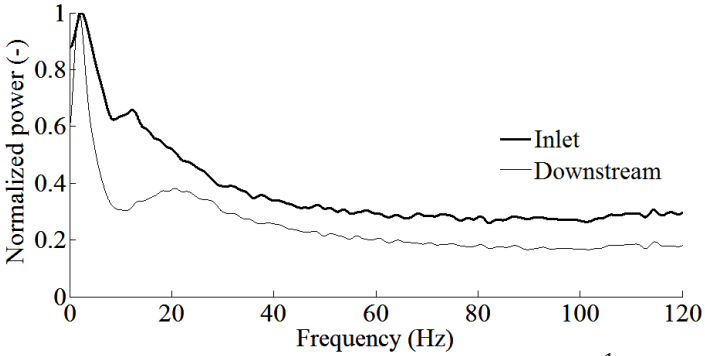

d. r = 0.70; U_{mix} = 1.25 ms^{-1}

Figures 6.11 Comparison of spectra for r < 1

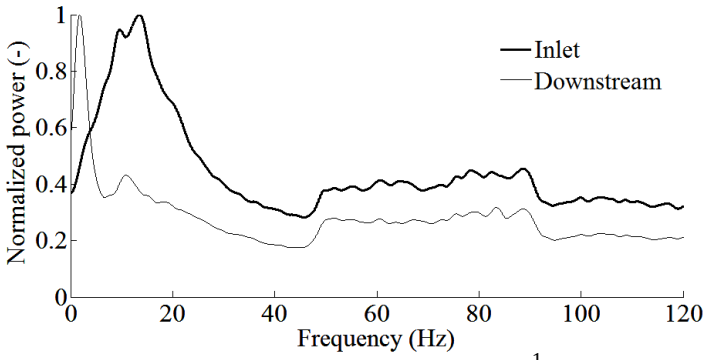

a. r = 2.25; U_{mix} = 0.96 ms^{-1}

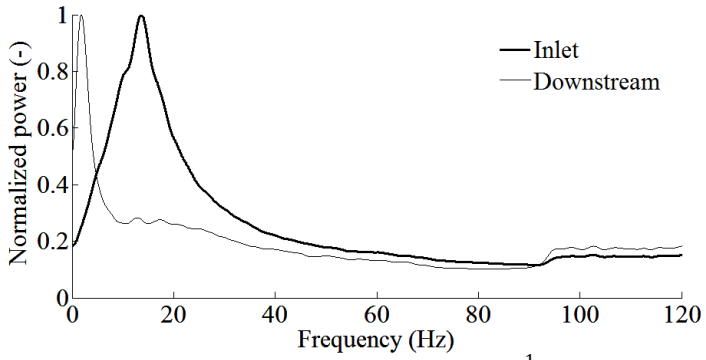

b. r = 2.5; U_{mix} = 1.03 ms^{-1}

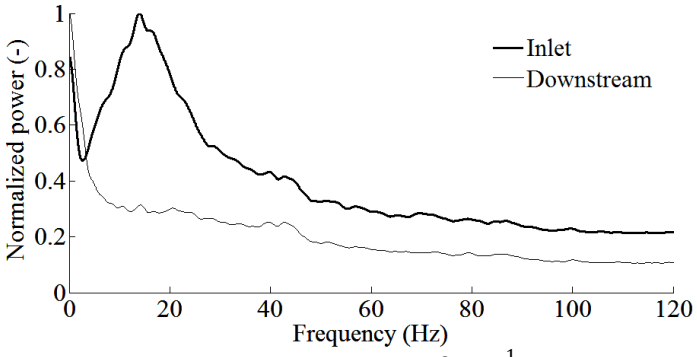

c. r = 2; U_{mix} = 1.10 ms^{-1}

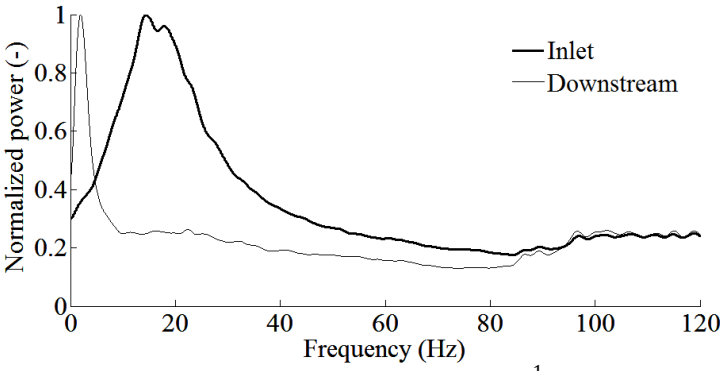

d. r = 2.2; U_{mix} = 1.18 ms^{-1}

Figures 6.12 Comparison of spectra for r > 1

6.3 COROLLARY

The fact that the 19 Hz frequency appears at all the different fluid flow rates tested suggests that it could be a property of the system of the fluids used rather than the result of the flow conditions. This frequency contribution, revealed by the spectral analysis, seems to determine the properties of the waves developed at the inlet in cases with $r \neq 1$. The waves appear as coherent, 2D structures and can be followed with the aid of high-speed imaging. In the following chapter, the characteristics of inlet waves are investigated optically with the purpose, first, of verifying the results presented. Interfacial waves have found always stable and seen to vanish downstream the pipe, which is an interesting phenomenon, not often found explicitly in the literature of oil-liquid flows. With the purpose of investigating the stability of inlet waves and their possible effect on drop formation (as dual-continuous flow has been observed to develop immediately at the inlet), the classic wave linear and stability analysis is applied also in the experimental findings of the next chapter.

CHAPTER 7

ANALYSIS AND STABILITY OF INLET INTERFACIAL WAVES

7.1 INVESTIGATION OF INLET INTERFACIAL WAVES

The interfacial waves that developed at the inlet in flows with $r \neq 1$ can be investigated with visual techniques, since they appear as clear 2D structures travelling along the test section. As two-dimensional, visually-identifiable waves did not develop at the inlet for r = 1, only flowrate ratios different than 1 were studied. The waves observed in more than 20 oil-water flowrate combinations (r = 0.6 – 2.5 and U_{mix} = 0.8 – 2 ms^{-1}) were analyzed via a high speed video camera (Phantom Miro 4). Figures 7.1a and 7.1b reproduce two snapshots of typical waves at the inlet, with input flowrate ratios higher and lower than 1, respectively. Images were taken along the inlet section (in an area of about 16 cm length) at 1000 frames per second (fps). Up to 4,200 frames could be stored in the camera memory giving a recording time of 4.2 seconds. This time span was found to be sufficient to capture the evolution of a large number of waves (i.e. interface developments were typically in the time scale of a few milliseconds). For each flow rate combination, 20 to 25 waves were followed as they travelled along the inlet and their characteristics were measured. The interfacial wave characteristics were acquired from the images taken using a pre-calibrated scale. Figure 7.2 shows a typical high-speed image and the reference lines used for analysis. Each image was divided in 4 regions and fixed locations were taken within the regions more or less equally spaced (the figure shows actual distances in cm). Waves were then identified and followed as they moved across the fixed locations of the regions. The time resolution was 5 ms. It can be seen that the high-speed image was taken a few centimetres after the inlet and that the beginning of the image was ignored; this was done because waves were not usually fully developed within that very initial length of the inlet.

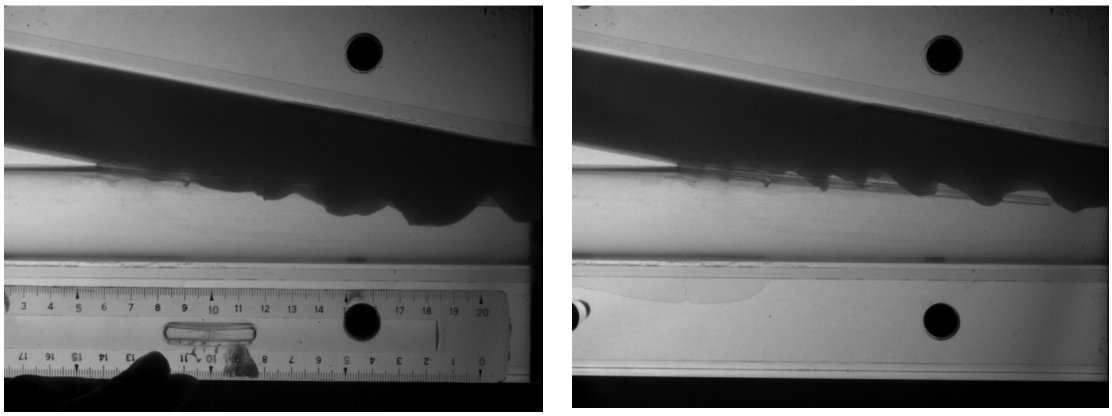

a. r = 2.6; U_{mix} = 1.13 ms^{-1} **b**. r = 0.60; U_{mix} = 1.2 ms^{-1}

Figures 7.1 Development of interfacial waves

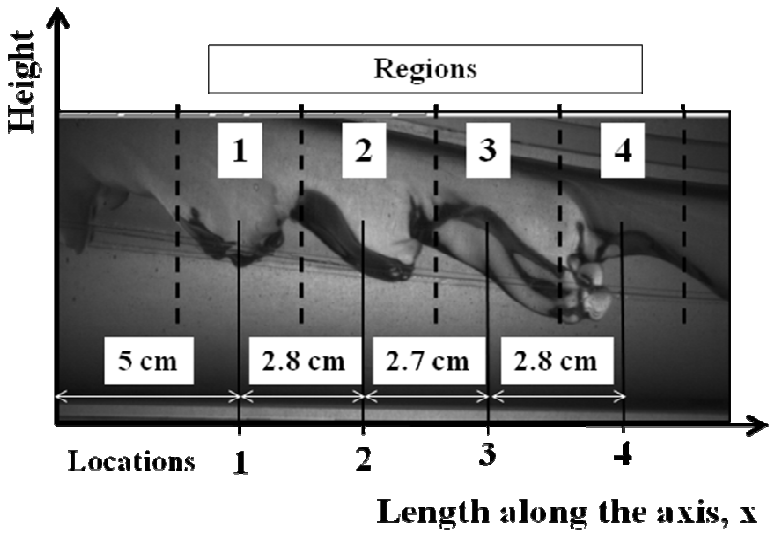

Figure 7.2 Typical high-speed image of the inlet and regions of analysis (r = 0.6; U_{mix} = 0.85 ms^{-1})

To calculate the average interface height, the height of the interface from the bottom of the pipe was recorded in each image at 25 locations equally spaced. A total of 38 images were collected for each set of flowrates over a period of 190 ms. Average interface height measurements were performed for all the oil-water flowrate combinations used in this work. It was found that the interface height typically

decreased along the inlet for all flowrate combinations. Figure 7.3 shows, as example, the development of the average interface height along the inlet at mixture velocity, U_{mix} = 1.03 ms^{-1}, and input ratio, r = 2.5.

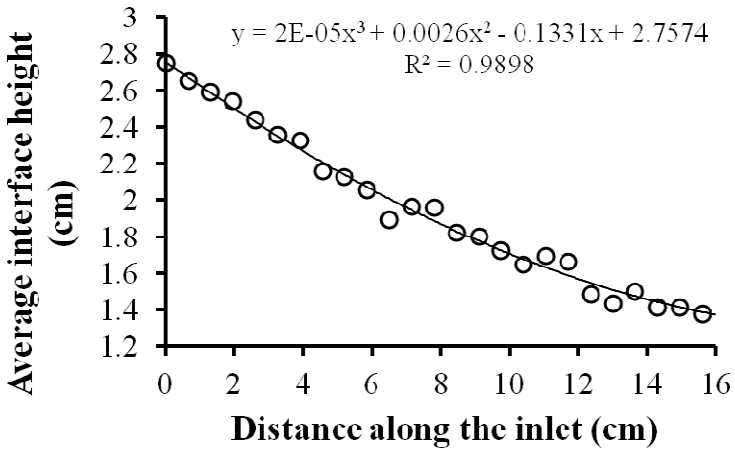

Figure 7.3 Evolution of interface height along the inlet (r = 2.5; U_{mix} = 1.03 ms^{-1})

Since the waves observed did not have perfect sinusoidal shapes, the wave crests were used to calculate the wave amplitudes. In these measurements, the height of each crest that passed from the given locations in the four regions was measured from the bottom of the pipe. The amplitude of the wave at each location was then found by subtracting the average interface height from the crest height.

Velocities were calculated from the time taken by a given wave crest to move from a fixed location in one region to another fixed location in the next region and the distance between the two locations. Three values were therefore computed along the inlet (i.e. between locations 1-2, 2-3 and 3-4). The frequency of the waves was taken as the inverse of the time interval between two crests at each fixed location; therefore, the frequencies could be measured four times along the inlet (i.e. at locations 1, 2, 3 and 4). The wavelengths between regions were calculated from the wave velocities and the frequencies.

The relative uncertainty in measuring distances on the image depends on the value of the distance measured, but the average error between the fixed locations in the 4 regions can be estimated as no more than 4 %, with an uncertainty of the measurement of ± 0.2 cm (from the origin (0,0) in Figure 7.2).

The uncertainty in velocities and wavelengths tends to decrease towards the end of the inlet, because both increase in value. To calculate an average uncertainty it is assumed that the error of time variable is negligible (at least compared to that of measurements on the image), and about 6.5 % error in velocity and 8 % in wavelength were found. The uncertainty of the amplitude increases along the inlet, because the amplitude of the waves decreases. The estimated error in measurements of amplitude is no more than 10 % in all cases. This figure comes from the propagation of errors in measuring the height of the crests (about 3.5 % at $r > 1$ and 1 % at $r < 1$), the average height of the interface (about 6.5 % at $r > 1$ and 4 % at $r < 1$) and the uncertainty of the regression line of the average interface height (Figure 7.3), which has an average of ~ 5 %.

7.2 EXPERIMENTAL WAVE CHARACTERISTICS

The evolution of the average interface height along the inlet section as a function of the oil-to-water ratio, r, is summarized in Figures 7.4a and 7.4b. To enable comparisons across different flow rates, the interface heights shown in Figure 7.4a are non-dimensionalised by dividing the measured interface heights by the maximum value, found at (0,0) in Figure 7.2. The actual interface height can be seen in Figure 7.4b, where it is plotted against the input ratio r. It was found that in all cases, the interface height decreases along the inlet. This trend reflects the geometry of the inlet where the top duct (i.e. oil inlet) still has a negative slope for a few centimetres after the junction point (Figure 4.10). As can be seen in Figure 7.4a, the decrease in interface height is larger for $r = 2$, where the oil flowrate is higher than that of water, compared to $r = 0.5$. This suggests that the interface adjusts faster in this case within the same distance.

Both Figures 7.4a and 7.4b show that the average interface height depends mainly on the input ratio and that it is not affected by the mixture velocity. The latter can be seen in Figure 7.4b where data obtained at different mixture velocities have similar interface heights (e.g. for $r = 2.2$). This result is in agreement with the unique relation between the interface height and the input ratio from the experimental data and the predictions of the two-fluid model.

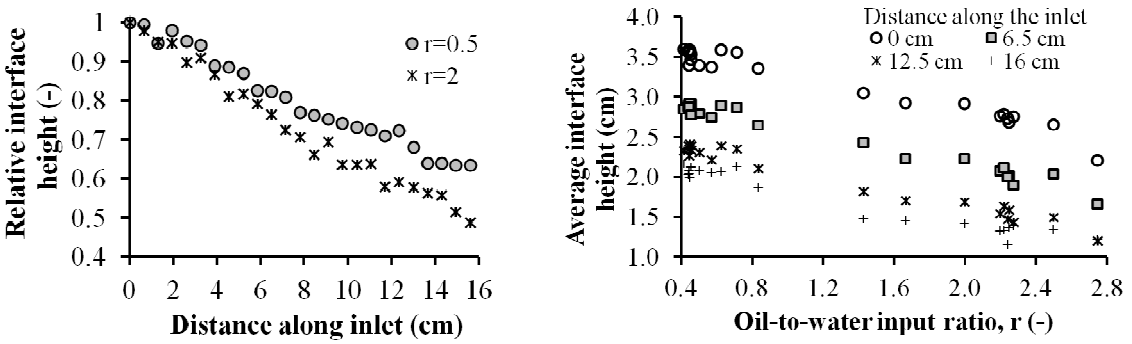

a. Evolution along the inlet **b.** Evolution against r

Figures 7.4 Average interface height in the inlet

The visual observations at the inlet showed that waves develop when the two fluids join but decrease in size further downstream until they eventually disappeared. Figure 7.5 shows the wave amplitudes from zones 2 to 4 relative to the amplitudes of the waves in zone 1. Relative average values and standard deviation are 0.85 ± 10.7 % in region 2, 0.707 ± 15.1 % in region 3 and 0.562 ± 19.0 % in region 4; the standard deviation of average measurements increases as the wave amplitudes reduce. In contrast, wavelengths increased along the inlet as can be seen in Figure 7.6 where the wavelengths have been normalised against the values in regions 1-2. The average values and standard deviations are 1.09 ± 5.4 % across regions 2 – 3 and 1.20 ± 6.5 % across regions 3-4.

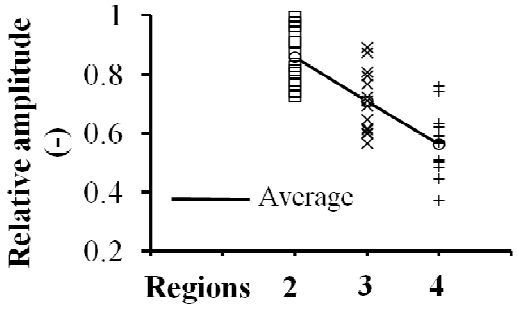

Figure 7.5 Relative amplitude evolution

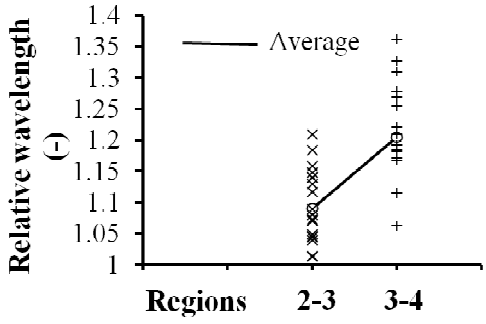

Figure 7.6 Relative wavelength evolution

The volume of the waves along the inlet has been estimated using the average normalised amplitudes and wavelengths at each flowrate combination. In general, the wave volume decreases as waves move downstream, but no trend has been found with respect to the input ratio or mixture velocity.

Interestingly, for all flowrate combinations tested, wave frequencies were found to be within the range of 11 – 20 Hz. As can be seen in Figures 7.7a – 7.7d the frequencies remained constant along the inlet, despite the changes in amplitude and wavelength noted.

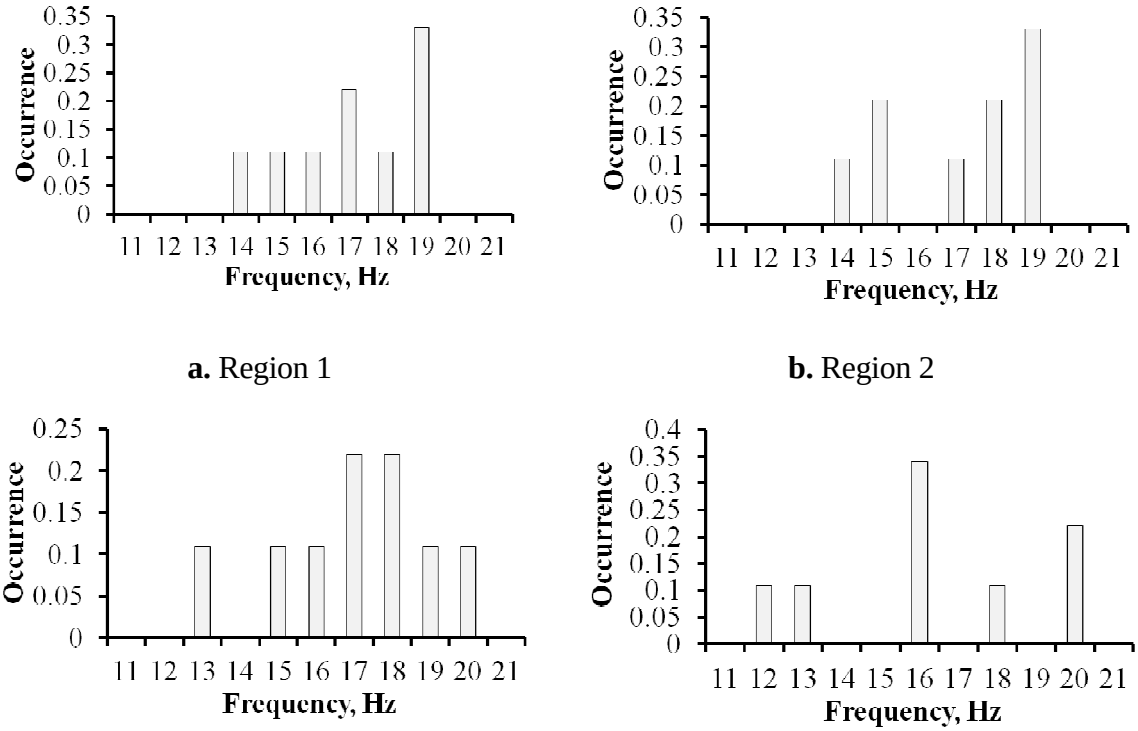

a. Region 1

b. Region 2

c. Region 3

d. Region 4

Figures 7.7 Frequency distributions (r = 1.6; U_{mix} = 1.18 ms^{-1})

While the wave frequencies do not change significantly, the wave velocities increase along the inlet. This result is somehow expected, since the frequencies appear to be constant and the wavelengths increase (Figure 7.6). Average wave velocities across regions 2 – 3 and 3 – 4 have been normalised against their respective mixture velocities for the purpose of comparison and can be seen in Figure 7.8. The average

relative velocities change from 1.10 ± 5.0 % across regions 2-3 to 1.23 ± 5.01 % across 3-4. The initial wave velocity in all cases was found to be around half the mixture velocity. Furthermore, it was found that the wave velocity increases almost linearly with the mixture velocity and is generally independent of the input ratio (Figure 7.9).

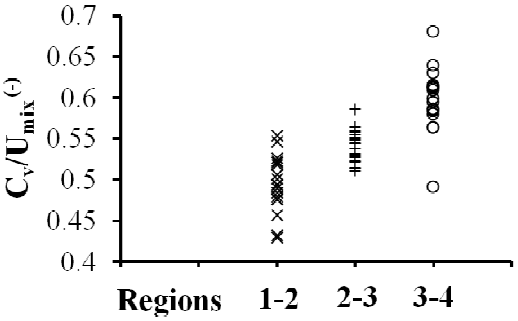

Figure 7.8 Wave velocity evolution

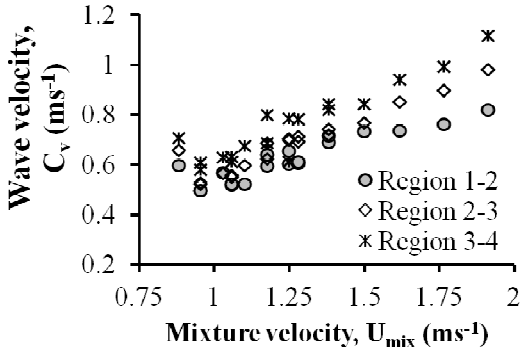

Figure 7.9 Wave velocity and mixture velocity

7.3 DISCUSSION AND STABILITY ANALYSIS

The experimental results reveal that interfacial waves develop at the inlet for input ratios different from 1 as soon as the two phases join. However, the waves disappear eventually; typically, no 2D waves are identifiable at a short distance after the inlet. In addition, wave frequencies are independent of the flowrates of the two fluids. The same frequency is found for different flows, and remains constant along the inlet. This is in agreement with results obtained from the spectral analysis of the interface signal, collected with conductance probes. It can be brought up for discussion that a constant frequency implies a constant wave period, and that this may suggest that the formation and, particularly, the dampening of the waves take place with very little energy dissipation.

At input ratios different from 1, oil and water phases flow with different velocities one on top of the other as they merge. This is a classic case of Kelvin-Helmholtz (KH) instability, which leads to the development of waves. At input ratios close to 1 phase velocities are equal at the junction, which would eliminate the instability and support the experimental observation that no waves develop at the inlet

unless the input ratio is different from 1. The stability condition of the flow at the junction point can be written as (Acheson, 1990; Drazin and Reid, 2004):

$$(u_w - u_o)^2 < 2\frac{\rho_o + \rho_w}{\rho_o \rho_w}\sqrt{g\sigma(\rho_w - \rho_o)}, \qquad (7.1)$$

where u_w and u_o are the average water and oil phase velocities respectively (equal to superficial velocities at the junction), ρ_w and ρ_o are the water and oil densities respectively and σ is the interfacial tension. Equation 7.1 is the classic solution of the inviscid problem, which neglects the shear stresses. This approach can be considered an appropriate approximation for the current data since the viscosity of the oil is low. Substituting the properties of the fluids used in the current work into Equation 7.1 (ρ_w = 1000 kgm^{-3}, ρ_o = 830 kgm^{-3}, σ = 0.039 Nm), the theory predicts that disturbances will be damped if $(u_w - u_o)^2 < 0.0357$ ms^{-1}. Expanding the bracket and dividing by the water velocity squared, u_w^2, the stability condition becomes:

$$1 - 2r + r^2 < \frac{0.0357}{u_w^2} \qquad (7.2)$$

According to Equation 7.2, the input ratio, r, determines whether the wave is stable or not, but the limit of stability depends on the phase velocity (i.e. water) and, in turn, on the mixture velocity. The theory predicts that as the input ratio approaches 1 (both from $r < 1$ or $r > 1$), the stability of the flow increases and that the case $r = 1$ is the limit of complete stability.

By applying Equation 7.2 to a collection of input ratios, the following limits of stability pair values were found (r; U_{mix}): (0.6; 0.823 ms^{-1}), (0.7; 1.125 ms^{-1}), (0.8; 1.588 ms^{-1}), (1.2; 1.941 ms^{-1}), (1.3; 1.522 ms^{-1}), (1.4; 1.235 ms^{-1}), (1.5; 1.103 ms^{-1}), and (1.6, 0.956 ms^{-1}). Using these points, a stability line can be plotted against the flow pattern map observed in the experimental flow facility at about 7 m downstream the inlet (Figure 4.1) where the flow is fully developed (Figure 7.10). At $r < 1$, the agreement is good, but the region of stratification is underestimated by the stability analysis at $r > 1$. At these conditions where the more viscous oil occupies a larger part of the pipe cross

sectional area it is possible that viscous effects, which are ignored in the inviscid analysis, become important. Discrepancies between the stability theory and experimentation have already been pointed out by Al-Wahaibi and Angeli (2007a, b).

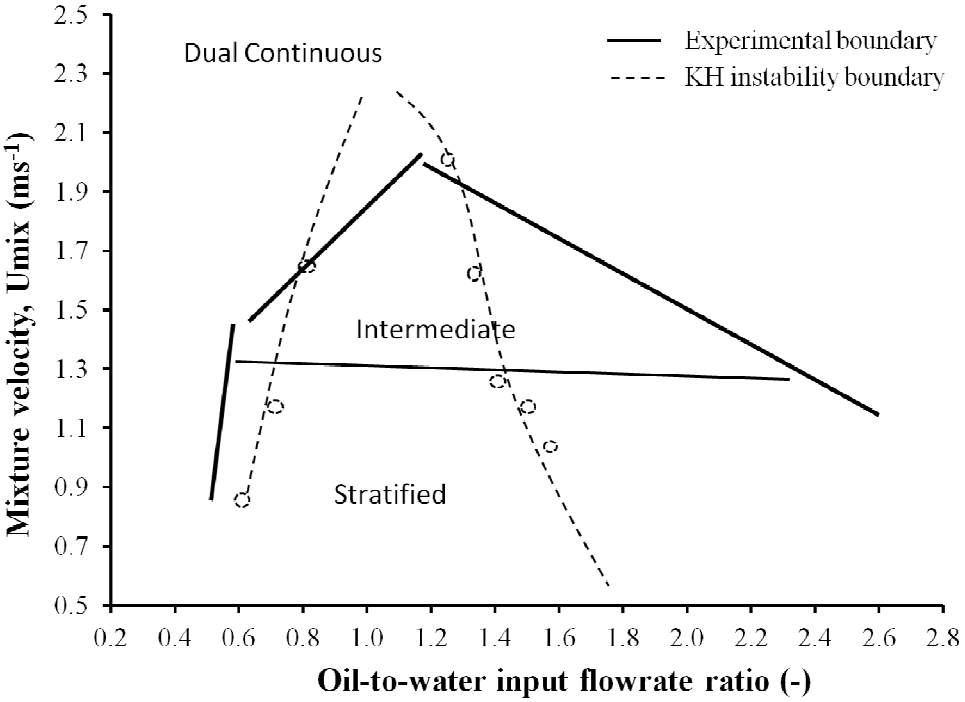

Figure 7.10 Experimental flow pattern map and stability line at inlet

It should be noted here that the stability analysis is carried out at the inlet while the flow pattern map is for the fully developed flow. However, the comparison is still relevant since it has been observed that the flow patterns develop at the inlet and little change is seen further downstream the pipe. In particular, the drops that signify the transition from stratified to dual continuous flow were seen to form at the inlet while hardly any news drops were seen to form further downstream. In addition, dual continuous flow is delayed to high mixture velocities at r = 1, when no waves appeared at the inlet. It is reasonable, therefore, to relate the formation of drops at the inlet to the KH instability waves, but this needs to be verified with further investigations.

As shown in the previous section, relative amplitudes (Figure 7.5) are always at a maximum at location 1 of the inlet (see Figure 7.2) regardless of the mixture velocity. This finding suggests that waves develop faster in faster flows and that the increase in wave amplitude depends on the mixture velocity. This result seems to agree with the theoretical predictions of Brauner and Moalem Maron (1992) for oil-water flows. Their analysis revealed that stratified flows were unstable if the imaginary part of the complex wave velocity, C_i, is positive. In this case, the wave amplification factor with respect to the top fluid (i.e. oil), C_i/u_o, increases with the velocity of the water phase, u_w. Eventually, however, waves dampen within the inlet. As indicated, studies of the fully developed flow revealed that the slip velocity between the two phases is very small in horizontal pipes (see Chapter 4). It can be argued, then, that the waves at the inlet vanish as the velocities of the phases become similar and the instability disappears.

The finding that waves at the inlet propagate at a velocity half of the mixture velocity was found to be in agreement with the predictions of the theory for dynamic waves. When considering the two main types of waves, dynamic and kinematic (or continuity), some investigators have pointed out that the stability of the flow can be entirely determined by the balance between kinematic and dynamic waves; when kinematic waves overcome dynamic ones, the flow is unstable (Wallis 1969; referenced by Trallero, 1995). This implies that dynamic waves are essentially a stabilizing factor to the flow. The velocity of a dynamic wave is given by (Wallis, 1969):

$$C_v = \frac{\dfrac{\rho_o u_o}{1-\alpha} + \dfrac{\rho_w u_w}{\alpha}}{\dfrac{\rho_o}{1-\alpha} + \dfrac{\rho_w}{\alpha}} \pm \frac{1}{\dfrac{\rho_o}{1-\alpha} + \dfrac{\rho_w}{\alpha}} \left[\frac{-\rho_o \rho_w (u_o - u_w)^2}{\alpha(1-\alpha)} - \left(\frac{\rho_o}{1-\alpha} + \frac{\rho_w}{\alpha} \right) f_{\nabla\alpha} \right]^{0.5}, \qquad (7.3)$$

where $f_{\nabla\alpha}$ is a stabilizing factor including viscous and body forces and α is the fraction of the pipe occupied by water. Equation 7.3 is re-arranged in terms of the mixture velocity and the oil-to-water input flowrate ratio to give:

$$C_v = \frac{U_{mix}}{r+1}\left[\frac{r\alpha\rho_o + (1-\alpha)\rho_w}{\alpha\rho_o + (1-\alpha)\rho_w}\right] \pm$$
$$\pm \frac{\alpha(1-\alpha)}{\alpha\rho_o + (1-\alpha)\rho_w}\left[\frac{-\rho_o\rho_w U_{mix}^2\left(\frac{r-1}{r+1}\right)^2}{\alpha(1-\alpha)} - \left(\frac{\alpha\rho_o + (1-\alpha)\rho_w}{\alpha(1-\alpha)}\right) f_{\nabla\alpha}\right]^{0.5} \quad (7.4)$$

Equation 7.4 consists of two parts. The first one (before the ± sign) is called the weighted mean velocity, W_u. The second part includes the effect of a de-stabilizing factor, which is only different from 0 if r is different from 1, and of a stabilizing factor, $f_{\nabla\alpha}$. Since the two phases join in the middle of the pipe, the KH wave develops from a starting point $\alpha_w = 0.5$. Substitution gives the theoretical velocity of the wave at the junction:

$$C_v = \frac{U_{mix}}{r+1}\left[\frac{r\rho_o + \rho_w}{\rho_o + \rho_w}\right] \pm$$
$$\pm \frac{1}{\rho_o + \rho_w}\left[-\rho_o\rho_w U_{mix}^2\left(\frac{r-1}{r+1}\right)^2 - \left(\frac{\rho_o + \rho_w}{2}\right) f_{\nabla\alpha}\right]^{0.5} \quad (7.5)$$

Equation 7.5 shows that the dynamic wave propagates with velocity relative to the weighted mean velocity. In the limit of equal phase densities, the weighted mean velocity of the fluid becomes half the mixture velocity. For different densities (i.e. 830 kgm^{-3} oil and 1,000 kgm^{-3} water), the weighted mean velocity is expected to change slightly with the input ratio, but values are around half the mixture velocity (Figure 7.11).

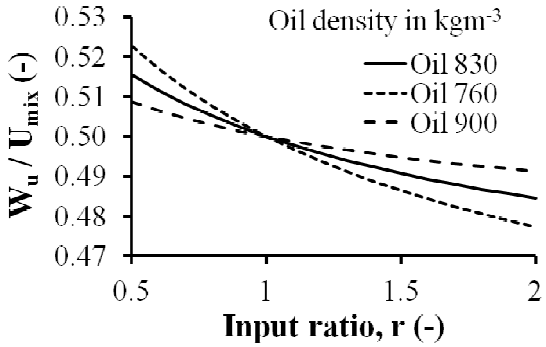

Figure 7.11 Ratio of weighted mean velocity to mixture velocity against input ratio

7.4 COROLLARY

The image analysis of oil-water interfacial waves has confirmed the results obtained from the conductance probe data in the previous chapter: 19-Hz frequency waves developed at the inlet when $r \neq 1$ with velocity about half the mixture velocity. This observation is in agreement with the predictions of the linear theory for dynamic waves. Inspection of wave images has also revealed spatial amplification of the wave amplitude (i.e. growth) immediately after the junction of the fluids, which decreases quickly downstream. This result, added to the fact that waves only developed when $r \neq 1$, suggests that the phenomenon is described by a Kelvin-Helmholtz mechanism. The dampening of waves can be, therefore, explained since the fluids adjust their actual velocities as to be roughly equal further downstream, which would remove the source of instability. During the appearance and growth of the waves, however, drops can be formed. This explains the main development of the flow near the inlet and the almost inexistent formation of drops downstream the pipe. Along with the effect of growing waves, the inlet geometry and any features of the experimental facility (seals, bends, etc.) seems to play a significant role on drop formation. The results presented in this Thesis led to the conclusions of this work, which are presented as follows.

CHAPTER 8
CONCLUSIONS AND FUTURE WORK

8.1 PRESENTATION OF CONCLUSIONS

In this work, the stratified flow of oil-water mixtures (Exxsol™ D140 and tap water) in a 38-mm ID acrylic pipe has been investigated with the aid of a high-speed camera and double-wire conductance probes. The nature and behaviour of the flow has been assessed both at the inlet section and further downstream the pipe, under fully-developed conditions.

The flow pattern boundaries were identified with high speed imaging. The stratified regime occurred at relatively low mixture velocities, but only within a range of oil-to-water input flow rate ratios around r = 1. At flow rates as low as 20 $Lmin^{-1}$, dual continuous flow was observed if the input ratio was less than 0.6 or larger than 2.4. The stratified to dual continuous flow transition was found to primarily depend on the oil-to-water input ratio with the stratified region further extended at r > 1. In both cases of input ratios larger or smaller than 1 and at moderate mixture velocities, drops formed in spite of a relatively smooth interface. It was found that the oil-water interface presents small, three dimensional fluctuations and that can be defined as fluctuating rather than wavy. As the mixture velocity increases, the fluctuations increase and, as a consequence, the interface appears rough. The Re numbers of the phases increase with the mixture velocity. However, these developments do not lead necessarily to the dual continuous pattern in the pipe, apart from tiny droplets entrained in the phases (intermediate flow). Other than that, stratification is favoured at input ratios close to 1 even at relatively high mixture velocities. The stratified regime is observed at mixture velocity as high as 1.9 ms^{-1} for r = 1.2, which is the ratio of water to oil densities. These observations and results (Chapter 4) lead to the following conclusions:

- The increase of mixture velocity does not necessarily lead to the development of waves or wavy structures clearly identifiable at the interface. Waves forming at the inlet tend to disappear soon after and are not sustained downstream the pipe, regardless of the input parameters.
- Drop formation is not seen to generally occur in the pipe and the phenomenon of drops detaching from waves has not been generally observed.
- The transition to dual continuous flow or drop formation in stratified oil-water flows along the pipe is not necessarily linked to high Re numbers of the phases alone or rough interfaces.

The details of the inlet design have been found relevant in this investigation (Chapter 4). Particularly, the area of stratification in the flow pattern map was found to expand if no split plate was used in the inlet. Differences in the flow introduced by the split plate are:

- The use of split plate in the inlet, far from enhancing stratification, had the opposite effect and the stratification area in the flow pattern map was reduced.
- The presence of the split plate seems to prevent the development of waves at the inlet when the input ratio is different from 1.

Observations in the lab have shown two different, general types of interfaces in the stratified oil-water flows investigated: 1) the fluctuating interface, composed of 3D, small contributions, seen downstream the pipe when the flow is fully-developed; and 2) the wavy interface displaying clearly identifiable wave structures, almost 2D in nature, at the inlet when no split plate was used and the input ratio was different from 1.

The necessity of analyzing the first type of interface statistically was discussed and justified and a full procedure of general validity has been developed (Chapter 5). Double-wire conductance probes have been used for this purpose. Waves at the inlet were also studied with conductance probes, while characteristics of these visible structures and their evolution along the inlet were further investigated via high-speed imaging.

The signal from the interface height was collected with the conductance probe at high-frequency (i.e. 256 Hz) and treated to ensure that any trends introduced by the acquisition systems and the variability of the water temperature and salinity were accounted for. A major conclusion was obtained after treatment:

- The oil-water interface signal of the flow as collected by the conductance probe and pre-treated is stationary and follows a Gaussian distribution at the 90% confidence level.

The randomness of the signal (Chapter 5) agrees particularly with the observations of the fluctuating interface. These important features of the flow (stationarity and normality) set a difference with the type of signal collected in the study of non-stratified flows, most often non-stationary, and allowed the use of well-established statistical techniques to analyze the data. Two different pieces of information on fully-developed flows have been obtained: 1) time-average parameters (i.e. water fractions, actual phase velocities and Re numbers); and 2) the power spectrum of the oil-water interface from the auto-correlation function of the signal, calculated from the extensive application of the Fast Fourier algorithm. Results on time-average parameters (Chapter 6) led to the following conclusion:

- In fully-developed, horizontal flow, the oil and water phases studied show very little slip at any input conditions. The fluids tend to flow with similar bulk velocity, roughly equal the mixture velocity.

The power spectrum of the oil-water interface downstream the pipe (Chapter 7) showed that: 1) there are two main contributing frequencies, one at 2 – 3 Hz, by far the most dominant, attributed to the mechanical vibrations of the flow system, and a range with a peak around 19 Hz; 2) the 19 Hz contribution was found to be always present, regardless of the flow conditions (i.e. input ratio or mixture velocity); 3) additionally, smaller contributions were found at higher frequencies, typically above 60 Hz; 4) both these high frequencies and the 19 Hz one tended to grow in importance as the mixture velocity increased, reflecting the fluctuating nature of the flow.

At $r \neq 1$ in the stratified regime waves developed at the inlet. Spectral analysis of the probe signal at this location and $r > 1$ (Chapter 6) revealed a different interface spectrum: 1) the 19 Hz contribution was clearly seen as the most relevant, almost the only contribution; 2) the importance of the system vibrations and any other higher frequencies was negligible. Investigation of inlet waves via high-speed imaging confirmed that the frequency of inlet waves agrees with the results of the spectrum. The spectra of the flow at $r < 1$ still presented the 2 – 3 Hz contribution as most significant, but it was seen that the waves were somehow disrupted by the inlet geometry in this case (they could collide against the top wall of the pipe), which may have affected the wave structure at the time it reached the position of the probe.

Investigation of inlet waves via high-speed imaging (Chapter 7) has shown that: 1) at $r \neq 1$, waves developed in a very short distance within the inlet increasing in amplitude (i.e. spatial amplification), but with constant frequency regardless of the input parameters of the flow; 2) the wave amplitudes quickly reduced in the inlet shortly after development, while wave velocity and wavelength increased. The wave frequencies, however, did not change considerably along the inlet and are within the range of 11 – 20 Hz, which agrees with the frequencies found previously from the spectral analysis of the interface height variation with time obtained with the conductance probe.

This observations and results suggest the following conclusions:

- When oil and water enter the inlet section with different velocities (i.e. different inlet flow rates, $r \neq 1$) waves develop due to instability. The instability seems not to occur if the input ratio is 1, as waves do not develop in that case.
- The source of instability disappears shortly after, as the average velocities of the two phases become equal. As a consequence, inlet waves vanish. The flow tends to stabilize always.
- The frequency of inlet waves is independent of the flow conditions and remains in the spectrum after the waves have disappeared. However, the spectra of the oil-water interface at the inlet and downstream the pipe show different contributions, which explain the existence of two different types of interfaces.

Further investigation of inlet waves via high-speed imaging (Chapter 7) has revealed spatial amplification during their development. This result linked to the observation of waves only seen when $r \neq 1$ suggests that there is a Kelvin-Helmholtz (KH) instability. The results of time-average parameters downstream the pipe showing no slip between the phases points further to this suggestion, since the absence of instability would dampen the waves. If so, the adjustment of the phases to fully-developed average parameters would have to take place shortly after the inlet, and the analysis of high-speed images supports this hypothesis. Based on these results, it can be concluded:

- Oil-water waves seen at the inlet develop because of a KH mechanism of instability.

The inlet waves seem to behave like dynamic waves. This means that the inlet wave velocity could be predicted in terms of the mixture velocity and the fluid properties.

8.2 SUGGESTIONS FOR FUTURE WORK

Entrainment due to drop detachment from rolling or unstable waves of significant amplitude has not been observed in the pipe. On the contrary, these structures (seen at the inlet at $r \neq 1$) vanished shortly after the junction point for all input conditions and mixture velocities. Additionally, instabilities are unlikely to appear in long, horizontal pipes with no disruptions, since the fluids tend to flow with almost no slip. The areas of dual continuous flow in the pattern map are characterized by large drops flowing near a smooth interface, otherwise affected by 3D perturbations. In these conditions, the water and oil phases do not have, as discussed, the highest Re numbers. On the contrary, the flow remained stratified at high mixture velocities with phases showing highest Re numbers for input rations close to 1, and having the roughest interface. These conclusions imply that the mixture velocity is not necessarily a main parameter determining drop formation in oil-water flows.

It was found that the flow patterns in this investigation tend to develop at the inlet. The flow pattern shortly after the inlet seems to remain unchanged along the pipe. The dampening of interfacial waves at the inlet at all conditions in stratified flow clearly shows the stability of the pattern further downstream the pipe. Similarly, in those cases where input conditions were sufficient to generate dual continuous flow, drops seem to form immediately at the inlet. The presence of inlet waves points to the contribution of KH instability as a suitable driver of drop formation. However, clean detachment of drops from the crest of such waves was not observed. Furthermore, it seems that the inlet geometry and the possibility of waves eventually colliding against the walls of the pipe at the inlet may be other reasons behind the formation of drops. The particular comparison of flows with and without split plate, showing an array of drops leaving the trail of the plate, where instability waves developed in the absence of it, reveals that other mechanisms apart from KH instability must explain the drop formation. There is a further example observed in the lab: whereas the flow downstream the inlet was stratified, the return pipe into the separator, after two bends of 90º was clearly dual continuous.

In accordance with these ideas, it seems that the phase turbulence or any *local* phenomenon of turbulence can play an important role in explaining possible mechanisms for drop entrainment. Particle Image Velocimetry (PIV) is a convenient technique to measure velocity profiles and the turbulence structure of the flow. This technique is currently being used to investigate the structure of the flow underneath the interfacial waves at the inlet and to clarify the influence that different inlet geometries can have on the flow. The technique could be further applied to analyze local velocity and Re stresses in a stratified mixture of oil and water suddenly subjected to an inertial change. If the evolution of the flow in time is needed as to investigate how the turbulence parameters change towards the onset of entrainment, it seems most appropriate to use high-speed PIV.

A natural extension of this work is the investigation of the oil-water interface in stratified flow with the split plate in place. The general methodology presented in this work could be applied to probe data at both the inlet and downstream locations, provided that any drops present at the inlet do not compromise the measurements. Perhaps, data could be collected at 256 Hz during 256 s (instead of 240 s or 4 min), as to readily have a

record of data-points that is already a power of 2. In calculating correction factors, all experimental records of oil-water flows, regardless of the use of different calibration curves when needed (i.e. after cleaning operations, repairs, etc.), should be compared to the signal of one standard single-phase calibration point in order to make all the records quantitatively comparable. Monitoring the fluids temperature in several points of the experimental rig would also be recommended. It is difficult to control the temperature at the exact location where measurements are collected due to the size of the facility, but values of temperature could be readily reported along with any data and observations

A personal word of encouragement towards constant observation seems opportune at this point. It is true that only quantitative data and its analysis can provide valuable results and useful solutions in the end, but many scientists and engineers have praised the riches that simple and careful observations have brought to their careers for the benefit of all. Vigilant time spent in the laboratory watching and wondering is not a waste time. It is still the physical world the object of investigation. The popular, almost mythological case of Alexander Fleming is clamorous, although it is true that, from the time he made his famous observation to the first commercial form of purified penicillin, 15 years have elapsed and that Fleming failed as much in isolating the molecule as in convincing others of the importance of the enterprise.

Finally, the conclusions of this work on time-average parameters, contributions to the power spectrum and inlet waves are conditioned to the pair of fluids and pipe diameter available in the laboratory (see Chapter 2). As discussed, interfaces that display the properties of randomness, stationarity, like those found in the current work can be properly investigated statistically. In this sense, one of the most powerful and attractive features of the methodology presented to analyze fluctuating interface is that it can be generally applied to other systems, regardless of the fluid properties or the pipe diameters. It would be interesting to further investigate whether a unique wave frequency develops due to KH instability and whether it is equal or different to 19 Hz in other oil-water or liquid-liquid systems. The properties of the interface, the availability of the instrumentation used and the well-established statistics presented would also allow for any improvements or further developments of the procedure that might be needed. In consequence, this work calls for collaboration.

REFERENCES

Acheson, D.J., 1990. Elementary fluid dynamics. Oxford University Press

Adrian, R.J., 2005. Twenty years of Particle Image Velocimetry. Exp Fluids 39: 159-169

Alamu, M.B., Azzopardi, B.J., 2011. Flow pattern and slug dynamics around a flow splitter. J Fluids Eng 133(12): 121105

Al-Wahaibi, T., 2006. Investigations on the transition between stratified and non-stratified horizontal oil-water flows. Ph. D. Thesis, University College London

Al-Wahaibi, T., Angeli, P., 2007. Transition between stratified and non-stratified horizontal oil–water flows. Part I: Stability analysis. Chem Eng Sci, 62, 2915-2928

Al-Wahaibi, T., Smith, M., Angeli, P., 2007. Transition between stratified and non-stratified horizontal oil-water flows. Part II: Mechanism of drop formation. Chem Eng Sci 62: 2929-2940

Al-Wahaibi, T., Angeli, P., 2011. Experimental study on interfacial waves in stratified horizontal oil-water flow. Int J Multiphase Flow 37(8): 930-940

Andritsos, N., Hanratty, T.J., 1987. Interfacial instabilities for horizontal gas-liquid flows in pipelines. Int J Multiphase Flow 13: 583-603

Andritsos, N., 1992. Statistical analysis of waves in horizontal stratified gas-liquid flow. Int J Multiphase Flow 18(3): 465-473

Angeli, P., 1996. Liquid-liquid dispersed flows in horizontal pipes. Ph.D. Thesis, Imperial College

Angeli, P., Hewitt, G., 1998. Pressure gradient in horizontal liquid-liquid flows. Int J Multiphase Flow 24: 1183-1203

Angeli, P., Hewitt, G., 2000. Flow Structure in Horizontal Oil-Water Flow. Int J Multiphase Flow 26: 1117-1140

Auñón, J.I., Chandrasekar, V., 1997. Introduction to probability and random processes. McGraw Hill

Arirachakaran, S., Oglesby, K.D., Malinowsky, M.S., Shoham, O., Brill, J.P., 1989. An analysis of oil-water flow phenomena in horizontal pipes. In SPE paper 18836, SPE Prod Operating Sym, Oklahoma, pp. 155-167

Azzopardi, B.J., 1986. Disturbance wave frequencies, velocities and spacing in vertical annular two-phase flow. Nucl Eng Des 92: 121-133

Azzopardi, B.J., 1997. Drops in annular two-phase flow. Int J Multiphase Flow 23(7): 1-53

Bai, R., 1995. Travelling waves in a high viscosity ratio and axisymmetric core annular flow. PhD Dissertation, University of Minnesota

Balakrishnan, A.V., 1995. Introduction to random processes in engineering. John Wiley & Sons

Bannwart, A.C., 1998. Wavespeed and volumetric fraction in core annular flow. Int J Multiphase Flow 24(6): 961-974

Bannwart, A.C., Rodriguez, O.M.H., De Carvalho, C.H.M., Wang, I.S., Vara, R.M.O., 2004. Flow patterns in heavy crude oil-water flow. J Energ Resour-ASME 126(3): 184-189

Baker, O., 1954. Simultaneous flow of oil & gas. Oil Gas J 53: 185

Barnea, D.S.O., Taitel, Y., 1993. Kelvin-Helmholtz stability criteria for stratified flow – viscous versus non-viscous (inviscid) approaches. Int J Multiphase Flow 19(4): 639-649

Barral, A.H., Edomwonyi-Otu, L.C., Angeli, P., 2013. Interfacial wave characteristics in stratified oil-water flows in pipes of different diameter. In Proc.: 8th International Conference of Multiphase Flow, Jeju, South Korea

Bendat, J.S., 1962. Interpretation and application of statistical analysis for random physical phenomena. IRE Trans Bio Med Electron 9(1): 31-43

Bendat, J.S., Piersol, A.G., 2010. Random data: analysis and measurement Procedures. Wiley, New Jersey

Bethea, R.M., Duran, B.S., Boullion, T.L., 1995. Statistical methods for engineers and scientists. Marcel Dekker, 3rd edition

Birvalski, M., Tummers, M.J., Delfos, R., Henkes, R.A.W.M., 2013. Particle Image Velocimetry measurements in stratified air/water flow in a horizontal pipe, pp. 337-351. 16th International Conference on Multiphase Production Technology, Cannes, France

Brauner, N., Moalem Maron, D., 1989. Two Phase Liquid-Liquid Stratified Flow. Physicochem Hydrodyn 11: 487-506

Brauner, N., Moalem Maron, D., 1992. Analysis of stratified/non-stratified transitional boundaries in inclined gas-liquid flows. Int J Multiphase Flow 18: 541-557

Brauner, N., Moalem Maron, D., 1992. Flow pattern transitions in two-phase liquid-liquid flow in horizontal tubes. Int J Multiphase Flow 18: 123-140

Brauner, N., Rovinsky, J., Moalem Maron, D., 1996. Determination of the interface curvature in stratified two-phase systems by energy considerations. Int J Multiphase Flow 22: 1167-1185

Brauner, N., Moalem Maron, D., Rovinsky, J., 1998. A two-fluid model for stratified flows with curved interfaces. Int J Multiphase Flow 24: 975-1004

Cengel, J.A., Faruqui, A.A., Finnigan, J.W., Wright, C.H., Kundsen, J.G., 1962. Laminar and turbulent flow of unstable liquid-liquid emulsions. AIChE J 8(3): 335-339

Chakrabarti, D.P., Das, G., Das, P.K., 2006. The transition from water continuous to oil continuous flow pattern. AIChE J 52(11): 3668-3678

Chakrabarti, D.P., Das, G., Das, P.K., 2007. Identification of stratified liquid–liquid flow through horizontal pipes by a non-intrusive optical probe. Chem Eng Sci 62: 1861-1876

Charles, M.E., Govier, G.W., Hodgson, G.W., 1961. The horizontal pipeline flow of equal density oil-water mixture. Can J Chem Eng 39: 27-36

Charles, M.E., Lilleleht, L.U., 1966. Correlation of pressure gradients for stratified laminar-turbulent pipeline flow of two immiscible liquids. Can J Chem Eng 44(1): 47

Chinaud, M., Barral, A.H., Angeli, P., 2014. In preparation

Chu, K. J., 1973. Statistical characterization and modelling of wavy liquid films in vertical two-phase flow. PhD Dissertation, University of Houston

Collins, S.B., Knudsen, J.G., 1970. Drop-size distributions produced by turbulent pipe flow of immiscible liquids. AIChE J 16(6): 1072

Cooley, J.W., Tuckey, J.W., 1965. An algorithm for the machine calculation of complex Fourier series. Math Comput Model 19: 297-301

Coulson, J.M., Richardson, J.F., 2010. Chemical Engineering: Vol.1 Fluid flow, heat transfer and mass transfer, Elsevier

Cox, A.L., 1985. A study of horizontal and downhill two-phase oil-water flow. M.Sc. Thesis, University of Texas

De Castro, M.S., Pereira, C.C., Dos Santos, J.N., Rodriguez, O.M.H., 2012. Geometrical and kinematic properties of interfacial waves in stratified oil-water flow in inclined pipe. Exp Therm Fluid Sci 37: 171-178

Du, M., Jin, N.D., Gao, Z.K., Wang, Z.Y., Chen, P., 2012. Time-frequency analysis of vertical upward oil-water two-phase flow. In Proc.: 7th Int Sym on Measurement Techniques for Multiphase Flows, AIP Conf Proc 1428: 107-114

Drazin, P.G., Reid, W.H., 2004. Hydrodynamic stability. University Cambridge Press

Elseth, G., Kvandal, H.K. & Melaaen, M.C., 2001. Measurement of velocity and phase fraction in stratified oil/water flow. In Proc.: 2nd Int Sym on Multiphase Flow and Transport Phenomena, Antalya, Turkey, pp. 341-348

Espedal, M., 1998. Experimental investigation of stratified two-phase pipe flow in small inclinations. PhD Dissertation, NTNU

Fossa, M., 1998. Design and performance of a conductance probe for measuring liquid fraction in two-phase gas-liquid flows. Flow Meas Instrum 9(2): 103-109

Guzhov, A.I.G., Medredev, V.F., Medredeva, O.P., 1973. Emulsion formation during the flow of two immiscible liquids in a pipe. Neft Khoz (in Russian) 8: 58-61

Hadžiabdić, M., Oliemans, R.V.A., 2007. Parametric study of a model for determining the liquid flow-rates from the pressure drop and water hold-up in oil–water flows. Int J Multiphase Flow 33: 1365-1394

Hall Taylor, N., Hewitt, G.F., Lacey, P.M.C., 1963. The motion and frequency of large disturbance waves in annular two-phase flow of air-water mixtures. Chem Eng Sci 18: 537-552

Harris, F.J., 1978. On the use of windows for harmonic analysis with the discrete Fourier Transform. Proc IEEE 66(1): 51-83

Hernández, L., Juliá, J.E., Chiva, S., Paranjape, S., Ishii, M., 2006. Fast classification of two-phase flow regimes based on conductivity signals and artificial neural networks. Meas Sci Technol 17(6): 1511-1521

Hinze, J.O., 1955. Fundamentals of the hydrodynamic mechanism of splitting in dispersion processes. AIChE Journal 1, 289-295

Holowach, M.J, Hochreiter, L.E., Cheung, F.B., 2002. A model for droplet entrainment in heated annular flow. Int J Heat Fluid Flow 23: 807-822

Hu, B., Angeli, P. 2006. Phase inversion and associated phenomena in oil-water vertical pipeline flow. Canadian Journal of Chemical Engineering 84(1): 94-107

Hu, B., Matar, O. K., Hewitt, G. F., Angeli, P. 2007. Mean and turbulent fluctuating velocities in oil-water vertical dispersed flows. *Chemical Engineering Science,* 62**,** 1199-1214.

Ioannou, K., Nydal, O.J., Angeli, P., 2005. Phase inversion in dispersed liquid-liquid flows. Exp Therm Fluid Sci 29: 331-339

Ishii, M., Grolmes, M.A., 1975. Inception criteria for droplet entrainment in two-phase concurrent film flow, AICHE J 21(2): 308-318

Jayawardena, S.S., Alkaya, B., Redus, C.L., Brill, J.P., 2000. A new model for dispersed multi-layer oil-water flow. 2nd North American Conference on Multiphase Technology. In Proc.: BHR Group Conf Series 40, pp. 77-89

Jin, N.D., Nie, X.B., Ren, Y.Y., Liu, X.B., 2003. Characterization of oil/water two-phase flow patterns based on non-linear time series analysis. Flow Meas Instrum 14: 169-175

Jurman, L.A., Bruno, K., McCready, M.J., 1989. Periodic and solitary waves on thin, horizontal, gas-sheared liquid films. Int J Multiphase Flow 15(3): 371-384

Kadri, U., Mudde, R. F., Oliemans, R. V. A., Bonizzi, M., Andreussi, P., 2009. Prediction of the transition from stratified to slug flow or roll-waves in gas-liquid horizontal pipes. Int J Multiphase Flow 35(11): 1001-1010

Karabelas, A.J., 1978. Droplet size spectra generated in turbulent pipe-flow of dilute liquid-liquid dispersions. AIChE 24(2): 170-180

Kim, S., Fu, X.Y., Wang, X., Ishii, M., 2000. Development of the miniaturized four-sensor conductivity probe and the signal processing scheme. Int J Heat Mass Transfer 43: 4101-18

Koskie, J.E. Mudawar, I., Tiederman, W.G., 1989. Parallel-wire probes for measurement of thick liquid films. Int J Multiphase Flow, 15: 521-530

Kreyszig, E., 1999. Advanced Engineering Mathematics. John Wiley & Sons, 8th ed.

Kubie, J., Gardner G.C., 1977. Drop sizes and drop dispersion in straight horizontal tubes and in helical-coils. Chem Eng Sci 32(2): 195-202

Kumara, W.A.S., Halvorsen, B.M., Melaaen, M.C., 2009. Velocity and turbulence measurements of oil-water flow in horizontal and slightly inclined pipes using PIV. Computational Methods in Multiphase Flow V. In: WIT Trans Eng Sci, pp. 277-292

Kumara, W.A.S., Elseth, G., Halvorsen, B.M., Melaaen, M.C., 2010. Comparison of Particle Image Velocimetry and Laser Doppler Anemometry measurement methods applied to the oil–water flow in horizontal pipe. Flow Meas Instrum 21: 105-117

Kumara W.A.S., Halvorsen, B.M., Melaaen, M.C., 2010. Single-beam gamma densitometry measurements of oil-water flow in horizontal and slightly-inclined pipes. Int J Multiphase Flow 36: 467-480

Kurban, A.P.A., Angeli, P., Mendestatsis, M.A., Hewitt, G.F., 1995. Stratified and dispersed oil-water flows in horizontal pipes. In Proc.: 7th International Conference on Multiphase Production Technology, Cannes, France. Mech Eng Publications, London, pp. 699-714

Lovick, J., Angeli, P., 2004. Experimental studies on the dual continuous flow pattern in oil–water flows. Int J Multiphase Flow 30: 139-157

Lowson, M.H., 1970. Our industry petroleum. The British Petroleum Company Ltd

Lum, J.Y., Lovick, J., Angeli, P., 2004. Low inclination oil-water flows. Can J Chem Eng 82(2): 303-315

Malinowsky, M.S., 1975. An experimental study oil-water and air-oil-water flowing mixtures in horizontal pipes. PhD Dissertation, University of Tulsa

Manolis, I.G., 1996. High-pressure gas-liquid slug flow. PhD Thesis, Imperial College London

McClarey, M.J., Mansoori, G.A., 1978. Factors affecting the phase inversion of dispersed immiscible liquid-liquid mixtures. AIChE Sym Series 74: 134-139

Mu, H., 2001. Experimental research on oil-water horizontal pipe flow. MSc Thesis, University of Petroleum

Nädler, M., Mewes, D., 1995. The effect of gas injection on the flow of immiscible liquids in horizontal pipes. Chem Eng Technol 18(3): 156-165

Nädler, M., Mewes, D., 1997. Flow induced emulsification in the flow of two immiscible liquids in horizontal pipes. Int J Multiphase Flow 23: 55-68

Ng, T.S., Lawrence, C.J., Hewitt, G.F., 2001. Interface shapes for two-phase laminar stratified flow in a circular pipe. Int J Multiphase Flow 27: 1301-1311

Ngan, K.H., Ioannou, K., Rhyne, L.D., Wang, W., Angeli, P., 2009. A methodology for predicting phase inversion during liquid-liquid dispersed pipeline flow. Chem Eng Research and Design, 87(3A): 318-324

Ngan, K.H., 2010. Phase inversion in disperse liquid-liquid pipe flow. PhD Thesis, University College London

Ngan, K.H., Ioannou, K., Rhyne, L.D., Angeli, P. 2011. Effect of glycerol addition on phase inversion in horizontal dispersed oil-water pipe flows. Exp Therm Fluid Sci 35: 628-635

Oglesby, K.D. 1979. An experimental study on the effects of oil viscosity, mixture velocity, and water fraction on horizontal oil-water flows. MSc Thesis, University of Tulsa

Oliemans, R.V.A., 1986. The lubricating-film model for core-annular flow. PhD Dissertation, Delft University

Oliemans, R.V.A., Ooms, G., Wu, H.L., Duijvestijn, A., 1987. Core-annular oil/water flow: the turbulent-lubricating film model and measurements in a 5 cm pipe loop. Int J Multiphase Flow 13(1): 23-31

Pal, R., 1993. Flow of oil-in-water emulsions through orifice and Venturi meters. Ind Eng Chem Res 32(6): 1212-1217

Raffel, M.E.A., 2007. Particle Image Velocimetry: a practical guide, Springer

Raj, T.S., Chakrabarti, D.P., Das, G., 2005. Liquid-liquid stratified flow through horizontal conduits. Chem Eng Technol 28(8): 899-907

Rhyne, L., 2014. Chevron Technology Company – Flow Assurance Team. Personal communication

Riano, A.B., Bannwart, A.C., Rodriguez, O.M.H., 2013. Hold-up estimation in core flow using image processing. IEEE International Instrumentation and Measurement Technology Conference: 334-338

Rodriguez, O.M.H., Bannwart, A.C., 2006. Analytical model for interfacial waves in vertical core flow. J Pet Sci Eng 54(3–4): 173-182

Rodriguez, O. M. H., Bannwart, A. C., 2006. Experimental study on interfacial waves in vertical core flow. J Petrol Sci Eng 54(3-4): 140-148

Rodriguez, O.M.H., Oliemans, R.V.A., 2006. Experimental study on oil–water flow in horizontal and slightly inclined pipes. Int J Multiphase Flow 32: 323-343

Russell, T.W., Hodgson, G.W., Govier, G.W., 1959. Horizontal pipeline flow of mixtures of oil and water. Can J Chem Eng, 37**,** 9-17

Scott, G.M., 1985. A study of two-phase liquid-liquid flow at variable inclinations. MSc Thesis, University of Texas

Shannon, C.E., 1949. Communications in the presence of noise. Proc. IRE 37:10-21

Simmons, M.J.H., Azzopardi, B., 2001. Drop sizes distributions in dispersed liquid-liquid pipe flow. Int J Multiphase Flow 27(5): 843-859

Sleicher, C.A., 1962. Maximum stable drop size in turbulent flow. AIChE J 8(4): 471-477

Soleimani, A., 1999. Phase distribution and associated phenomena in oil-water flows in horizontal tubes. PhD Thesis, Imperial College London

Soleimani, A., Lawrence, C.J., Hewitt, G.F., 2000. Spatial distribution of oil and water in horizontal pipe flow. SPE J 5(4): 394-401

Stapelberg, H.H., Mewes, D., 1994. The pressure loss and slug frequency of liquid-liquid-gas slug flow in horizontal pipes. Int J Multiphase Flow 20(2): 285-303

Stapelberg, H.H., Dorstewitz, F., Nädler, M., Mewes, D., 1991. The slug flow of oil, water and gas in horizontal pipelines. In Proc.: 5th International Conference on Multi-Phase Production Technology, Cannes, France, pp. 527-532

Sun, B., Wang, E.P., Zhang, Y.J., 2011. Time-frequency spectral analysis of gas-liquid two-phase flow's fluctuations. Acta Phys Sin 60(1): 014701

Taitel, Y., Dukler, A.E., 1976. A model for predicting flow regime transitions in horizontal and near horizontal gas-liquid flow. AIChE Journal 22: 47-55

Trallero, J.L., 1995. Oil-water flow patterns in horizontal pipes. PhD Dissertation, University of Tulsa

Trallero, J. L., Sarica, C., Brill, J. P. 1997. A study of oil/water flow patterns in horizontal pipes. *Spe Production & Facilities*, 12**,** 165-172.

Tsochatzidis, N.A., Karapantsios, T.D., Kostoglou, M.V., Karabelas, A.J., 1992. A conductance probe for measuring liquid fraction in pipes and packed beds. Int J Multiphase Flow 18(5): 653-667

Ullmann, A., Brauner, N., 2006. Closure relations for two-fluid models for two-phase stratified smooth and stratified wavy flows. Int J Multiphase Flow 32, 82-105

Valle, A., Kvandal, H.K., 1995. Pressure drop and dispersions characteristics of separated oil-water flow. In Proc.: 1st Int Sym on Two-Phase Flow Modelling and Experimentation, Rome, Italy, pp. 583-591

Valle, A., Utvik, O.H., 1998. Pressure drop, flow pattern and slip for two phase crude oil/water flow: experiments and model predictions. In: Proc Int Symp on Liquid-Liquid Two Phase Flow and Transport Phenomena, Antalya, Turkey, 3-7 Nov: 63-74

Valle, A., 2000. Three phase gas-oil-water pipe flow. PhD Thesis, Imperial College London

Vedapuri, D.B. Jepson, W.P., 1997. A segregated flow model to predict water layer thickness in oil-water flows in horizontal and slightly inclined pipes. In Proc.: 8th International Conference on Multiphase Production, Cannes, France

Wallis, G. B., 1969. One-dimensional two-phase flow. McGraw Hill

Wang, Z., Gabriel, K.S., Manz, D.L., 2004. The influences of wave height on the interfacial friction in annular gas–liquid flow under normal and microgravity conditions. Int J Multiphase Flow 30(10): 1193-1211

Wang, W., Gong, J., Angeli, P., 2011. Investigation on heavy crude-water two phase flow and related flow characteristics. Int J Multiphase Flow 37(9): 1156-1164

Ward, J.P., Knudsen, J.G., 1967. Turbulent flow of unstable liquid-liquid dispersions – drop sizes and velocity distributions. AIChE J 13(2): 356

Webb, D. 1970. Studies of the characteristics of downward annular flow two-phase flow. PhD Thesis, University of Cambridge

Westerweel, J., 1997. Fundamentals of digital Particle Image Velocimetry. Meas Sci Technol 8: 1379-1398

Wicks, M., Fraser, J.P., 1975. Entrainment of water by flowing oil. Mater Performance 14(5): 9-12

Woodmansee, D.E., Hanratty, T.J., 1969. Mechanism for the removal of droplets from a liquid surface by a parallel air flow. Chem Eng Sci 24(2): 299-307

Wu, Q., Ishii, M., 1999. Sensitivity study on double-sensor conductivity probe for the measurement of interfacial area concentration in bubbly flow. Int J Multiphase Flow 25: 445-453

Xiao-Xuan, X., 2007. Study on oil–water two-phase flow in horizontal pipelines. J Pet Sci Eng 59: 43-58

Xu, X.X., 2007. Study on oil-water two-phase flow in horizontal pipelines. J Pet Sci Eng 59: 43-58

Xu, W.F., Xu, L.J., Cao, Z., Chen, J.J., Liu, X.B., Hu, J.H., 2012. Normalized least-square method for water hold-up measurements in stratified oil-water flow. Flow Meas Instrum 27: 71-80

Yao, H.Y., 2006. Experimental research on oil-water pipeflows. PhD Thesis, University of Petroleum

Yao, H.Y., Gong, J., 2004. An experimental investigation on flow patterns and pressure gradients of heavy oil-water flows in horizontal pipes. In Proc.: 3rd Int Sym Multiphase, Non-Newtonian and Reacting flows, Hangzhou, China

Yeh, G.H., Moses, R.A., 1964. Phase-volume relationship at the point of phase inversion in liquid dispersions. AIChE J 10: 260-265

Yih, C. S., 1980. Stratified flows. Academic Press, New York

Zhai, L., Jin, N., Zong, Y., Wang, Z., Gu, M., 2012. The development of a conductance method for measuring liquid hold-up in horizontal oil-water two-phase flows. Meas Sci Technol 23(2): 025304

Zhao, D., Guo, L., Hu, X., Zhang, X., Wang, X., 2006. Experimental study on local characteristics of oil–water dispersed flow in a vertical pipe. Int J Multiphase Flow 32: 1254-1268

PUBLICATIONS AND CONFERENCE PAPERS

Barral, A.H., Angeli, P., 2013. Investigation of stratified, horizontal oil-water flow via statistical analysis of conductance probe data. Exp Fluids 54(10): 1604

Barral, A.H., Angeli, P., 2014. Spectral density analysis of the interface in stratified oil-water flows. Int J Multiphase Flow 65: 117-126

Barral, A.H., Angeli, P., 2014. Investigations of interfacial waves at the inlet section in stratified oil-water flows. In proofs (accepted in Exp Therm Fluid Sci): http://dx.doi.org/10.1016/j.expthermflusci.2014.08.007

Barral, A.H., Edomwonyi-Otu, L.C., Angeli, P., 2013. Interfacial wave characteristics in stratified oil-water flows in pipes of different diameter. In Proc.: 8th International Conference of Multiphase Flow, Jeju, South Korea

Edomwonyi-Otu, L.C., Barral, A.H., Angeli, P, 2013. Influence of drag reducing agents on interfacial wave characteristics in horizontal oil-water flow. 16th International Conference on Multiphase Production Technology, Cannes, France, pp. 353-361

Barral, A.H., Dore, V., Angeli, P., 2012. Velocity measurements and wave characteristics in separated horizontal oil-water flows. In Proc.: Int Sym on Multiphase Flow and Transport Phenomena, Agadir, Morocco, p. 41

APPENDIXES

APPENDIX 1
EXPERIMENTAL PROCEDURES

A1.1 INTRODUCTION

The work presented in this Thesis is an experimental work.

The purpose of performing experiments, in general, is the generation of data that, after proper analysis, can lead to insights of the phenomena under study and conclusions. The ultimate goal of experiments is, therefore, data and results. Despite the urgency for this, there is the personal conviction that good laboratory practices should be observed in all cases. These practices go beyond the usual care and honesty in preparing and conducting experiments and in collecting the data. Concern for reproducibility, for example, shall also be kept. Thoughtfulness (even during routine work), cleanliness and order are other qualities that experimentation should bring. Attention to the detail and practical thinking would only come with regular practice and training. Laboratory experiments give opportunity to observe the physics of the problem under study and, frequently, provide a rich understanding of the phenomena that could hardly being obtained in any other way. It usually is a powerful vaccine against prejudices and prefabricated mind images. Against the temptation of disconnecting the final results during the analysis from the conditions under which the data was collected, experimentation keeps the researcher focus and helps sharpen in him/her a natural sense of reality.

The following section presents the general procedure to operate the oil-water facility, along with suggestions and indications for maintenance, cleaning and safety. These details are considered important and worthy to be reported as complement of this investigation and for information in the future.

Procedures to calibrate the parallel-wire probes, prepare the experimental data and to estimate time-average parameters and spectra are presented and discussed in Chapters and other Appendices.

A1.2 OIL-WATER FACILITY OPERATION

Rig operations and experimental practices have been continuously improved as details and insights of the oil-water flow in the facility were acquired. Procedures are opened for discussion and further improvement. The sketch of the experimental facility in Figure 3.2 is here reproduced for convenience:

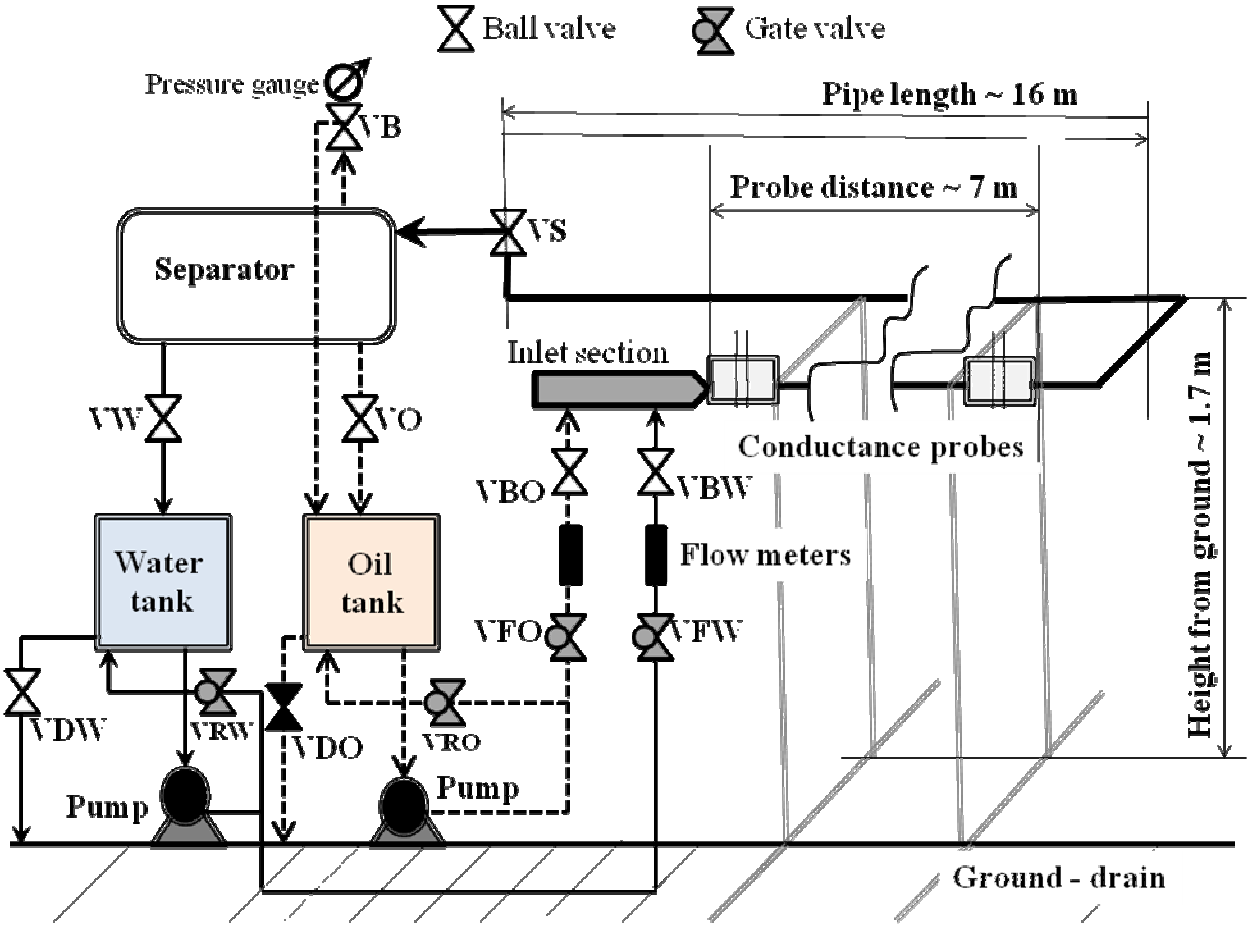

Figure 3.2 Sketch of the experimental facility

A.1.2.1 Routine start-up

The water tank is maintained empty when the rig is not in operation (i.e. nights, weekends). On the contrary, oil is kept in the oil tank.

Before any experimentation, water is poured into the water tank and, for one or two minutes, the water drain VDW is initially opened with the purpose of rinsing the bottom of the tank. Once the tank is filled about 1/3, VDW is closed and both return valves VW and VO from the separator are opened. The level of liquid in the

vessel decreases then quickly. At the same time, the water drain VDW is opened again, in order to replace the water inside the separator by fresh water.

As soon as the liquid inside the separator exits, smell may occur produced by the accumulated microbiological activity on the stagnant liquid. The smell is particularly notorious after the weekend or any idle period. Replacement of the water inside the separator is a relatively easy process that helps maintain the water quality similar to that of the tap. The level inside the separator can be monitored by means of a level tube on the front side. Typically, the separator is operated keeping the oil-water interface in the level tube between 1/3 (low mark) and 2/3 (high mark) of its height. This is to prevent the interface reaching too close to the oil or water exits. Due to bacterial activity, the oil-water interface is generally populated by colonies of micro-organisms and their metabolites, which tend to develop appreciably only a few days after contact.

Once the level in the separator reaches the low mark, the water exit is closed (VW) is closed. The water drain VDW is closed after a few minutes. In order to comply with legislation, the oil drain VDO is kept closed at all times and if any significant loss of oil occurs accidentally, the incident shall be reported and assessed conveniently as soon as it happens.

Open VS and valves VBO and VBW. Once ball valves are opened, start the water pump ensuring that VFW is closed and that all the flow is returned to the water tank. In practice, a suitable aperture of VRW (and VRO) was found and fixed. Finally, VFW is opened and the flow of water is verified by means of the flow rate. A flow rate of 50 $Lmin^{-1}$ is maintained along the pipes to rinse the rig for a about 10 minutes. When needed, the verifications are repeated in the same way with the oil valves and the oil pump is switched on. VFO allows oil into the pipes.

A.1.2.2 Two-phase flow operation

Gate valves VFO and VFW allow selecting the flow rate of oil and water, respectively. During the operation, the level of water in the tank as well as the level of the interface in the separator must be monitored. The former is controlled by continuously adding fresh water to the tank and opening and closing the drain VDW as needed. The level of liquid in the separator is controlled by manually operating the

VW, which allows water to be discharged into the tank: the valve is closed when the level is low; and it is open when the level is high. These procedures are successful and straightforward, but require constant monitoring.

During the experimentation with PIV, seeding particles are added to the water tank on the surface above the suction pipe. The mixing provided by the recirculation of the pump is sufficient to disperse the particles. This procedure, however, produces a short pulse of particles in the pipe that allows for experimentation only for a few second. Another seeding is required afterwards. In order to minimize the use of particles, the water drain VW could be closed in these cases, at the expense of additional temperature increase.

The small valve VB in the bleeding line is kept always open, as a safety measurement. The line sinks below the surface into the oil tank. In this way, it is expected to allow air to enter or exit the separator freely during the operation as well as in periods of inactivity. The reading from the pressure gauge allows, nevertheless, monitoring the pressure inside the separator at all times. This bleeding line in the separator was designed and installed for the experimentation of this Thesis.

Finally, when VFO opens to let the oil flow in the test pipe, small air drops are seen for low flow rates or mixture velocities (20 $Lmin^{-1}$ or 0.29 ms^{-1}, respectively). In order to remove such drops, a sufficient flow of oil is maintained for a few seconds (up to 60 $Lmin^{-1}$, for example), and then adjusted to the desired flow rate.

A.1.2.3 Collection of conductance probe data and correction factors

In order to compensate for variations in water temperature and salinity, one run of single-phase water at 60 $Lmin^{-1}$ is performed before and after a given two-phase combination. Each water phase run lasts 60 seconds. Probe and flow rate data is collected at 256 Hz in order to calculate correction factors. After, the oil pump is switched and the flow rates adjusted as convenient. A 4-min oil-water flow is run, collecting probe and flow rate data at 256 Hz. Immediately after, a second single-phase, 60 $Lmin^{-1}$ water flow is run.

The probe data of each single phase is properly treated and an overall average of the signal computed. The value is then compared to the predicted signal at 100 % water by the calibration curve, and a relative factor is found (Equation 5.5). All the

data-points of the two-phase flow probe signal are multiplied by the correction factor. Finally, the second single-phase run serves as the first one of the following two-phase flow combination. Figure A1.1 shows a schematic of the procedure.

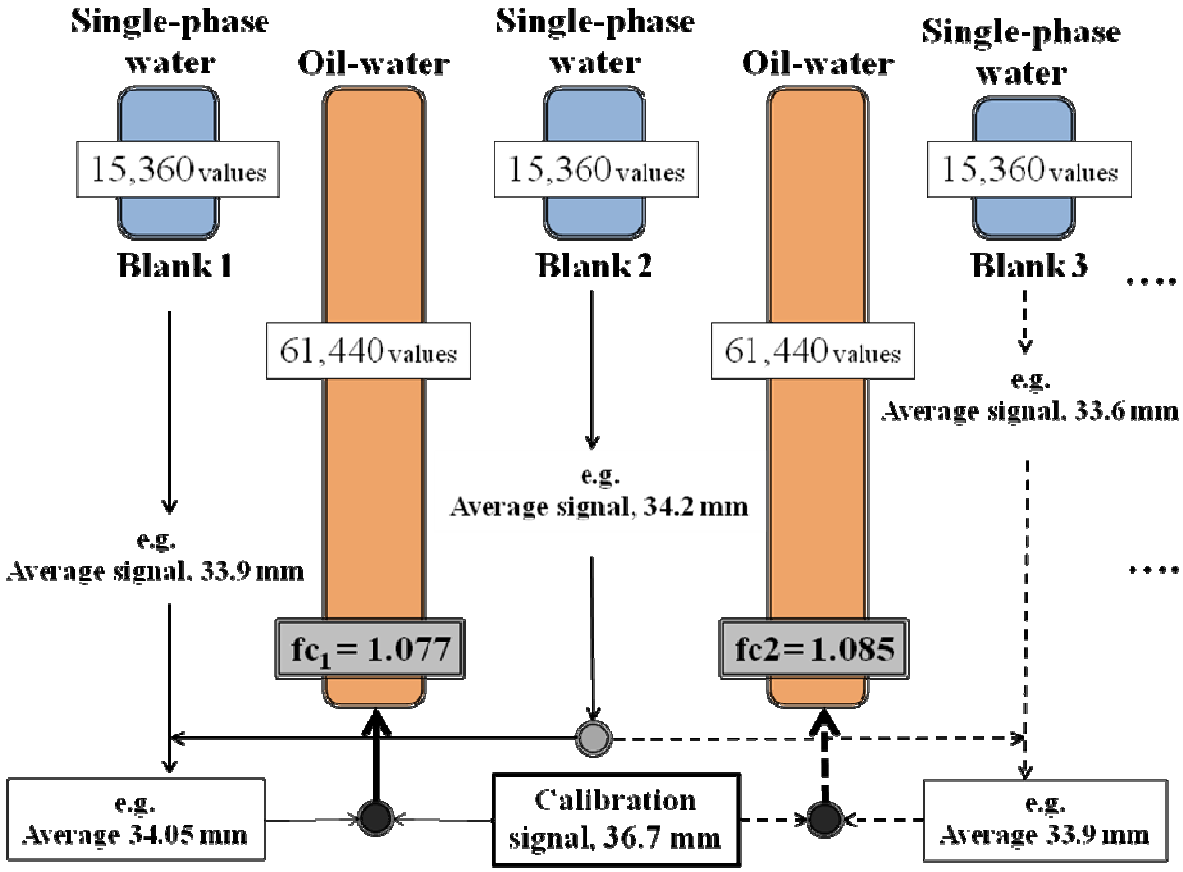

Figure A1.1 Schematic example of correction factors calculation

During the single-phase runs, the oil pump was switched off. Water tends to occupy entirely the pipeline but some oil is trapped in the top duct of the inlet section. Water may drag oil as drops because of turbulence. This is unavoidable. In order to ensure repeatability, the signal from the single-phase runs was collected after at least 30 seconds of stopping the oil flow or after drops had been significantly reduced in the inlet section. This instance could be identified.

For the future, it is suggested to use the single-phase signal of a unique calibration to relate all two-fluid records when computing correction factors. This way, the data measured with different calibration curves could be quantitatively comparable.

A.1.2.4 Routine shut-down

After the experimentation, the oil valve VFO is slowly closed, the oil pump switched off and the ball valve VBO closed. A flow of water of 60 $Lmin^{-1}$ is then adjusted and maintained for 2 or 3 minutes, in order to sweep all the oil into the separator and rinse the pipes. After this, the water valve VFW is closed, the water pump switched off and VBW closed. The inlet to the separator VS is closed and the water drain VDW opened.

A.1.2.5 Rinsing

Between daily operations, the pipe is maintained full with water. If the rig has not been used, a routine starting-up is performed with water no later than 2 – 3 days after the experimentation or every other day in longer idle periods. The water in the separator is partially renewed and a flow of 60 $Lmin^{-1}$ of water pumped into the pipes for 3 – 5 min. This procedure has proved satisfactory to maintain the pipes clean for extended periods of time and thus, avoiding frequently disassembling the rig.

A.1.2.6 Draining

The tanks, the acrylic pipes and the instrumentation (i.e. conductance probes) are frequently cleaned as needed. In such cases, the pipes are drained (removing the pressure-drop ports and opening the vent on top of one pipe section in the return side, to allow air to replace the liquid), the pipes taken apart and the instruments disassembled. Soap and water are used to carefully clean the acrylic; methanol can be employed exceptionally (for example, to remove small marks or writings on the pipe section), but acetone should be avoided. Figure A1.2 shows the SOP written to establish instructions to dispose of oily or wash water during cleaning or maintenance procedures.

A.1.2.7 Safety and risk assessment

Valves VO, VW and VS are kept closed when the rig is not in operation. Closure of the inlet separator (VS) is particularly important to prevent any possible diffusion of oil into the piping. After operation, the pipes are washed with clean water and left flooded to maintain the circuit as clean as possible.

When operating the rig, it must be confirmed that the three ball valves, VS, VBO and VBW are opened before opening VFO and VFW. If any of the valves controlling the flow rate is accidentally opened while VBO or VBW are closed, stop the pumps and only then close VFO or VFW before opening the ball valves. Do not attempt to operate VBO or VBW with the rig in operation. Failure in doing so might compromise the integrity of the rig, because the section would be pressurized.

Risk assessments were in place conveniently. Figure A1.3 presents the first page of the risk assessment written for the operation of the rig.

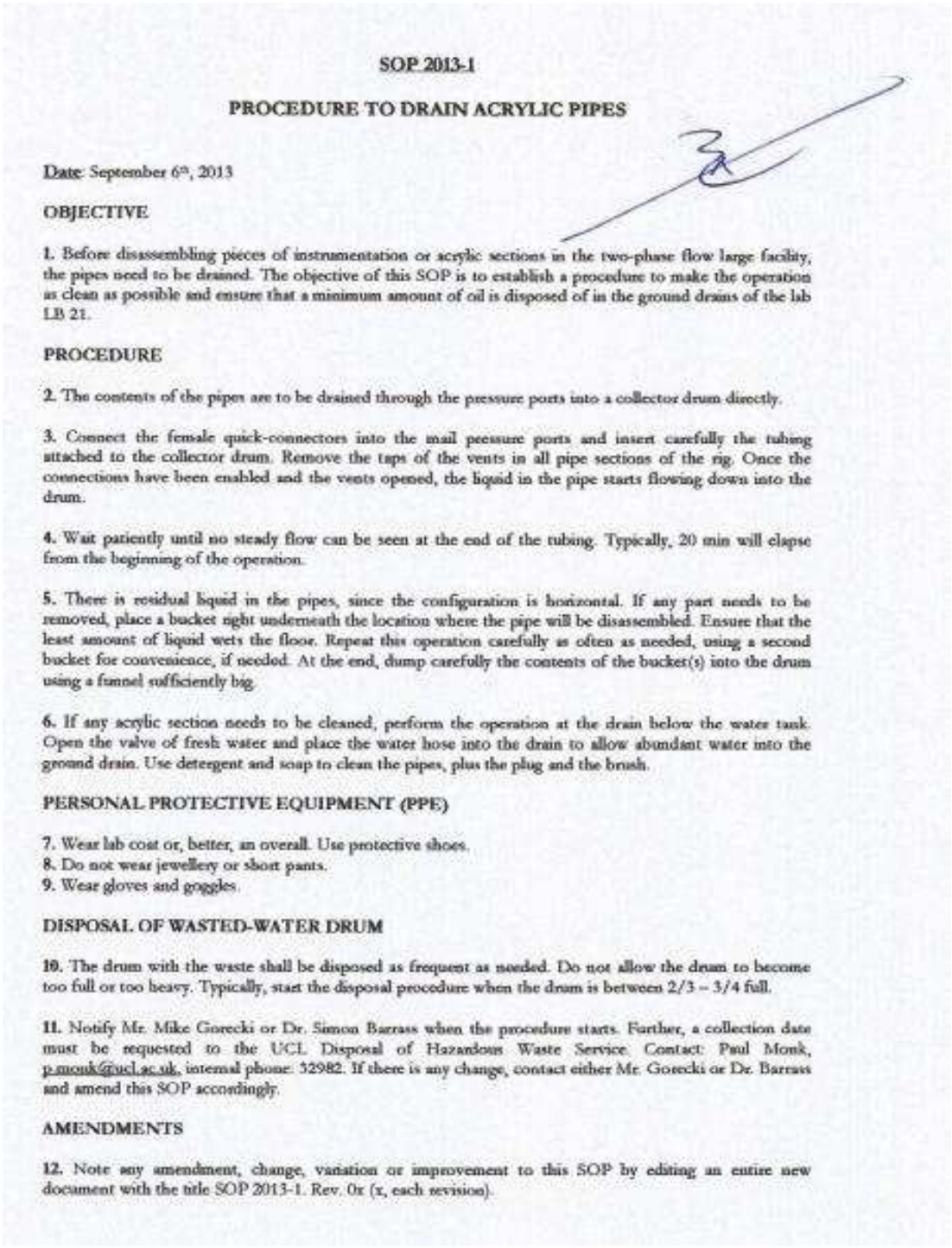

SOP 2013-1

PROCEDURE TO DRAIN ACRYLIC PIPES

Date: September 6th, 2013

OBJECTIVE

1. Before disassembling pieces of instrumentation or acrylic sections in the two-phase flow large facility, the pipes need to be drained. The objective of this SOP is to establish a procedure to make the operation as clean as possible and ensure that a minimum amount of oil is disposed of in the ground drains of the lab LB 21.

PROCEDURE

2. The contents of the pipes are to be drained through the pressure ports into a collector drum directly.

3. Connect the female quick-connectors into the mail peessure ports and insert carefully the tubing attached to the collector drum. Remove the taps of the vents in all pipe sections of the rig. Once the connections have been enabled and the vents opened, the liquid in the pipe starts flowing down into the drum.

4. Wait patiently until no steady flow can be seen at the end of the tubing. Typically, 20 min will elapse from the beginning of the operation.

5. There is residual liquid in the pipes, since the configuration is horizontal. If any part needs to be removed, place a bucket right underneath the location where the pipe will be disassembled. Ensure that the least amount of liquid wets the floor. Repeat this operation carefully as often as needed, using a second bucket for convenience, if needed. At the end, dump carefully the contents of the bucket(s) into the drum using a funnel sufficiently big.

6. If any acrylic section needs to be cleaned, perform the operation at the drain below the water tank. Open the valve of fresh water and place the water hose into the drain to allow abundant water into the ground drain. Use detergent and soap to clean the pipes, plus the plug and the brush.

PERSONAL PROTECTIVE EQUIPMENT (PPE)

7. Wear lab coat or, better, an overall. Use protective shoes.
8. Do not wear jewellery or short pants.
9. Wear gloves and goggles.

DISPOSAL OF WASTED-WATER DRUM

10. The drum with the waste shall be disposed as frequent as needed. Do not allow the drum to become too full or too heavy. Typically, start the disposal procedure when the drum is between 2/3 – 3/4 full.

11. Notify Mr. Mike Gorecki or Dr. Simon Barrass when the procedure starts. Further, a collection date must be requested to the UCL Disposal of Hazardous Waste Service. Contact: Paul Monk, p.monk@ucl.ac.uk, internal phone: 52982. If there is any change, contact either Mr. Gorecki or Dr. Barrass and amend this SOP accordingly.

AMENDMENTS

12. Note any amendment, change, variation or improvement to this SOP by editing an entire new document with the title SOP 2013-1. Rev. 0x (x, each revision).

Fig. A1.2 Standard Operating Procedure to drain the pipes prior to cleaning

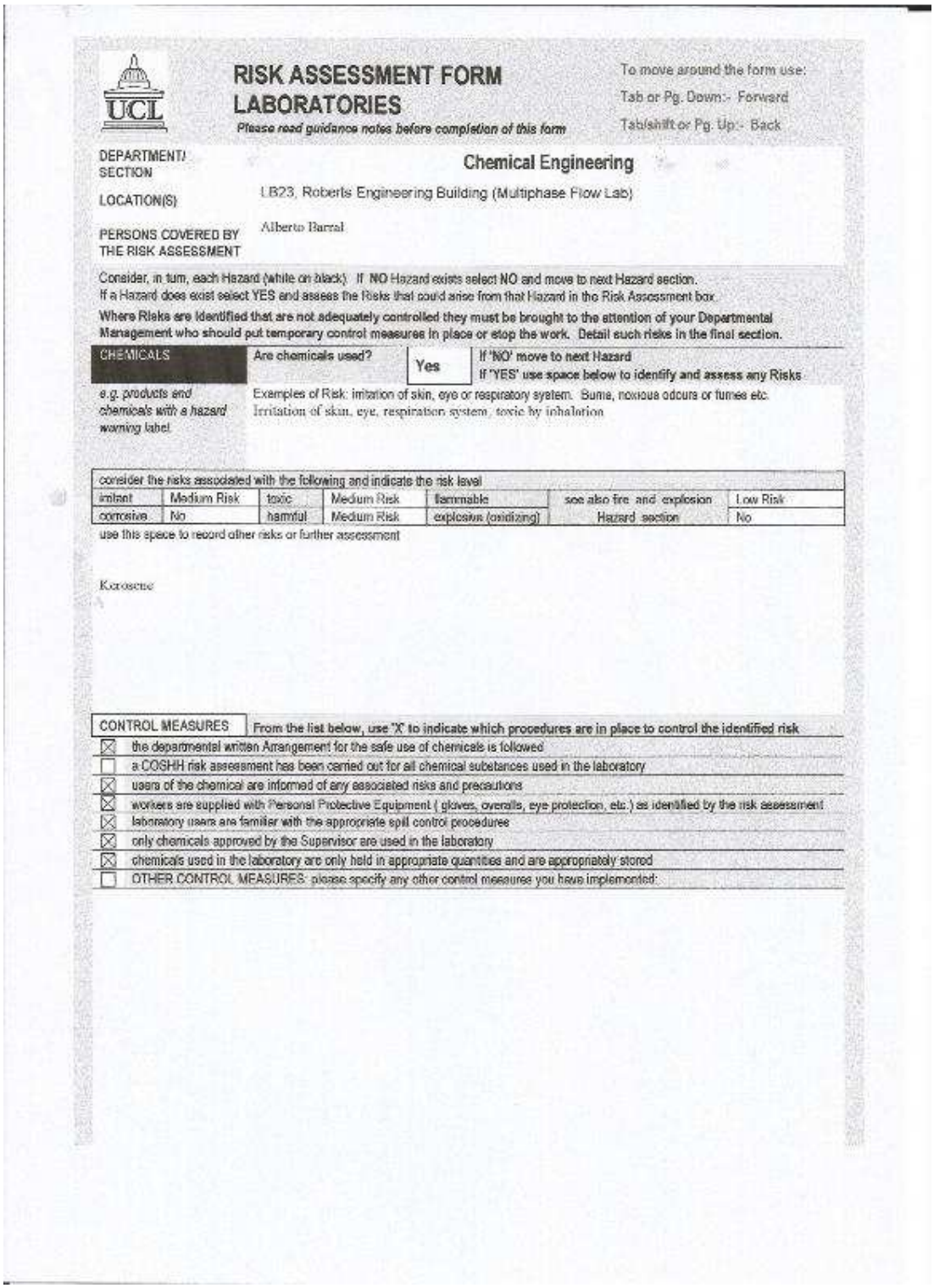

UCL

RISK ASSESSMENT FORM
LABORATORIES
Please read guidance notes before completion of this form

To move around the form use:
Tab or Pg. Down:- Forward
Tab/shift or Pg. Up:- Back

DEPARTMENT/ SECTION	Chemical Engineering
LOCATION(S)	LB23, Roberts Engineering Building (Multiphase Flow Lab)
PERSONS COVERED BY THE RISK ASSESSMENT	Alberto Barral

Consider, in turn, each Hazard (white on black). If NO Hazard exists select NO and move to next Hazard section.
If a Hazard does exist select YES and assess the Risks that could arise from that Hazard in the Risk Assessment box.
Where Risks are identified that are not adequately controlled they must be brought to the attention of your Departmental Management who should put temporary control measures in place or stop the work. Detail such risks in the final section.

CHEMICALS	Are chemicals used?	Yes	If 'NO' move to next Hazard If 'YES' use space below to identify and assess any Risks

e.g. products and chemicals with a hazard warning label

Examples of Risk: irritation of skin, eye or respiratory system. Burns, noxious odours or fumes etc.
Irritation of skin, eye, respiration system, toxic by inhalation

consider the risks associated with the following and indicate the risk level

irritant	Medium Risk	toxic	Medium Risk	flammable	see also fire and explosion	Low Risk
corrosive	No	harmful	Medium Risk	explosive (oxidizing)	Hazard section	No

use this space to record other risks or further assessment

Kerosene

CONTROL MEASURES	From the list below, use 'X' to indicate which procedures are in place to control the identified risk
☒	the departmental written Arrangement for the safe use of chemicals is followed
☐	a COSHH risk assessment has been carried out for all chemical substances used in the laboratory
☒	users of the chemical are informed of any associated risks and precautions
☒	workers are supplied with Personal Protective Equipment (gloves, overalls, eye protection, etc.) as identified by the risk assessment
☒	laboratory users are familiar with the appropriate spill control procedures
☒	only chemicals approved by the Supervisor are used in the laboratory
☒	chemicals used in the laboratory are only held in appropriate quantities and are appropriately stored
☐	OTHER CONTROL MEASURES: please specify any other control measures you have implemented:

Fig. A1.3 Oil-water flow facility risk assessment (first page)

A1.3 PARTICLE IMAGE VELOCIMETRY

Particle Image Velocimetry (PIV) is a relatively recent technology (i.e. 1980s) introduced to measure velocity vectors of the flow field. It is not a particle-tracking technique. Instead, velocity is computed from correlating the position of multiple particles within small interrogation areas in a pair of images. The position of seeding particles is determined by capturing the light scattered by the particles when illuminated by a double-pulse solid state laser (Sutton et al., 1983). Figure A1.4 shows a schematic drawing of the fundamentals of PIV measurement.

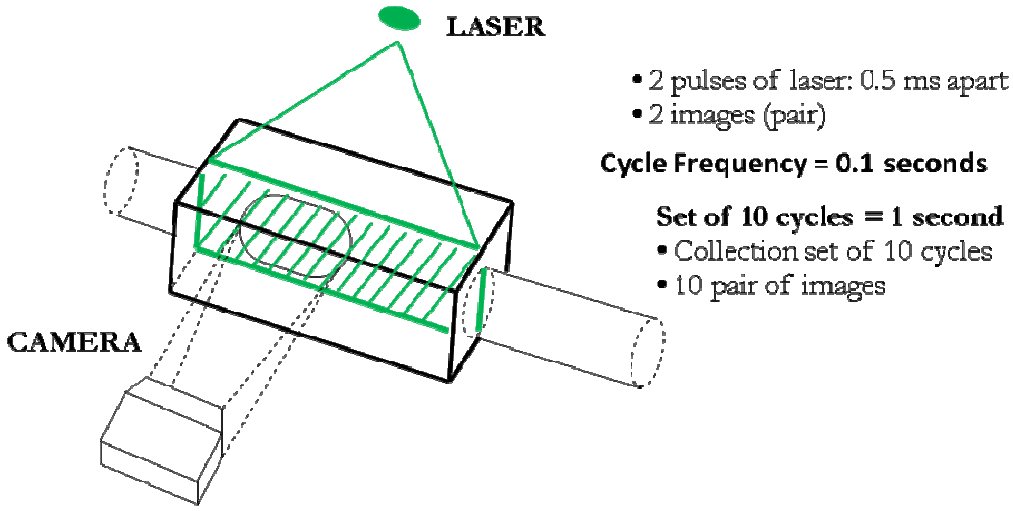

Figure A1.4 Schematic of PIV laser illumination of the flow field

The introduction and advances of digital recording techniques during the last 15 years have made possible the application of PIV to industrial research and processes. Raffel et al. (1998) gives in the preface a good example of the impressive developments of the last years. The time required to prepare an experiment in the mid 1980s, obtain quality photographs, process the film and evaluate one single image via optical techniques was nearly 1 week. Today, electronic cameras and powerful computers are readily available to researches via schemes of loans or collaboration. Several quality images of velocity fields can be captured per second on the spot. The generalized use of digital image analysis makes preliminary evaluations possible in a matter of seconds. Only the alignment of the laser or any calibration procedure needed take longer. However, once these operations are accomplished and the experimental facility is set-up, measurements can be collected immediately with only regular

checks needed. Enormous amounts of information can be treated in a reasonable time. The development of software and hardware in the last few years has been staggering, which has led to considerable improvements in a short amount of time, including memory capacity. There is a number of independent fields contributing to the advances of PIV, which implies that the overall advances of the technique are limited by the particular challenges pose by each of the fields that contribute (i.e. cameras and lenses, lasers, seeding particles, materials, etc.). In his review of PIV, Adrian (2005) outlined directions of current investigation.

The number of PIV applications has increased considerable from the aerospace applications to biology, combustion, mixing applications, two-phase flow and, recently, to micro-flows and micro-devices. In oil-water flows, apart from the papers of Kumara et al. (2009; 2010), the work is yet to be developed. During the course of the Thesis, work was initiated to investigate oil-water flows via Particle Image Velocimetry. The experimental frame was designed and installed and preliminary experiments were done in both single-phase water and oil-water flows. Velocity vectors were calculated. It was particularly interesting to attempt measurements near the pipe wall and at the oil-water interface. Good measurements are difficult to obtain at those locations, however, due to light reflections and the mismatch between refractive indices, which constitutes one of the challenges PIV in two-phase flows. The preliminary measurements of the velocity field in the water phase in oil-water flows were presented in the International Symposium on Multiphase Flow and Transport Phenomena, held in Agadir, Morocco in April 2012 via an oral communication. The paper has two parts: the first is dedicated to flow pattern observations and the work with conductance probes, while the second present PIV measurements. The information presented in the conference has been superseded and improved later on, but the paper is included in Appendix 6. It can be seen that 1) the concepts discussed in this Thesis developed slowly and, 2) that the preliminary efforts with PIV have served to start a valuable work in the future. Apart for the papers of Kumara et al. (2009; 2010; 2011), the PIV work with oil-water flows is almost inexistent. The flow structure and phase turbulence of oil-water flows is currently being investigated via PIV against the oil-water interface described in this Thesis (Chinaud et al., 2004).

For the initial experimentation, the PIV system used (TSI Instruments) was a loan from the UK EPSRC. It consisted of a double-head Nd:YAG lased (class 4; energy, 2 x 120 mJ; wavelength, λ = 532 nm; and repetition rate up to 15 Hz), pulse synchronizer, optical lenses and a CCD camera with 4 mega-pixels and 12-bit pixel resolution, everything controlled by the Insight™ 3D software. With the purpose of performing PIV experiments, a solid frame was designed and installed (parts were acquired from Thorlabs). The Chemical Engineering workshop prepared a metallic stand for the set-up. A photograph of the PIV system set at the inlet as used during experimentation can be seen in Figure A1.5.

A new test section was prepared for the purpose of being used at both the inlet and downstream locations. Measurements on the flow were performed through a view box made of acrylic material and surrounded the pipe, filled with glycerol. The use of the view box was to match the refractive index of the material. Kumara et al. (2010) estimated the deviation of the light beam due to refraction at the centre of the pipe. In order to fill the box with glycerol, a simple methodology was devised, involving the use of a small peristaltic pump and a heater plate, as to reduce the viscosity of the glycerol and make the filling as easy as possible.

The laser was located on top of the view box with the aid of a flexible arm, at a distance of about 50 cm (Figure A1.5). The laser generates a plane sheet of light, parallel to the axis of the flow through the top flat side of the view box. This is achieved by attaching two lenses at the end of the arm. The first one is spherical and yields a laser dot, while the second lens is cylindrical and produces the usual “fish-tail” sheet of light (Figure A1.4). The CCD camera was placed perpendicular to the laser in front of the illuminated area of the flow in order to collect the light scattered by the seeding particles (added to the water tank at the moment of starting the experimentation). The camera objective can be varied, but 60-mm and 120-mm ones were used.

Seeding particles must be selected in accordance to the fluid of study. Since the properties of oil and water are different (i.e. density and viscosity), it is likely that the same type of particle cannot be used in both cases. During the tests, glass bead-hollow, silver-coated particles with a mean size of 10 μm and specific gravity 1.03 were used (Potters Industrial Inc.). Only the water phase could be successfully seeded.

The use of these particles in the water phase seems appropriate, since the calculate Stokes number is of the order of 10^{-3} ms^{-1} (Raffel et al., 2007), which is significantly smaller than the velocity of the flows investigated (of the order of 1 ms^{-1}). Therefore, particles were expected to follow the flow faithfully.

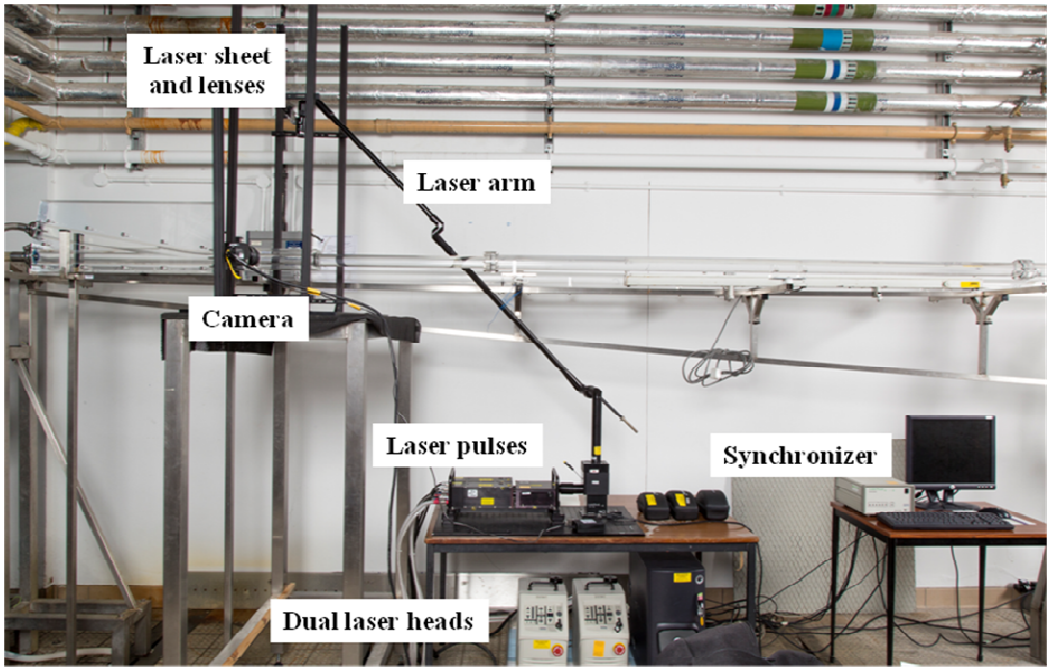

Figure A1.5 PIV experimental set-up at the oil-water inlet section

A1.4 DOCUMENTATION

The following documentation is included below: 1) Typical specifications of the oil; 2) hydraulic datasheet of the pumps; and 3) PIV Standard Operating Procedure.

Specification

Multisol Limited
Huntsman Drive
Northbank Industrial Park, Irlam
Greater Manchester, M44 5EG
Main: +44 (0)161 775 1622
Fax: +44 (0)161 777 9345
Email: sales@multisolgroup.com
Web: www.multisolgroup.com

Multisol Group

PRINTED DATE : 19/01/11
ISSUE DATE : 06/01/11
PRODUCT 124 D140

Properties	Units	Min.	Max	Typical Values	Test Methods
* Distillation Range Initial	Deg C	272	-	279	ASTM D86
Distillation Range 50%	Deg C	-	-	294	ASTM D86
* Distillation Range Dry	Deg C	310	-	313	ASTM D86
Distillation Range Final	Deg C	-	320	314	ASTM D86
* Flash Point Pensky	Deg C	129	-	137	ASTM D93
Aromatic Content	wt%	-	1.5	1.1	UV1
* Colour Saybolt	-	+30	-	+30	ASTM D6045
Aniline Point	Deg C	-	-	86	ASTM D611
Benzene Content	mg/kg	-	5	<3	GC2
* Density @ 15°C	kg/dm3	-	-	0.836	ISO 12185
Refractive Index @ 20 Deg C	-	-	-	1.459	ASTM D1218
Viscosity @ 25 Deg C	mm2/s	-	-	6.8	ASTM D7042
Viscosity @ 40 Deg C	mm2/s	3.5	5.0	4.58	ASTM D445
* FTIR	%	99.5	-	-	QCM 09
* Appearance	-	Clear bright liquid		CBL	QCM 01

* Quoted on Certificate of Analysis
Controlled Minor variations of published ASTM methods may be applied, and other suitable elemental test methods may sometimes be used

This specification will be automatically updated to accomodate changes. A revised issue will be sent to customers who have received this copy within the last 12 months or who have dealt commercially within the last 12 months against this specification.

Welsh House, 83 Welsh Row, Nantwich, Cheshire, CW5 5ET
Tel No: (01270)610444 Fax No: (01270) 610555 E-mail:sales@multisolgroup.com Website:www.multisolgroup.com

Figure A1.6 Typical Exxsol D140 oil specifications

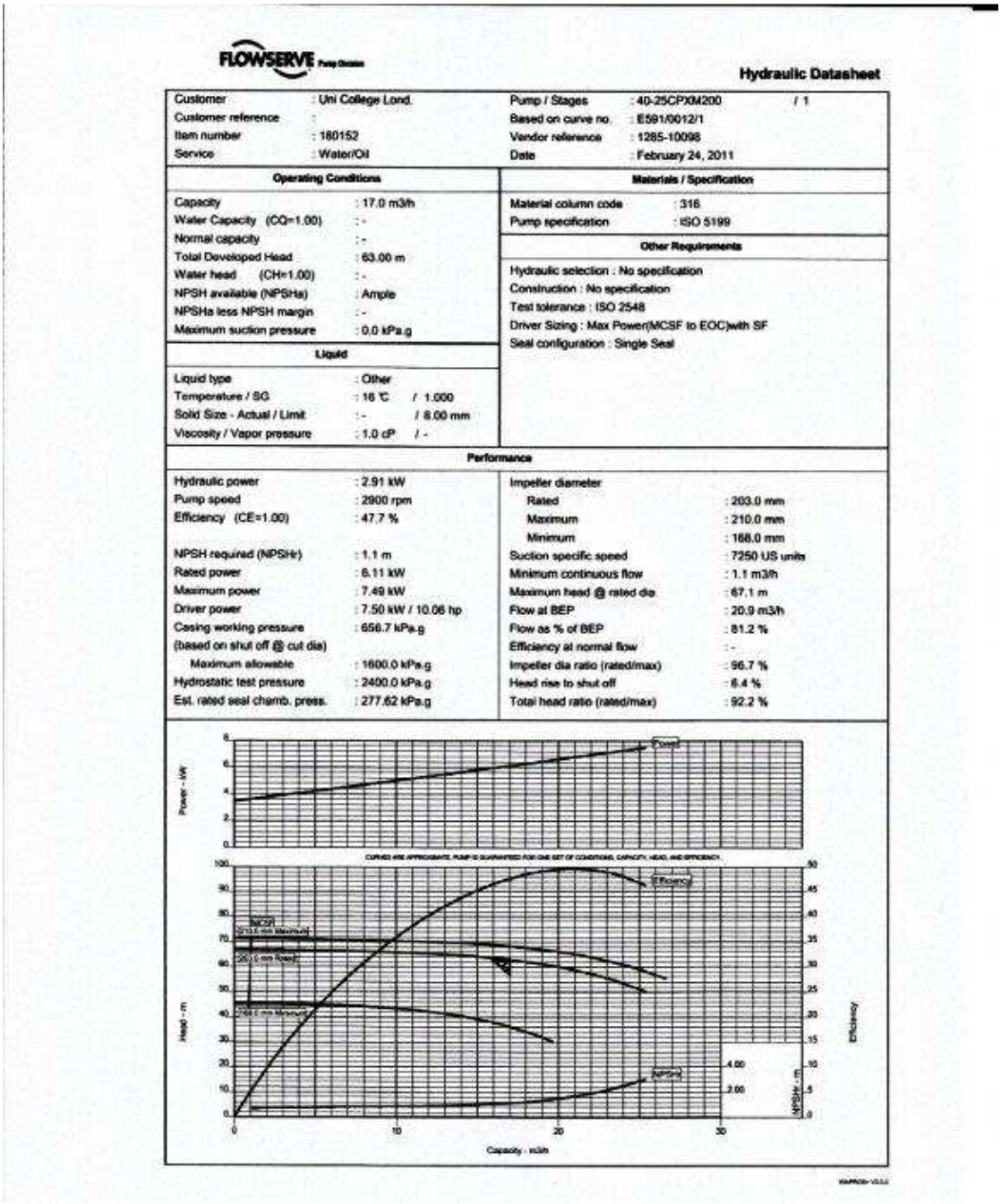

FLOWSERVE Pump Division

Hydraulic Datasheet

Customer	: Uni College Lond.	Pump / Stages	: 40-25CPXM200	/ 1
Customer reference	:	Based on curve no.	: E591/0012/1	
Item number	: 180152	Vendor reference	: 1285-10098	
Service	: Water/Oil	Date	: February 24, 2011	

Operating Conditions

Capacity	: 17.0 m3/h
Water Capacity (CQ=1.00)	: -
Normal capacity	: -
Total Developed Head	: 63.00 m
Water head (CH=1.00)	: -
NPSH available (NPSHa)	: Ample
NPSHa less NPSH margin	: -
Maximum suction pressure	: 0.0 kPa.g

Liquid

Liquid type	: Other	
Temperature / SG	: 16 °C	/ 1.000
Solid Size - Actual / Limit	: -	/ 8.00 mm
Viscosity / Vapor pressure	: 1.0 cP	/ -

Materials / Specification

Material column code	: 316
Pump specification	: ISO 5199

Other Requirements

Hydraulic selection : No specification
Construction : No specification
Test tolerance : ISO 2548
Driver Sizing : Max Power(MCSF to EOC)with SF
Seal configuration : Single Seal

Performance

Hydraulic power	: 2.91 kW	Impeller diameter	
Pump speed	: 2900 rpm	Rated	: 203.0 mm
Efficiency (CE=1.00)	: 47.7 %	Maximum	: 210.0 mm
		Minimum	: 168.0 mm
NPSH required (NPSHr)	: 1.1 m	Suction specific speed	: 7250 US units
Rated power	: 6.11 kW	Minimum continuous flow	: 1.1 m3/h
Maximum power	: 7.49 kW	Maximum head @ rated dia	: 67.1 m
Driver power	: 7.50 kW / 10.06 hp	Flow at BEP	: 20.9 m3/h
Casing working pressure	: 656.7 kPa.g	Flow as % of BEP	: 81.2 %
(based on shut off @ cut dia)		Efficiency at normal flow	: -
Maximum allowable	: 1600.0 kPa.g	Impeller dia ratio (rated/max)	: 96.7 %
Hydrostatic test pressure	: 2400.0 kPa.g	Head rise to shut off	: 6.4 %
Est. rated seal chamb. press.	: 277.62 kPa.g	Total head ratio (rated/max)	: 92.2 %

Fig. A1.7 Pump hydrolic datasheet

SOP Standard Operating Procedure

IMPLEMENTATION OF SAFETY MEASURES IN USING THE EPSRC PIV SYSTEM IN LB21

Roberts Building
Chemical Engineering, UCL

1. **Scope and General Indications**

This SOP regulates the safety measures that must be followed any time the TSI Class 4 Laser and the TSI High Speed PIV system installed are used. It also accounts for all safety features in place.

A copy of the specifications of the Laser as well as manufacturer or supplier recommendations for use shall be attached to this SOP.

The Laser and the PIV shall only be used when properly enclosed in a suitable and covered frame. All metallic parts within the enclosure, when possible or appropriate, should be painted in black. During normal operation the beam will exiting the delivery arm is dispersed by a fishtail lens.

The handle of the laser as well as of the camera shall be easy and at no risk of the user when performing certain operations, such as the alignment. Further instructions are in this SOP.

The Laser and the PIV system must be used only by the authorized personnel who have been trained in the use of the laser by the supplier, namely Alberto Hernandez Barral and Dimitrios Tsaoulidis. When not in use the laser activation keys will be kept in a secure location.

The user of the Laser and PIV is allowed only for the following tasks, as those for which the equipment shall be used:

1. Alignment of the beam within the flexible arm.
2. Positioning of the beam delivery arm and alignment of the camera.
3. Use of Software to collect, save, process and transfer data.

Any technical issues or concerns shall be addressed to TSI personnel, namely Mr. Martin Hyde. It is forbidden to remove the flexible arm or perform any other task apart from the ones stated in this SOP.

When operating the Laser, warning signs shall be in place outside LB21 and the doors shall be locked. Switches connected to the laser shall be implemented which disable the laser when the lab doors are opened.

Fig. A1.8 PIV Standard Operating Procedure (page 1 / 3)

SOP Standard Operating Procedure (Cont.)

IMPLEMENTATION OF SAFETY MEASURES IN USING THE EPSRC PIV SYSTEM IN LB21

Roberts Building
Chemical Engineering, UCL

2. **Procedure to Switch on the Equipment**

1) Ensure that all parts and pieces of the system are in place and properly installed.
2) Turn signs on lab doors to 'Laser On' and lock doors.
2) Switch ON the mains power.
3) Switch ON the computer.
4) Switch ON the synchronizer.
5) Switch ON the Laser sources by performing, in the following order:
    a) Turn on the main key
    b) Press the button to switch on the source
    c) Verify that the information displayed by the Laser sources is correct. Ensure that the level of intensity (voltage) is low.
7) Switch ON the camera, by connecting the mains to the feeder.
8) Ensure that both Q-switch delays are at low level in the software (output power equivalent to class 1 laser)
9) Switch on the laser in the software.
10) Open the shutter at the base of the flexible arm.
6) Open the shutter of the lenses at the point of use.
11) Increase slowly the intensity of both sources (voltage) until the Laser is just visible.

3. **Alignment of Beam Within the Flexible Arm**

1) Before switching on the laser, remove the two divergent lenses at the delivery end of the flexible arm (cylindrical and spherical, assembly lenses), in order to visualize a dot of Laser.
2) Switch ON the laser at low level as described above.
3) Align the beam in the arm using the suitable tool provided by the supplier. Turn the tool clock or anti-clockwise as needed, until the beam appears as a single dot (not a line).
4) Switch OFF the Laser in the software, close the shutters, and replace the lenses.

4. **Positioning of the beam delivery arm of use and alignment of the camera**

1) Switch ON the Laser at low power as described above.
2) Put on laser safety goggles
3) Increase the laser power until an image from the camera can be seen on the computer monitor.
3) If necessary, adjust camera position and focus while wearing goggles and gloves.
4) After the alignment is concluded, fully close the curtains around the laser and camera.
5) Increase as needed the level of radiation, but at no risk of saturation or damage for the camera during the operation.

Fig. A1.8 PIV Standard Operating Procedure (page 2 / 3)

SOP Standard Operating Procedure (End)

IMPLEMENTATION OF SAFETY MEASURES IN USING THE EPSRC PIV SYSTEM IN LB21

Roberts Building
Chemical Engineering, UCL

5. **Shut down the Laser**

1) Switch OFF the Laser sources (computer controlled).
2) Switch OFF the Laser sources (press button on sources panel).
3) Switch OFF the Key of Laser sources.
4) Switch OFF the synchronizer.
5) Switch OFF the computer.
6) Switch OFF the camera, by unplugging the mains from the feeder.
7) Switch OFF the mains power.
8) Remove keys from laser power supplies.
9) Unlock doors to lab and change signs to show it is safe to enter.

6. **Emergency Shutdown**

1) Press the emergency stop buttons on the two laser power supplies.

7. **Summary of safety levels**

Per this SOP, there are different levels of security when using the Laser and the attached PIV equipment that shall be in place and operative at any time.

Level 1: Laser beam is contained within a black heavy fabric enclosure.
Level 2: Door switches.
Level 3: Safety stop buttons to quench readily the Laser sources.
Level 4: Keys are required to operate the Laser sources.
Level 5: Laser filters and shutters at the exit of sources and at the point of use.
Level 6: Safe, remote operation control via the computer.
Level 7: The intensity of the Laser is controlled during the alignment and the operation of the Laser.
Level 8: Wear safety goggles.

Written by: Alberto H. Barral 11 May 2011

Reviewed by:

Approved by:

Fig. A1.8 PIV Standard Operating Procedure (page 3 / 3)

APPENDIX 2
CONDUCTANCE PROBE CALIBRATION

A2.1 INTRODUCTION

Parallel-wire conductance probes were used in this investigation to measure the height of the oil-water interface and its variation over time. The signal collected with the probes was converted to the height interface via a calibration curve. The link between the signal of the probe and height interface (i.e. calibration) could be performed using water and oil, but it was found that this approach posed practical difficulties. Added to the operational inconvenience of handling oil, it was difficult to achieve a complete flat interface due to wettability issues between the oil and the water in the test section. Using the fact that the oil is not conductive compared to the water used in the experimentation, a calibration procedure involving only water (and air) was found more appropriate and quite convenient.

The calibration method presented is an off-line one. Some authors followed on-line methods (e.g. Al-Wahaibi, 2006; 2011). In the experience gathered in the laboratory, however, the off-line calibration seems simpler and convenient, since on-line procedures are conditioned to the flow pattern developed in the pipe and can be cumbersome or time-consuming from a practical point of view. The off-line calibration has proved to be a clean, fast and straightforward method.

It is worth to note that the electronics box that carries the input signal to the probes can be designed in different ways. The box used in this research was tuned specifically to return a linear response. At early stages in the research, while using a different box, a phenomenon of signal saturation was observed in the measurements collected (i.e. the signal value froze at certain heights and stop responding to changes in the water content). It turned out that such box configuration was properly used in

the study of phase-inversion transition in dispersed flows, for which a sharp and unique change in the signal was needed, rather than a linear response.

A2.2 CALIBRATION PROCEDURE

A.2.2.1 Procedure and results

Figure A2.1 shows a photograph of the off-line experimental set prepared to calibrate the conductance probe. The test section can be rotated to be conveniently emptied or filled with water or to achieve a horizontal position in order to collect the signal. Two blind flanges of stainless steel could be clamped to the test section as to enclose the volume inside.

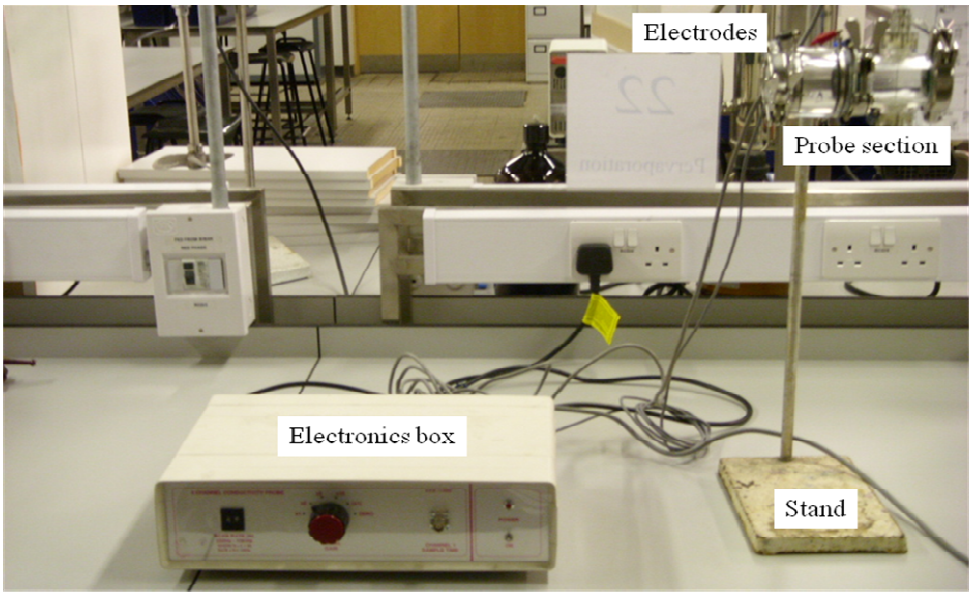

Figure A2.1 Experimental calibration set-up

At the beginning of each calibration, the section was completely filled with water using a graduate cylinder and measuring the volume inside by difference (i.e. V_{total} = 83 mL). Placing the section in horizontal position, the signal collected with the probes at 256 Hz during 60 s, treated and de-trended, provided the value of 100 % or full, single-phase water. Further, for each calibration point **i,** the section was consecutively filled with an increasing volume of water, as to have different values of the water fraction:

$$\alpha_w = \frac{V_i}{V_{total}}, \qquad \text{(A2.1)}$$

where V_i is the volume of each calibration point and V_{total} is the volume of the test section as measured. The signal collected in each case at 256 Hz during 60 s, was treated and averaged. In this way, a record of experimental water fractions and corresponding signals was obtained. The relationship between the water fraction, α_w, and the interface height, h_i, in a cylindrical geometry is reproduced here for convenience (Brauner and Moalem Maron, 1989), where D is the diameter of the pipe and h_i is the interface height:

$$\alpha_w = \frac{1}{\pi}\left[\pi - \arccos\left(2\frac{h_i}{D}-1\right) + \left(2\frac{h_i}{D}-1\right)\left(\left(1-\left(2\frac{h_i}{D}-1\right)^2\right)^{\frac{1}{2}}\right)\right] \qquad \text{(A2.2)}$$

An interpolation table linking water fractions and the interface height via Equation A2.2 was developed, since Equation A2.2 seems insoluble for h_i analytically. The table allow quickly converting water fraction to interface height, and is included in the following section. Finally, the calibration curved was a plot of the interface height against the treated signal of the probe.

Although some authors have reported issues with the measured signal over time (Ng, 2002) or found the data to fit a second-order polynomial (Al-Wahaibi, 2011), the calibration procedure described led to a straight line, reproducible at all times. Figure A2.2 shows the typical calibration line obtained for different conductance probes. The slope is higher for the 2-mm parallel probe and, as such, this instrument seems more sensitive to interface height variations.

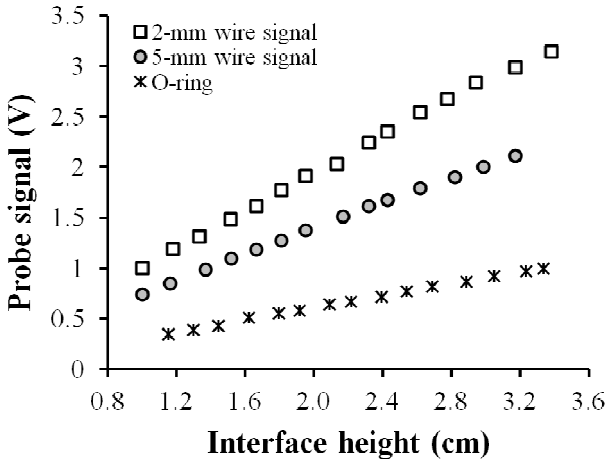

Figure A2.2 Typical calibration lines for different conductance probes

A.2.2.2 Uncertainty analysis

The uncertainty of the values of interface height read using the calibration curve is a combination of the experimental uncertainty of the calibration procedure, the uncertainty of the signal given by the instrument and the uncertainty introduced by the calibration curve. It is assumed that the interpolation table does not introduce any significant uncertainty at this stage, since the accuracy of the values is larger than that of the experimental measurements. The graduated cylinders used allow reading down to 1 mL, thus an uncertainty for the instrument of ± 0.5 mL can be taken. The measurement of the section volume was done by difference of two readings, x_1 and x_2. The absolute uncertainty of the measurements, ω_{Vtotal}, is:

$$\omega_{Vtotal} = \left[\left(\frac{\partial Meas}{\partial x_1} \omega_{x_1} \right)^2 + \left(\frac{\partial Meas}{\partial x_2} \omega_{x_2} \right)^2 \right]^{\frac{1}{2}}, \qquad \text{(A2.3)}$$

where ω_{x1} ω_{x2} are the uncertainties of each reading, respectively. Solving Equation A2.3, the absolute uncertainty of the measurement becomes ± 0.707 mL, and the relative, ε_{Vtotal} = ± 0.85 %. Each individual measurement of water volume has absolute and relative uncertainties ω_{Vi} = ± 0.5 mL and ε_{Vi} = ± 1.25 %, respectively, taking the nominal case of a 40 mL measurement (i.e. α_w = 0.5).

The propagation of error when Equation A2.1 is applied produces an overall uncertainty of the experimental procedure, ε_{ex}:

$$\omega_{ex} = \left[\left(\frac{\partial \alpha_w}{\partial V_i} \omega_{V_i} \right)^2 + \left(\frac{\partial \alpha_w}{\partial V_{total}} \omega_{V total} \right)^2 \right]^{\frac{1}{2}} = \ldots = 0.009 \qquad \text{(A2.4)}$$

This result gives a relative uncertainty $\varepsilon_{ex} = \pm 1.8$ % for the nominal $\alpha_w = 0.5$.

Figure A2.3 shows the uncertainty of the signal when collecting data from the conductance probes. Results are typical of any other calibration curve. As expected, the error tends to increase significantly towards lower values of water fraction. For the purpose of uncertainty analysis, the error at intermediate values of the water fractions can be considered, i.e. $\varepsilon_s = 0.7$ %.

25-Aug
Channel 2
Parallel Wire, 2 mm
V = 83 mL

		Temp, C		Signal		
Alpha	hi, cm	Before	After	Average	STD	Rel Error, %
0.084	**0.528**	21.5	21.5	0.56	0.02	3.2
0.145	**0.770**	22	21.8	0.86	0.05	5.5
0.211	**1.002**	21.6	21.5	1	0.02	1.6
0.265	**1.181**	21.6**		1.19	0.02	1.4
0.313	**1.333**	21.4	21.5	1.31	0.02	1.3
0.373	**1.517**	21.5**		1.48	0.02	1.1
0.422	**1.666**	21.3	21.3	1.61	0.02	1.0
0.47	**1.809**	21.5	21.3	1.77	0.02	0.9
0.518	**1.954**	21.5	21.5	1.91	0.02	0.8
0.578	**2.134**	21.5	21.5	2.03	0.02	0.8
0.639	**2.318**	21.5	21.5	2.24	0.02	0.7
0.675	**2.429**	21.5	21.5	2.35	0.02	0.7
0.735	**2.619** **		21.5	2.54	0.02	0.6
0.783	**2.777**	21.5	21.5	2.67	0.02	0.6
0.831	**2.943**	21.5	21.5	2.83	0.02	0.6
0.892	**3.173**	21.5	21.5	2.98	0.02	0.5
0.94	**3.382** **	**		3.14	0.02	0.5
1	**3.800** **	**		3.51	0.01	0.4

Figure A2.3 Uncertainty of the probe signal

Finally, the error when the calibration curve is applied must be estimated. Figure A2.4 shows the uncertainty found when the calibration curve was used to estimate the interface height from the experimental probe signal. At nominal values, the uncertainty can be taken as ε_c = 1.3 %. Notice, however, that the error is above 2 % at the 100 % water or single phase point. This error was considered when estimating the uncertainty introduced by the correction factors.

25-Aug
Channel 2
Parallel Wire, 2 mm
V = 83 mL

		Interface height (cm)		
Alpha	Signal	Experimental	Calibration	Error, %
0.084	0.56	0.528	0.501	5.1
0.145	0.86	0.770	0.829	7.6
0.211	1	1.002	0.981	2.0
0.265	1.19	1.181	1.189	0.6
0.313	1.31	1.333	1.320	1.0
0.373	1.48	1.517	1.505	0.8
0.422	1.61	1.666	1.647	1.1
0.47	1.77	1.809	1.822	0.7
0.518	1.91	1.954	1.975	1.1
0.578	2.03	2.134	2.106	1.3
0.639	2.24	2.318	2.335	0.7
0.675	2.35	2.429	2.455	1.1
0.735	2.54	2.619	2.662	1.7
0.783	2.67	2.777	2.804	1.0
0.831	2.83	2.943	2.979	1.2
0.892	2.98	3.173	3.142	1.0
0.94	3.14	3.382	3.317	1.9
1	3.51	3.800	3.721	2.1

Figure A2.4 Error introduced by the calibration curve

Considering that the three error contributions are independent from each other, an overall uncertainty can be estimated for the entire calibration process:

$$\varepsilon_{\text{calibration}} = \left(\varepsilon_{ex}^2 + \varepsilon_s^2 + \varepsilon_c^2\right)^{\frac{1}{2}} \cong 2.4\% \qquad \text{(A2.5)}$$

This uncertainty affects all experimental data before analysis.

A2.3 DOCUMENTS AND RECORDS

A summary of calibrations performed over time is given in Tables A2.1 and A2.2. The calibrations were performed following a routine procedure and any observations were carefully reported. The laboratory forms of three different calibrations of the 2-mm probe performed at different times are presented in Figures A2.5 – A2.7. The water fraction – interface height interpolation table calculated from Equation A2.2 is given in Table A2.3 (1.6 cm – 2.2 cm interface height).

Table A2.1 Sumnmary of 2-mm conductance probes calibrations*

Date	Regression line	Coefficient, r^2
25-August-2011	h_i (cm) = 1.0915 Signal (V) – 0.1101	0.9980
2-July-2012**	h_i (cm) = 1.466 Signal (V) – 0.0730	0.9942
2-July-2012	h_i (cm) = 1.0847 Signal (V) – 0.1748	0.9976
20-September 2012	h_i (cm) = 0.9636 Signal (V) + 0.2198	0.9997
28-November-2012	h_i (cm) = 1.0987 Signal (V) – 0.3168	0.9955
26-February-2013	h_i (cm) = 0.8348 Signal (V) – 0.2404	0.9985

Table A2.2 Sumnmary of 5-mm conductance probes calibrations*

Date	Regression line	Coefficient, r^2
25-August-2011	h_i (cm) = 1.5793 Signal (V) – 0.1925	0.9990
26-February-2013	h_i (cm) = 1.2712 Signal (V) – 0.1306	0.9972

* All calibrations refer to the same 2-mm or 5-mm probe.

** A second 2-mm probe was calibrated with the purpose of investigating the interface both at the inlet and downstream the pipe on the 2nd of July of 2012. However, this particular probe was found faulty and was discarded. In the future, the 5-mm probe was used.

CALIBRATION OF PROBES
DATA SHEET

Date of Calibration: **28 November 2012** → C-03-11-12
Instrument: **E4096**
Sampling Frequency: **256 Hz**

PROBE: O-Ring ☐ 5-mm Wire ☐ 2-mm Wire ☒

Verify connections:

O-Ring	Channel 1	☐
5-mm Wire	Channel 2	☐
2-mm Wire	Channel 2	☒

Volume of Test Section: **V = 85 mL**

α theoretical	Vw to add mL, α*Vw	Temperature	Actual Vw mL	Actual α	Comments
0.008	**	21 – 23 °C	**		
0.15	12.75		12.5	**0.147**	
0.20	17		17	**0.200**	
0.25	21.25		21	**0.247**	
0.30	25.5		25	**0.294**	
0.35	29.75		29	**0.341**	
0.40	34		34	**0.400**	
0.45	38.25		38	**0.447**	
0.50	42.5		42	**0.494**	
0.55	46.75		47	**0.553**	
0.60	51.0		51	**0.600**	
0.65	55.25		55	**0.647**	
0.70	59.5		60	**0.706**	
0.75	63.75		63	**0.741**	
0.80	68		68	**0.800**	
0.85	**		**	**	
0.90	**		**	**	
0.92	**		**	**	
0.94	**		**	**	
0.96	**		**	**	
1.00	85		85	**1.00**	

Signature & Date:

Figure A2.5 Calibration datasheet (November 2012)

CALIBRATION OF PROBES
DATA SHEET

Date of Calibration: September 20th 2012 → C-02-09-12

Instrument: E4096

Frequency of AC

N =

Frequency = N * 125 hz = 256Hz

Gain =

PROBE: O-Ring ☐ 5-mm Wire ☐ 2-mm Wire ☒

Verify Connections:

O-Ring	Channel 1	Grey cable ☐
5-mm Wire	Channel 2	Black cable ☐
2-mm Wire	Channel 2	Black cable ☐ N/A

22–23°C

Volume of Test Section, V = 87 mL

α theoretical	Vw to add* mL	Temperature, C Before	After	Vw actual mL	α actual	Comments
0.008	6.96			7.5	0.086	
0.15	13.05			12.5	0.144	
0.20	17.40			18.5	0.213	
0.25	21.75			21.5	0.247	
0.30	26.10			27.0	0.310	
0.35	30.45			31.0	0.356	
0.40	34.80			35.0	0.402	
0.45	39.15			41.0	0.471	
0.50	43.50			44.0	0.506	
0.55	47.85			47.0	0.540	
0.60	52.20			53.0	0.609	
0.65	56.55			57.0	0.655	
0.70	60.90			60.0	0.690	
0.75	65.25			64.0	0.736	
0.80	69.60			71.0	0.816	
0.85	73.95			75.0	0.862	
0.90	78.30			79.0	0.908	
0.92	80.04					
0.94	81.78					
0.96	83.52					
1.00	87.00			87.0	1.000	

* These values are based on an 87-mL test section. They can be used for the purpose of acquiring data, but the actual volume must be measure and use in the calculations.

** The signal values shall be collected with the computer and saved electronically.

Figure A2.6 Calibration datasheet (September 2012)

CALIBRATION OF PROBES
DATA SHEET

Date of Calibration: August 25, 2011 — C-01-08-11

Instrument: E4096

PROBE: O-Ring ☐ 5-mm Wire ☐ 2-mm Wire ☒

Verify Connections:

O-Ring	Channel 1	☐
5-mm Wire	Channel 2	☐
2-mm Wire	Channel 2	☒

Volume of Test Section, V = 83 mL
Name and location of all electronic files with data =

α Theoretical	V_w to add* (mL)	Temperature (C) Before	After	Actual V_w (mL)	Actual α	Comments
0.008	6.96	21.5	21.5	7.0	0.084	
0.15	13.05	22.0	21.8	12.0	0.145	
0.20	17.40	21.6	21.5	17.5	0.211	
0.25	21.75	21.6	–	22.0	0.265	
0.30	26.10	21.4	21.5	26.0	0.313	
0.35	30.45	21.5	–	31.0	0.373	
0.40	34.80	21.3	21.3	35.0	0.422	
0.45	39.15	21.5	21.3	39.0	0.470	
0.50	43.50	21.5	21.5	43.0	0.518	
0.55	47.85	21.5	21.5	48.0	0.578	
0.60	52.20	21.5	21.5	53.0	0.639	
0.65	56.55	21.5	21.5	56.0	0.675	
0.70	60.90	–	21.5	61.0	0.735	
0.75	65.25	21.5	21.5	65.0	0.783	
0.80	69.60	21.5	21.5	69.0	0.831	
0.85	73.95	21.5	21.5	74.0	0.892	
0.90	78.30	21.5	–	78.0	0.940	
0.92	80.04	–	–	–	–	Bubble formation
0.94	81.78	–	–	–	–	
0.96	83.52	–	–	–	–	
1.00	87.00	–	–	83.0	1.000	

* These values are based on an 87-mL test section. They can be used for the purpose of acquiring data, but the actual volume must be measure and use in the calculations.

** The signal values shall be collected with the computer and saved electronically.

Figure A2.7 Calibration datasheet (August 2011)

Table A2.3 Interface height – water fraction (1.60 cm – 1.75 cm)

hi, cm	Wat. Fraction	hi, cm	Wat. Fraction	hi, cm	Wat. Fraction	hi, cm	Wat. Fraction
1.596	0.399	**1.634**	0.411	**1.672**	0.424	**1.71**	0.436
1.597	0.399	1.635	0.411	1.673	0.424	1.711	0.436
1.598	0.400	1.636	0.412	1.674	0.425	1.712	0.437
1.599	0.400	1.637	0.412	1.675	0.425	1.713	0.437
1.6	0.400	1.638	0.412	1.676	0.425	1.714	0.437
1.601	0.401	1.639	0.413	1.677	0.426	1.715	0.438
1.602	0.401	1.64	0.413	1.678	0.426	1.716	0.438
1.603	0.401	1.641	0.413	1.679	0.426	1.717	0.438
1.604	0.402	1.642	0.414	1.68	0.427	1.718	0.439
1.605	0.402	1.643	0.414	1.681	0.427	1.719	0.439
1.606	0.402	1.644	0.414	1.682	0.427	1.72	0.439
1.607	0.402	1.645	0.415	1.683	0.427	1.721	0.440
1.608	0.403	1.646	0.415	1.684	0.428	1.722	0.440
1.609	0.403	1.647	0.415	1.685	0.428	1.723	0.440
1.61	0.403	1.648	0.416	1.686	0.428	1.724	0.441
1.611	0.404	1.649	0.416	1.687	0.429	1.725	0.441
1.612	0.404	1.65	0.416	1.688	0.429	1.726	0.441
1.613	0.404	1.651	0.417	1.689	0.429	1.727	0.442
1.614	0.405	1.652	0.417	1.69	0.430	1.728	0.442
1.615	0.405	1.653	0.418	1.691	0.430	1.729	0.443
1.616	0.405	1.654	0.418	1.692	0.430	1.73	0.443
1.617	0.406	1.655	0.418	1.693	0.431	1.731	0.443
1.618	0.406	1.656	0.419	1.694	0.431	1.732	0.444
1.619	0.406	1.657	0.419	1.695	0.431	1.733	0.444
1.62	0.407	1.658	0.419	1.696	0.432	1.734	0.444
1.621	0.407	1.659	0.420	1.697	0.432	1.735	0.445
1.622	0.407	1.66	0.420	1.698	0.432	1.736	0.445
1.623	0.408	1.661	0.420	1.699	0.433	1.737	0.445
1.624	0.408	1.662	0.421	1.7	0.433	1.738	0.446
1.625	0.408	1.663	0.421	1.701	0.433	1.739	0.446
1.626	0.408	1.664	0.421	1.702	0.433	1.74	0.446
1.627	0.409	1.665	0.422	1.703	0.434	1.741	0.447
1.628	0.409	1.666	0.422	1.704	0.434	1.742	0.447
1.629	0.409	1.667	0.422	1.705	0.434	1.743	0.447
1.63	0.410	1.668	0.423	1.706	0.435	1.744	0.448
1.631	0.410	1.669	0.423	1.707	0.435	1.745	0.448
1.632	0.410	1.67	0.423	1.708	0.435	1.746	0.448
1.633	0.411	1.671	0.424	1.709	0.436	1.747	0.449

Table A2.3 Interface height – water fraction (1.75 cm – 1.90 cm)

hi, cm	Wat. Fraction	hi, cm	Wat. Fraction	hi, cm	Wat. Fraction	hi, cm	Wat. Fraction
1.748	0.449	**1.786**	0.462	**1.824**	0.475	**1.862**	0.487
1.749	0.449	1.787	0.462	1.825	0.475	1.863	0.487
1.75	0.450	1.788	0.463	1.826	0.476	1.864	0.488
1.751	0.450	1.789	0.463	1.827	0.476	1.865	0.488
1.752	0.450	1.79	0.463	1.828	0.476	1.866	0.488
1.753	0.451	1.791	0.464	1.829	0.477	1.867	0.489
1.754	0.451	1.792	0.464	1.83	0.477	1.868	0.489
1.755	0.451	1.793	0.464	1.831	0.477	1.869	0.489
1.756	0.452	1.794	0.465	1.832	0.478	1.87	0.490
1.757	0.452	1.795	0.465	1.833	0.478	1.871	0.490
1.758	0.452	1.796	0.465	1.834	0.478	1.872	0.490
1.759	0.453	1.797	0.466	1.835	0.478	1.873	0.491
1.76	0.453	1.798	0.466	1.836	0.479	1.874	0.491
1.761	0.453	1.799	0.466	1.837	0.479	1.875	0.491
1.762	0.454	1.8	0.467	1.838	0.479	1.876	0.492
1.763	0.454	1.801	0.467	1.839	0.480	1.877	0.492
1.764	0.454	1.802	0.467	1.84	0.480	1.878	0.492
1.765	0.455	1.803	0.468	1.841	0.480	1.879	0.493
1.766	0.455	1.804	0.468	1.842	0.481	1.88	0.493
1.767	0.456	1.805	0.469	1.843	0.481	1.881	0.494
1.768	0.456	1.806	0.469	1.844	0.481	1.882	0.494
1.769	0.456	1.807	0.469	1.845	0.482	1.883	0.494
1.77	0.457	1.808	0.470	1.846	0.482	1.884	0.495
1.771	0.457	1.809	0.470	1.847	0.482	1.885	0.495
1.772	0.457	1.81	0.470	1.848	0.483	1.886	0.495
1.773	0.458	1.811	0.471	1.849	0.483	1.887	0.496
1.774	0.458	1.812	0.471	1.85	0.483	1.888	0.496
1.775	0.458	1.813	0.471	1.851	0.484	1.889	0.496
1.776	0.459	1.814	0.472	1.852	0.484	1.89	0.497
1.777	0.459	1.815	0.472	1.853	0.484	1.891	0.497
1.778	0.459	1.816	0.472	1.854	0.484	1.892	0.497
1.779	0.460	1.817	0.473	1.855	0.485	1.893	0.498
1.78	0.460	1.818	0.473	1.856	0.485	1.894	0.498
1.781	0.460	1.819	0.473	1.857	0.485	1.895	0.498
1.782	0.461	1.82	0.474	1.858	0.486	1.896	0.499
1.783	0.461	1.821	0.474	1.859	0.486	1.897	0.499
1.784	0.461	1.822	0.474	1.86	0.486	1.898	0.499
1.785	0.462	1.823	0.475	1.861	0.487	1.899	0.500

Table A2.3 Interface height – water fraction (1.90 cm – 2.05 cm)

hi, cm	Wat. Fraction	hi, cm	Wat. Fraction	hi, cm	Wat. Fraction	hi, cm	Wat. Fraction
1.9	0.5	**1.938**	0.513	**1.976**	0.525	**2.014**	0.538
1.901	0.500	1.939	0.513	1.977	0.525	2.015	0.538
1.902	0.501	1.94	0.514	1.978	0.526	2.016	0.539
1.903	0.501	1.941	0.514	1.979	0.526	2.017	0.539
1.904	0.501	1.942	0.514	1.98	0.526	2.018	0.539
1.905	0.502	1.943	0.515	1.981	0.527	2.019	0.540
1.906	0.502	1.944	0.515	1.982	0.527	2.02	0.540
1.907	0.502	1.945	0.515	1.983	0.527	2.021	0.540
1.908	0.503	1.946	0.516	1.984	0.528	2.022	0.541
1.909	0.503	1.947	0.516	1.985	0.528	2.023	0.541
1.91	0.503	1.948	0.516	1.986	0.528	2.024	0.541
1.911	0.504	1.949	0.516	1.987	0.529	2.025	0.542
1.912	0.504	1.95	0.517	1.988	0.529	2.026	0.542
1.913	0.504	1.951	0.517	1.989	0.529	2.027	0.542
1.914	0.505	1.952	0.517	1.99	0.530	2.028	0.543
1.915	0.505	1.953	0.518	1.991	0.530	2.029	0.543
1.916	0.505	1.954	0.518	1.992	0.530	2.03	0.543
1.917	0.506	1.955	0.518	1.993	0.531	2.031	0.544
1.918	0.506	1.956	0.519	1.994	0.531	2.032	0.544
1.919	0.507	1.957	0.519	1.995	0.532	2.033	0.545
1.92	0.507	1.958	0.519	1.996	0.532	2.034	0.545
1.921	0.507	1.959	0.520	1.997	0.532	2.035	0.545
1.922	0.508	1.96	0.520	1.998	0.533	2.036	0.546
1.923	0.508	1.961	0.520	1.999	0.533	2.037	0.546
1.924	0.508	1.962	0.521	2	0.533	2.038	0.546
1.925	0.509	1.963	0.521	2.001	0.534	2.039	0.547
1.926	0.509	1.964	0.521	2.002	0.534	2.04	0.547
1.927	0.509	1.965	0.522	2.003	0.534	2.041	0.547
1.928	0.510	1.966	0.522	2.004	0.535	2.042	0.548
1.929	0.510	1.967	0.522	2.005	0.535	2.043	0.548
1.93	0.510	1.968	0.522	2.006	0.535	2.044	0.548
1.931	0.511	1.969	0.523	2.007	0.536	2.045	0.549
1.932	0.511	1.97	0.523	2.008	0.536	2.046	0.549
1.933	0.511	1.971	0.523	2.009	0.536	2.047	0.549
1.934	0.512	1.972	0.524	2.01	0.537	2.048	0.550
1.935	0.512	1.973	0.524	2.011	0.537	2.049	0.550
1.936	0.512	1.974	0.524	2.012	0.537	2.05	0.550
1.937	0.513	1.975	0.525	2.013	0.538	2.051	0.551

Table A2.3 Interface height – water fraction (2.05 cm – 2.20 cm)

hi, cm	Wat. Fraction	hi, cm	Wat. Fraction	hi, cm	Wat. Fraction	hi, cm	Wat. Fraction
2.052	0.551	**2.09**	0.564	**2.128**	0.576	**2.166**	0.589
2.053	0.551	2.091	0.564	2.129	0.576	2.167	0.589
2.054	0.552	2.092	0.565	2.13	0.577	2.168	0.590
2.055	0.552	2.093	0.565	2.131	0.577	2.169	0.590
2.056	0.552	2.094	0.565	2.132	0.577	2.17	0.590
2.057	0.553	2.095	0.566	2.133	0.578	2.171	0.591
2.058	0.553	2.096	0.566	2.134	0.578	2.172	0.591
2.059	0.553	2.097	0.566	2.135	0.578	2.173	0.591
2.06	0.554	2.098	0.567	2.136	0.579	2.174	0.592
2.061	0.554	2.099	0.567	2.137	0.579	2.175	0.592
2.062	0.554	2.1	0.567	2.138	0.579	2.176	0.592
2.063	0.555	2.101	0.567	2.139	0.580	2.177	0.592
2.064	0.555	2.102	0.568	2.14	0.580	2.178	0.593
2.065	0.555	2.103	0.568	2.141	0.580	2.179	0.593
2.066	0.556	2.104	0.568	2.142	0.581	2.18	0.593
2.067	0.556	2.105	0.569	2.143	0.581	2.181	0.594
2.068	0.556	2.106	0.569	2.144	0.581	2.182	0.594
2.069	0.557	2.107	0.569	2.145	0.582	2.183	0.594
2.07	0.557	2.108	0.570	2.146	0.582	2.184	0.595
2.071	0.558	2.109	0.570	2.147	0.583	2.185	0.595
2.072	0.558	2.11	0.570	2.148	0.583	2.186	0.595
2.073	0.558	2.111	0.571	2.149	0.583	2.187	0.596
2.074	0.559	2.112	0.571	2.15	0.584	2.188	0.596
2.075	0.559	2.113	0.571	2.151	0.584	2.189	0.596
2.076	0.559	2.114	0.572	2.152	0.584	2.19	0.597
2.077	0.560	2.115	0.572	2.153	0.585	2.191	0.597
2.078	0.560	2.116	0.572	2.154	0.585	2.192	0.597
2.079	0.560	2.117	0.573	2.155	0.585	2.193	0.598
2.08	0.561	2.118	0.573	2.156	0.586	2.194	0.598
2.081	0.561	2.119	0.573	2.157	0.586	2.195	0.598
2.082	0.561	2.12	0.573	2.158	0.586	2.196	0.598
2.083	0.562	2.121	0.574	2.159	0.587	2.197	0.599
2.084	0.562	2.122	0.574	2.16	0.587	2.198	0.599
2.085	0.562	2.123	0.574	2.161	0.587	2.199	0.599
2.086	0.563	2.124	0.575	2.162	0.588	2.2	0.600
2.087	0.563	2.125	0.575	2.163	0.588	2.201	0.600
2.088	0.563	2.126	0.575	2.164	0.588	2.202	0.600
2.089	0.564	2.127	0.576	2.165	0.589	2.203	0.601

APPENDIX 3
STATISTICAL METHODS OF ANALYSIS: APPLICATION TO OIL-WATER FLOW DATA

A3.1 REVERSE ARRANGEMENTS TEST

The *test of reverse arrangements* is a well-established statistical tool to verify the independence of the data-points of a sample from each other. Particularly, it allows to decide whether or not the sample is stationary and to confirm that the data collected contains no trend. This statistical tool is non-parametric or distribution-free, because it allows detecting a trend in the data without making assumptions concerning its probability distribution (Bendat and Piersol, 2010).

The procedure is as follows: 1) break up the data record in n intervals of equal size and keep them in the same order as collected; 2) calculate the mean or mean-square (variance) of each interval as to test the stationarity of the means or variances of the record, respectively; 3) find the number of total arrangements, A_r.

In a sequence of n mean-square values, a delta operator, δ_{ij}, is defined:

$$\delta_{ij} = \begin{cases} 1, \overline{x}_i > \overline{x}_j \\ 0, \text{otherwise} \end{cases} \qquad \text{(A3.1)},$$

where $\overline{x}_i$ and $\overline{x}_j$ are mean-square values, and j > i. The subscript i can take values from 1 to n, while j will take values from i + 1 to n.

The parameter A_i is defined then as:

$$A_i = \sum_{j=i+1}^{N} \delta_{ij} \qquad \text{(A3.2)}$$

The total number of arrangements is:

$$A_r = \sum_{j=i+1}^{N} A_i \tag{A3.3}$$

The method is based on the fact that if the sequence of n mean-square values of the same random variable is independent from each other (i.e. no trends), the number of total reverse arrangements is a random variable with mean and variance (Kendal and Stuart, 1961):

$$\mu_A = \frac{n(n-1)}{4} \tag{A3.4}$$

$$\sigma_A^2 = \frac{N(2N+5)(N-1)}{72} \tag{A3.5}$$

The confidence intervals have been written for this distribution as a function of the parameter n and different levels of significance, ζ, in Table A3.1 (Bendat and Piersol, 2010). The number of reverse arrangements of a random process can be calculated in accordance to a certain number of samples, n. Then, it is hypothesized that the collection of n mean-square values of the signal is independent and shows no trend. The hypothesis can be accepted at the 100ζ % level of significance if the calculated A_r (Equation A3.3) is found within the limit:

$$A_{r,N;1-\varsigma/2} < A_r \leq A_{r,N;\varsigma/2} \tag{A3.6}$$

The signal record of the conductance probes was broken into 20 intervals of 12 seconds each in this investigation (n = 20). At 10 % level of significance (or 90 % confidence), data is independent and stationary if the total number of reverse arrangement is found between 69 and 120. Table A3.2 summarizes results of the application of the test to all experimental data of this research. It can be seen that all records were found stationary after trend removal. Finally, the MatLab™ code to readily compute is included in Figures A3.1 and A3.2.

Table A3.1 Distribution percentiles of the Reverse Arrangement distribution

	Significance level					
n	0.99	0.975	0.95	0.05	0.025	0.01
10	9	11	13	31	33	35
12	16	18	21	44	47	49
14	24	27	30	60	63	66
16	34	38	41	78	81	85
18	45	50	54	98	102	107
20	59	64	**69**	**120**	125	130
30	152	162	171	263	272	282
40	290	305	319	460	474	489
50	473	495	514	710	729	751
60	702	731	756	1013	1038	1067
70	977	1014	1045	1369	1400	1437
80	1299	1344	1382	1777	1815	1860
90	1668	1721	1766	2238	2283	2336
100	2083	2145	2198	2751	2804	2866

Table A3.2 Total Reverse Arrangements of experimental data

				Reverse Arrangements		
Exper. No.	**File name**	**r (-)**	**Umix (ms^{-1})**	**Raw data**	**Treated data**	
6	C_11Oct_5,5	1.63	0.84	84	101	Pass
6'	C_15Oct_3,5	1.67	0.84	105	110	Pass
7	C_11Oct_6,5	1.92	0.91	117	93	Pass
7'	C_11Oct_6,10	2.13	0.99	108	126	Failed
8	C_11Oct_6,15	2.4	1.06	105	115	Pass
9	C_11Oct_2,10	0.83	0.85	13	89	Pass
9'	C_22Oct_3,5	0.86	0.84	176	89	Pass
11	C_11Oct_3,10	1.17	0.85	124	129	Failed
12	C_11Oct_4,5	1.38	0.92	129	110	Pass
13	C_11Oct_4,10	1.55	0.99	113	103	Pass
14	C_11Oct_5,10	1.75	1.07	96	101	Pass
14'	C_15Oct_5,10	1.8	1.07	90	68	Failed
15	C_9Oct_6,10	1.91	1.14	124	93	Pass
16	C_9Oct_6,15	2.11	1.2	90	84	Pass
18	C_11Oct_1,10	0.73	0.91	130	94	Pass
18'	C_22Oct_2,15	0.72	0.92	9	119	Pass
20	C_11Oct_1,5	0.75	1.06	54	122	Failed
20'	C_22Oct_4,10	0.76	1.06	105	97	Pass
21	C_11Oct_2,5	0.84	0.98	51	113	Pass
21'	C_22Oct_5,5	0.87	0.99	100	109	Pass
22	C_11Oct_2,15	0.99	0.92	179	103	Pass
23	C_11Oct_3,5	1.16	0.98	150	115	Pass
26	C_9Oct_5,10	1.62	1.2	132	99	Pass
27	C_9Oct_6,5	1.77	1.3	71	119	Pass
34	C_9Oct_4,5	1.29	1.21	95	111	Pass
35	C_9Oct_4,10	1.43	1.26	99	89	Pass
36	C_9Oct_5,5	1.56	1.35	80	108	Pass
40	C_9Oct_1,5	0.81	1.33	104	63	Failed

Table A3.2 Total Reverse Arrangements of experimental data (Cont.)

				Reverse Arrangements		
Exper. No.	**File name**	**r (-)**	**Umix (ms^{-1})**	**Raw data**	**Treated data**	
42	C_9Oct_2,15	1.04	1.21	44	97	Pass
43	C_9Oct_3,5	1.16	1.27	76	104	Pass
44	C_9Oct_3,10	1.26	1.34	122	77	Pass
45	C_9Oct_1,10	0.9	1.27	70	112	Pass
48	C_9Oct_2,5	0.92	1.42	27	67	Failed
50	C_9Oct_2,10	0.99	1.34	145	91	Pass
101	C_15Oct_1,5	0.69	0.78	38	82	Pass
101'	C_22Oct_1,5	0.68	0.76	49	67	Failed
102	C_15Oct_1,10	0.79	0.7	157	74	Pass
102'	C_22Oct_1,10	0.83	0.7	74	112	Pass
103	C_15Oct_1,15	1.01	0.77	81	82	Pass
104	C_15Oct_2,5	1	0.63	114	104	Pass
105	C_15Oct_2,10	1.23	0.7	131	128	Failed
106	C_15Oct_2,15	1.42	0.77	41	90	Pass
107	C_15Oct_3,10	0.78	1.21	62	118	Pass
107'	C_22Oct_6,10	0.8	1.2	58	67	Failed
108	C_15Oct_3,15	0.88	1.13	46	115	Pass
108'	C_22Oct_6,15	0.88	1.11	115	119	Pass
109	C_15Oct_4,5	1	1.06	76	91	Pass
110	C_15Oct_4,10	1.13	1.13	107	106	Pass
111	C_15Oct_4,15	1.33	1.07	43	117	Pass
112	C_15Oct_5,5	1.48	1.13	55	116	Pass
201	C_22Oct_2,5	0.82	0.77	43	120	Pass
202	C_22Oct_2,10	0.7	0.83	32	96	Pass
203	C_22Oct_3,10	0.87	0.9	29	102	Pass
204	C_22Oct_4,5	0.75	0.98	60	86	Pass
205	C_22Oct_5,10	0.89	1.05	29	107	Pass
206	C_22Oct_6,5	0.78	1.12	53	67	Failed

TOTAL REVERSE ARRANGEMENTS TEST

This code readily computes the Total Reverse Arrangements of oil-water flow data collected with conductance probes.

(Beginning)

Data is read from a convenient Excel file and converted in matrix form for analysis.
```
x=xlsread('C_11Oct_2',10);
```

The function "REMOVAL" was previously created to remove the trend of raw signal data. It can be found in Appendix Xx.
```
r=REMOVAL(240,256,x);
```

Sampling period (240 s).
```
T=240;
```

Time of each interval (12 s).
```
t=12;
```

Sampling frequency (256 Hz).
```
fs=256;
```

Number of intervals.
```
n=T/t;
```

Total number of data-points in each interval: 3,072.
```
N=fs*t;
```

Matrix (nxN).
```
V=zeros(n,N);
```

Matrix (nx1).
```
v=zeros(n,1);
```

Signal is broken in 20 intervals. The data of each interval is written in each column of matrix V consecutively as collected - V(20,3072).
```
for i=1:n
  V(i,1:N)=r(i*N-N+1:i*N);
end
```

Computation of the mean of each interval.
```
for j=1:n
  v(j)=(mean(V(j,1:N)))^2;
end
```

Figure A3.1 MatLab™ code Reverse Arrangements Test

TOTAL REVERSE ARRANGEMENTS TEST

This code readily computes the Total Reverse Arrangements of oil-water flow data collected with conductance probes.

(Cont'd)

Definition of working matrices

```
S=size(v,1);
h=zeros(S-1,S-1);
```

Computation of Reverse Arrangements for each interval.

```
for i=1:(S-1)
  for j=(i+1):S
    if v(i)>v(j)
       h(j,i)=1;
    else 0;
  end
  end
end
```

Computation of Total Reverse Arrangements.

```
s=sum(h(:))
```

(END)

Figure A3.1 MatLab™ code Reverse Arrangements Test

A3.2 CHI SQUARE GOODNESS-OF-FIT TEST

Given a collection of n independent variables, X_i, all of them normally distributed with mean 0 and variance 1, $X_i \sim N(0,1)$, the new variable constructed as:

$$Y = \sum_{i=0}^{n} X_i \qquad \text{(A3.7)}$$

is the so-called Chi-Square distribution with n degrees of freedom, written as $Y \sim \chi^2(n)$. In fact, this distribution is one of the members of the Gamma distribution family, with shape n/2 and scale parameter 2. The mean, μ, is n and the variance, σ, is 2n. A few, convenient percentiles of the cumulative function of the Chi-Square distribution are shown in Table A3.3, where df means "degrees of freedom".

The Chi-Square distribution can be used to investigate whether a record of experimental data follows any specific probability distribution. It has been employed in this work to verify the normality of oil-water data in the so-called goodness-of-fit test. The steps followed are those of R. A. Fisher (1890 – 1962), the English statistician (Kreyszig, 1999).

First, the experimental record of 4 min was divided into 240 intervals of 1 second. The average and standard deviation of each interval was computed. Second, the normalized parameter, Z, was calculated for all 240 averages:

$$Z = \frac{\bar{y}_i - \bar{\bar{y}}_i}{s}, \qquad \text{(A3.8)}$$

where s is the standard deviation of all the averages and $\bar{\bar{y}}_i$, the average of averages. The 240 normalized values were ordered in 12 class-intervals (K=12) with limits: $Z < -2$; $-2 < Z < -1.6$; $-1.6 < Z < -1.2$; $-1.2 < Z < -0.8$; $-0.8 < Z < -0.4$; $-0.4 < Z < 0$; $0 < Z < 0.4$; $0.4 < Z < 0.8$; $0.8 < Z < 1.2$; $1.2 < Z < 1.6$; $1.6 < Z < 2$; $Z > 2$. The number of sub-intervals in which the experimental record is divided allows that a sufficiently large number of values are within each class interval (i.e. > 5).

Third, based on the number of values in each class interval respect to the total, the experimental probability is calculated, A_i. Furthermore, the expected probability if the data followed any probability distribution, F_i, is also calculated for each class interval. The overall deviation, χ_0^2, is computed as:

$$\chi_0^2 = \sum_{i=0}^{K=12} \frac{(A_i - F_i)^2}{F_i} \tag{A3.9}$$

Finally, choosing a significance level of 10 % (90 % confidence), the test is satisfied if χ_0^2 is less than the corresponding percentile in Table A3.3. For the particular case of a goodness-of-fit to a Gaussian distribution, the number of degrees of freedom is calculated from K – 3, i.e. 9. The limit value in Table A3.3 for these conditions is 14.684. Therefore, if the value calculated with Equation A3.9 is *less than* or *equal to* 14.684, the hypothesis of the experimental data following a Gaussian distribution has found to be true. Verification of Gaussian behaviour of experimental data is shown in Table A3.4. It can be seen that, in general, this feature is not improved by the pre-treatment of the data (i.e. trend removal). Finally, the proposed code to readily perform a goodness-of-fit test can be found in Figure A3.3

Table A3.3 Distribution percentiles of the Chi-Square distribution

	Confidence level					
Df	0.01	0.05	0.1	0.90	0.95	0.99
1	--	0.004	0.016	2.706	3.841	6.635
2	0.020	0.103	0.211	4.605	5.991	9.210
3	0.115	0.352	0.584	6.251	7.815	11.345
4	0.297	0.711	1.064	7.779	9.488	13.277
5	0.554	1.145	1.610	9.236	11.070	15.086
6	0.872	1.635	2.204	10.645	12.592	16.812
7	1.239	2.167	2.833	12.017	14.067	18.475
8	1.646	2.733	3.490	13.362	15.507	20.090
9	2.088	3.325	4.168	**14.684**	16.919	21.666
10	2.558	3.940	4.865	15.987	18.307	23.209
12	3.571	5.226	6.304	18.549	21.026	26.217
14	4.660	6.571	7.790	21.064	23.685	29.141
16	5.812	7.962	9.312	23.542	26.296	32.000
20	8.260	10.851	12.443	28.412	31.410	37.566

Table A3.4 Chi-Square test of experimental data

				Chi-Square		
Exper. No.	**File name**	**r (-)**	**Umix (ms^{-1})**	**Raw data**	**Treated data**	
6	C_11Oct_5,5	1.63	0.84	15.183	7.479	Pass
6'	C_15Oct_3,5	1.67	0.84	9.039	13.002	Pass
7	C_11Oct_6,5	1.92	0.91	6.656	4.6213	Pass
7'	C_11Oct_6,10	2.13	0.99	11.81	15.329	Fail
8	C_11Oct_6,15	2.4	1.06	4.37	3.614	Pass
9	C_11Oct_2,10	0.83	0.85	11.931	13.323	Pass
9'	C_22Oct_3,5	0.86	0.84	1.697	10.504	Pass
11	C_11Oct_3,10	1.17	0.85	10.085	6.007	Pass
12	C_11Oct_4,5	1.38	0.92	3.286	9.274	Pass
13	C_11Oct_4,10	1.55	0.99	5.919	7.638	Pass
14	C_11Oct_5,10	1.75	1.07	11.327	12.671	Pass
14'	C_15Oct_5,10	1.8	1.07	6.381	7.174	Pass
15	C_9Oct_6,10	1.91	1.14	5.963	5.789	Pass
16	C_9Oct_6,15	2.11	1.2	8.927	10.689	Pass
18	C_11Oct_1,10	0.73	0.91	1.951	0.45	Pass
18'	C_22Oct_2,15	0.72	0.92	15.288	12.206	Pass
20	C_11Oct_1,5	0.75	1.06	5.906	7.454	Pass
20'	C_22Oct_4,10	0.76	1.06	13.086	6.104	Pass
21	C_11Oct_2,5	0.84	0.98	19.363	19.107	Fail
21'	C_22Oct_5,5	0.87	0.99	40.181	28.485	Fail
22	C_11Oct_2,15	0.99	0.92	6.567	12.46	Pass
23	C_11Oct_3,5	1.16	0.98	4.669	6.749	Pass
26	C_9Oct_5,10	1.62	1.2	12.635	5.989	Pass
27	C_9Oct_6,5	1.77	1.3	11.151	11.773	Pass
34	C_9Oct_4,5	1.29	1.21	4.235	7.599	Pass
35	C_9Oct_4,10	1.43	1.26	7.026	9.964	Pass
36	C_9Oct_5,5	1.56	1.35	17.101	13.937	Pass
40	C_9Oct_1,5	0.81	1.33	4.154	8.447	Pass

Table A3.4 Chi-Square test of experimental data (Cont.)

				Chi-Square		
Exper. No.	**File name**	**r (-)**	**Umix (ms^{-1})**	**Raw data**	**Treated data**	
42	C_9Oct_2,15	1.04	1.21	8.951	2.95	Pass
43	C_9Oct_3,5	1.16	1.27	4.744	12.164	Pass
44	C_9Oct_3,10	1.26	1.34	17.472	10.268	Pass
45	C_9Oct_1,10	0.9	1.27	7.131	8.385	Pass
48	C_9Oct_2,5	0.92	1.42	7.388	8.058	Pass
50	C_9Oct_2,10	0.99	1.34	0.569	7.952	Pass
101	C_15Oct_1,5	0.69	0.78	6.806	8.9	Pass
101'	C_22Oct_1,5	0.68	0.76	7.222	3.455	Pass
102	C_15Oct_1,10	0.79	0.7	3.916	2.538	Pass
102'	C_22Oct_1,10	0.83	0.7	9.029	13.138	Pass
103	C_15Oct_1,15	1.01	0.77	6.206	5.622	Pass
104	C_15Oct_2,5	1	0.63	9.496	17.299	Fail
105	C_15Oct_2,10	1.23	0.7	5.534	9.991	Pass
106	C_15Oct_2,15	1.42	0.77	7.895	11.125	Pass
107	C_15Oct_3,10	0.78	1.21	5.275	9.145	Pass
107'	C_22Oct_6,10	0.8	1.2	5.303	6.924	Pass
108	C_15Oct_3,15	0.88	1.13	5.772	9.874	Pass
108'	C_22Oct_6,15	0.88	1.11	10.643	15.671	Fail
109	C_15Oct_4,5	1	1.06	10.779	9.673	Pass
110	C_15Oct_4,10	1.13	1.13	10.59	9.039	Pass
111	C_15Oct_4,15	1.33	1.07	5.743	9.679	Pass
112	C_15Oct_5,5	1.48	1.13	8.162	7.532	Pass
201	C_22Oct_2,5	0.82	0.77	22.405	5.577	Pass
202	C_22Oct_2,10	0.7	0.83	8.063	6.826	Pass
203	C_22Oct_3,10	0.87	0.9	13.052	11.581	Pass
204	C_22Oct_4,5	0.75	0.98	13.804	16.38	Pass
205	C_22Oct_5,10	0.89	1.05	23.41	21.713	Fail
206	C_22Oct_6,5	0.78	1.12	11.711	17.169	Fail

CHI-SQUARE GOODNESS-OF-FIT TEST

This code computes the Chi-Square parameter of experimental oil-water interface data for a Gaussian distribution with a confidence level of 90 %. The number of class intervals used is 12. The number of degrees of freedom, df, is 9 (12 – 3 = 9).

(Beginning)

Sampling period (240 s).
```
T=240;
```

Length of intervals (1 s).
```
t=12;
```

Total number of intervals (240).
```
n=T/t;
```

Data is read from a convenient Excel file and converted in matrix form for analysis.
```
x=xlsread('C_11Oct_2',10);
```

The function "REMOVAL" was previously created to remove the trend of raw signal data. Idem for function "INT_HEI".
```
Re=REMOVAL(240,256,x);
B0=INT_HEI(T,256,C);
R=Re+B0;
```

The sample in 240 intervals of 1 second each. The length of 1 second is to allow a sufficiently large number of data in each class-interval. The collection of 1-s data points (i.e. 256) is big enough to allow the non-stationary trends to be differentiated from random fluctuations.
```
c=BREK(T,t,256,R);
```

The mean value of all 240 intervals is calculated.
```
ic=zeros(n,1);
for j=1:n
  ic(j)=(mean(c(j,:)));
end
```

Figure A3.2 MatLab™ code Chi-Square Goodness-of-fit Test

CHI-SQUARE GOODNESS-OF-FIT TEST

This code computes the Chi-Square parameter of experimental oil-water interface data for a Gaussian distribution with a confidence level of 90 %. The number of class intervals used is 12. The number of degrees of freedom, df, is 9 (12 – 3 = 9).

(Cont'd)

```
Properties of the sequence of 240 intervals.
s=sort(ic);
M=mean(ic);
S=std(ic);

Preparation of 12 class-intervals.
Z=[-2;-1.6;-1.2;-0.8;-0.4;0;0.4;0.8;1.2;1.6;2;100];
X=zeros(12,1);

X=M+(S.*Z);
X(12,1)=0;

Calculation of theoretical Gaussian probability values.
P=[0.0228;0.032;0.0603;0.0968;0.1327;0.1554;0.1554;0.1327;0.0968;0.0603;0.032;0.0228];
F=P.*T;

Calculation of experimental probability values.
A=zeros(12,1);
FF=find(s<X(1,1));
A(1,1)=size(FF,1);
clear FF;

FF=find(s>X(11,1));
A(12,1)=size(FF,1);
clear FF;

for i=2:11
  FF=find(s>X(i-1,1) & s<X(i,1));
  SS=size(FF,1);
  A(i,1)=SS;
  clear FF;
  clear SS;
end

Comparison of experimental results against Gaussian expected values – Error.
Rat=((F-A).^2)./F;

Calculation of Chi-Square parameter.
SUM=sum(Rat)
```

(END)

Figure A3.2 MatLab™ code Chi-Square Goodness-of-fit Test (Cont.)

A3.3 THE t DISTRIBUTION

Given a random Gaussian distribution, Z, with mean 0 and variance 1, Z ~ N(0,1), and another independent variable that follows a Chi-Square distribution of n degrees of freedom, Y ~ $\chi^2(n)$, the random variable X constructed as

$$X = \frac{Z}{\sqrt{\frac{Y}{n}}} \tag{A3.10}$$

is the so-called t-Student distribution with n degrees of freedom, X ~ t(n). This distribution was famously introduced by William Gossett (1876 – 1937) around 1908, and is especially useful in providing valid statistical information from small records of experimental data.

Since the Chi-Square distribution is indeed a Gamma distribution with shape and scale parameters n/2 and 2, respectively, Γ(n/2,2), the probability distribution of the t-Student can be written in terms of the Gamma distribution as:

$$f_X(n) = \frac{\Gamma\left(\frac{n+1}{2}\right)}{\Gamma\left(\frac{n}{2}\right)\sqrt{n\pi}}\left[\left(\frac{x^2}{n}\right)+1\right]^{-\frac{n+1}{2}} \tag{A3.11}$$

A few useful percentiles of this distribution are presented in Table A3.5 for convenience. The t-Student, like the Gaussian distribution, is symmetric respect to a mean value, but has higher kurtosis (i.e. it is more “peaked”). As the record of data becomes larger, the distribution approaches to normal; the percentile values given in the table for an infinite number of degrees of freedom as those of a Gaussian distribution.

Although the variance of the data-points of the experimental sample can be calculated, s^2, the variance of the process, σ^2, is unknown. The t-Student distribution provides a practical way of calculating confidence intervals when the variance of the process is unknown (as it is the case of oil-water interface data). The following random variable defined using the variance of the sample:

$$t = \frac{\bar{y}_i - \mu}{\sqrt{\frac{s^2}{n}}}, \qquad \text{(A3.12)}$$

where y_i are the experimental data points; $\bar{y}_i$, its average; s^2, the variance of the sample and n, its size; and μ, the mean of the random process) follows the t-Student distribution. From Equation A3.12, confidence intervals given in Equation 5.9 are easily derived and the t-Student distribution becomes valid and convenient in deciding how well the variance of the sample estimates the variance of the process from small samples of data. In this investigation, confidence intervals of interface height are calculated from 20 or less average values of experimental data.

Table A3.5 Distribution percentiles of the t distribution

	Confidence level					
df	0.90	0.95	0.975	0.99	0.995	0.999
1	3.078	6.314	12.71	31.82	63.66	318.3
2	1.886	2.920	4.303	6.965	9.925	22.33
3	1.638	2.353	3.182	4.541	5.841	10.21
4	1.533	2.132	2.776	3.747	4.604	7.173
5	1.476	2.015	2.571	3.365	4.032	5.893
6	1.440	1.943	2.447	3.143	3.707	5.208
7	1.415	1.895	2.365	2.998	3.499	4.785
8	1.397	1.860	2.306	2.896	3.355	4.501
9	1.383	1.833	2.262	2.821	3.250	4.297
10	1.372	1.812	2.228	2.764	3.169	4.144
11	1.363	1.796	2.201	2.718	3.106	4.025
12	1.356	1.782	2.179	2.681	3.055	3.930
13	1.350	1.771	2.160	2.650	3.012	3.852
14	1.345	**1.761**	2.145	2.624	2.977	3.787
15	1.341	**1.753**	2.131	2.602	2.947	3.733
16	1.337	**1.746**	2.120	2.583	2.921	3.686
17	1.333	**1.740**	2.110	2.567	2.898	3.646
18	1.330	**1.734**	2.101	2.552	2.878	3.610
19	1.328	**1.729**	2.093	2.539	2.861	3.579
120	1.289	1.658	1.980	2.358	2.617	3.160
∞	1.282	1.645	1.960	2.326	2.576	3.090

APPENDIX 4
EXPERIMENTAL DATA: MANIPULATIONS AND CODES

A4.1 PRACTICAL PREPARATION OF DATA

In this section, the details of the practical manipulations done on the conductance probe data in order to estimate the time-average parameters and the power spectrum of the flow are given. The purpose is also to provide an account of the steps followed that can be readily used or repeat in the future. Naturally, the information presented in this section, as well as the codes, could be further improved.

The signal collected with the conductance probes was stored initially as a **.txt** file. For convenience, the data was exported to an Excel™ file.

For each two-phase flow rate, 6 different pages on the same Excel file were used. Each page contained just a column of numerical values. The first and sixth pages contained the 15,360 data-values of signal collected when the single-phase water was run before and after, respectively, of the two-phase test. As mentioned, single-phase water records of the conductance probes at 60 $Lmin^{-1}$ were collected with the purpose of estimating the correction factors. The second and third columns contained the 61,440 data-values of the water and oil flow rates, respectively, as recorded during the 4-min sampling period. These values, properly averaged, provided the pieces of information needed in the computation of superficial velocities and, therefore, actual velocities of the phases and the Re numbers.

Finally, the fourth and fifth pages contained the data-points of the conductance probe signal. The forth column was the raw signal collected, while the fifth column contained the data once the correction factors had been applied. Table A4.1 shows, as example, the six pages mentioned for experiment **No. 23** ($r = 1.16$; $U_{mix} = 0.98\ ms^{-1}$) for only the first 20 data-points (i.e. 80 ms). Notice that the probe signals have already been converted to interface height (in mm) using the corresponding calibration curve.

Table A4.1 Example of data preparation

1st page	2nd	3rd	4th	5th	6th
6-page preparation of data					
Blank before (Water at 60 $Lmin^{-1}$)	**Qw** ($Lmin^{-1}$)	**Qo** ($Lmin^{-1}$)	**Raw signal** (mm)	**Corrected** (mm)	**Blank after** (Water at 60 $Lmin^{-1}$)
32.539285	30.7622	35.6801	14.812893	16.307514	35.645701
36.312083	30.6849	35.6801	13.742648	15.129281	32.677273
32.623424	30.6849	35.6704	13.87727	15.277487	32.465243
32.623424	30.6656	35.7284	14.870108	16.370502	34.198508
35.144232	30.6849	35.7863	16.357682	18.008172	32.505629
32.377738	30.7236	35.796	17.377445	19.130829	32.761412
32.673908	30.8782	35.738	16.690872	18.374981	33.023926
33.478277	30.9265	35.7187	16.637023	18.315699	32.761412
32.586403	30.9651	35.7284	18.568851	20.442448	32.710929
32.774874	30.8395	35.7767	16.694238	18.378687	32.879207
32.963346	30.7719	35.8057	18.777516	20.672167	33.747522
32.640252	30.8298	35.7863	15.179739	16.711375	32.660445
36.281793	30.9265	35.7767	18.252489	20.094165	32.768143
32.401297	30.9748	35.796	15.701399	17.28567	33.340289
32.525823	30.8395	35.825	16.993772	18.708444	33.262881
35.40338	30.8492	35.8057	17.727463	19.516164	32.791702
32.589768	30.8975	35.8347	18.589045	20.46468	32.445049
32.418125	30.8782	35.8347	16.108631	17.733992	34.642763
34.006671	30.9265	35.8153	17.851988	19.653254	32.529188
32.694101	30.8492	35.8926	17.04089	18.760316	32.909497
Down to 15,360 values	**Down to 61,440 values**				**Down to 15,360 values**

Although the information is shown altogether, it must be noticed that the files were in separate pages of the same Excel™ files. Due to memory issues, typically 3 or 4 different two-phase flow combinations were included within the same Excel™ file and 5 or 6 different files were needed to collect all the results of an experimental day. The files were saved with the name **'C_11Oct_3'**: C stands for "conductivity", 11Oct is the date of the test and 3 is the file number. The fifth page of each combination was used in the estimation of time-average parameters and spectra and therefore (as it can be seen in the codes in the following sections), the re-call instruction for the data was **'C_11Oct_3, 5'**. The last number is always 5 or a multiple of 5.

Table A4.2 shows the correction factors computed for different experimental oil-water flows downstream the pipe. Results for test at the inlet section are given in Table A4.3. Codes are included in the final section.

Table A4.2 Experimental correction factors downstream the pipe

CORRECTION FACTORS							
C_9Oct				C_11Oct			
Exper. No.	r (-)	Umix (ms^{-1})	Correction	Exper. No.	r (-)	Umix (ms^{-1})	Correction
40	0.81	1.33	1.1008	20	0.75	1.06	1.1056
45	0.9	1.27	1.0678	18	0.73	0.91	1.0959
48	0.92	1.42	1.0574	21	0.84	0.98	1.0968
50	0.99	1.34	1.0606	9	0.83	0.85	1.093
42	1.04	1.21	1.073	22	0.99	0.92	1.0954
43	1.16	1.27	1.0794	23	1.16	0.98	1.1009
44	1.26	1.34	1.0819	11	1.17	0.85	1.0984
34	1.29	1.21	1.0837	12	1.38	0.92	1.0923
35	1.43	1.26	1.0852	13	1.55	0.99	1.0896
36	1.56	1.35	1.0875	6	1.67	0.84	1.0896
26	1.62	1.2	1.0884	14	1.75	1.07	1.0894
27	1.77	1.3	1.088	7	1.92	0.91	1.0892
15	1.91	1.14	1.0891	7’	2.13	0.99	1.0866
16	2.11	1.2	1.0878	8	2.4	1.06	1.025

CORRECTION FACTORS							
C_15Oct				C_22Oct			
Exper. No.	r (-)	Umix (ms^{-1})	Correction	Exper. No.	r (-)	Umix (ms^{-1})	Correction
101	0.69	0.78	1.0892	101	0.68	0.76	1.1066
102	0.79	0.7	1.0866	102	0.83	0.7	1.1029
103	1.01	0.77	1.0825	201	0.82	0.77	1.1062
104	1	0.63	1.0947	202	0.7	0.83	1.1064
105	1.23	0.7	1.0985	18	0.72	0.92	1.1057
106	1.42	0.77	1.1104	9	0.86	0.84	1.1083
6	1.67	0.84	1.11	203	0.87	0.9	1.1118
107	0.78	1.21	1.1044	204	0.75	0.98	1.1126
108	0.88	1.13	1.1007	20	0.76	1.06	1.1141
109	1	1.06	1.1002	21	0.87	0.99	1.1157
110	1.13	1.13	1.0996	205	0.89	1.05	1.1117
111	1.33	1.07	1.0961	206	0.78	1.12	1.1095
112	1.48	1.13	1.0918	107	0.8	1.2	1.1107
14	1.8	1.07	1.0906	108	0.88	1.11	1.1109

Table A4.3 Experimental correction factors at the inlet section

CORRECTION FACTORS							
C_3Dec				C_10Dec			
Exper. No.	r (-)	Umix (ms^{-1})	Correction	Exper. No.	r (-)	Umix (ms^{-1})	Correction
101	0.69	0.77	1.1901	21	0.87	0.98	1.2217
102	0.61	0.85	1.2024	22	0.78	1.07	1.2228
103	0.54	0.91	1.211	23	0.69	1.11	1.2292
104	0.46	0.99	1.2227	24	0.61	1.21	1.2397
105	0.43	1.07	1.2285	25	0.57	1.27	1.2446
C_17Jan				26	0.51	1.35	1.2447
501	0.99	0.63	1.3992	31	1.68	0.35	1.2524
502	0.99	0.91	1.3701	32	1.9	0.92	1.2419
503	1	1.05	1.3646	33	2.16	0.99	1.2383
504	1.01	1.64	1.3618	34	2.33	1.07	1.2452
503Prime	1.02	1.05	1.3468	35	2.56	1.14	1.2526
603	0.68	1.05	1.3375	36	2.81	1.21	1.2599
703	2.09	1.06	1.3419	37	3.09	1.28	1.2584

A4.2 EXPERIMENTAL RESULTS

A4.2.1 Time-average results and uncertainty

The data, as treated, is ready for analysis. The time-average parameters have been estimated following the general procedure outlined in Figure 4.10. Codes are included in the next section. Tables A4.4 and A4.5 compile most of the experimental results of interface height, water fraction, actual velocities and Re numbers, from which the graphs of the Thesis have been produced. The uncertainty of the interface heights is that calculated with Equation 5.10.

Table A4.4 Equilibrium interface heights and uncertainty

				Interf. Height	Uncertainty
Exper. No.	File name	r (-)	Umix (ms^{-1})	(mm)	
6	C_11Oct_5,5	1.63	0.84	14.7	0.01
6'	C_15Oct_3,5	1.67	0.84	14.6	0.01
7	C_11Oct_6,5	1.92	0.91	13.8	0.01
7'	C_11Oct_6,10	2.13	0.99	13.1	0.02
8	C_11Oct_6,15	2.4	1.06	11.6	0.01
9	C_11Oct_2,10	0.83	0.85	19.7	0.01
9'	C_22Oct_3,5	0.86	0.84	19.5	0.01
11	C_11Oct_3,10	1.17	0.85	17.1	0.01
12	C_11Oct_4,5	1.38	0.92	15.9	0.01
13	C_11Oct_4,10	1.55	0.99	15.2	0.01
14	C_11Oct_5,10	1.75	1.07	14.7	0.01
14'	C_15Oct_5,10	1.8	1.07	14.5	0.01
15	C_9Oct_6,10	1.91	1.14	14.1	0.01
16	C_9Oct_6,15	2.11	1.2	13.4	0.01
18	C_11Oct_1,10	0.73	0.91	20.2	0.01
18'	C_22Oct_2,15	0.72	0.92	20.5	0.01
20	C_11Oct_1,5	0.75	1.06	19.7	0.02
20'	C_22Oct_4,10	0.76	1.06	19.9	0.01
21	C_11Oct_2,5	0.84	0.98	19.0	0.01
21'	C_22Oct_5,5	0.87	0.99	19.0	0.01
22	C_11Oct_2,15	0.99	0.92	18.2	0.01
23	C_11Oct_3,5	1.16	0.98	16.9	0.01
26	C_9Oct_5,10	1.62	1.2	15.1	0.02
27	C_9Oct_6,5	1.77	1.3	14.3	0.01
34	C_9Oct_4,5	1.29	1.21	16.0	0.02
35	C_9Oct_4,10	1.43	1.26	15.6	0.02
36	C_9Oct_5,5	1.56	1.35	15.0	0.01
40	C_9Oct_1,5	0.81	1.33	18.8	0.02

Table A4.4 Equilibrium interface heights and uncertainty (Cont.)

				Interf. Height	Uncertainty
Exper. No.	**File name**	**r (-)**	**Umix (ms^{-1})**	**(mm)**	
42	C_9Oct_2,15	1.04	1.21	17.2	0.01
43	C_9Oct_3,5	1.16	1.27	16.8	0.01
44	C_9Oct_3,10	1.26	1.34	16.4	0.01
45	C_9Oct_1,10	0.9	1.27	18.1	0.02
48	C_9Oct_2,5	0.92	1.42	17.9	0.02
50	C_9Oct_2,10	0.99	1.34	17.6	0.01
101	C_15Oct_1,5	0.69	0.78	20.6	0.01
101'	C_22Oct_1,5	0.68	0.76	21.5	0.02
102	C_15Oct_1,10	0.79	0.7	20.0	0.01
102'	C_22Oct_1,10	0.83	0.7	19.9	0.01
103	C_15Oct_1,15	1.01	0.77	18.0	0.01
104	C_15Oct_2,5	1	0.63	18.6	0.01
105	C_15Oct_2,10	1.23	0.7	16.8	0.01
106	C_15Oct_2,15	1.42	0.77	15.7	0.01
107	C_15Oct_3,10	0.78	1.21	19.1	0.01
107'	C_22Oct_6,10	0.8	1.2	19.0	0.01
108	C_15Oct_3,15	0.88	1.13	18.4	0.01
108'	C_22Oct_6,15	0.88	1.11	18.8	0.01
109	C_15Oct_4,5	1	1.06	18.2	0.01
110	C_15Oct_4,10	1.13	1.13	17.2	0.01
111	C_15Oct_4,15	1.33	1.07	16.2	0.01
112	C_15Oct_5,5	1.48	1.13	15.5	0.02
201	C_22Oct_2,5	0.82	0.77	19.9	0.01
202	C_22Oct_2,10	0.7	0.83	20.7	0.01
203	C_22Oct_3,10	0.87	0.9	19.1	0.01
204	C_22Oct_4,5	0.75	0.98	19.8	0.02
205	C_22Oct_5,10	0.89	1.05	18.8	0.01
206	C_22Oct_6,5	0.78	1.12	19.3	0.02

Table A4.5 Time-average parameters

				Time-averaged parameters				
				α	u_o	u_w	Re_o	Re_w
Exper. No.	**File name**	**r (-)**	**Umix (ms^{-1})**	**	**ms^{-1}**	**ms^{-1}**	**	**
6	C_11Oct_5,5	1.63	0.84	0.38	0.91	0.92	3567	16852
6'	C_15Oct_3,5	1.67	0.84	0.38	0.92	0.91	3590	16686
7	C_11Oct_6,5	1.92	0.91	0.35	1.00	0.98	4041	16957
7'	C_11Oct_6,10	2.13	0.99	0.32	1.08	1.07	4500	17544
8	C_11Oct_6,15	2.4	1.06	0.28	1.13	1.24	4916	18304
9	C_11Oct_2,10	0.83	0.85	0.55	0.94	0.91	2910	21673
9'	C_22Oct_3,5	0.86	0.84	0.54	0.93	0.91	2936	21470
11	C_11Oct_3,10	1.17	0.85	0.46	0.92	0.93	3266	19470
12	C_11Oct_4,5	1.38	0.92	0.42	1.00	1.01	3734	19864
13	C_11Oct_4,10	1.55	0.99	0.39	1.08	1.07	4155	20234
14	C_11Oct_5,10	1.75	1.07	0.38	1.19	1.12	4637	20504
14'	C_15Oct_5,10	1.8	1.07	0.37	1.19	1.13	4687	20366
15	C_9Oct_6,10	1.91	1.14	0.36	1.27	1.18	5073	20962
16	C_9Oct_6,15	2.11	1.2	0.33	1.34	1.26	5473	21172
18	C_11Oct_1,10	0.73	0.91	0.57	0.97	1.01	2932	24492
18'	C_22Oct_2,15	0.72	0.92	0.58	1.00	1.00	2963	24688
20	C_11Oct_1,5	0.75	1.06	0.55	1.10	1.19	3435	28420
20'	C_22Oct_4,10	0.76	1.06	0.56	1.13	1.17	3469	28122
21	C_11Oct_2,5	0.84	0.98	0.53	1.03	1.10	3334	25316
21'	C_22Oct_5,5	0.87	0.99	0.53	1.06	1.09	3414	25164
22	C_11Oct_2,15	0.99	0.92	0.50	1.00	1.01	3349	22422
23	C_11Oct_3,5	1.16	0.98	0.46	1.06	1.09	3765	22629
26	C_9Oct_5,10	1.62	1.2	0.39	1.33	1.27	5097	23836
27	C_9Oct_6,5	1.77	1.3	0.36	1.42	1.40	5639	24995
34	C_9Oct_4,5	1.29	1.21	0.42	1.29	1.36	4782	27027
35	C_9Oct_4,10	1.43	1.26	0.41	1.36	1.38	5145	26708
36	C_9Oct_5,5	1.56	1.35	0.39	1.47	1.47	5650	27529
40	C_9Oct_1,5	0.81	1.33	0.52	1.35	1.54	4405	35290

Table A4.5 Time-average parameters (Cont.)

				Time-averaged parameters				
				α	u_o	u_w	Re_o	Re_w
Exper. No.	**File name**	**r (-)**	**Umix (ms^{-1})**	**	**ms^{-1}**	**ms^{-1}**	**	**
42	C_9Oct_2,15	1.04	1.21	0.46	1.25	1.39	4409	29377
43	C_9Oct_3,5	1.16	1.27	0.45	1.35	1.42	4852	29403
44	C_9Oct_3,10	1.26	1.34	0.44	1.45	1.49	5284	30062
45	C_9Oct_1,10	0.9	1.27	0.50	1.30	1.47	4384	32492
48	C_9Oct_2,5	0.92	1.42	0.49	1.45	1.64	4946	36032
50	C_9Oct_2,10	0.99	1.34	0.48	1.40	1.53	4825	33189
101	C_15Oct_1,5	0.69	0.78	0.58	0.83	0.86	2449	21216
101'	C_22Oct_1,5	0.68	0.76	0.61	0.86	0.80	2421	20487
102	C_15Oct_1,10	0.79	0.7	0.56	0.77	0.76	2363	18343
102'	C_22Oct_1,10	0.83	0.7	0.56	0.78	0.74	2404	17813
103	C_15Oct_1,15	1.01	0.77	0.49	0.83	0.85	2832	18687
104	C_15Oct_2,5	1	0.63	0.51	0.70	0.67	2319	15121
105	C_15Oct_2,10	1.23	0.7	0.45	0.77	0.76	2759	15823
106	C_15Oct_2,15	1.42	0.77	0.41	0.84	0.84	3147	16347
107	C_15Oct_3,10	0.78	1.21	0.53	1.24	1.39	3978	32309
107'	C_22Oct_6,10	0.8	1.2	0.53	1.23	1.37	3955	31660
108	C_15Oct_3,15	0.88	1.13	0.51	1.18	1.29	3908	29031
108'	C_22Oct_6,15	0.88	1.11	0.52	1.18	1.24	3854	28340
109	C_15Oct_4,5	1	1.06	0.50	1.16	1.16	3889	25778
110	C_15Oct_4,10	1.13	1.13	0.46	1.22	1.24	4278	26157
111	C_15Oct_4,15	1.33	1.07	0.43	1.17	1.16	4289	23284
112	C_15Oct_5,5	1.48	1.13	0.41	1.23	1.22	4669	23437
201	C_22Oct_2,5	0.82	0.77	0.56	0.86	0.83	2639	19821
202	C_22Oct_2,10	0.7	0.83	0.59	0.90	0.91	2662	22536
203	C_22Oct_3,10	0.87	0.9	0.53	0.97	0.99	3115	22951
204	C_22Oct_4,5	0.75	0.98	0.55	1.03	1.10	3195	26303
205	C_22Oct_5,10	0.89	1.05	0.52	1.12	1.17	3656	26683
206	C_22Oct_6,5	0.78	1.12	0.54	1.16	1.28	3690	29836

In summary, the uncertainty of these results have been estimated as given in Chapter 5: 1) 3.8 % for the water fraction, ε_α; 2) 5.5 % for the actual velocities of the phases, ε_{uo} and ε_{uw}; 3) 6.5 % for the actual Re numbers of the phases, ε_{Reo} and ε_{Rew}, taken the nominal actual velocity of each phase as 1 ms^{-1}.

Since the water fraction is a unique function of the interface height (Equation 5.13), the absolute uncertainty of the water fraction when it is computed from the interface height can be estimated as:

$$\omega_\alpha = \frac{\partial \alpha}{\partial h_i} \omega_{h_i} \,, \tag{A4.1}$$

where ω_α and ω_{hi} are the uncertainties of the water fraction and the interface height, respectively, and the rest of symbols, as usual. The error given by the equation generally depends on the height of water in the pipe, but a reference value can be calculated for a reference and convenient case, for example $\alpha_w = 0.5$. It can be shown that the partial derivative of the water fraction with the interface height in that special case becomes 4 / (π D) or D / A. The experimental uncertainty in computing the interface height was found around 3 % (Equation 5.18). In this case, the uncertainty of the water fraction becomes:

$$\omega_\alpha = \frac{D}{A} \omega_{h_i} = 33.523 \text{m}^{-1} \cdot 0.03 \cdot 0.019 \text{m}^{-1} = 0.0191 \tag{A4.2}$$

Dividing the uncertainty by $\alpha = 0.5$, the relative error is found, $\varepsilon_\alpha = 3.8$ %.

The uncertainty of the flow rate meters is 1 % in the full range. Per definition of superficial velocity, taking Q = 60 Lmin^{-1} as nominal case, considering the cross-sectional area of the pipe as a constant and following the same procedure of propagation of errors, the relative uncertainty in computing superficial quantities, ε_{us}, was found to be 0.9 %.

Actual velocities were computed using Equations 5.14 and 5.15. Assuming that the errors affecting the superficial velocities and the water fraction are independent, the absolute uncertainty of the actual velocity of oil, for example, can be found:

$$\omega_{uo} = \left[\left(\frac{\partial u_o}{\partial u_{so}} \omega_{us} \right)^2 + \left(\frac{\partial u_o}{\partial \alpha_w} \omega_\alpha \right)^2 \right]^{\frac{1}{2}} \tag{A4.3}$$

At 60 $Lmin^{-1}$, the superficial velocity is 0.9 ms^{-1}. Using this nominal value and $\alpha_w = 0.5$, $\omega_{uo} = 0.07$ ms^{-1}. Under this conditions, considering a somewhat larger actual velocity (i.e. 1.35 ms^{-1}), $\varepsilon_{uo} = 5.5$ %. The same estimation is found if the analysis is repeated to the water phase.

Finally, the uncertainty of the Re number for the oil phase is:

$$\omega_{Re\,o} = \left[\left(\frac{\partial Re_o}{\partial u_o} \omega_u \right)^2 + \left(\frac{\partial Re_o}{\partial D_o} \omega_D \right)^2 \right]^{\frac{1}{2}} \qquad \text{(A4.4)}$$

Using the definition of effective diameter (Equation 5.11) and relationships in Appendix 5 (A5.1, A5.3 and A5.5), it can be shown that the effective diameter, D_o, when $\alpha_w = 0.5$, is 0.6 D (60 % of the pipe diameter). Assuming a 3 % error in the effective diameter (i.e. the same as that of the interface height):

$$\omega_{Re\,o} = \left[\begin{array}{l} \left(\frac{830 \cdot 0.6 \cdot 0.038}{0.0055} \cdot 0.07 \right)^2 + \\ \left(\frac{830 \cdot 1.35}{0.0055} 0.03 \cdot 0.6 \cdot 0.038 \right)^2 \end{array} \right]^{\frac{1}{2}} = \ldots \cong 280 \qquad \text{(A4.5)}$$

The actual Re number for the oil phase under these conditions is 4,640, which gives a relative uncertainty, ε_{Reo}, about 6 %. (and the same for Re_w).

A4.2.2 Spectral density analysis results

Most of the results of the validation of the power spectrum are shown in Table A4.6. The three values computed with Equation 5.27 are reported. Table A4.7 collects the relative importance of spectral frequencies lower than 30 Hz and that of those between 10 and 30 Hz. The difference between both values is due to the mechanical vibrations and is concentrated on the frequency 2 – 3 Hz. Finally, Table A4.8 shows a few calculations of the weighted frequency of the range 10 – 30 Hz. The 19-Hz contribution was found in all cases regardless the flow conditions.

Table A4.6 Average power

SPECTRAL DENSITY ANALYSIS - OCTOBER 2012							
					Average power		
Exper. No.	Probe	Location	r (-)	Umix (ms^{-1})	Spectrum	Auto-correlation	Time data
1	2-mm	Downstream	0.81	1.33	2.7887	2.7146	2.7146
2	2-mm	Downstream	0.90	1.27	2.6884	2.6285	2.6285
3	2-mm	Downstream	0.92	1.42	3.6311	3.7058	3.7058
4	2-mm	Downstream	0.99	1.34	4.3949	4.5225	4.5225
26	2-mm	Downstream	1.92	0.91	2.2801	2.1042	2.1042
6	2-mm	Downstream	1.16	1.27	2.9317	2.7947	2.7947
7	2-mm	Downstream	1.26	1.34	3.0811	2.9191	2.9191
8	2-mm	Downstream	1.29	1.21	2.7021	2.5980	2.5980
9	2-mm	Downstream	1.43	1.26	2.7601	2.6683	2.6683
10	2-mm	Downstream	1.56	1.35	2.9499	2.8261	2.8261
11	2-mm	Downstream	1.62	1.20	2.6784	2.5524	2.5524
12	2-mm	Downstream	1.77	1.30	2.9535	2.7878	2.7878
38	2-mm	Downstream	1.00	1.06	2.3716	2.2986	2.2986
14	2-mm	Downstream	2.11	1.20	2.9905	2.7644	2.7644
29	2-mm	Downstream	0.69	0.78	1.7583	1.6782	1.6782
46	2-mm	Downstream	0.70	0.83	2.2822	2.2166	2.2166
17	2-mm	Downstream	0.84	0.98	2.4915	2.3664	2.3664
18	2-mm	Downstream	0.83	0.85	3.3888	3.4253	3.4253
31	2-mm	Downstream	1.01	0.77	2.2038	1.9961	1.9961
34	2-mm	Downstream	1.42	0.77	2.2724	2.1545	2.1545
41	2-mm	Downstream	1.48	1.13	2.5726	2.4416	2.4416
19	2-mm	Downstream	0.99	0.92	3.6413	3.7739	3.7739
23	2-mm	Downstream	1.55	0.99	2.2706	2.1897	2.1897
22	2-mm	Downstream	1.38	0.92	2.2989	2.1654	2.1654
30	2-mm	Downstream	0.79	0.70	1.5102	1.3570	1.3570
24	2-mm	Downstream	1.63	0.84	2.1138	1.9139	1.9139
27	2-mm	Downstream	2.13	0.99	2.4409	2.2432	2.2432
28	2-mm	Downstream	2.40	1.06	2.7256	2.3834	2.3834
16	2-mm	Downstream	0.73	0.91	2.1546	1.9717	1.9717
5	2-mm	Downstream	1.04	1.21	3.0106	2.9814	2.9814
36	2-mm	Downstream	0.78	1.21	2.4876	2.4477	2.4477
32	2-mm	Downstream	1.00	0.63	3.1704	3.1841	3.1841
21	2-mm	Downstream	1.17	0.85	2.3512	2.2153	2.2153
65	2-mm	Downstream	1.21	1.24	2.9306	2.8652	2.8652
35	2-mm	Downstream	1.67	0.84	2.2300	2.0816	2.0816
15	2-mm	Downstream	0.75	1.06	2.6214	2.5151	2.5151
37	2-mm	Downstream	0.88	1.13	2.4281	2.3612	2.3612
33	2-mm	Downstream	1.23	0.70	2.6412	2.5681	2.5681
39	2-mm	Downstream	1.13	1.13	2.5058	2.4115	2.4115
40	2-mm	Downstream	1.33	1.07	2.6254	2.3767	2.3767
13	2-mm	Downstream	1.91	1.14	2.7747	2.5809	2.5809
42	2-mm	Downstream	1.80	1.07	2.5828	2.4591	2.4591
43	2-mm	Downstream	0.68	0.76	1.7981	1.7079	1.7079
44	2-mm	Downstream	0.83	0.70	1.5274	1.3678	1.3678
45	2-mm	Downstream	0.82	0.77	1.7916	1.6486	1.6486
20	2-mm	Downstream	1.16	0.98	2.6887	2.6724	2.6724
47	2-mm	Downstream	0.72	0.92	3.7343	3.8845	3.8845
48	2-mm	Downstream	0.86	0.84	3.3927	3.5302	3.5302
49	2-mm	Downstream	0.87	0.90	2.6958	2.6004	2.6004
50	2-mm	Downstream	0.75	0.98	2.4319	2.3945	2.3945
51	2-mm	Downstream	0.76	1.06	2.5668	2.4809	2.4809
52	2-mm	Downstream	0.87	0.99	2.5396	2.2710	2.2710
53	2-mm	Downstream	0.89	1.05	2.6078	2.3825	2.3825
54	2-mm	Downstream	0.78	1.12	2.4844	2.4073	2.4073
55	2-mm	Downstream	0.80	1.20	2.5340	2.4770	2.4770
56	2-mm	Downstream	0.88	1.11	2.4152	2.3377	2.3377

Table A4.6 Average power (Cont.)

SPECTRAL DENSITY ANALYSIS - NOVEMBER 2012 AND FEBRUARY 2013							
					Average power		
Exper. No.	Probe	Location	r (-)	Umix (ms^{-1})	Spectrum	Auto-correlation	Time data
57	2-mm	Downstream	0.99	1.20	3.1036	3.0326	3.0326
58	2-mm	Downstream	1.00	1.35	3.2474	3.1244	3.1244
59	2-mm	Downstream	1.02	1.48	6.6796	6.2553	6.2553
60	2-mm	Downstream	1.01	1.63	7.2505	6.9768	6.9768
61	2-mm	Downstream	1.02	1.77	8.5534	8.7915	8.7915
62	2-mm	Downstream	1.02	1.92	9.3789	9.5991	9.5991
63	2-mm	Downstream	1.02	2.07	8.3234	8.5413	8.5413
64	2-mm	Downstream	1.04	2.35	8.7176	8.9952	8.9952
25	2-mm	Downstream	1.75	1.07	2.4936	2.3579	2.3579
66	2-mm	Downstream	1.18	1.38	3.1271	3.0384	3.0384
67	2-mm	Downstream	1.22	1.51	7.9722	7.4961	7.4961
68	2-mm	Downstream	1.21	1.64	8.6794	8.3011	8.3011
69	2-mm	Downstream	1.22	1.77	8.4587	8.2600	8.2600
70	2-mm	Downstream	1.25	1.89	8.3035	8.2698	8.2698
71	2-mm	Downstream	1.39	1.17	3.1827	2.8451	2.8451
72	2-mm	Downstream	1.42	1.33	3.1736	3.0227	3.0227
73	2-mm	Downstream	1.45	1.40	3.3352	3.2733	3.2733
74	2-mm	Downstream	1.42	1.54	8.8629	8.3584	8.3584
75	2-mm	Downstream	1.43	1.67	9.5978	9.2500	9.2500
76	2-mm	Downstream	1.44	1.90	9.1347	9.1511	9.1511
77	5-mm	Downstream	0.22	0.84	3.7772	3.4483	3.4483
78	5-mm	Downstream	0.20	0.78	3.8504	3.4223	3.4223
79	5-mm	Downstream	0.23	0.98	4.1743	3.7565	3.7565
80	5-mm	Downstream	0.22	0.92	4.2195	3.8120	3.8120
81	2-mm	Downstream	0.83	0.84	2.9652	2.8203	2.8203
82	2-mm	Downstream	0.86	0.99	2.7346	2.6162	2.6162
83	2-mm	Downstream	0.90	1.14	3.5341	3.4687	3.4687
84	2-mm	Downstream	0.97	0.77	4.8445	4.8613	4.8613
85	2-mm	Downstream	1.01	0.93	3.1339	3.1222	3.1222
86	2-mm	Downstream	1.57	0.99	3.0072	2.9454	2.9454
87	2-mm	Downstream	1.62	1.20	3.7779	3.7523	3.7523
88	2-mm	Downstream	1.92	0.91	3.2405	2.8793	2.8793
89	2-mm	Downstream	1.94	1.14	3.9255	3.7455	3.7455
90	2-mm	Downstream	0.82	0.85	5.7241	5.9956	5.9956
91	2-mm	Downstream	1.00	0.77	4.0667	3.9639	3.9639
92	2-mm	Downstream	1.58	1.00	3.4906	3.5041	3.5041
109i	5-mm	Inlet	0.42	1.25	0.0733	0.0634	0.0634
109p	2-mm	Downstream	0.42	1.25	0.0311	0.0314	0.0314
104i	5-mm	Inlet	0.57	0.81	0.0104	0.0104	0.0104
104p	2-mm	Downstream	0.57	0.81	0.0215	0.0214	0.0214
103i	5-mm	Inlet	0.63	0.96	0.0120	0.0119	0.0119
103p	2-mm	Downstream	0.63	0.96	0.0222	0.0216	0.0216
102i	5-mm	Inlet	0.67	1.10	0.0127	0.0127	0.0127
102p	2-mm	Downstream	0.67	1.10	0.0303	0.0292	0.0292
101i	5-mm	Inlet	0.70	1.25	0.0151	0.0151	0.0151
101p	2-mm	Downstream	0.70	1.25	0.0376	0.0370	0.0370
106i	5-mm	Inlet	2.00	1.10	0.0321	0.0304	0.0304
106p	2-mm	Downstream	2.00	1.10	0.0722	0.0682	0.0682
105i	5-mm	Inlet	2.20	1.18	0.0413	0.0383	0.0383
105p	2-mm	Downstream	2.20	1.18	0.0534	0.0530	0.0530
107i	5-mm	Inlet	2.25	0.96	0.0182	0.0184	0.0184
107p	2-mm	Downstream	2.25	0.96	0.0463	0.0469	0.0469
108i	5-mm	Inlet	2.50	1.03	0.0402	0.0349	0.0349
108p	2-mm	Downstream	2.50	1.03	0.0430	0.0411	0.0411

Table A4.7 Relative importance of frequency contributions

SPECTRAL DENSITY ANALYSIS - OCTOBER 2012						
					Frequency	
Exper. No.	Probe	Location	r (-)	Umix (ms^{-1})	< 30 Hz	10 - 30 Hz
1	2-mm	Downstream	0.81	1.33	40.44%	25.20%
2	2-mm	Downstream	0.90	1.27	40.68%	24.46%
3	2-mm	Downstream	0.92	1.42	35.49%	21.69%
4	2-mm	Downstream	0.99	1.34	31.69%	20.93%
26	2-mm	Downstream	1.92	0.91	45.59%	23.77%
6	2-mm	Downstream	1.16	1.27	39.93%	25.41%
7	2-mm	Downstream	1.26	1.34	42.32%	27.26%
8	2-mm	Downstream	1.29	1.21	40.37%	22.95%
9	2-mm	Downstream	1.43	1.26	39.92%	22.55%
10	2-mm	Downstream	1.56	1.35	41.11%	23.38%
11	2-mm	Downstream	1.62	1.20	41.47%	23.54%
12	2-mm	Downstream	1.77	1.30	41.92%	22.08%
38	2-mm	Downstream	1.00	1.06	41.20%	25.10%
14	2-mm	Downstream	2.11	1.20	43.71%	22.17%
29	2-mm	Downstream	0.69	0.78	43.06%	22.13%
46	2-mm	Downstream	0.70	0.83	40.62%	22.17%
17	2-mm	Downstream	0.84	0.98	43.49%	24.86%
18	2-mm	Downstream	0.83	0.85	34.65%	19.23%
31	2-mm	Downstream	1.01	0.77	47.90%	23.46%
34	2-mm	Downstream	1.42	0.77	41.81%	20.65%
41	2-mm	Downstream	1.48	1.13	40.67%	24.26%
19	2-mm	Downstream	0.99	0.92	31.44%	18.92%
23	2-mm	Downstream	1.55	0.99	41.40%	24.11%
22	2-mm	Downstream	1.38	0.92	42.14%	25.59%
30	2-mm	Downstream	0.79	0.70	48.27%	22.23%
24	2-mm	Downstream	1.63	0.84	46.46%	24.85%
27	2-mm	Downstream	2.13	0.99	43.63%	23.00%
28	2-mm	Downstream	2.40	1.06	49.65%	24.13%
16	2-mm	Downstream	0.73	0.91	47.35%	25.88%
5	2-mm	Downstream	1.04	1.21	38.22%	23.27%
36	2-mm	Downstream	0.78	1.21	39.36%	24.17%
32	2-mm	Downstream	1.00	0.63	30.97%	13.88%
21	2-mm	Downstream	1.17	0.85	41.98%	24.39%
65	2-mm	Downstream	1.21	1.24	39.87%	23.46%
35	2-mm	Downstream	1.67	0.84	43.44%	23.83%
15	2-mm	Downstream	0.75	1.06	42.73%	24.76%
37	2-mm	Downstream	0.88	1.13	40.76%	25.49%
33	2-mm	Downstream	1.23	0.70	39.23%	18.44%
39	2-mm	Downstream	1.13	1.13	40.59%	26.42%
40	2-mm	Downstream	1.33	1.07	45.62%	25.45%
13	2-mm	Downstream	1.91	1.14	43.97%	23.05%
42	2-mm	Downstream	1.80	1.07	42.03%	23.81%
43	2-mm	Downstream	0.68	0.76	43.28%	21.80%
44	2-mm	Downstream	0.83	0.70	48.48%	21.91%
45	2-mm	Downstream	0.82	0.77	46.86%	23.38%
20	2-mm	Downstream	1.16	0.98	38.96%	23.26%
47	2-mm	Downstream	0.72	0.92	29.08%	16.78%
48	2-mm	Downstream	0.86	0.84	29.52%	17.47%
49	2-mm	Downstream	0.87	0.90	39.08%	23.44%
50	2-mm	Downstream	0.75	0.98	38.36%	22.63%
51	2-mm	Downstream	0.76	1.06	38.16%	23.43%
52	2-mm	Downstream	0.87	0.99	49.10%	49.10%
53	2-mm	Downstream	0.89	1.05	47.08%	29.04%
54	2-mm	Downstream	0.78	1.12	39.22%	23.83%
55	2-mm	Downstream	0.80	1.20	39.70%	24.37%
56	2-mm	Downstream	0.88	1.11	40.86%	25.42%

Table A4.7 Relative importance of frequency contributions (Cont.)

SPECTRAL DENSITY ANALYSIS - NOVEMBER 2012						
					Frequency	
Exper. No.	Probe	Location	r (-)	Umix (ms^{-1})	< 30 Hz	10 - 30 Hz
57	2-mm	Downstream	0.99	1.20	40.68%	24.16%
58	2-mm	Downstream	1.00	1.35	39.62%	25.32%
59	2-mm	Downstream	1.02	1.48	43.31%	27.52%
60	2-mm	Downstream	1.01	1.63	40.36%	26.09%
61	2-mm	Downstream	1.02	1.77	34.16%	22.78%
62	2-mm	Downstream	1.02	1.92	32.45%	22.61%
63	2-mm	Downstream	1.02	2.07	33.52%	23.05%
64	2-mm	Downstream	1.04	2.35	31.61%	21.55%
25	2-mm	Downstream	1.75	1.07	43.20%	23.88%
66	2-mm	Downstream	1.18	1.38	40.19%	24.77%
67	2-mm	Downstream	1.22	1.51	43.53%	26.83%
68	2-mm	Downstream	1.21	1.64	41.50%	25.67%
69	2-mm	Downstream	1.22	1.77	38.03%	24.60%
70	2-mm	Downstream	1.25	1.89	37.11%	25.01%
71	2-mm	Downstream	1.39	1.17	47.12%	26.89%
72	2-mm	Downstream	1.42	1.33	41.24%	26.08%
73	2-mm	Downstream	1.45	1.40	38.18%	23.97%
74	2-mm	Downstream	1.42	1.54	42.84%	25.84%
75	2-mm	Downstream	1.43	1.67	40.70%	24.61%
76	2-mm	Downstream	1.44	1.90	36.59%	23.36%
77	5-mm	Downstream	2.77	0.84	30.31%	14.42%
78	5-mm	Downstream	2.35	0.78	33.14%	14.80%
79	5-mm	Downstream	3.23	0.98	30.37%	17.60%
80	5-mm	Downstream	3.00	0.92	30.70%	15.93%
81	2-mm	Downstream	0.83	0.84	43.33%	22.13%
82	2-mm	Downstream	0.86	0.99	43.37%	25.54%
83	2-mm	Downstream	0.90	1.14	39.04%	24.29%
84	2-mm	Downstream	0.97	0.77	36.03%	19.64%
85	2-mm	Downstream	1.01	0.93	37.33%	21.70%
86	2-mm	Downstream	1.57	0.99	38.72%	22.22%
87	2-mm	Downstream	1.62	1.20	39.07%	24.11%
88	2-mm	Downstream	1.92	0.91	49.27%	24.33%
89	2-mm	Downstream	1.94	1.14	42.83%	25.23%
90	2-mm	Downstream	0.82	0.85	27.71%	15.39%
91	2-mm	Downstream	1.00	0.77	38.26%	17.74%
92	2-mm	Downstream	1.58	1.00	36.80%	20.90%

Table A4.8 Estimated weighted frequency of the range 10 – 30 Hz

SPECTRAL DENSITY ANALYSIS - FREBRUARY 2013						
					Weighted frequency (Hz)	
Exper. No.	Probe	Location	r (-)	Umix (ms^{-1})	Average	Variation
26	2-mm	Downstream	1.92	0.91	19.1940	0.3193
109i	5-mm	Inlet	0.42	1.25	19.0779	0.3824
109p	2-mm	Downstream	0.42	1.25	19.6679	0.3606
104i	5-mm	Inlet	0.57	0.81	19.2399	0.3681
104p	2-mm	Downstream	0.57	0.81	19.8674	0.3784
103i	5-mm	Inlet	0.63	0.96	**	**
103p	2-mm	Downstream	0.63	0.96	**	**
102i	5-mm	Inlet	0.67	1.10	**	**
102p	2-mm	Downstream	0.67	1.10	**	**
101i	5-mm	Inlet	0.70	1.25	18.8751	0.8368
101p	2-mm	Downstream	0.70	1.25	19.7409	0.2956
106i	5-mm	Inlet	2.00	1.10	19.0867	0.9333
106p	2-mm	Downstream	2.00	1.10	19.8526	0.2508
105i	5-mm	Inlet	2.20	1.18	**	**
105p	2-mm	Downstream	2.20	1.18	**	**
107i	5-mm	Inlet	2.25	0.96	**	**
107p	2-mm	Downstream	2.25	0.96	**	**
108i	5-mm	Inlet	2.50	1.03	**	**
108p	2-mm	Downstream	2.50	1.03	**	**

A4.2.3 High-speed investigation of inlet waves

The experimental conditions under which inlet waves were investigated with the aid of high-speed images are presented in the following. Table A4.9 give the evolution of average wave amplitudes and wave velocities for each flow combination and Table A4.10 reports the wavelength. Finally, Table A4.11 presents the evolution of the frequency of 17 inlet waves along the inlet in two example cases, one at r < 1 and another at r > 1. It can be seen that the frequencies remain constant as the wave dampens. In all cases, histograms like those shown in Figures 7.7a – 7.7d were found.

Table A4.9 Average amplitude and velocity of inlet waves

Input conditions				Amplitude				Wave celerity		
Oil	Water	r	Umix	(actual cm)				(actual cm)		
($Lmin^{-1}$)	($Lmin^{-1}$)	(-)	(ms^{-1})	R-1	R-2	R-3	R-4	R-12	R-23	R-34
55	20	2.75	1.10	5.233	5.033	4.567	3.967	0.524	0.600	0.678
40	20	2.00	0.88	2.385	2.077	1.923	1.769	0.600	0.659	0.708
50	30	1.67	1.18	2.636	2.182	2.091	1.273	0.642	0.689	0.800
50	35	1.43	1.25	2.250	2.125	1.600	1.400	0.605	0.706	0.614
50	60	0.83	1.62	1.889	1.444	1.222	0.700	0.738	0.853	0.943
50	70	0.71	1.76	2.900	2.364	2.100	1.455	0.763	0.900	0.995
50	80	0.63	1.91	1.929	1.400	1.154	1.100	0.820	0.983	1.118
25	55	0.45	1.18	5.556	5.056	3.389	3.176	0.595	0.626	0.689
32	70	0.46	1.50	3.765	3.750	2.889	2.389	0.734	0.769	0.844
22	50	0.44	1.06	4.947	4.824	4.412	2.813	0.523	0.553	0.613
27	60	0.45	1.28	5.778	4.278	3.556	2.941	0.614	0.714	0.783
29	65	0.45	1.38	5.833	4.529	3.294	2.933	0.716	0.743	0.845
20	45	0.44	0.96	4.632	4.211	3.211	2.059	0.498	0.523	0.582
25	60	0.42	1.25	6.273	5.045	3.773	3.706	0.658	0.699	0.787

Table A4.10 Average wavelength of inlet waves

Input conditions				Wavelength			Relative wavelength		
Oil	Water	r	Umix	(actual cm)			(-)		
($Lmin^{-1}$)	($Lmin^{-1}$)	(-)	(ms^{-1})	R-12	R-23	R-34	R-12	R-23	R-34
55	20	2.75	1.10	2.066	2.355	2.705	1.000	1.140	1.309
50	20	2.50	1.03	3.383	3.433	3.770	1.000	1.015	1.114
45	20	2.25	0.96	3.532	3.782	4.483	1.000	1.071	1.269
50	22	2.27	1.06	3.733	4.008	4.516	1.000	1.074	1.210
65	29	2.24	1.38	3.925	4.103	4.680	1.000	1.045	1.192
60	27	2.22	1.28	3.741	4.228	4.783	1.000	1.130	1.279
40	20	2.00	0.88	4.185	4.673	4.952	1.000	1.117	1.183
50	30	1.67	1.18	3.764	4.066	4.722	1.000	1.080	1.255
50	35	1.43	1.25	4.935	5.666	5.247	1.000	1.148	1.063
50	60	0.83	1.62	3.935	4.558	4.807	1.000	1.158	1.221
50	70	0.71	1.76	4.722	5.593	6.269	1.000	1.184	1.328
50	80	0.63	1.91	5.149	6.230	7.011	1.000	1.210	1.362
25	55	0.45	1.18	3.130	3.270	3.698	1.000	1.045	1.182
32	70	0.46	1.50	6.151	6.229	6.865	1.000	1.013	1.116
22	50	0.44	1.06	3.637	3.963	4.336	1.000	1.090	1.192
27	60	0.45	1.28	4.565	5.202	5.830	1.000	1.140	1.277
29	65	0.45	1.38	5.008	5.206	5.936	1.000	1.040	1.185
20	45	0.44	0.96	4.144	4.348	4.838	1.000	1.049	1.167
25	60	0.42	1.25	5.007	5.364	5.864	1.000	1.071	1.171

Table A4.11 Examples of inlet wave frequencies

CALCULATED FREQUENCY			
Region	(actual Hz)		
1st	2nd	3rd	4th
16.9	16.1	15.2	14.9
16.4	14.3	15.6	15.6
16.7	14.5	17.2	15.6
14.1	14.3	13.3	14.9
20.8	20.8	19.2	15.9
14.3	16.1	16.4	19.2
20.8	18.9	19.2	16.4
17.5	17.2	17.9	22.7
14.5	14.5	14.5	13.2
17.9	18.2	20.4	20.4
14.3	13.3	12.2	12.8
17.2	18.9	22.7	23.3
21.3	17.9	18.2	17.2
19.6	20.4	18.9	19.6
16.7	17.2	15.4	14.5
15.4	15.2	17.2	19.2
16.1	16.4	14.3	13.9

a. Input ratio r < 1

CALCULATED FREQUENCY			
Region	(actual Hz)		
1st	2nd	3rd	4th
13.2	13.2	14.9	15.6
12.3	11.2	10.0	9.0
14.5	16.1	17.9	22.2
13.7	13.2	13.7	11.9
13.7	14.7	14.5	17.2
15.4	14.5	14.5	13.0
12.7	11.6	11.2	11.8
14.1	15.9	16.4	14.7
13.2	13.3	12.3	14.1
12.5	12.7	13.7	13.7
13.7	12.8	12.7	11.4
13.9	13.9	13.3	14.7
14.9	14.9	14.9	14.1
14.9	16.4	17.2	16.7
14.9	13.9	14.5	15.9
13.7	13.3	13.9	12.8
13.8	13.9	14.1	14.3

b. Input ratio r > 1

A4.3 CODES

FUNCTION TO CALCULATE CORRECTION FACTORS

This function allows estimating the correction factors for a given oil-water flow, provided that the experimental single-phase data is available and that the pipe diameter estimated by the calibration curve at the 100 % water point is also known.

(Beginning)

The function requires 1 arguments: n, which is the page number of the last blank data in the Excel™ file. Typically, n = 16 or 21, corresponding to 3 or 4 oil-flow combinations contained in the same file.

```
function [AVE] = CORRECTION(n)

Definitions.
A=zeros(15360,n);
R=zeros(15360,n);

Sampling frequency and length of the blank, single-phase record. Notice that T = 60 s.
fs=256;
T=60;

Computation of the averages of the single-phase data. The signal is de-trended.
for i=1:5:n
  A(:,i)=xlsread('C_615Feb_1',i); %Name of the file to be writen.
  r(:,i)=REMOVAL(T,fs,A(:,i));
  B(i)=INT_HEI(T,fs,A(:,i));
  R(:,i)=r(:,i)+B(i);
  m(i)=mean(R(:,i));
end

Preparation.
M=nonzeros(m(:));
AVE=zeros(size(M,1)-1,1);

Calculation of correction factors as average of both blank averages.
for j=1:size(AVE,1)
AVE(j)=(M(j+1)+M(j))/2;
fAVE(j)=36.82/AVE(j); 36.428 is the value found in the calibration for full pipe.
end

The function returns a column vector, FAVE, with all the factors in the file.
FAVE=transpose(fAVE);
end
```

(END)

Figure A4.1 MatLab™ code Function to find correction factors

EXPORTING CORRECTED DATA TO EXCEL™

This code simply applies the correction factors to the raw data (page 4 of each oil-water flow) and writes it into the 5th page.

(Beginning)

Calculated correction factors.

```
F=[1.2691; 1.2243;
   1.2230; 1.2347; 1.2489;
   1.2584; 1.2762; 1.2762;
   1.2618; 1.2738; 1.2931; 1.2831];
```

Read raw signal.

```
A=xlsread('C_615Feb_4',19);
```

Apply correction factors.

```
Ac=F(12).*A;
```

Write corrected data.

```
xlswrite('C_615Feb_4',Ac,20);
```

The process requires that the appropriate page number and factor allocation in the matrix be manually introduced for each computation.

(END)

Figure A4.2 MatLab™ code to export corrected data into Excel™ for further analysis

FUNCTION TO DE-TREND CONDUCTANCE PROBE DATA

This function allows removing any trend introduced by the acquisition system. A least-square regression method is employed. For the case of averages, a linear regression has been found sufficient to remove trends.

(Beginning)

The function requires 3 arguments: T, total time of the record (240 s); fs, sampling frequency (256 Hz); and A, the column vector containing the raw probe data.

```
function [U] = REMOVAL(T,fs,A)

Time interval between each data-point.
Delta_t=1/fs;

Total number of data-points in the record.
N=T*fs;

Preparation.
n=transpose(1:N);
U=zeros(N,1);
sum1=sum(A);
sum2=sum(n.*A);

Least-square, regression coefficients.
B0=((2*((2*N)+1)*sum1)-(6*sum2))/(N*(N-1));
B1=((12*sum2)-((6*(N+1))*sum1))/(Delta_t*N*(N-1)*(N+1));

The function returns a column vector, U (N,1), with all data de-trended
for j=1:N
  U(j)=A(j)-(B0+B1*(j*Delta_t));
end

end
```

(END)

Figure A4.3 MatLab™ code Function to de-trend conductance probe data

FUNCTION TO CALCULATE THE INTERCEPT OF THE LEAST-SQUARE REGRESSION

This function provides the intercept of the linear regression used to de-trend the experimental data (i.e of averages). This is a convenient function to use in the code estimation of time-averaged interface height.

(Beginning)

The function requires 3 arguments: T, total time of the record (240 s); fs, sampling frequency (256 Hz); and A, the column vector containing the raw probe data.

```
function [B0] = INT_HEI(T,fs,A)
```

Time interval between each data-point.

```
Delta_t=1/fs;
```

Total number of data-points in the record.

```
N=T*fs;
```

Preparation.

```
n=transpose(1:N);
U=zeros(N,1);
sum1=sum(A);
sum2=sum(n.*A);
```

Least-square, intercept coefficient.

```
B0=((2*((2*N)+1)*sum1)-(6*sum2))/(N*(N-1));

end
```

(END)

Figure A4.4 MatLab™ code Function to calculate the intercept of the least-square regression

FUNCTION TO BREAK THE DATA RECORD IN SUB-INTERVALS

This function readily breaks the data record in convenient sub-intervals to be used in the codes to estimate time-averaged interfaces or spectra.

(Beginning)

The function requires 4 arguments: T, total time of the record (240 s); t, length of each sub-interval (12 s); fs, sampling frequency (256 Hz); and A, the column vector containing the de-trended data.

```
function [V] = BREK(T,t,fs,A)

Number of subintervals.
n=T/t;

Data-points in each sub-interval.
N=fs*t;

The function returns a matrix V (n,N).
V=zeros(n,N);

for i=1:n
  V(i,1:N)=A(i*N-N+1:i*N);
end

end
```

(END)

Figure A4.5 MatLab™ code Function to break the data record in sub-intervals

FUNCTION TO CALCULATE THE t-STUDENT PARAMETER

This function readily calculates the t-Student parameter of a sequence of average values. The code is used in the estimation of the interface height of oil-water interfaces and confidence intervals.

(Beginning)

The function requires 4 arguments: n, total number of values (i.e. sub-intervals or averages); a, average of an individual sub-interval; m, average of all averages; and s, standard deviation of all averages.

```
function [t] = T_Student(n,a,m,s)
```

The function returns a real number (t-Student parameter).

```
t=((abs(a-m))*sqrt(n))/s;

end
```

(END)

Figure A4.6 MatLab™ code Function to calculate the t parameter

ESTIMATION OF INTERFACE HEIGHT AND CONFIDENCE INTERVALS

This code computes the equilibrium interface height of oil-water flows from conductance probe data (4-min samples, collected at 256 Hz). After treatment, the record is broken into 20 12-s intervals and means are estimated for each. The normality of the sub-sample of means is ensured using t-Student distribution. Time-averaged interface height and confidence intervals for the mean value are estimated.

(Beginning)

Sampling period (240 s).
```
T=240;
```
Length of intervals (12 s).
```
t=12;
```
Total number of intervals (240).
```
n=T/t;
```

Data is read from a convenient Excel file and converted in matrix form for analysis.
```
x=xlsread('C_11Oct_2',10);
```

The function "REMOVAL" was previously created to remove the trend of raw signal data. Idem for function "INT_HEI".
```
Re=REMOVAL(240,256,x);
B0=INT_HEI(T,256,C);
R=Re+B0;
```

The sample in 240 intervals of 12 second each. Each sub-interval is verified to be stationary.
```
c=BREK(T,t,256,R);
```

Working matrix.
```
ic=zeros(n,1);
```

Matrix of averages of each sub-interval and average and standard deviation of averages.
```
for j=1:n
  ic(j)=mean(c(j,:));
end

Ic=transpose(ic);
I=Ic;
M=mean(I);
S=std(I);
```

Calculation of the t-Student parameter of each sub-interval using the function "T_Student".
```
T=T_Student(size(I,1),I(:),M,S);
sol=zeros(size(I,2),2);
sol(:,1)=I(:);
sol(:,2)=T(:);
```

Figure A4.7 MatLab™ code Interface height and confidence intervals

ESTIMATION OF INTERFACE HEIGHT AND CONFIDENCE INTERVALS

This code computes the equilibrium interface height of oil-water flows from conductance probe data (4-min samples, collected at 256 Hz). After treatment, the record is broken into 20 12-s intervals and means are estimated for each. The normality of the sub-sample of means is ensured using t-Student distribution. Time-averaged interface height and confidence intervals for the mean value are estimated.

(Cont.)

Percentiles of t-Student at 0.95 (to ensure 90 % confidence level).

```
t_Stu=[1,0; 2,6.314; 3,2.920; 4,2.353; 5,2.132; 6,2.015; 7,1.943; 8,1.895;
9,1.860; 10,1.833; 11,1.812; 12,1.796; 13,1.782; 14,1.771; 15,1.761;
16,1.753; 17,1.746; 18,1.740; 19,1.734; 20,1.729];
```

Sieve of sub-interval averages that do not comply with t-Student criterion.

```
st=zeros(size(I,2),2);

for j=1:size(I,2)
  x(j)=T(j)-t_Stu(n,2);
    if (x(j)<0)
       st(j,1)=j;
       st(j,2)=I(j);
    end
end

St=[nonzeros(st(:,1)),nonzeros(st(:,2))];
Si=size(St,1);
mst=mean(St(:,2));
sst=std(St(:,2));
```

Calculation of time-averaged interface height.

```
L_MEAN=((sst*t_Stu(Si,2))/sqrt(Si));
```

Figure A4.7 MatLab™ code Interface height and confidence intervals (Cont.)

ESTIMATION OF INTERFACE HEIGHT AND CONFIDENCE INTERVALS

This code computes the equilibrium interface height of oil-water flows from conductance probe data (4-min samples, collected at 256 Hz). After treatment, the record is broken into 20 12-s intervals and means are estimated for each. The normality of the sub-sample of means is ensured using t-Student distribution. Time-averaged interface height and confidence intervals for the mean value are estimated.

(Cont.)

Confidence intervals of the variance of the calculation can be written in terms of the Chi-Square distribution. To ensure 90 % confidence, the lower and upper percentile limits of the distribution are taken at 0.05 and 0.95, respectively (Bendat and Piersol, 2010). The first term in each bracket is the number of elements, n (i.e. n = df + 1).

```
X_Chi_LOW=[1,0; 2,0; 3,0.10; 4,0.35; 5,0.71; 6,1.15; 7,1.64; 8,2.17; 9,2.73; 10,3.33; 11,3.94; 12,4.57; 13,5.23; 14,5.89; 15,6.57; 16,7.26; 17,7.96; 18,8.67; 19,9.39; 20,10.12];

X_Chi_UPP=[1,0; 2,3.84; 3,5.99; 4,7.81; 5,9.49; 6,11.07; 7,12.59; 8,14.07; 9,15.51; 10,16.92; 11,18.31; 12,19.68; 13,21.03; 14,22.36; 15,23.68; 16,25.00; 17,26.30; 18,27.59; 19,28.87; 20,30.14];

LOW_VAR=(Si*(sst^2))/X_Chi_LOW(Si,2);
UP_VAR=(Si*(sst^2))/X_Chi_UPP(Si,2);

Results.
Res=[mst, L_MEAN; LOW_VAR, UP_VAR];

Interface height and confidence intervals.
RES=[Res(1,1);Res(1,2)];

Confidence intervals of the variance.
RES=[Res(1,3);Res(1,4)];
```

(END)

Figure A4.7 MatLab™ code Interface height and confidence intervals (Cont.)

FUNCTION TO ESTIMATE TIME-AVERAGE WATER FRACTION

This function allows estimating the time-averaged water fraction from the previously estimated interface height.

(Beginning)

The function requires 1 argument, the time-averaged interface height.

```
function [Alpha_water] = ALPHA_WATER (a)

D=36.4;
hbar=a/D;
Hbar=(2*hbar)-1;
Alpha_water=(1/pi)*(pi-acos(Hbar)+Hbar*((1-(Hbar^2))^(0.5)));

end
```

(END)

Figure A4.8 MatLab™ code Function to estimate time-average water fraction

FUNCTION TO ESTIMATE TIME-AVERAGE ACTUAL VELOCITIES

This function calculates the actual velocity of oil and water phases.

(Beginning)

The function requires 3 arguments, the flow rates of oil and water and the time-averaged interface height.

```
function [m] = ACT_VEL(Qo, Qw, a) %ACT_VEL(Qw, Qo, T,fs,a)
```

The function returns a matrix, m, with actual phase velocities.

```
D=36.4;
hbar=a/D;
Hbar=(2*hbar)-1;
Alpha_water=(1/pi)*(pi-acos(Hbar)+Hbar*((1-(Hbar^2))^(0.5)));

Usw=(4*Qw)/(60000*pi*(0.0364^2));
Uso=(4*Qo)/(60000*pi*(0.0364^2));

Uw=Usw/Alpha_water;
Uo=Uso/(1-Alpha_water);

m=[Uo, Uw];

end
```

(END)

Figure A4.9 MatLab™ code Function to estimate actual phase velocities

FUNCTION TO ESTIMATE THE EFFECTIVE DIAMETER

This function calculates the effective diameter of any stratified oil-water flow, needed to estimate the actual Re numbers of the oil and water phases.

(Beginning)

The function requires 2 arguments: a, the time-averaged interface height; and R, the ratio of actual oil-to-water velocities. In gas-liquid, it is usual to present two different definitions of effective diameter depending of R being < 1, > 1 or = 1. In this work, since the superficial velocities of oil and water are similar and of the same order of magnitude, a unique definition for the effective ratio has been used.

```
function [m] = DIA_EFF (a,R)
```

Preparation.

```
D=36.4;
hbar=a/D;
Hbar=(2*hbar)-1;
```

Computation of water fraction.

```
Aw=((D^2)/4)*(pi-acos(Hbar)+Hbar*((1-(Hbar^2))^(0.5)));
Ao=((D^2)/4)*(acos(Hbar)-Hbar*((1-(Hbar^2))^(0.5)));
```

Computation of wetted perimeters.

```
Sw=(D*(pi-acos(Hbar)));
So=(D*acos(Hbar));
Si=D*sqrt(1-(Hbar^2));
```

Computation of the effective diameter.

```
 if R>1
  Do=(4*Ao)/(So+Si);
  Dw=(4*Aw)/(Sw+Si);
    else
    Do=(4*Ao)/(So+Si);
    Dw=(4*Aw)/(Sw+Si);
end
```

The function returns a matrix, m, with the effective diameter for both the oil and water phases.

```
m=[Do, Dw];


end
```

(END)

Figure A4.10 MatLab™ code Function to estimate the effective diameter

FUNCTION TO ESTIMATE TIME-AVERAGE ACTUAL REYNOLDS NUMBERS

This function calculates the actual Re numbers of oil and water phases.

(Beginning)

The function requires 3 arguments, the flow rates of oil and water and the time-averaged interface height.
function [Re] = REYNOLDS (Qo, Qw, a)

Calculation of actual velocities.
V=ACT_VEL(Qo, Qw, a);

Ratio of actual velocities.
R=V(1)/V(2);

Calculation of effective diameter.
D=DIA_EFF(a,R);

Calculation of Re numbers.
Reo=(830*D(1)*V(1))/0.0055;
Rew=(1000*D(2)*V(2))/0.001;

The function returns a matrix, Re, with actual phase velocities.

Re=[Reo,Rew];

end

(END)

Figure A4.11 MatLab™ code Function to estimate actual Reynolds numbers

ESTIMATION OF THE AUTO-CORRELATION FUNCTION WITH TRUNCATION VIA HAMMING WINDOW

This code estimates the auto-correlation function of an experimental record of conductance probe signal using extensively the FFT command in MatLab™. It applies the Hamming window as a truncation procedure.

(Beginning)

Definitions and pre-treatment.

```
x=xlsread('C_9Oct_1',5);
fs=256;
T=240;
r=REMOVAL(T,fs,x);
z=zeros(69632,1);
y=[r;z];
N=61440;
M=2^17;
```

Computation of the auto-correlation function.

```
X=fft(y);
X1=X.*conj(X);
Y=ifft(X1)./M;
W=Y(1:N)*(M/N);
Gx=zeros(size(W,1),1);
```

Application of Hamming window to data collected at time, t < 0.5 s.

```
for i=1:128
  Gx(i)=W(i).*(0.54+(0.46*cos(2*pi*(i/fs))));
end
```

Report of results.

```
x=linspace(0,240,size(Gx,1));
plot(x,Gx);
```

(END)

Figure A4.12 MatLab™ code Interface height and confidence intervals

ESTIMATION OF THE POWER SPECTRUM AND PROPERTIES

This code estimates the power spectrum of conductance probe signal using extensively the FFT command in MatLab™ via previous calculation of the auto-correlation function (Wiener – Khinchine theorem).

It also gives the average power and provides a guide to compute the relative importance of frequency contributions.

(Beginning)

Definitions and pre-treatment.

```
x=xlsread('C_9Oct_1',5);

N=61440;
fs=256;
T=240

r=REMOVAL(T,fs,x);
z=zeros(69632,1); Zero-padding. A few more 0 added (equivalent to 32 s).
y=[r;z];
M=2^17;
```

Computation of the auto-correlation function.

```
X=fft(y);
X1=X.*conj(X);
Y=ifft(X1)./M;
W=Y(1:N);
Gx=zeros(size(W,1),1);
```

Application of Hamming window to data collected at time, t < 0.5 s.

```
for i=1:128
  Gx(i)=W(i).*(0.54+(0.46*cos(2*pi*(i/fs))));
end
```

Figure A4.13 MatLab™ code Estimation of power spectrum and properties

ESTIMATION OF THE POWER SPECTRUM AND PROPERTIES

This code estimates the power spectrum of conductance probe signal using extensively the FFT command in MatLab™ via previous calculation of the auto-correlation function (Wiener – Khinchine theorem).

It also gives the average power and provides a guide to compute the relative importance of frequency contributions.

(Cont.)

Estimate of the spectrum.

```
S=abs(fft(Gx));
```

In order to zoom on the first part of the spectrum (1 - 128 Hz), we divide the record in 2 parts.

```
SS=S(1:N/2);
```

The spectrum calculated is the 2-sided (i.e. it also holds for negative frequencies. This result is a direct consequence of the auto-correlation function being even. By eliminating the negative frequencies, the power of the spectrum increases. The 1-sided spectrum is found by multiplying by 2 the 2-sided (G = 2*SS) Thus:

```
G=2.*SS;
REL=G./max(G);
f=linspace(0,fs/2,N/2);
```

Report of spectrum estimate

```
plot(f,G);
```

Figure A4.13 MatLab™ code Estimation of power spectrum and properties (Cont.)

ESTIMATION OF THE POWER SPECTRUM AND PROPERTIES

This code estimates the power spectrum of conductance probe signal using extensively the FFT command in MatLab™ via previous calculation of the auto-correlation function (Wiener – Khinchine theorem).

It also gives the average power and provides a guide to compute the relative importance of frequency contributions.

(Cont.)

Average power of the random process.
In order to find the total power of the spectrum, all contributions of the spectrum are added. Further, contributions are divided by the total number of data-points just to have a manageable number.

Summation of all frequencies of the spectrum.
```
T=sum(G)/(N/2);
TT=T/max(G);
Twithout = (sum(G)-max(G))/(N/2);
```

This number must be equal to the first term of the auto-correlation function. The factor is needed to eliminate the effect of the zero-padding.

First term of the auto-correlation (Eq. 5.27).
```
A_Corr = Y(1)*(M/N);
```

These values must be equal to the expectation of the square of the signal values.
Expectation of the time-series data (values of the probe signal).
```
Exp_Data = (sum(y.^2))/N;
```

Report of results of average power.
```
RES=[T, A_Corr, Exp_Data];
```

Figure A4.13 MatLab™ code Estimation of power spectrum and properties (Cont.)

ESTIMATION OF THE POWER SPECTRUM AND PROPERTIES

This code estimates the power spectrum of conductance probe signal using extensively the FFT command in MatLab™ via previous calculation of the auto-correlation function (Wiener – Khinchine theorem).

It also gives the average power and provides a guide to compute the relative importance of frequency contributions.

(Cont.)

Computation of power within a range of certain frequencies:
fr = 5, n = 1200
fr = 10, n = 2400
fr = 20, n = 4800
fr = 30, n = 7200
fr = 40, n = 9600
fr = 50, n = 12000
fr = 60, n = 14400
fr = 100, n = 24000

For example, frequencies within 0 – 30 Hz.
```
fr=30;
z=(f/fs)*N;
```

Power.
```
P=sum(G(1:7200))/(N/2);
Pwithout = (sum(G(1:7200))-max(G))/(N/2); Range < 30 Hz..
R=sum(G(2400:7200))/(N/2); Range 10 – 30 Hz
```

Report of fraction power.
```
F = P/T;
FF=R/T;
Fwithout = Pwithout/Twithout;
```

Peaks and contributing frequencies.
```
[pks,locs]=findpeaks(SS);

P=transpose(pks);
L=(transpose(locs)./240);
```

Figure A4.13 MatLab™ code Estimation of power spectrum and properties (Cont.)

ESTIMATION OF THE POWER SPECTRUM AND PROPERTIES

This code estimates the power spectrum of conductance probe signal using extensively the FFT command in MatLab™ via previous calculation of the auto-correlation function (Wiener – Khinchine theorem).

It also gives the average power and provides a guide to compute the relative importance of frequency contributions.

(Cont.)

```
FF = transpose(f);

Weighted average of frequencies of the spectrum in the range 10 – 30 Hz.
WA10 = (sum(G(2400:7200).*FF(2400:7200))) / sum(G(2400:7200));
po10 = round(WA10*240);
Int10 = REL(po10);

Weighted average of frequencies of the spectrum in the range 60 – 100 Hz.
WA60 = (sum(G(14400:24000).*FF(14400:24000))) / sum(G(14400:24000));
po60 = round(WA60*240);
Int60 = REL(po60);

Pump noise (0 Hz – 5 Hz).
WA0 = (sum(G(1:1200).*FF(1:1200)))/sum(G(1:1200));
po0=round(WA0*240);
Int0=REL(po0);

Report of results.
ZZ = [WA10, Int10; WA60, Int60];
ZNoise = [WA0, Int0];
```

(END)

Figure A4.13 MatLab™ code Estimation of power spectrum and properties (Cont.)

APPENDIX 5
TWO-FLUID MODEL

A5.1 MODEL ASSUMPTIONS AND FUNDAMENTAL RELATIONS

The models and assumptions proposed to describe gas-liquid flows have been frequently found inadequate to represent liquid-liquid systems and to draw reliable predictions. Differences in density and viscosity of liquids and gasses, larger slip ratios between the gas and liquid phases and the fact that gases are compressible are a few reasons to account for. The initial basis for investigating liquid-liquid flows was established by Neima Brauner and David Moalem Maron, from the University of Tel-Aviv, with a collection of papers aimed at properly modelling the two-phase flow of liquids and improving predictions. The first of these publications was concerned with pressure-driven, stratified oil-water flows in circular pipes and rectangular channels (Brauner and Moalem Maron, 1989). The authors started by showing that the physical system and the parameters of the flow (wetted perimeters and phase velocities) can be described uniquely by the time-average interface height of the flow at equilibrium, steady-state conditions. Figure A5.1 shows a schematic representation of stratified oil-water flows and the relation of the parameters with the interface height is summarized in Table A5.1.

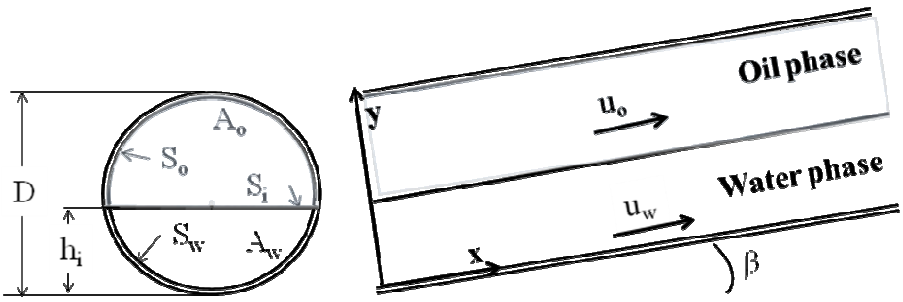

Figure A5.1 Schematic representation of oil-water stratified flow (Brauner and Moalem Maron, 1989)

Table A5.1 Definitions of time-average parameters in pipes
(Brauner and Moalem Maron, 1989)

Parameter	Equation	No.
$\mathbf{A_o}$	$\frac{D^2}{4}\left[\arccos\left(2\frac{h_i}{D}-1\right)-\left(2\frac{h_i}{D}-1\right)\left(\left(1-\left(2\frac{h_i}{D}-1\right)^2\right)^{\frac{1}{2}}\right)\right]$	(A5.1)
$\mathbf{A_w}$	$\frac{D^2}{4}\left[\pi-\arccos\left(2\frac{h_i}{D}-1\right)+\left(2\frac{h_i}{D}-1\right)\left(\left(1-\left(2\frac{h_i}{D}-1\right)^2\right)^{\frac{1}{2}}\right)\right]$	(A5.2)
$\mathbf{S_o}$	$D\left[\arccos\left(2\frac{h_i}{D}-1\right)\right]$	(A5.3)
$\mathbf{S_w}$	$D\left[\pi-\arccos\left(2\frac{h_i}{D}-1\right)\right]$	(A5.4)
$\mathbf{S_i}$	$D\left[1-\left(2\frac{h_i}{D}-1\right)^2\right]^{\frac{1}{2}}$	(A5.5)
$\mathbf{u_o}$	$\frac{\pi u_{s,o}}{\arccos\left(2\frac{h_i}{D}-1\right)-\left(2\frac{h_i}{D}-1\right)\left(\left(1-\left(2\frac{h_i}{D}-1\right)^2\right)^{\frac{1}{2}}\right)}$	(A5.6)
$\mathbf{u_w}$	$\frac{\pi u_{s,w}}{\pi-\arccos\left(2\frac{h_i}{D}-1\right)+\left(2\frac{h_i}{D}-1\right)\left(\left(1-\left(2\frac{h_i}{D}-1\right)^2\right)^{\frac{1}{2}}\right)}$	(A5.7)

The assumptions of the two-fluid model are: 1) the flow of both phases is fully-developed and has reached steady-state; 2) the interface is flat; 3) continuity and momentum of each phase is conserved along the pipe, as well as the continuity and momentum of the mixture; 4) the system is isothermal;5) the flow is pressure-driven and the pressure drop of each phase is equal to each other and to that of the overall mixture. This simple model allows investigating the bulk properties of the flow via the continuity and momentum equations of both phases and produces two pieces of information: the equilibrium interface height and the pressure drop of the mixture.

A5.1.1 Continuity equations

The mass flow rate of oil and water along the pipe shall be constant by virtue of a fundamental axiom of classic mechanics:

$$\rho_o u_{s,o} A = \rho_o u_o A_o \tag{A5.8}$$

$$\rho_w u_{s,w} A = \rho_w u_w A_w , \tag{A5.9}$$

where ρ_o and ρ_w is the density of oil and water, respectively; A is the area of the pipe and A_o and A_w, the section of pipe occupied by only oil and water, respectively, downstream; and u_o and u_w are actual phase velocities. Since liquids are incompressible, the volume flow rate must also be conserved and is immediate from Equations A5.8 and A5.9 that:

$$u_o = \frac{u_{s,o}}{1-\alpha_w} \tag{A5.10}$$

$$u_w = \frac{u_{s,w}}{\alpha_w} \tag{A5.11}$$

$$U_{mix} = u_o(1-\alpha) + u_w\alpha \tag{A5.12}$$

Equations A5.10 – A5.12 represent the continuity of the oil-water, stratified flow model that must be satisfied.

A5.1.2 Momentum equations

The linear momentum of each phase must also be conserved in the model. In its most original form, rooted back in time when the fundamentals of flow dynamics were established by L. Euler (1707 – 1783) and G. Stokes (1819 – 1903), the linear momentum theorem is a thoughtful re-phrase of Newton's Second Law to fluid systems: the acceleration of the flow is the result of all internal and external (or body) forces acting on the fluid. Given the assumption of steady-state, that no acceleration term is present and considering the pressure and shear stresses as internal forces and gravity as the external one, a linear momentum equation can be written for each phase as (Brauner and Moalem Maron, 1989):

$$0 = -A_o\left(\frac{dp}{dx}\right)_o - \tau_{s,o}S_o \mp \tau_{s,i}S_i + \rho_o A_o g \sin\beta \qquad \text{(A5.13)}$$

$$0 = -A_w\left(\frac{dp}{dx}\right)_w - \tau_{s,w}S_w \pm \tau_{s,i}S_i + \rho_w A_w g \sin\beta\,, \qquad \text{(A5.14)}$$

where the subscripts o and w refer to oil and water, respectively; $\frac{dp}{dx}$ is the pressure drop of each phase along the pipe; τ_s, the shear stress per unit of area against the wall wetted by each phase; A_o and A_w, the areas of pipe occupied by the oil and water, respectively; S_o and S_w, the wetted perimeters; ρ is density; and the external forces are included in the last term, with the gravity g and the pipe inclination, β. The upper sign of the double-sign is used when the flow rate of oil is larger than that of water (i.e. r > 1). Otherwise, vice versa. In the present case, since the flows investigated are horizontal, $\beta = 0$ and the contribution of gravity vanishes.

$$0 = -A_o\left(\frac{dp}{dx}\right)_o - \tau_{s,o}S_o \mp \tau_{s,i}S_i \qquad \text{(A5.15)}$$

$$0 = -A_w\left(\frac{dp}{dx}\right)_w - \tau_{s,w}S_w \pm \tau_{s,i}S_i \qquad \text{(A5.16)}$$

Finally, in fully-developed flow, the pressure drop of each phase is taken to be constant and equal to the overall pressure drop of the flow. Combination of Equations A5.15 and A5.16 leads to the momentum relation of the model that must be satisfied:

$$\tau_{s,o}\frac{S_o}{A_o}-\tau_{s,w}\frac{S_w}{A_w}\pm\tau_{s,i}S_i\left(\frac{1}{A_o}+\frac{1}{A_w}\right)=0 \qquad \text{(A5.17)}$$

A5.1.3 Estimation of shear stresses

The wetted parameters S_o, S_w and S_i as well as the areas A_o and A_w can be formally written in terms of the interface height (see Table A5.1). However, in order to solve Equation A5.17, a suitable estimation of the shear stresses is also needed. Brauner and Moalem Maron (1989) use the historical definition that links the shear stresses of the fluids at the wall of the pipe with the kinetic energy per unit of volume of the fluid through a proportional, *friction* factor:

$$\tau_{s,o}=f_o\rho_o\frac{u_o^{\,2}}{2} \qquad \text{(A5.18)}$$

$$\tau_{s,w}=f_o\rho_o\frac{u_w^{\,2}}{2} \qquad \text{(A5.19)}$$

These relationships have been corroborated experimentally in the classic works of Stanton and Pannell (1914) and Moody (1944) and are supported by dimensional analysis. The friction factors, f_o and f_w, are a function of the Re number and represent the resistance encountered by the flow per unit of area. In the model, the friction factors are defined, therefore:

$$f_o=C_o\,Re_o^{\,-n} \qquad \text{(A5.20)}$$

$$f_w=C_w\,Re_w^{\,-n}, \qquad \text{(A5.21)}$$

where C and n are constants taken as C = 16 and n = 1 for laminar flow and C = 0.046 and n = 0.2 for turbulent, in accordance to the results of Moody (1944). The case of laminar flow, as is well-known, can be verified analytically (Hagen, 1839 and Poiseuille, 1846). The values of C are taken as in Brauner and Moalem Maron (1989) but it can be noticed that different friction factors, only different by a factor of 2 or 8, are commonly used in literature and confusion should be avoided. Perhaps, it is worth to indicate that this definition of friction factors, although well-justified, introduces a discontinuity in the model and convergence of iterations when solving Equation A5.17 can be difficult sometimes.

The definition of actual Re numbers is given in terms of the effective or hydraulic diameter. It is usual in gas-liquid literature to propose different definitions of effective diameter for each phase, depending on which one flows faster. However, since superficial velocities of oil and water are of the same order of magnitude in stratified flows, it has been preferred to use one single definition of effective diameter for convenience. Results are affected but, nevertheless, the suggestion is to use the two-fluid model with this modification to compare oil-water data. The Re numbers of both oil and water are, thus, calculated as:

$$\mathrm{Re}_o = \frac{\rho_o u_o}{\mu_o} \frac{4A_o}{S_o + S_i} \tag{A5.22}$$

$$\mathrm{Re}_w = \frac{\rho_w u_w}{\mu_w} \frac{4A_w}{S_w + S_i}, \tag{A5.23}$$

where u_o and u_w are the actual oil and water velocities; ρ and μ are density and viscosity of either oil or water, respectively. All other symbols refer to the usual parameters. In this way, the shear stresses of both phases against the wall pipe can be written in terms of the equilibrium interface height.

A higher level of difficulty exists in finding an acceptable expression for the shear stress at the interface. This has been a matter of discussion for years and still is. Different closure relations have been suggested in both gas-liquid (Taitel, 1976; Barnea and Taitel, 1992; Brauner and Moalem Maron, 1993) and liquid-liquid (Brauner and Moalem Maron, 1992). New techniques, such as Particle Image Velocimetry, might help

in finding better correlations of this parameter, although this optical technique presents its own difficulties in dealing with flows dealing with fluids of different refractive indexes or, particularly, rough interfaces. In this work, the analytical approximation proposed by Brauner and Moalem Maron (1989), constructed *mutatis mutandis* from the definitions in single-phase (Equations A5.18 and A5.19), has been used:

$$\tau_{s,i} = f_i \frac{\rho_i (u_o - u_w)^2}{2} \text{sign}(u_o - u_w), \qquad \text{(A5.24)}$$

where the friction factor at the interface, f_i, and the value ρ_i are taken equal to those of the faster phase.

All the terms in Equation A5.17 can be written in terms of the interface height. The equation shall be satisfied at one unique value between the 0 and the diameter of the pipe, D. An iterative procedure has been conveniently established to find the equilibrium interface height. Flow parameters in steady-state, fully-developed flow were calculated afterwards using relationships in the Table A5.1 and the found value of interface, as well as the pressure drop of the flow using either Equation A5.13 or Equation A5.14. The results, summarized in the following section, have been used in this Thesis to compare against experimental values obtained with the conductance probes. The MatLab™ code developed is included at the end.

A5.2 TWO-FLUID MODEL PREDICTIONS

For 38-mm ID pipes, the two-fluid model predicts a unique relation between the interface height or the water fraction and the oil-to-water input ratio. Only with pipes of smaller diameter, the mixture velocity has seen to affect the relation. Figure A5.2 shows the results with pipes of 38 mm and 14 mm, and comparisons with experimental data available. It seems that the constant line found at 38-mm is the limiting case towards lines of small pipes tend as the mixture velocity increases and the Re numbers based on mixture velocities become turbulent. Similarities and differences in the interface structure of pipes of different diameters (i.e. 14 mm and 38 mm ID) were further investigated during the course of the Thesis and presented in the

International Conference of Multiphase Flow 2013 in Jeju, South Korea (see in "Publications and conference communications").

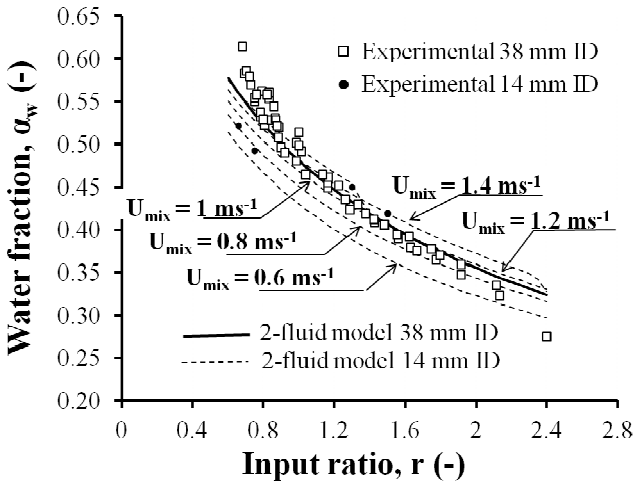

Figure A5.2 Two-fluid model water fraction prediction for different pipe diameters (ρ_o = 830 kgm^{-3}; μ_o = 0.0055 kgm^{-1}s^{-1})

This observation was confirmed when the influence of oil viscosity was investigated in the larger pipe. Figure A5.2 shows that the water fraction – input ratio line predicted by the two-fluid model tends to shift downwards as the viscosity of the oil increases and the Re numbers of the flow, based on mixture velocities, reduce. As the viscosity increases, the calculated values of water fraction tend to change with the mixture velocity towards a constant figure, starting from low input ratios. 2 % differences have been found in the case of μ = 10 cp, at r = 0.6 and 1 % at r = 1. At larger ratios, the same water fraction is predicted at all mixture velocities. In the case of μ = 20 cp, a difference of 3.5 – 4 % has been found across the entire range of input ratios. In Figure A5.3, the lines calculated at μ = 10 cp and μ = 20 cp are averages at each input ratio.

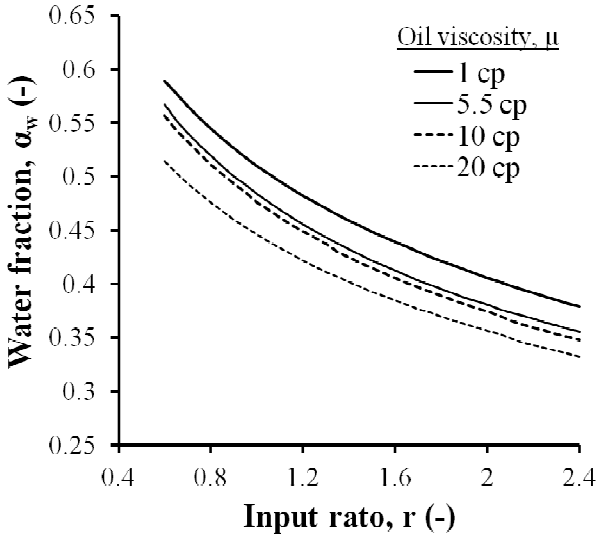

Figure A5.3 Two-fluid model water fraction prediction at different oil viscosities (ρ_o = 830 kgm^{-3}; D = 0.038 m)

On the other side, changes in density, as predicted by the two-fluid model, seem to increase the slope of the water fraction – input ratio line, in a way that the same input fraction of water, for example, would lead the water phase to occupy a smaller portion of the pipe in fully-developed flow (Figure A5. 4).

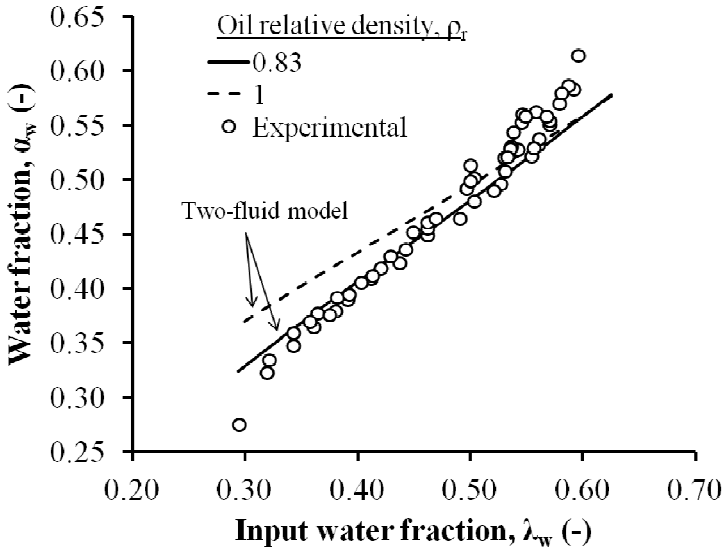

Figure A5.4 Two-fluid model water fraction prediction at different oil densities (μ_o = 0.0055 kgm^{-1}s^{-1}; D = 0.038 m)

Finally, the effect of the oil viscosity on the pressure drop of the stratified flow predicted by the two-fluid model is presented in Figure A5.5. As expected, the pressure drop increases as the flow involves oils more viscous.

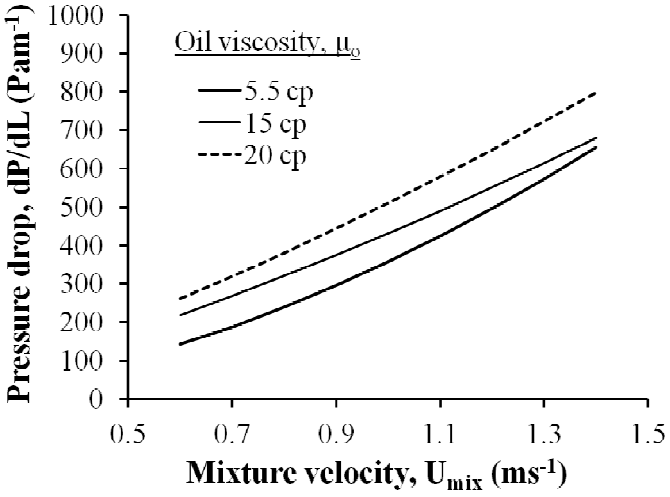

Figure A5.5 Two-fluid model pressure drop prediction at different oil viscosities (ρ_o = 830 kgm^{-3}; D = 0.038 m)

A5.3 MatLab™ CODE

STRATIFIED TWO-FLUID MODEL – ITERATIVE SOLUTION

This code establishes a procedure to estimate the interface height at equilibrium and the pressure drop of the standard model of stratified oil-water flows.

(Beginning)

Definition of pipe geometry.
```
D=0.038;
A=(3.14*D^2)/4;
```
Pipe inclination.
```
beta=0;
```
Gravity.
```
g=9.8;
```

Input parameters. The code calculates interface height and pressure drop for a range of input ratios and mixture velocities for convenience.
```
ra=0.6:0.05:2.4;
r=transpose(ra);

Umixx=0.6:0.1:1.4;
Umix=transpose(Umixx);
```

Fluid properties.
```
DenO=1000;
DenW=830;
VisO=0.0055;
VisW=0.001;
```

Starting point: definition of vector with interface heights for iteration: a 1-micron pass is used (0.001 mm).
```
h1=0.000001:0.000001:D-0.000001;
h=transpose(h1);
H=h./D;
Hbar=(2.*(H))-1;
```

Definition of the matrix containing the solution.
```
Sol=zeros(size(r,1),size(Umix,1));
```

Figure A5.6 MatLab™ code Stratified two-fluid model

STANDARD TWO-FLUID MODEL – ITERATIVE SOLUTION

This code establishes a procedure to estimate the interface height at equilibrium and the pressure drop of oil-water flows.

(Cont.)

This loop repeats the calculation of equilibrium interface height and pressure drop for each r-U_{mix} combination.

```
for k=1:size(r,1)
  for y=1:size(Umix,1)

  Uso=Umix(y)*(r(k)/(1+r(k)));
  Usw=Umix(y)*(1/(1+r(k)));

  Definion of the matrix with values of Eq. Xx for each interface height.
  E=zeros(size(Hbar,1),1);
```

This loop finds the interface height of equilibrium and pressure drop for each r-U_{mix} combination. Parameters of Eq. Xx are calculated for each member of matrix Hbar.

```
for i=1:size(Hbar,1)
  Ao=((D^2)/4)*(acos(Hbar(i))-(Hbar(i)*(sqrt(1-(Hbar(i)^2)))));
  Aw=((3.14*(D^2))/4)-Ao;
  So=D*(acos(Hbar(i)));
  Sw=(3.14*D)-So;
  Si=D*sqrt(1-(Hbar(i)^2));
  Uo=(Uso*A)/Ao;
  Uw=(Usw*A)/Aw;
  Alpha=Aw/A;
  Do=(4*Ao)/(So+Si);
  Dw=(4*Aw)/(Sw+Si);
  R=Uo/Uw;
  Reo=(DenO*Uo*Do)/VisO;
  Rew=(DenW*Uw*Dw)/VisW;
  if  Reo<2000
    fo=16*((Reo)^(-1));
    else
    fo=0.046*((Reo)^(-0.2));
  end
  if Rew<2000
    fw=16*((Rew)^(-1));
    else
    fw=0.046*((Rew)^(-0.2));
  end
  To=(fo*DenO*(Uo^2))/2;
  Tw=(fw*DenW*(Uw^2))/2;
```

Figure A5.6 MatLab™ code Stratified two-fluid model (Cont'd)

STANDARD TWO-FLUID MODEL – ITERATIVE SOLUTION

This code establishes a procedure to estimate the interface height at equilibrium and the pressure drop of oil-water flows.

(Cont.)

```
if R>1
Ti=(fo*DenO*((Uo-Uw)^2))/2;
else
Ti=-(fw*DenW*((Uo-Uw)^2))/2;
end
```

For each value of Hbar, Eq. Xx is computed.

```
 E(i)=((To*(So/Ao))-(Tw*(Sw/Aw))+(Ti*Si*((1/Ao)+(1/Aw)))+
((DenW-DenO)*g*sin(beta*(3.14/180))))^2;
```

End of loop for a combination r-U_{mix}.

```
end

clear m;
clear j;
```

Finally, the minimum value found for Eq. Xx (close to 0), m, and the index in matrix Hbar, j:

```
[m,j]=min(E);
```

Computations below provide interface height and pressure drop for the index j. In this way, the steady-state interface height and pressure drop of the flow can be calculated.

```
Ao=((D^2)/4)*(acos(Hbar(j))-(Hbar(j)*(sqrt(1-(Hbar(j)^2)))));
Aw=((3.14*(D^2))/4)-Ao;
So=D*(acos(Hbar(j)));
Sw=(3.14*D)-So;
Si=D*sqrt(1-(Hbar(j)^2));
Uo=(Uso*A)/Ao;
Uw=(Usw*A)/Aw;
Alpha=Aw/A;
Uo=Uso/(1-Alpha);
Uw=Usw/Alpha;
R=Uo/Uw;
Do=(4*Ao)/(So+Si);
Dw=(4*Aw)/(Sw+Si);
Reo=(DenO*Uo*Do)/VisO;
Rew=(DenW*Uw*Dw)/VisW;
```

Figure A5.6 MatLab™ code Stratified two-fluid model (Cont'd)

STANDARD TWO-FLUID MODEL – ITERATIVE SOLUTION

This code establishes a procedure to estimate the interface height at equilibrium and the pressure drop of oil-water flows.

(Cont.)

```
 if  Reo<2000
 fo=16*((Reo)^(-1));
 else
 fo=0.046*((Reo)^(-0.2));
 end

 if Rew<2000
 fw=16*((Rew)^(-1));
 else
 fw=0.046*((Rew)^(-0.2));
 end

To=(fo*DenO*(Uo^2))/2;
Tw=(fw*DenW*(Uw^2))/2;

 if R>1
 Ti=(fo*DenO*((Uo-Uw)^2))/2;
 else
 Ti=-(fw*DenW*((Uo-Uw)^2))/2;
 end
```

Calculation of the pressure drop of both phases (shall be very similar).

```
Delta_P_o=((To/Ao)*So)-(Ti*Si)+(DenO*Ao*g*sin(beta*(3.14/180)));
Delta_P_w=((Tw/Aw)*Sw)+(Ti*Si)+(DenW*Aw*g*sin(beta*(3.14/180)));
```

Solution for each combination r-U_{mix}.

```
sol=[h(j);Delta_P_o; Delta_P_w];
```

The interface height of all combinations is written in a matrix.

```
Sol_Height(k,y)=h(j);
```

The pressure drop of the mixture of all combinations, calculated as the average of the computed oil and water pressure drops, is written in a matrix.

```
Sol_PressureDrop(k,y)=(Delta_P_o+Delta_P_w)/2;
 clear Delta_P_o;
 clear Delta_P_w;

 end
end

Sol_Height;
```

(END)

Figure A5.6 MatLab™ code Stratified two-fluid model (Cont'd)

APPENDIX 6
CONFERENCE PAPERS

A6.1 INTRODUCTION

The investigation of the oil-water interface and waves at the section inlet was completed with additional and related studies of the flow via collaboration with other Ph.D students or post-doctorate staff. Results were produced in papers accepted for oral communication in Multiphase Flow Conferences. For completeness, the 3 papers are included in this Appendix. The first paper presents PIV results; the second one provides comparisons between two pipes of different diameter; and the last paper investigates the problem of drag-reducing agents in oil-water flows. References are given in the appropriate section.